Part I: Longitudinal Static and Dynamic Effects in Semiconductor Lasers

Part II: Spectral Characteristics of Passively Mode-Locked Quantum Well Lasers

Thesis by

Thomas Schrans

In Partial Fulfillment of the Requirements

for the Degree of

Doctor of Philosophy

California Institute of Technology

Pasadena, California

1994

(Defended on May 23, 1994)

Acknowledgements

During my many years at the California Institute of Technology I have had the opportunity to interact with many interesting people, the first of which is my advisor Professor Amnon Yariv. It has been a great pleasure for me to be able to perform research under his invaluable guidance and expertise in the field of semiconductor lasers. His physical insight, which goes far beyond just the field of optoelectronics, has been of great value to me during my research, as well as his ability to provide the necessary resources and atmosphere for exciting research. His continuous encouragement and his trust in my growing abilities as a scientist will always be appreciated.

It has been a true privilege to be able to work in his creative research group, and special thanks go to Dr. Steve Sanders who introduced me to the experimental world of semiconductor lasers, by teaching me the fabrication and measurement techniques for semiconductor lasers, and by collaborating with me on the mode-locking projects. The fruitful discussions I had with him on the laser modeling of Part I are truly appreciated. Special thanks also go to Dr. Michael Mittelstein who collaborated with me during my early years, and Randy Salvatore with whom I collaborated during the last years on the mode-locking. I would like to thank Dr. Lars Eng, who's MBE expertise was very valuable in many discussions. Many thanks also go to John Iannelli, Dr. David Mehuys, Dr. Bin Zhao, Dr. Chuck Neugebauer, John Kitching, Ali Shakouri, John O'Brien, Richard Boyd, Jing Feng, Dr. T. R. Chen, and Dr. Giora Griffel.

I would like to express my appreciation to Jana Mercado, Ali Ghaffari, Desmond

Armstrong, Kevin Cooper, Paula Samazan, and Linda Dosza, as well as Larry Begay for his technical support.

I would like to acknowledge the support of a one year fellowship from the Belgian American Educational Foundation, allowing me to pursue my doctoral degree in the United States, and I would like to thank Professors Jan Van Bladel, Paul Lagasse and Roel Baets for introducing me to the field of electromagnetics and optoelectronics, and for helping me in obtaining the opportunity of coming to Caltech.

Finally, but not least, I would like to express my deepest appreciation to Khanh Do, who's continuous love and support through the final four years of my graduate student life have helped me through easier and more difficult periods, and to my mother for her love and support during my education from elementary school through graduate school.

Abstract

In the first part of this thesis a study of the effect of the longitudinal distribution of optical intensity and electron density on the static and dynamic behavior of semiconductor lasers is performed. A static model for above threshold operation of a single mode laser, consisting of multiple active and passive sections, is developed by calculating the longitudinal optical intensity distribution and electron density distribution in a self-consistent manner. Feedback from an index and gain Bragg grating is included, as well as feedback from discrete reflections at interfaces and facets. Longitudinal spatial holeburning is analyzed by including the dependence of the gain and the refractive index on the electron density. The mechanisms of spatial holeburning in quarter wave shifted DFB lasers are analyzed. A new laser structure with a uniform optical intensity distribution is introduced and an implementation is simulated, resulting in a large reduction of the longitudinal spatial holeburning effect.

A dynamic small-signal model is then developed by including the optical intensity and electron density distribution, as well as the dependence of the grating coupling coefficients on the electron density. Expressions are derived for the intensity and frequency noise spectrum, the spontaneous emission rate into the lasing mode, the linewidth enhancement factor, and the AM and FM modulation response. Different chirp components are identified in the FM response, and a new adiabatic chirp component is discovered. This new adiabatic chirp component is caused by the nonuniform longitudinal distributions, and is found to dominate at low frequencies. Distributed feedback lasers with partial gain coupling are analyzed, and it is shown how the de-

pendence of the grating coupling coefficients on the electron density can result in an enhancement of the differential gain with an associated enhancement in modulation bandwidth and a reduction in chirp.

In the second part, spectral characteristics of passively mode-locked two-section multiple quantum well laser coupled to an external cavity are studied. Broad-band wavelength tuning using an external grating is demonstrated for the first time in passively mode-locked semiconductor lasers. A record tuning range of 26 nm is measured, with pulse widths of typically a few picosecond and time-bandwidth products of more than 10 times the transform limit. It is then demonstrated that these large time-bandwidth products are due to a strong linear upchirp, by performing pulse compression by a factor of 15 to a record pulse widths as low 320 fs.

A model for pulse propagation through a saturable medium with self-phase-modulation, due to the α-parameter, is developed for quantum well material, including the frequency dependence of the gain medium. This model is used to simulate two-section devices coupled to an external cavity. When no self-phase-modulation is present, it is found that the pulses are asymmetric with a sharper rising edge, that the pulse tails have an exponential behavior, and that the transform limit is 0.3. Inclusion of self-phase-modulation results in a linear upchirp imprinted on the pulse after each round-trip. This linear upchirp is due to a combination of self-phase-modulation in a gain section and absorption of the leading edge of the pulse in the saturable absorber.

Contents

List of Figures

List of Tables

Part I

Longitudinal static and dynamic effects in semiconductor lasers

Chapter 1

Introduction

1.1 High performance optical fiber communication

High speed and long haul optical fiber communication is in most applications limited by the performance of the transmitter. The optical fiber bandwidth extends over several tens of nm at the preferred communication wavelengths of 1.3 μm and 1.55 μm [1], and the bandwidth of erbium doped fiber amplifiers (EDFA) is on the order of 20 nm [2]. The fastest transmitters use Fabry-Perot (FP) or distributed feedback (DFB) lasers for which the highest reported modulation bandwidth is 25 GHz (FP) [3] and 22.5 GHz (DFB) [4] at 1.55 μm, while commercial devices are only reaching into the 10 GHz range. In order to make a more efficient use of the available fiber bandwidth of 2.5 THz (= 20 nm), techniques such as wavelength division multiplexing

(WDM) have to be used [5].

In addition to this limited modulation bandwidth of the transmitter, fiber dispersion and loss [1] play an important role, such that the laser transmitters have to satisfy several of the following conditions to be suitable for high speed, long haul optical communication:

- high power operation
- single longitudinal mode (SLM) operation at high power
- linear dependence of optical power on injection current for analog modulation
- large modulation bandwidth
- low frequency chirping under AM modulation
- narrow linewidth
- low relative intensity noise (RIN)
- and others, such as long lifetime, high temperature operation, low threshold currents, low cost, ...

1.2 Single mode lasers and spatial holeburning

The SLM operation requirement is usually solved by using distributed feedback (DFB) lasers, which use a frequency selective feedback from a Bragg grating, to obtain wavelength predictable SLM operation at threshold [6,7]. As the feedback in DFB

lasers extends over the whole cavity length, the optical intensity is concentrated near the center of the device. This nonuniformity in the optical intensity increases with increasingly stronger gratings as less and less power gets transmitted to the end regions of the device. Through stimulated emission the optical intensity will induce a nonuniformity in the electron density and the associated gain and refractive index, resulting in a power dependent optical cavity. The laser characteristics become power dependent through the nonuniform longitudinal distribution of optical power and electron density [8].

In the last few years a considerable amount of research has concentrated on improving the material parameters (differential gain and α-parameter) [9,10], and the electronic structure (state filling, carrier transport and capture effects) [11,12,13,14], while only a limited effort has concentrated on the effects of the optical cavity and the longitudinal distributions on the lasing characteristics. Most models consider the oversimplified uniform cavity, where the complete optical cavity structure is lumped into one parameter, the photon lifetime. From the above arguments however it is obvious that the longitudinal distributions and their power dependence play an important role in the performance of DFB laser transmitters for high speed and long haul optical communication. One can for example take a FP laser and a DFB laser with the same photon lifetime, and still measure completely different dynamic characteristics as the modal distributions and modal dynamics are different for each laser.

1.3 Outline of part I

In the first part of this thesis, the effects of the longitudinal distributions on the laser characteristics will be investigated. A nonlinear static and dynamic theory for SLM lasers will be developed, where the longitudinal distribution of the power and the electron density will be taken into account in a self-consistent way, as well as the structural effects on the dynamic parameters. Chapter 2 describes the static theory which calculates the power and electron density distribution in a self-consistent manner. Chapter 3 applies this static theory to DFB lasers, and demonstrates how the interaction between the power distribution and the electron density distribution (longitudinal spatial holeburning (LSHB)) affects the static lasing characteristics leading to loss of SLM operation at high power in some cases. Chapter 3 also discusses how the nonlinearity due to LSHB can be reduced, and a new ideal structure that completely eliminates LSHB is introduced and analyzed. Chapter 4 decribes a small-signal dynamic theory including the longitudinal power and electron density distributions, as well as structural effects. This results in an expression for the spontaneous emission linewidth using structural parameters instead of material parameters, and expressions for the intensity and frequency noise spectra. Expressions for the AM and FM modulation response are derived, and different chirp components in the FM response will be identified. This dynamic theory is then applied to a standard DFB laser, and to a partially gain coupled DFB laser where the feedback depends on the electron density.

References

[1] B. E. A. Saleh, and M. C. Teich, **Fundamentals of Photonics**, ch. 8, 22, John Wiley & Sons (1991)

[2] W. J. Miniscalco, *J. Lightw. Technol.*, **9**, 234 (1991)

[3] P. A. Morton, R. A. Logan, T. Tanbun-Ek, P. F. Sciortino, A. M. Sergent, R. K. Montgomery, and B. T. Lee, *Electron. Lett.*, **29**, 136 (1993)

[4] P. A. Morton, T. Tanbun-Ek, R. A. Logan, P. F. Sciortino, A. M. Sergent, and K. W. Wecht, *Electron. Lett.*, **29**, 1429 (1993)

[5] P. E. Green, **Fiber Optic Networks**, Prentice Hall (1993)

[6] H. Kogelnik, and C. V. Shank, *J. Appl. Phys.*, **43**, 2327 (1972)

[7] K. Sekartedjo, N. Eda, K. Furuya, Y. Suematsu, F. Koyama, and T. Tanbun-Ek, *Electron. Lett.*, **20**, 80 (1984)

[8] H. Soda, Y. Kotaki, H. Sudo, H. Ishikawa, S. Yamakoshi, and H. Imai, *IEEE J. Quantum Electron.*, **23**, 804 (1987)

[9] Y. Arakawa, and A. Yariv, *IEEE J. Quantum Electron.*, **21**, 1666 (1985)

[10] L. F. Lester, S. S. O'Keefe, W. J. schaff, and L. F. Eastman, *Electron. Lett.*, **28**, 383 (1992)

[11] W. Rideout, W. F. Sharfin, E. S. Koteles, M. O. Vassel, and B. Elman, *IEEE Photon. Technol. Lett.*, **3**, 784 (1991)

[12] R. Nagarajan, M. Ishikawa, T. Fukushima, R. S. Geels, and J. E. Bowers, *IEEE J. Quantum Electron.*, **28**, 1990 (1992)

[13] S. C. Kan, and K. Y. Lau, *IEEE Photon. Technol. Lett.*, **4**, 528 (1992)

[14] B. Zhao, **Threshold and Dynamics in Semiconductor Quantum Well Lasers**, *Ph. D. Thesis*, California Institute of Technology (1994)

Chapter 2

Nonlinear theory of single longitudinal mode lasers

2.1 Introduction

A nonlinear theory for above threshold operation of single longitudinale mode (SLM) semiconductor lasers is developed in this chapter. The longitudinal dependence of the two counter propagating optical waves and the electron density is included in a self-consistent way through the dependence of the electron density on the optical intensity (resulting in longitudinal spatial holeburning (LSHB)), and the dependence of the gain and the refractive index on the electron density.

It is assumed that all the optical power is contained in one longitudinal mode and the theory fails when a significant amount of power is present in a second mode. To correctly include multi longitudinal mode operation, the amount of spontaneous

emission coupled into each mode has to be taken into account. This will not be considered here, and as a result all the power in the lasing mode is assumed to come from stimulated emission. This assumption simplifies the lasing condition to one that requires that the round-trip gain be equal to 1 in amplitude and phase.

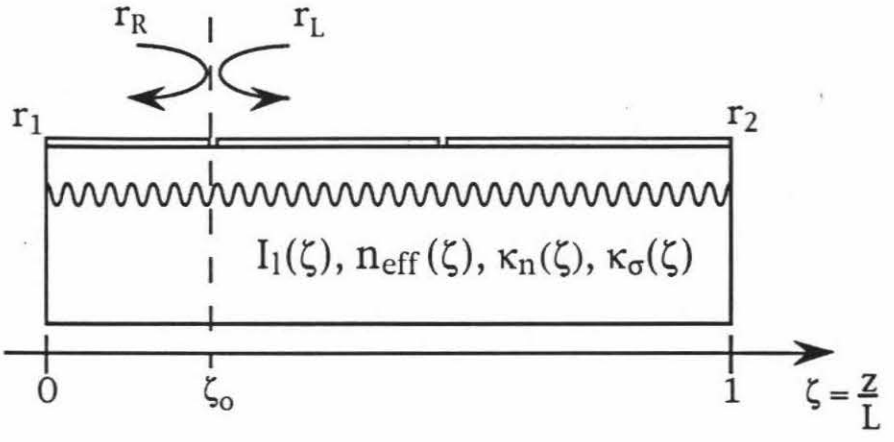

Figure 2.1: General laser structure

The theory can be applied to any combination of active and passive sections including distributed feedback from index and/or gain gratings, as well as discrete reflections from facets or section interfaces (Fig. 2.1). Each section can have z-dependent index ($\kappa_n(z)$) and loss ($\kappa_\sigma(z)$) coupling coefficients, waveguide structure ($n_{eff}(z)$), and current injection ($I_t(z)$), where the z axis represents the longitudinal direction. Each section is characterized by its own specific material parameters, and a discontinuous shift in the grating phase can only occur between two sections. The material gain and the refractive index are assumed to be linear functions of the electron density, and the enhancement of the stimulated emission rate due to the presence of a gain grating is included.

After deriving the relevant equations and describing the solution algorithm, two characteristics of semiconductor lasers are discussed. First a general expression for the external differential efficiency and the optical efficiency is derived and applied to a few simple examples. Finally an expression for the amplified spontaneous emission spectrum is derived.

In recent years several models for DFB lasers above threshold have been developed [1]-[12]. All of them are slightly different, but are based on the same basic ideas used in the theory described below.

2.2 The optical field and the coupled mode equations

In general the optical field in a laser can be described as a superposition of cavity modes with each cavity mode determined by a transverse (or waveguide) mode and a longitudinal mode. Single mode lasers operate in a single waveguide mode and a single longitudinal mode (composed of two counter propagating waves). The electric field $\mathbf{E}$ and magnetic field $\mathbf{H}$ in the frequency domain can then be written as (for simplicity TE-modes are assumed, $\mathbf{E}_{pz} \equiv 0$; for TM modes see appendix A)

$$\mathbf{E}(x,y,z) = \left[a(z)e^{-i\beta_o z} + b(z)e^{+i\beta_o z}\right]\mathbf{E}_{pt}(x,y) \tag{2.1}$$

$$\mathbf{H}(x,y,z) = \left[a(z)e^{-i\beta_o z} - b(z)e^{+i\beta_o z}\right]\mathbf{H}_{pt}(x,y) + \left[a(z)e^{-i\beta_o z} + b(z)e^{+i\beta_o z}\right]\mathbf{H}_{pz}(x,y) \tag{2.2}$$

where $\mathbf{E}_{pt}$, $\mathbf{H}_{pt}$, and $\mathbf{H}_{pz}$ are the transversal and longitudinal component of the waveguide modes for the structure without the grating and zero net gain. The reference wavevector β_o is typically chosen as the Bragg wavevector of the grating, but in absence of a grating, e.g., FP section, the choice of β_o is arbitrary. The complex function $E_F(z) = a(z)e^{-i\beta_o z}$ ($E_B(z) = b(z)e^{+i\beta_o z}$) is the complex amplitude of the forward (backward) propagating wave, and has to satisfy the coupled mode equations, which are derived in appendix A:

$$\frac{da}{d\zeta} = \left[\tilde{\gamma}(\zeta) - i\Delta\tilde{\beta}(\zeta)\right] a(\zeta) + \left[\tilde{\kappa}_n(\zeta) - i\tilde{\kappa}_\sigma(\zeta)\right] e^{-i\phi(\zeta)} b(\zeta) \tag{2.3}$$

$$\frac{db}{d\zeta} = \left[\tilde{\kappa}_n(\zeta) - i\tilde{\kappa}_\sigma(\zeta)\right] e^{+i\phi(\zeta)} a(\zeta) - \left[\tilde{\gamma}(\zeta) - i\Delta\tilde{\beta}(\zeta)\right] b(\zeta) \tag{2.4}$$

with $\zeta = z/L$ (L is the total length of the laser), $\tilde{\gamma}(\zeta) = \gamma(\zeta)L$ the normalized net amplitude gain, $\Delta\tilde{\beta}(\zeta) = \Delta\beta(\zeta)L$ the detuning factor, $\tilde{\kappa}_n(\zeta) = \kappa_n(\zeta)L$ ($\tilde{\kappa}_\sigma(\zeta) = \kappa_\sigma(\zeta)L$) the normalized index (loss) coupling coefficient. The coupling coefficients $\tilde{\kappa}_n$ and $\tilde{\kappa}_\sigma$ are real numbers, and the phase of the grating is included in $\phi(\zeta)$ with the grating given by

$$\sin\left[2\tilde{\beta}_o\zeta + \phi(\zeta)\right] \tag{2.5}$$

where $\tilde{\beta}_o = \beta_o L$ is the normalized reference wavevector, and the ζ-dependence of ϕ allows for chirped gratings, in which case the phase $\phi(\zeta)$ can be split in two parts. A continuous part $\phi_c(\zeta)$ which accounts for the chirp in the grating, and a multiple step function ϕ_s which accounts for the phase shifts in the grating. The local Bragg wavevector $\tilde{\beta}_o(\zeta)$ is then given by

$$\tilde{\beta}_o(\zeta) = \tilde{\beta}_o + \frac{1}{2}\frac{d\phi_c}{d\zeta} \tag{2.6}$$

and the total phase is

$$2\tilde{\beta}_o\zeta + \phi(\zeta) = 2\int_0^{\zeta} \tilde{\beta}_o(\zeta')d\zeta' + \phi_s. \tag{2.7}$$

In order to remove the ζ-dependence in the phase of the coupling coefficient, the following substitution is made in the coupled mode equations (2.3,2.4)

$$\tilde{a}(\zeta) = a(\zeta)e^{\frac{1}{2}i\phi_c(\zeta)} \tag{2.8}$$

$$\tilde{b}(\zeta) = b(\zeta)e^{-\frac{1}{2}i\phi_c(\zeta)} \tag{2.9}$$

giving

$$\frac{d\tilde{a}}{d\zeta} = \left[\tilde{\gamma}(\zeta) - i\Delta\tilde{\beta}'(\zeta)\right]\tilde{a}(\zeta) + \left[\tilde{\kappa}_n(\zeta) - i\tilde{\kappa}_\sigma(\zeta)\right]e^{-i\phi_s}\tilde{b}(\zeta) \tag{2.10}$$

$$\frac{d\tilde{b}}{d\zeta} = \left[\tilde{\kappa}_n(\zeta) - i\tilde{\kappa}_\sigma(\zeta)\right]e^{+i\phi_s}\tilde{a}(\zeta) - \left[\tilde{\gamma}(\zeta) - i\Delta\tilde{\beta}'(\zeta)\right]\tilde{b}(\zeta) \tag{2.11}$$

with the detuning factor $\Delta\tilde{\beta}'(\zeta)$ defined as

$$\Delta\tilde{\beta}'(\zeta) = \Delta\tilde{\beta}(\zeta) - \frac{1}{2}\frac{d\phi_c}{d\zeta} = \Delta\tilde{\beta}(\zeta) + \tilde{\beta}_o - \tilde{\beta}_o(\zeta). \tag{2.12}$$

A chirped grating has the same effect as a ζ-dependent effective index with the only difference being that the chirped grating has a wavelength independent effect on the detuning factor while a variable effective index has a λ^{-1}-dependent effect on the detuning factor. The choice of a chirped grating or a variable effective index will therefore result in a similar effect on the lasing condition and the lasing mode.

The forward and backward propagating waves have to satisfy the boundary conditions at the facets, as well as at interfaces where discrete reflections occur. Any discrete reflection will interfere with the reflection from the grating such that the

relative phase between the grating and the discrete reflection is important. As the grating phase changes over 2π every $\lambda/2$, the interface location has to be known with an accuracy much smaller than $\lambda/2$ ($\sim$ 100nm). The present technologies do not allow localization of interfaces with such an accuracy and the relative phase between discrete reflections and the grating is therefore a random variable. The magnitude of the grating response is much less sensitive to the exact grating length (typically $> 100\lambda$) and can be taken as deterministic. From here on the laser and section lengths are assumed to be deterministic, and a random phase is added to the reflection coefficients of the interfaces and facets. For nonzero discrete reflection coefficients, a statistical analysis in function of the relative phases should be performed to evaluate the laser characteristics.

The boundary conditions at the facets are

$$E_F(0) = r_1 E_B(0) \tag{2.13}$$

$$E_B(1) = r_2 E_F(1) \tag{2.14}$$

with $r_i = \sqrt{R_i} e^{\varphi_i}$ $(i = 1, 2)$, R_i the power reflection coefficient at the facets and φ_i the random phase.

2.3 Solution of the coupled mode equations

The coupled mode equations (2.10)-(2.11) with the boundary conditions (2.13)-(2.14) form an eigenvalue problem with ζ-dependent coefficients in the differential equations. In general this problem has to be solved numerically, as analytical solutions are only

possible in a few specific cases, e.g., constant coefficients. Equations (2.10)-(2.11), (2.13)-(2.14) are solved using the fundamental or transfer matrix approach, where the laser is approximated as a cascade of segments $\Delta\zeta$ of constant $\tilde{\gamma}$, n_{eff}, $\tilde{\kappa}_n$, $\tilde{\kappa}_\sigma$, and ϕ [13].

If E_F and E_B are known on one side of a segment $\Delta\zeta$ with constant coefficients, the coupled mode equations (2.10), (2.11) can be solved to find E_F and E_B on the other side of the segment.

For forward propagation one finds:

$$\begin{bmatrix} E_F(\zeta+\Delta\zeta) \\ E_B(\zeta+\Delta\zeta) \end{bmatrix} = \mathcal{F}(\zeta,\Delta\zeta) \begin{bmatrix} E_F(\zeta) \\ E_B(\zeta) \end{bmatrix} \tag{2.15}$$

and for backward propagation:

$$\begin{bmatrix} E_F(\zeta-\Delta\zeta) \\ E_B(\zeta-\Delta\zeta) \end{bmatrix} = \mathcal{F}(\zeta,-\Delta\zeta) \begin{bmatrix} E_F(\zeta) \\ E_B(\zeta) \end{bmatrix}. \tag{2.16}$$

The transfer matrix $\mathcal{F}$ is given by

$$\mathcal{F}(\zeta,\Delta\zeta) = \begin{bmatrix} e^{-i\tilde{\beta}_o\Delta\zeta}\left(\cosh\tilde{S}\Delta\zeta + \frac{\tilde{\gamma}-i\Delta\tilde{\beta}'}{\tilde{S}}\sinh\tilde{S}\Delta\zeta\right) & e^{-i\tilde{\beta}_o\Delta\zeta}e^{-i\phi_o}\,\frac{\tilde{\kappa}_n-i\tilde{\kappa}_\sigma}{\tilde{S}}\sinh\tilde{S}\Delta\zeta \\ e^{+i\tilde{\beta}_o\Delta\zeta}e^{+i\phi_o}\,\frac{\tilde{\kappa}_n-i\tilde{\kappa}_\sigma}{\tilde{S}}\sinh\tilde{S}\Delta\zeta & e^{+i\tilde{\beta}_o\Delta\zeta}\left(\cosh\tilde{S}\Delta\zeta - \frac{\tilde{\gamma}-i\Delta\tilde{\beta}'}{\tilde{S}}\sinh\tilde{S}\Delta\zeta\right) \end{bmatrix} \tag{2.17}$$

where $\tilde{S}$ is

$$\tilde{S}^2 = \left(\tilde{\gamma}-i\Delta\tilde{\beta}'\right)^2 + (\tilde{\kappa}_n - i\tilde{\kappa}_\sigma)^2 \tag{2.18}$$

and the coefficients $\tilde{\gamma}$, n_{eff}, $\tilde{\kappa}_n$, $\tilde{\kappa}_\sigma$, and $\tilde{\beta}_o$ are sampled at $\zeta+\frac{1}{2}\Delta\zeta$. The phase ϕ_o is the grating phase at $\zeta = m\Delta\zeta$ and is given by

$$\begin{aligned}\phi_o(\zeta = m\Delta\zeta) &= \phi_o\left[(m-1)\,\Delta\zeta\right] + 2\tilde{\beta}_o\left[\left(m-\frac{1}{2}\right)\Delta\zeta\right]\Delta\zeta \\ &\quad + \underbrace{\phi_s\left[m\Delta\zeta\right] - \phi_s\left[(m-1)\,\Delta\zeta\right]}_{\text{phase shift at } m\Delta\zeta} \\ &= \phi(0) + \sum_{1}^{m} 2\tilde{\beta}_{om}\Delta\zeta + \phi_s(m\Delta\zeta) \\ &= 2m\tilde{\beta}_o\Delta\zeta + \phi(m\Delta\zeta) \qquad (2.19)\end{aligned}$$

with $\tilde{\beta}_{om} = \tilde{\beta}_o\left[(m-1/2)\,\Delta\zeta\right]$ and given by

$$\tilde{\beta}_{om} = \tilde{\beta}_o + \frac{\phi_c(m\Delta\zeta) - \phi_c\left((m-1)\Delta\zeta\right)}{2\Delta\zeta}. \qquad (2.20)$$

For chirped gratings the piecewise constant grating approximation has to result in a continuous grating phase, except where physical phase shifts are present. Hence the local Bragg wavevector is approximated as piecewise constant and not the phase. The phase of the grating is approximated as a continuous piecewise linear function.

The boundary conditions at the facets are

$$\begin{bmatrix} E_F(0) \\ E_B(0) \end{bmatrix} = \begin{bmatrix} r_1 \\ 1 \end{bmatrix} \qquad (2.21)$$

and

$$\begin{bmatrix} E_F(1) \\ E_B(1) \end{bmatrix} = \begin{bmatrix} 1 \\ r_2 \end{bmatrix}. \qquad (2.22)$$

The lasing condition requires that the complex round-trip gain G_{rt} of the cavity equals 1, where the round-trip gain is given by $r_L r_R$, where r_L and r_R are the complex reflection coefficients seen from an appropriately chosen reference plane ζ_o (fig. 2.1):

$$r_L = \frac{E_F^L(\zeta_o)}{E_B^L(\zeta_o)} \quad ; \quad r_R = \frac{E_B^R(\zeta_o)}{E_F^R(\zeta_o)} \qquad (2.23)$$

where $E^L_{F,B}(\zeta_o)$ is obtained by forward propagation (2.15) of boundary condition (2.21)

$$\begin{bmatrix} E^L_F(\zeta_o) \\ E^L_B(\zeta_o) \end{bmatrix} = \mathcal{F}(\zeta_o - \Delta\zeta, \Delta\zeta) \cdots \mathcal{F}(0, \Delta\zeta) \begin{bmatrix} r_1 \\ 1 \end{bmatrix} \tag{2.24}$$

and $E^R_{F,B}(\zeta_o)$ by backward propagation (2.16) of boundary condition (2.22)

$$\begin{bmatrix} E^R_F(\zeta_o) \\ E^R_B(\zeta_o) \end{bmatrix} = \mathcal{F}(\zeta_o + \Delta\zeta, -\Delta\zeta) \cdots \mathcal{F}(1, -\Delta\zeta) \begin{bmatrix} 1 \\ r_2 \end{bmatrix}. \tag{2.25}$$

The eigenvalue equation to solve becomes then

$$G_{rt}(\omega, I) = r_L(\omega, I) r_R(\omega, I) = 1 \tag{2.26}$$

with I the total current. In general the round-trip gain G_{rt} depends on the location of the reference plane (fig. 2.1) . When the round-trip gain is equal to 1, however, it is equal to 1 for all locations of the reference plane. Out of numerical considerations however, choice of the reference plane should not be completely arbitrary, but such that $|r_L| \sim |r_R|$. Solution of equation (2.26) at and above threshold will be discussed in section 2.6.

2.4 The gain and the effective index

The net amplitude gain $\tilde{\gamma}$ and the detuning factor $\Delta\tilde{\beta}'$ in the coupled mode equations (2.10)-(2.11) depend on the electron density through the modal gain $\tilde{g}$ and the effective index n_{eff}

$$\tilde{\gamma}(\zeta) = \frac{\tilde{g}(\zeta) - \tilde{\alpha}_i}{2} \tag{2.27}$$

with $\tilde{\alpha}_i = \alpha_i L$ the normalized internal losses, and

$$\Delta\tilde{\beta}'(\zeta) = \frac{\omega}{c} n_{eff}(\zeta) L - \tilde{\beta}_o(\zeta). \tag{2.28}$$

The modal gain is a function of the electron density and the wavelength. The wavelength dependence of the gain will be neglected, as the bandwidth of the gain is usually much larger than the bandwidth of the grating response. In some cases however, e.g., broadly tunable two-section DFB lasers, this approximation is not justified. The material gain g_m is assumed to be linearly dependent on the electron density:

$$g_m(\zeta) = A\,[N(\zeta) - N_o] \tag{2.29}$$

where A is the material differential gain, and N_o the transparency density for a particular section. This assumption is not essential for the theory, but it speeds up the numerical calculations.

The normalized modal gain $\tilde{g}$ is then given by

$$\tilde{g}(\zeta) = \Gamma_o g_m(\zeta) L = \tilde{A}\left[\tilde{N}(\zeta) - 1\right] \tag{2.30}$$

with $\tilde{A}$ the normalized differential gain

$$\tilde{A} = \Gamma_o A N_o L \tag{2.31}$$

Γ_o the optical confinement factor, and $\tilde{N}(\zeta)$ is the normalized electron density

$$\tilde{N}(\zeta) = \frac{N(\zeta)}{N_o}. \tag{2.32}$$

The effective index can be seperated into a component $n_{eff,o}(\zeta)$ that is independent of the electron density, and a component $\Delta n_{eff,N}(\zeta)$ that depends on the electron density.

$$n_{eff}(\zeta) = n_{eff,o}(\zeta) + \Delta n_{eff,N}(\zeta).$$

The ζ-dependence of $n_{eff,o}$ comes from longitudinal variations of the waveguide, and slowly varying average perturbations from the grating (A.67). The component $\Delta n_{eff,N}$ is assumed to vary linearly with the electron density, and in general decreases with increasing electron density.

$$\Delta n_{eff,N}(\zeta) = -\frac{\alpha\lambda\Gamma_o A}{4\pi} N(\zeta)$$

with α the linewidth enhancement factor, which is the ratio of the differential index to the differential gain, and λ the vacuum wavelength.

In normalized parameters, the effective index becomes

$$n_{eff}(\zeta) = n_{eff,o}(\zeta) - \tilde{C}\tilde{N}(\zeta) \tag{2.33}$$

with the normalized differential index $\tilde{C}$ given by

$$\tilde{C} = \frac{\tilde{A}\alpha\lambda}{4\pi L} = \Gamma_o N_o \frac{dn}{dN} \tag{2.34}$$

and dn/dN the material differential index.

2.5 The electron density

2.5.1 The rate equation

The electron density $\tilde{N}(\zeta)$ is determined by a rate equation that takes into account the pumping, the spontaneous emission and the stimulated emission. In steady state ($\partial/\partial t \equiv 0$) this rate equation is

$$0 = \frac{\tilde{I}_l(\zeta)}{LS_a(\zeta)e} - \frac{N_o}{\tau_s}\tilde{N}(\zeta) - v_g g_m(\zeta)p(\zeta) \tag{2.35}$$

with $\tilde{I}_l(\zeta)$ the normalized longitudinal current density, $S_a(\zeta)$ the area of the active layer cross-section, e the electron charge, τ_s the spontaneous recombination lifetime, $p(\zeta)$ the photon density, and v_g the group velocity. Diffusion in the longitudinal direction has been neglected as the electron density does not change much over one diffusion length. For increased speed in the calculations, bimolecular ($\sim N^2$) and Auger ($\sim N^3$) recombination have been neglected.

The total current I is determined by

$$I = \int_0^1 \tilde{I}_l(\zeta)d\zeta + I_{leak} \tag{2.36}$$

with I_{leak} the leakage current.

When an interface of the active layer contains a grating to provide gain coupling, the area S_a of a cross-section of the active layer depends on ζ

$$S_a(\zeta) = \Gamma(\zeta)S_{opt} = \left[\Gamma_o + \Gamma_1 \sin\left(2\tilde{\beta}_o\zeta + \phi\right)\right] S_{opt} \tag{2.37}$$

with S_{opt} the optical mode area, which is not affected by the grating for separate confinement structures.

The total power $P(\zeta)$ in the cavity is related to the photon density $p(\zeta)$ by

$$P(\zeta) = h\nu v_g S_{opt} p(\zeta)$$

with $h\nu$ the photon energy. Substitution in (2.35) gives

$$0 = \tilde{I}_l(\zeta) - \frac{eN_o L S_a(\zeta)}{\tau_s}\tilde{N}(\zeta) - \frac{e}{h\nu}\Gamma(\zeta)\tilde{g}_m(\zeta)P(\zeta). \tag{2.38}$$

The electron density $\tilde{N}$, and thus also the material gain $\tilde{g}_m$, varies slowly over a diffusion length. Seperating all terms in (2.38) into their slowly varying component and their component varying with the grating gives

$$\begin{aligned} 0 \;=\; & \tilde{I}_{lo}(\zeta) + \tilde{I}_{l1}(\zeta)\sin\left(2\tilde{\beta}_o\zeta + \phi\right) \\ & - \frac{V_{opt}N_o e}{\tau_s}\left[\Gamma_o + \Gamma_1\sin\left(2\tilde{\beta}_o\zeta + \phi\right)\right]\tilde{N}(\zeta) \\ & - \frac{e}{h\nu}\tilde{g}_m(\zeta)\left[\Gamma_o + \Gamma_1\sin\left(2\tilde{\beta}_o\zeta + \phi\right)\right]P(\zeta). \end{aligned} \tag{2.39}$$

The total power $P(\zeta)$ is given by

$$P(\zeta) = P_F(\zeta) + P_B(\zeta) + 2\mathcal{C}^2 Re\left[E_F(\zeta)E_B^*(\zeta)\right] \tag{2.40}$$

with $P_F = \mathcal{C}^2|E_F|^2$ ($P_B = \mathcal{C}^2|E_B|^2$) the forward (backward) propagating power, and $\mathcal{C}$ a normalization constant. The third term in (2.40) represents the standing wave (with the * denoting complex conjugate). This standing wave term is usually neglected in the rate equation (2.38), as it has a spatial variation that has a periodicity much shorter than the diffusion length. In the presence of an active layer thickness

modulation ($\Gamma_1 \neq 0$), this standing wave term cannot be neglected, as it mixes with the modal gain modulation and contributes to a slowly varying term in (2.39).

$$\left[\Gamma_o + \Gamma_1 \sin\left(2\tilde{\beta}_o\zeta + \phi\right)\right]\left[P_F(\zeta) + P_B(\zeta) + 2\mathcal{C}^2 Re\left[E_F(\zeta)E_B^*(\zeta)\right]\right] =$$

$$\Gamma_o\left[P_F(\zeta) + P_B(\zeta)\right] + \Gamma_1\mathcal{C}^2 Im\left[e^{i\phi}a(\zeta)b^*(\zeta)\right] + O\left(e^{\pm i2\tilde{\beta}_o\zeta}\right). \qquad (2.41)$$

The second term on the right-hand side in (2.41) is proportional to $Im\left[e^{i\phi}a(\zeta)b^*(\zeta)\right]$, the component of the standing wave that is in phase with the grating. Substituting (2.41) into (2.39) and taking only the slowly varying part gives the following final equation for the electron density

$$0 = \tilde{I}_{lo}(\zeta) - I_{trans}\tilde{N}(\zeta) - \frac{e}{h\nu}\tilde{g}(\zeta)\left[P_F(\zeta) + P_B(\zeta) + \frac{\Gamma_1}{\Gamma_o}\mathcal{C}^2 Im\left[e^{i\phi}a(\zeta)b^*(\zeta)\right]\right] \qquad (2.42)$$

with

$$I_{trans} = \frac{eV_aN_o}{\tau_s} \qquad (2.43)$$

the transparency current, V_a the volume of the active layer, and

$$\tilde{g}(\zeta) = \Gamma_o\tilde{g}_m(\zeta) \qquad (2.44)$$

the modal gain.

The total current can be written as the sum of the spontaneous emission current I_{spon} ,the stimulated emission current I_{stim} and the leakage current I_{leak}.

$$I = I_{spon} + I_{stim} + I_{leak} \qquad (2.45)$$

with (using (2.36) and (2.42))

$$I_{spon} = \int_0^1 I_{trans}\tilde{N}(\zeta)d\zeta \qquad (2.46)$$

$$I_{stim} = \frac{e}{h\nu}\int_0^1 \tilde{g}(\zeta)\left[P_F(\zeta)+P_B(\zeta)+\frac{\Gamma_1}{\Gamma_o}\mathcal{C}^2 Im\left[e^{i\phi}a(\zeta)b^*(\zeta)\right]\right]d\zeta \quad (2.47)$$

$$I_{leak} = (1-\eta_i)\,I \quad (2.48)$$

where η_i is the internal quantum efficiency, and will be taken as 1.

Solving (2.42) for the electron density, using (2.30) for the modal gain gives

$$\tilde{N}(\zeta) = \frac{\tilde{I}_{lo}(\zeta)+\frac{e}{h\nu}\tilde{A}\left[P_F(\zeta)+P_B(\zeta)+\frac{\Gamma_1}{\Gamma_o}\mathcal{C}^2 Im\left[e^{i\phi}a(\zeta)b^*(\zeta)\right]\right]}{I_{trans}+\frac{e}{h\nu}\tilde{A}\left[P_F(\zeta)+P_B(\zeta)+\frac{\Gamma_1}{\Gamma_o}\mathcal{C}^2 Im\left[e^{i\phi}a(\zeta)b^*(\zeta)\right]\right]}. \quad (2.49)$$

2.5.2 The gain coupling coefficient

The modulation ($\Gamma_1 \neq 0$) of the active layer thickness results in a gain and index grating, and can be related to the coupling coefficients $\tilde{\kappa}_\sigma$ and $\tilde{\kappa}_n$. The modulated modal gain can be written as (A.68), (A.70)

$$\begin{aligned}\tilde{g}_{mod}(\zeta) &= \tilde{g}(\zeta)+\tilde{g}(\zeta)\frac{\Gamma_1}{\Gamma_o}\sin\left(2\tilde{\beta}_o\zeta+\phi\right)\\ &= \tilde{g}(\zeta)-4\tilde{\kappa}_{\sigma 1}\sin\left(2\tilde{\beta}_o\zeta+\phi\right).\end{aligned} \quad (2.50)$$

The gain coupling coefficient of the active layer thickness modulation is thus given by

$$\tilde{\kappa}_{\sigma 1}(\zeta) = -\frac{1}{4}\frac{\Gamma_1}{\Gamma_o}\tilde{g}(\zeta). \quad (2.51)$$

The total gain coupling coefficient is the sum of the modal gain modulation $\tilde{\kappa}_{\sigma 1}$ and any other loss modulation $\tilde{\kappa}_{\sigma 2}$

$$\tilde{\kappa}_\sigma(\zeta) = \tilde{\kappa}_{\sigma 1}(\zeta)+\tilde{\kappa}_{\sigma 2}(\zeta). \quad (2.52)$$

For a grating given by (2.5), $\tilde{\kappa}_\sigma$ is positive for a net loss modulation, and negative for a net gain modulation. It is important to note that $\tilde{\kappa}_{\sigma 1}$ depends on the electron

density and will thus be affected by spatial holeburning, while $\tilde{\kappa}_{\sigma 2}$ is independent of the electron density. Gain coupled DFB lasers with the same gain coupling coefficient can have different behaviors above threshold, depending on whether the gain coupling comes from an active layer modulation or from a loss layer modulation. For modulation of the active layer thickness, the coupling coefficient depends on the threshold gain, while the threshold gain depends on the coupling coefficient. The gain coupling coefficient of the laser is thus a priori unknown, and will depend on the laser length and the internal losses [14].

2.6 Solution of the lasing condition

The lasing condition (2.26) has to be solved numerically to determine the lasing wavelength and the total current. Two different cases have to be considered. One is determining the threshold condition, and the other is determining the total current needed for a given power level in the laser. The power level in the laser is set by the output power P_{out1} out of the left facet with

$$P_{out1} = (1 - R_1) \, |E_B(0)|^2. \tag{2.53}$$

The output power P_{out2} out of the right facet is then

$$P_{out2} = (1 - R_2) \, |E_F(1)|^2 \tag{2.54}$$

where the fields $E_{F,B}$ have been normalized such that $\mathcal{C} = 1$

The lasing wavelength will be close to the Bragg wavelength, so a relative deviation

of the Bragg condition will be used as a representation of the wavelength:

$$\Delta\tilde{\beta}_{th} = \frac{2\pi L}{\lambda} n_{eff,th} - \tilde{\beta}_o \tag{2.55}$$

where $n_{eff,th}$ is the average effective index at threshold

$$n_{eff,th} = \int_0^1 n_{eff,th}(\zeta) d\zeta. \tag{2.56}$$

The detuning factor $\Delta\tilde{\beta}'(\zeta)$ (2.28)is then given by

$$\Delta\tilde{\beta}'(\zeta) = \frac{n_{eff}(\zeta)}{n_{eff,th}} \Delta\tilde{\beta}_{th} + \tilde{\beta}_o \left[\frac{n_{eff}(\zeta)}{n_{eff,th}} - \frac{\tilde{\beta}_o(\zeta)}{\tilde{\beta}_o} \right]. \tag{2.57}$$

Tuning of the lasing wavelength due to spatial holeburning will occur for two reasons. The first one is a change in average effective index $n_{eff,av}$ resulting in a change in the average Bragg wavelength. The second one is the nonuniformity in the effective index and the gain resulting in tuning of the wavelength with respect to the average Bragg wavelength. This last effect can be represented by calculating the detuning factor $\Delta\tilde{\beta}_{av}$ with respect to the average Bragg wavelength

$$\begin{aligned} \Delta\tilde{\beta}_{av} &= \frac{2\pi L}{\lambda} n_{eff,av} - \tilde{\beta}_o \\ &= \frac{n_{eff,av}}{n_{eff,th}} \Delta\tilde{\beta}_{th} + \tilde{\beta}_o \left[\frac{n_{eff,av}}{n_{eff,th}} - 1 \right] \end{aligned} \tag{2.58}$$

with $n_{eff,av} = \int_0^1 n_{eff}(\zeta) d\zeta$ depending on the power level.

2.6.1 Solution at threshold

At threshold the stimulated emission rate in the cavity is zero. The total current is equal to the spontaneous emission current, and the electron density is given by (2.49)

$$\tilde{N}(\zeta) = \frac{\tilde{I}_{lo}(\zeta)}{I_{trans}}. \tag{2.59}$$

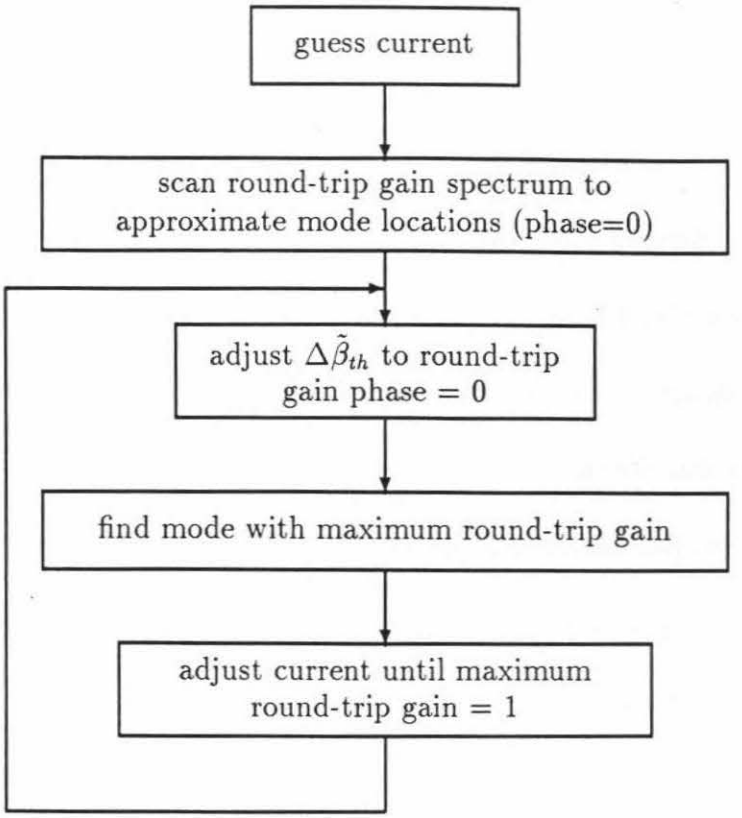

Figure 2.2: Algorithm to solve lasing condition

The lasing condition (2.26) is solved using (2.17), (2.23)-(2.25), (2.27), (2.30), (2.33), (2.45), (2.46), (2.51), (2.52), (2.57) and (2.59) as illustrated in Fig. 2.2. At a fixed total current the longitudinal modes $\Delta\tilde{\beta}_{th}$ for which the phase of the round-trip gain $r_L(\Delta\tilde{\beta}_{th}, I)r_R(\Delta\tilde{\beta}_{th}, I)$ is equal to zero are determined. The longitudinal mode with the maximum round-trip gain magnitude is then determined, after which the current is adjusted to get this maximum round-trip gain equal to 1. Each time the current is changed the modes $\Delta\tilde{\beta}_{th}$ are readjusted to have a round-trip gain phase of zero. This iteration goes on until the current with a maximum modal round-trip gain of 1 is found.

2.6.2 Solution above threshold

Above threshold the current is determined by spontaneous emission as well as stimulated emission. The stimulated emission term in (2.42) depends on the output power (P_{out1}) of the laser, as well as on the field distribution ($E_F(\zeta)$ and $E_B(\zeta)$). The field distribution itself depends on the electron distribution through the effective index (2.33) and the modal gain (2.30). The field distribution will therefore depend on the output power of the laser, and has to be determined self-consistently. The algorithm used to solve for the field distribution is shown in Fig. 2.3. The output power P_{out1} out of the left facet is chosen as the independent variable, and remains fixed to determine the operating point. While keeping the field distribution fixed, the total current is adjusted to satisfy the lasing condition (2.26), using the same algorithm as in the solution at threshold, but with (2.49) instead of (2.59) to determine the electron density. During this iteration only one mode $\Delta\tilde{\beta}_{th}$ is considered. Once the total current that satisfies the lasing condition has been determined, self-consistency of the assumed field distribution and the used field distribution is checked. If the calculated field distribution differs from the used field distribution by more than a predetermined relative error, a new guess for the field distribution is made. This new field distribution can be either the newly calculated field distribution or an average of the calculated and the previously used field distribution. An initial guess for the field distribution is typically either the distribution at threshold or a field distribution self-consistently calculated at another output power P_{out1}. As only one mode was con-

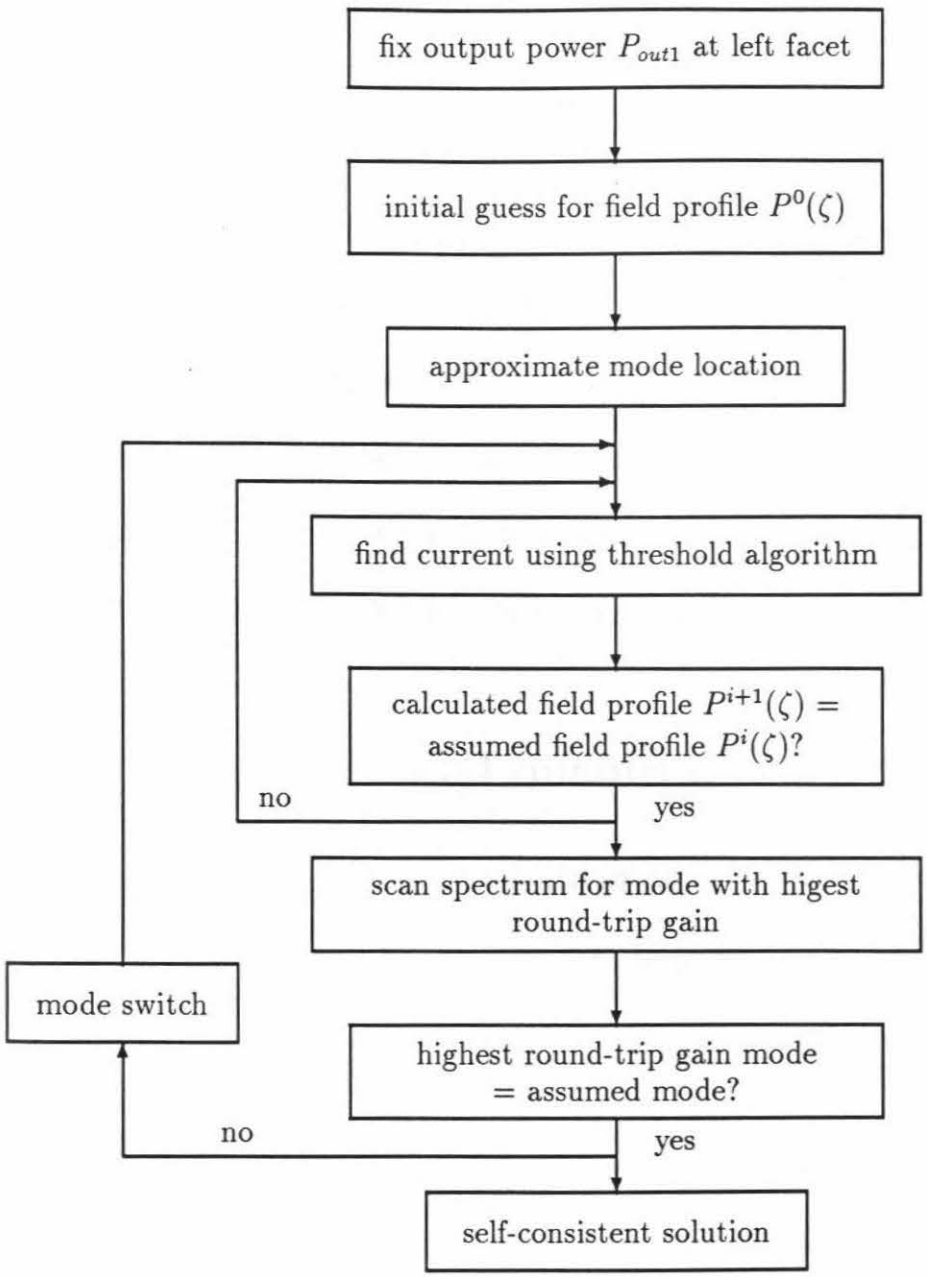

Figure 2.3: Algorithm for self-consistency above threshold

sidered while determining the field distribution, a final check has to be performed on the other longitudinal modes once the field distribution converges. If a longitudinal mode is found with a round-trip gain magnitude larger than 1, the iteration starts over using this new mode. If this new mode turns out to be the maximum round-trip gain mode, it is assumed that a mode switch has occurred. If the algorithm keeps switching between different modes without ever finding the highest round-trip gain mode, then it is assumed that no single mode operation exists. In the case of an actual mode switch, the model is not reliable as it assumes that all the power is present in one mode, while just before the mode switch, and just after the mode switch a considerable amount of power should be present in the side mode. Prediction of mode switches using this model is thus not very accurate.

2.7 The differential quantum efficiency

The external differential efficiency or slope efficiency per facet is defined as the derivative of the output power with respect to the current:

$$\eta_{Di} = \frac{e}{h\nu}\frac{dP_{outi}}{dI}. \tag{2.60}$$

This efficiency can be derived from the measured or calculated L-I characteristics, but it can also be predicted from the optical field distributions. The most general expression published so far for η_D [15]-[16] is only valid for uniform gain and internal losses. In this section a general expression for η_D is derived, including nonunifrom gain and losses, and index and gain coupling.

The slope efficiency η_D is determined by two processes. The first one is the probability that an injected electron will contribute to a photon in the lasing mode, and the second one is the probability that a photon in the lasing mode will end up in one of the two facet output powers. This second probability is called the optical efficiency η_{opt}.

2.7.1 The optical efficiency

Above threshold the flow of photons into the lasing mode at a plane ζ is given by the stimulated emission rate R_{stim} (2.47, 2.51)

$$R_{stim}(\zeta) = \frac{1}{h\nu V_a}\left\{\tilde{g}(\zeta)\left[P_F(\zeta) + P_B(\zeta)\right] - 4\tilde{\kappa}_{\sigma 1}(\zeta)\mathcal{C}^2 Im\left[e^{i\phi}a(\zeta)b^*(\zeta)\right]\right\}. \qquad (2.61)$$

As all the lasing power is assumed to come from stimulated emission, the expressions that will be derived are only valid high enough above threshold.

Using (2.27) the stimulated emission power $P_{stim}(\zeta) = R_{stim}(\zeta)h\nu V_a$ is then equal to

$$P_{stim}(\zeta) = 2\tilde{\gamma}(\zeta)\left[P_F(\zeta) + P_B(\zeta)\right] + \tilde{\alpha}_i\left[P_F(\zeta) + P_B(\zeta)\right] - 4\tilde{\kappa}_{\sigma 1}(\zeta)\mathcal{C}^2 Im\left[e^{i\phi}a(\zeta)b^*(\zeta)\right]. \qquad (2.62)$$

From the coupled mode equations (2.10), (2.11) the following coupled mode equations for the powers can be derived

$$\frac{dP_F}{d\zeta} = 2\tilde{\gamma}(\zeta)P_F(\zeta) + 2\tilde{\kappa}_n(\zeta)\mathcal{C}^2 Re\left[e^{i\phi}a(\zeta)b^*(\zeta)\right] - 2\tilde{\kappa}_\sigma(\zeta)\mathcal{C}^2 Im\left[e^{i\phi}a(\zeta)b^*(\zeta)\right] \tag{2.63}$$

$$-\frac{dP_B}{d\zeta} = 2\tilde{\gamma}(\zeta)P_B(\zeta) - 2\tilde{\kappa}_n(\zeta)\mathcal{C}^2 Re\left[e^{i\phi}a(\zeta)b^*(\zeta)\right] - 2\tilde{\kappa}_\sigma(\zeta)\mathcal{C}^2 Im\left[e^{i\phi}a(\zeta)b^*(\zeta)\right] \tag{2.64}$$

.

The factor $e^{i\phi}a(\zeta)b^*(\zeta)$ is the standing wave pattern of the two counter propagating fields, with its phase referred to the grating phase, such that the imaginary part is the component in phase with the grating and the real part is the component $\pi/2$ out of phase with the grating. Feedback due to index coupling occurs through the out-of-phase component, and is an exchange of power between the forward and the backward waves as the signs in (2.63), (2.64) indicate. On the other hand feedback due to gain coupling occurs through the in-phase component of the standing wave, and is not a simple power exchange between the two counter propagating waves, but rather a modulation at the grating period of the total power distribution. Regions of maximum modal gain experience more stimulated emission than regions of minimum modal gain, and the total gain seen by the the mode is maximum if the standing wave is in phase with the gain grating.

Substituting (2.63), (2.64) into (2.62) to eliminate $\tilde{\gamma}$ gives

$$P_{stim}(\zeta) = \frac{dP_F}{d\zeta} - \frac{dP_B}{d\zeta} + 4\tilde{\kappa}_{\sigma 2}(\zeta)\mathcal{C}^2 Im\left[e^{i\phi}a(\zeta)b^*(\zeta)\right] + \tilde{\alpha}_i\left[P_F(\zeta) + P_B(\zeta)\right] \tag{2.65}$$

where $\tilde{\kappa}_{\sigma 2}$ is the component of the loss coupling coefficient that is independent of the electron density (2.52). The local stimulated emission power $P_{stim}(\zeta)$ contributes to a

growth of the two counter propagating waves (first two terms in (2.65)) and internal losses (last two terms in (2.65)). Depending on the sign of the in phase component of the standing wave, the loss modulation can either increase or decrease the net internal losses.

The total stimulated emission power P_{stim} is found by integrating (2.65) over the total laser length, using (2.53) and (2.54)

$$P_{stim} = P_{out1} + P_{out2} + P_{\alpha_i} + P_{\kappa_\sigma} \tag{2.66}$$

with

$$P_{\alpha_i} = \int_0^1 \tilde{\alpha}_i \left[P_F(\zeta) + P_B(\zeta)\right] d\zeta \tag{2.67}$$

$$P_{\kappa_\sigma} = 4 \int_0^1 \tilde{\kappa}_{\sigma 2}(\zeta) \mathcal{C}^2 Im \left[e^{i\phi} a(\zeta) b^*(\zeta)\right] d\zeta. \tag{2.68}$$

The optical efficiency η_{opti} for facet i is then given by

$$\eta_{opti} = \frac{P_{outi}}{P_{stim}} \qquad (i = 1, 2) \tag{2.69}$$

2.7.2 The external differential efficiency

The optical efficiency relates the output power to the stimulated emission current (2.47) through

$$P_{outi} = \eta_{opti}(I) I_{stim}(I) \frac{h\nu}{e}. \tag{2.70}$$

The optical efficiency and the stimulated emission current depend on the total current due to the dependence of the field distribution on the total current. Using (2.45) and

(2.48) the current dependency of the output power becomes

$$P_{outi} = \frac{h\nu}{e}\eta_{opti}(I)\left[\eta_i I - I_{spon}(I)\right]. \tag{2.71}$$

The external differential efficiency (2.60) is then given by

$$\eta_{Di} = \eta_{opti}\left(\eta_i - \frac{dI_{spon}}{dI}\right) + \frac{d\eta_{opti}}{dI}\left(\eta_i I - I_{spon}\right). \tag{2.72}$$

When spatial holeburning is neglected, the optical efficiency and spontaneous emission current become independent of the total current, and (2.72) reduces to the more familiar expression

$$\eta_{Di} = \eta_{opti}\eta_i. \tag{2.73}$$

It should be noted that through this whole derivation of the external quantum efficiency, the temperature dependence has been neglected and the internal efficiency has been assumed to be constant. This is justified as the object is to study the effect of spatial holeburning on the linearity of the light power versus current characteristic.

2.7.3 Examples

To illustrate the use of (2.67)-(2.69) a few examples will be discussed, using the field distributions at threshold.

Fabry-Perot laser

For a Fabry-Perot laser with facet power reflectivities R_1, R_2 the optical power distribution at threshold is given by

$$P_F(\zeta) = P_F(0)e^{(\bar{g}-\bar{\alpha}_i)\zeta}$$

$$P_B(\zeta) = R_2 e^{2(\tilde{g}-\tilde{\alpha}_i)} P_F(0) e^{-(\tilde{g}-\tilde{\alpha}_i)\zeta}$$

where $\tilde{g}$ is a solution of the lasing condition

$$R_1 R_2 e^{2(\tilde{g}-\tilde{\alpha}_i)} = 1.$$

The optical efficiency η_{opt1} is then given by

$$\eta_{opt1} = \frac{1-R_1}{1-R_1+(1-R_2)\sqrt{\frac{R_1}{R_2}} + \frac{2\tilde{\alpha}_i(\sqrt{R_1R_2}-1)}{ln(R_1R_2)}(\sqrt{\frac{R_1}{R_2}}+1)}$$

and a similar expression for η_{opt2}.

When $R_1 = R_2 = R$ this expression reduces to the familiar

$$\eta_{opt1} = \eta_{opt2} = \frac{1}{2}\frac{ln\left(\frac{1}{R}\right)}{ln\left(\frac{1}{R}\right)+\tilde{\alpha}_i}.$$

Quarter wave shifted DFB laser

The quarter wave shifted (QWS) DFB lasers, which has a phase shift of π in the center of the grating and zero facet reflectivities, lases at the Bragg wavelength at threshold. The optical field distribution is given by

$$\zeta < \tfrac{1}{2} \begin{cases} a(\zeta) = -\tilde{\kappa}_n \sinh\left(\tilde{S}\zeta\right) \\ b(\zeta) = \tilde{S}\cosh\left(\tilde{S}\zeta\right) - \tilde{\gamma}\sinh\left(\tilde{S}\zeta\right) \end{cases}$$

$$\zeta > \tfrac{1}{2} \begin{cases} a(\zeta) = -\tilde{S}\cosh\left[\tilde{S}(1-\zeta)\right] + \tilde{\gamma}\sinh\left[\tilde{S}(1-\zeta)\right] \\ b(\zeta) = \tilde{\kappa}_n \sinh\left[\tilde{S}(1-\zeta)\right] \end{cases}$$

where $\tilde{S}$ is defined in (2.18) and $\tilde{\gamma}$ is a solution of the lasing condition

$$\tilde{\kappa}_n \sinh\left(\frac{\tilde{S}}{2}\right) = \tilde{S}\cosh\left(\frac{\tilde{S}}{2}\right) - \tilde{\gamma}\sinh\left(\frac{\tilde{S}}{2}\right).$$

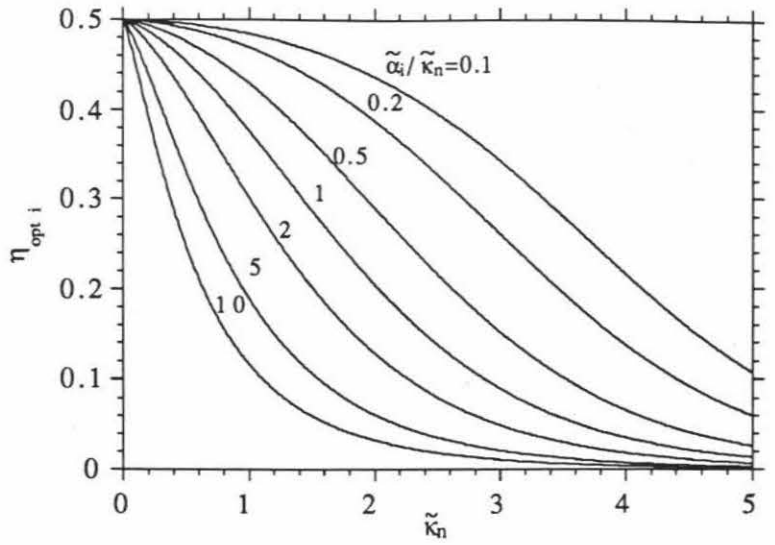

Figure 2.4: Optical efficiency of QWS DFB laser

The powers P_{out1}, P_{out2}, P_{α_i} and P_{κ_σ} are given by

$$\begin{aligned} P_{out1} &= P_{out2} = \tilde{S}^2 \\ P_{\alpha_i} &= 2\tilde{\alpha}_i\tilde{\kappa}_n \sinh^2\left(\frac{\tilde{S}}{2}\right) \\ P_{\kappa_\sigma} &= 0 \end{aligned}$$

and the optical efficiency per facet is

$$\eta_{opt1} = \eta_{opt2} = \frac{1}{2}\frac{\tilde{S}^2}{\tilde{S}^2 + \tilde{\alpha}_i\tilde{\kappa}_n \sinh^2\left(\frac{\tilde{S}}{2}\right)}.$$

The optical efficiency using the threshold fields is shown in fig. 2.4 in function of the normalized index coupling coefficient for different ratio's of internal losses to index coupling coefficient.

Gain or loss coupled DFB laser

Pure ($\tilde{\kappa}_n \equiv 0$) and uniform gain or loss coupled DFB lasers with zero facet reflectivities have their lasing mode at the Bragg wavelength at threshold and their optical fields and powers are given in table 2.1.

	$\lvert\tilde{\kappa}_\sigma\rvert < 1$	$\lvert\tilde{\kappa}_\sigma\rvert = 1$	$\lvert\tilde{\kappa}_\sigma\rvert > 1$
lasing condition	$\sinh\lvert\tilde{S}\rvert = \frac{\lvert\tilde{S}\rvert}{\lvert\tilde{\kappa}_\sigma\rvert}$	$\tilde{\gamma} = 1$	$\sin\lvert\tilde{S}\rvert = \frac{\lvert\tilde{S}\rvert}{\lvert\tilde{\kappa}_\sigma\rvert}$
$P_F(\zeta)$	$\sinh^2\left[\lvert\tilde{S}\rvert\zeta\right]$	ζ^2	$\sin^2\left[\lvert\tilde{S}\rvert\zeta\right]$
$P_B(\zeta)$	$\sinh^2\left[\lvert\tilde{S}\rvert(1-\zeta)\right]$	$(1-\zeta)^2$	$\sin^2\left[\lvert\tilde{S}\rvert(1-\zeta)\right]$
$\mathcal{C}^2 Im\left(e^{i\phi}ab^*\right)$	$\frac{\cosh\left[\lvert\tilde{S}\rvert(2\zeta-1)\right]-\cosh\lvert\tilde{S}\rvert}{2}$	$-\zeta(1-\zeta)$	$\frac{\cos\lvert\tilde{S}\rvert-\cos\left[\lvert\tilde{S}\rvert(2\zeta-1)\right]}{2}$
$\frac{P_{\alpha_i}}{\tilde{\alpha}_i}$	$\frac{\sinh\left[2\lvert\tilde{S}\rvert\right]}{2\lvert\tilde{S}\rvert} - 1$	$\frac{2}{3}$	$1 - \frac{\sin\left[2\lvert\tilde{S}\rvert\right]}{2\lvert\tilde{S}\rvert}$
$\frac{P_{\kappa_\sigma}}{\tilde{\kappa}_{\sigma 2}}$	$\frac{2\sinh\lvert\tilde{S}\rvert}{\lvert\tilde{S}\rvert} - 2\cosh\lvert\tilde{S}\rvert$	$-\frac{2}{3}$	$2\cos\lvert\tilde{S}\rvert - \frac{2\sin\lvert\tilde{S}\rvert}{\lvert\tilde{S}\rvert}$
$P_{out1} = P_{out2}$	$\sinh^2\lvert\tilde{S}\rvert$	1	$\sin^2\lvert\tilde{S}\rvert$

Table 2.1: Power distributions for gain or loss coupled DFB laser

To calculate the optical efficiency, a distinction has to be made between loss coupled DFB's, where the coupling comes from modulation of a loss layer ($\tilde{\kappa}_{\sigma 1} = 0$), and gain coupled DFB's, where the coupling comes from a modulation of the active layer ($\tilde{\kappa}_{\sigma 2} = 0$).

In the first case, loss coupling, the coupling coefficient is independent of the gain and determined by the structure. The lasing condition can be solved in a straightfor-

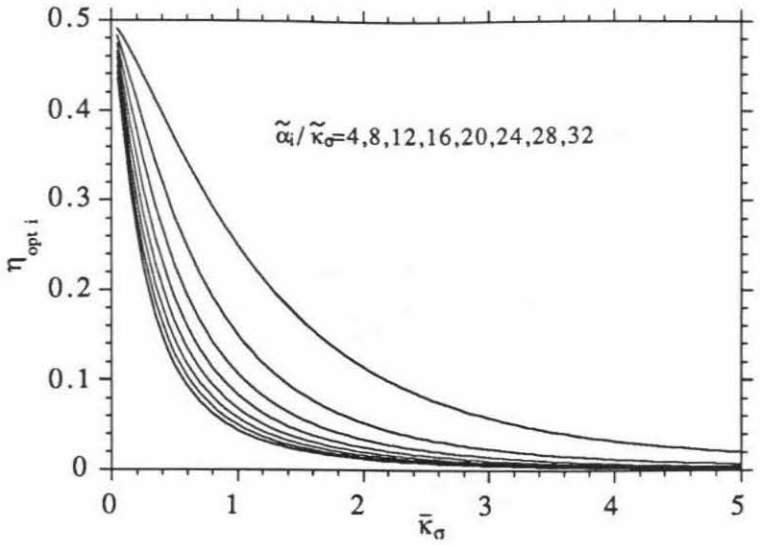

Figure 2.5: Optical efficiency of loss coupled DFB laser

ward way. For a loss modulation the coupling coefficient must satisfy the following relationship with the internal losses:

$$0 \leq \tilde{\kappa}_\sigma \equiv \tilde{\kappa}_{\sigma 2} \leq \frac{\tilde{\alpha}_i}{4}$$

where the last inequality is a requirement to keep the internal loss positive everywhere. Using the expressions from table 2.1, the optical efficiency is given by

$$\eta_{opt1} = \eta_{opt2} = \begin{cases} \dfrac{\sinh^2|\tilde{S}|}{2\sinh^2|\tilde{S}| + \tilde{\alpha}_i\left(\frac{\sinh(2|\tilde{S}|)}{2|\tilde{S}|} - 1\right) + 2\tilde{\kappa}_{\sigma 2}\left(\frac{\sinh|\tilde{S}|}{|\tilde{S}|} - \cosh|\tilde{S}|\right)} & \tilde{\kappa}_{\sigma 2} < 1 \\ \dfrac{3}{4 + 2\tilde{\alpha}_i} & \tilde{\kappa}_{\sigma 2} = 1 \\ \dfrac{\sin^2|\tilde{S}|}{2\sin^2|\tilde{S}| + \tilde{\alpha}_i\left(1 - \frac{\sin(2|\tilde{S}|)}{2|\tilde{S}|}\right) + 2\tilde{\kappa}_{\sigma 2}\left(\cos|\tilde{S}| - \frac{\sin|\tilde{S}|}{|\tilde{S}|}\right)} & \tilde{\kappa}_{\sigma 2} > 1 \end{cases} .$$

For loss coupled lasers P_{κ_σ} is always negative because the standing wave phase is adjusted to minimize the total loss. The optical efficiency for a loss coupled DFB laser is shown in fig. 2.5 in function of the loss coupling coefficient for different ratios

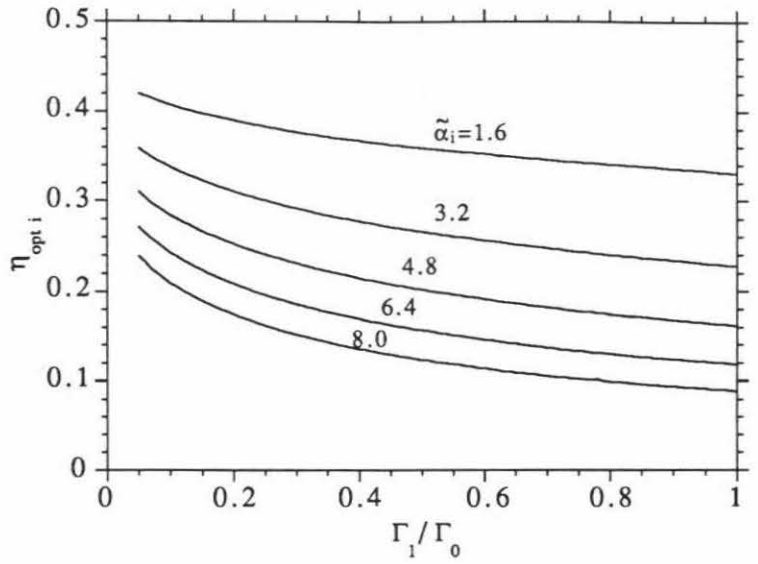

Figure 2.6: Optical efficiency of gain coupled DFB laser

of internal loss to coupling coefficient.

In the case of gain coupling ($\tilde{\kappa}_\sigma \equiv \tilde{\kappa}_{\sigma 1} < 0$), the coupling coefficient depends on the modal gain (2.51) and the lasing condition has to be solved together with

$$\tilde{\gamma} = 2\frac{\Gamma_o}{\Gamma_1}|\tilde{\kappa}_{\sigma 1}| - \frac{1}{2}\tilde{\alpha}_i.$$

For simplicity it is assumed that the internal losses of the cladding layers are the same as the internal losses of the active layer, resulting in $\tilde{\kappa}_{\sigma 2} \equiv 0$. The normalized threshold gain and coupling coefficient depend on the internal losses and the modulation depth of the active layer, and are independent of the total laser length. The optical

efficiency is given by

$$\eta_{opt1} = \eta_{opt2} = \begin{cases} \frac{\sinh^2|\tilde{S}|}{2\sinh^2|\tilde{S}|+\tilde{\alpha}_i\left(\frac{\sinh(2|\tilde{S}|)}{2|\tilde{S}|}-1\right)} & \tilde{\kappa}_{\sigma 1} < 1 \\ \frac{3}{6+2\tilde{\alpha}_i} & \tilde{\kappa}_{\sigma 1} = 1 \\ \frac{\sin^2|\tilde{S}|}{2\sin^2|\tilde{S}|+\tilde{\alpha}_i\left(1-\frac{\sin(2|\tilde{S}|)}{2|\tilde{S}|}\right)} & \tilde{\kappa}_{\sigma 1} > 1 \end{cases} .$$

The optical efficiency for gain coupling is shown in fig. 2.6 in function of the modulation depth of the optical confinement factor for different values of internal loss. For the same magnitude of coupling coefficient, and the same internal losses, loss coupling results in a higher optical efficiency than gain coupling.

2.8 The amplified spontaneous emission spectrum

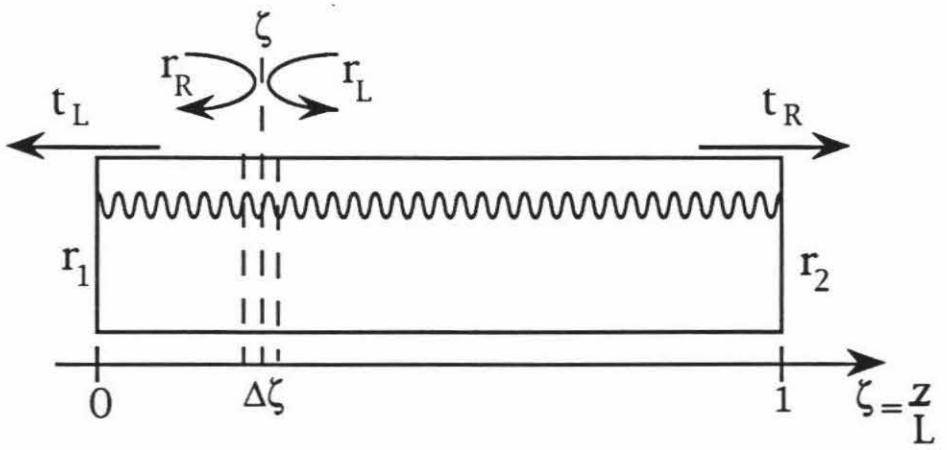

Figure 2.7: Spontaneous emission generated in SLM laser

Below threshold the light emitted by a laser is given by the amplified spontaneous emission (ASE) spectrum . As the power levels are usually low, the effect of stimulated emission on the electron density can be neglected. The ASE spectrum can then be

calculated from a superposition of amplified spontaneous emission from each segment $\Delta\zeta$ [17]-[19]. Each segment $\Delta\zeta$ (Fig. 2.7) has a left and a right complex reflection coefficients $r_L(\omega,\zeta)$, $r_R(\omega,\zeta)$, and complex transmission coefficients $t_L(\omega,\zeta)$, $t_R(\omega,\zeta)$. Each spontaneously emitted photon at plane ζ creates an electric field $E_{ph}(\omega)$. The electric field at the left output facet for such a photon is then given by

$$\begin{aligned} E^R_{out1}(\omega,\zeta) &= t_L(\omega,\zeta)E_{ph}(\omega)\left[1 + r_L r_R + (r_L r_R)^2 + \cdots\right] \\ &= \frac{t_L(\omega,\zeta)E_{ph}(\omega)}{1 - r_L(\omega,\zeta)r_R(\omega,\zeta)} \end{aligned} \tag{2.74}$$

for a photon emitted to the left, and

$$\begin{aligned} E^L_{out1}(\omega,\zeta) &= t_L(\omega,\zeta)r_R(\omega,\zeta)E_{ph}(\omega)\left[1 + r_L r_R + (r_L r_R)^2 + \cdots\right] \\ &= \frac{t_L(\omega,\zeta)r_R(\omega,\zeta)E_{ph}(\omega)}{1 - r_L(\omega,\zeta)r_R(\omega,\zeta)} \end{aligned} \tag{2.75}$$

for a photon emitted to the right, and similar expressions for the electric field at the right output facet. As this is the field from one photon, the electric field can be added. To calculate the total power from the photons emitted at plane ζ, the intensities have to be added. If $R_{spon}(\omega,\zeta)$ is the spontaneous emission rate at plane ζ, then the total power at the left output facet from photons sponteously emitted at plane ζ is given by

$$|E_{out1}(\omega,\zeta)|^2 = \frac{R_{spon}(\omega,\zeta)}{2}\left[\left|E^L_{out1}(\omega,\zeta)\right|^2 + \left|E^R_{out1}(\omega,\zeta)\right|^2\right]. \tag{2.76}$$

The spontaneous emission rate at plane ζ is given by

$$R_{spon}(\omega,\zeta) = \left[\Gamma_o + \Gamma_1 \sin\left(2\tilde{\beta}_o\zeta + \phi\right)\right]\frac{S_{opt}N_o\tilde{N}(\zeta)}{\tau_s} \times f(\omega) \tag{2.77}$$

where $f(\omega)$ is proportional to the lineshape function. The total power at the left output facet from all planes ζ is given by integrating (2.76), using (2.77), and neglecting the fast varying terms in the integrand, as they average out to zero.

$$|E_{out1}(\omega)|^2 = \frac{|E_{ph}(\omega)|^2}{2} \int_0^1 \frac{\Gamma_o S_{opt} N_o \tilde{N}(\zeta)}{\tau_s} f(\omega) \frac{|t_L(\omega,\zeta)|^2 \left[1 + |r_R(\omega,\zeta)|^2\right]}{|1 - r_L(\omega,\zeta) r_R(\omega,\zeta)|^2} d\zeta. \quad (2.78)$$

If the spontaneous emission line shape $f(\omega)$ is much broader than the cavity response, it can be taken as constant, and the relative ASE spectrum $P_{ASEi}(\omega)$ is then given by

$$P_{ASE1}(\omega) = \frac{\int_0^1 \tilde{N}(\zeta) \frac{|t_L(\omega,\zeta)|^2 \left[1+|r_R(\omega,\zeta)|^2\right]}{|1-r_L(\omega,\zeta) r_R(\omega,\zeta)|^2} d\zeta}{\int_0^1 \tilde{N}(\zeta) d\zeta} \quad (2.79)$$

$$P_{ASE2}(\omega) = \frac{\int_0^1 \tilde{N}(\zeta) \frac{|t_R(\omega,\zeta)|^2 \left[1+|r_L(\omega,\zeta)|^2\right]}{|1-r_L(\omega,\zeta) r_R(\omega,\zeta)|^2} d\zeta}{\int_0^1 \tilde{N}(\zeta) d\zeta}. \quad (2.80)$$

The complex reflection and transmission coefficients are given by

$$r_L(\omega,\zeta) = \frac{E_F^L(\omega,\zeta)}{E_B^L(\omega,\zeta)} \quad (2.81)$$

$$r_R(\omega,\zeta) = \frac{E_B^R(\omega,\zeta)}{E_F^R(\omega,\zeta)} \quad (2.82)$$

$$t_L(\omega,\zeta) = \frac{\sqrt{1-R_1}}{E_B^L(\omega,\zeta)} \quad (2.83)$$

$$t_R(\omega,\zeta) = \frac{\sqrt{1-R_2}}{E_F^R(\omega,\zeta)} \quad (2.84)$$

where the fields $E_{F,B}^{L,R}(\omega,\zeta)$ are determined by (2.24)-(2.25).

Above threshold the ASE spectrum can be used to calculate the total lasing spectrum, and the side mode supression ratio, if the self-consistent fields are used and if the total spontaneous emission rate into the lasing mode is known. This total

spontaneous emission rate determines the electron density, which is not clamped to the threshold value, but is always slightly lower due to the presence of spontaneous emission (see section 4.3.2).

References

[1] K. O. Hill, and A. Watanabe, *Appl. Opt.*, **14**, 950 (1975)

[2] H. Soda, Y. Kotaki, H. Sudo, H. Ishikawa, S. Yamakoshi, and H. Imai, *IEEE J. Quaantum Electron.*, **23**, 804 (1987)

[3] Y. Nakano, O. Kamatani, and K. Tada, presented at 11th *IEEE Internat. Semiconductor Laser Conf.*, H2 (1988)

[4] G. P. Agrawal, and A. H. Bobeck, *IEEE J. Quantum electron.*, **24**, 2407 (1988)

[5] M. Okai, S. Tsuji, and N. Chinone, *IEEE J. Quamtum Electron.*, **25**, 1314 (1989)

[6] M. Usami, and S. Akiba, *IEEE J. Quantum Electron.*, **25**, 1245 (1989)

[7] J. E. A. Whiteaway, G. H. B. Thompson, A. J. Collar, and C. J. Armistead, *IEEE J. Quantum Electtron.*, **25**, 1261 (1989)

[8] K. Kikuchi, and H. Tomofuji, *IEEE J. Quantum Electron.*, **26**, 1717 (1990)

[9] P. Vankwikelberge, G. Morthier, and R. Baets, *IEEE J. Quantum Electron.*, **26**, 1728 (1990)

[10] M. G. Davis, and R. F. O'Dowd, *IEEE Photon. Technol. Lett.*, **3**, 603 (1991)

[11] I. Orfanos, T. Sphicopoulos, A. Tsigopoulos, and C. Caroubalos, *IEEE J. Quantum Electron.*, **27**, 946 (1991)

[12] T. Yamanaka, S. Seki, and K. Yokoyama, *IEEE Photon. Technol. Lett.*, **3**, 610 (1991)

[13] M. Yamada, and K. Sakuda, *Appl. Opt.*, **26**, 3474 (1987)

[14] K. David, J. Buus, G. Morthier, and R. Baets, *IEEE Photon. Technol. Lett.*, **3**, 439 (1991)

[15] J. R. Biard, W. N. Carr, and B. S. Reed, *Trans. of the Metallurgical Society of AIME*, **230**, 286 (1964)

[16] D. T. Cassidy *Appl. Optics*, **23**, 2870 (1984)

[17] H. Soda, and H. Imai, *IEEE J. Quantum Electron.*, **22**, 637 (1986)

[18] T. Makino, and J. Glinski, *IEEE J. Quamtum Electron.*, **24**, 1507 (1988)

[19] Y. Nakano, and K. Tada, *IEEE J. Quantum Electron.*, **24**, 2017 (1988)

Chapter 3

Semiconductor lasers with reduced longitudinal spatial holeburning

3.1 Introduction

In the previous chapter a static model for above threshold operation of single longitudinal mode (SLM) semiconductor lasers was developed. This model will now be used to study longitudinal spatial holeburning (LSHB) in quarter wave shifted (QWS) distributed feedback (DFB) lasers. At threshold QWS DFB lasers are SLM; under certain conditions however LSHB can cause loss of stable SLM operation through mode-hopping or multimode operation at higher output powers [1]. If SLM operation is preserved, LSHB will be seen to stabilize at high output powers, resulting in lasing

characteristics that become quasi power independent.

The state of the art for reduction of LSHB will be discussed, resulting in narrow linewidth operation at high output powers. Finally it will be shown that the structures used so far to reduce LSHB cannot completely eliminate LSHB, and new structures will be introduced, resulting in a uniform longitudinal intensity distribution at threshold. These ideal structures are therefore not affected by LSHB and indicate which direction to follow to minimize LSHB.

3.2 Longitudinal spatial holeburning

3.2.1 Single longitudinal mode lasers

High speed coherent optical communication requires a stable, narrow linewidth dynamic SLM light source. The main candidate for such a light source is the DFB semiconductor laser, due to its wavelength selective feedback mechanisme. To achieve SLM operation in DFB lasers the symmetry between the two degenerate lasing modes for a uniform grating [2] has to be broken. Different schemes can be used to achieve SLM operation. The simplest method is to use an asymmetry in the facet reflection phase or magnitude [3,4]. Due to the random nature of the phase of the reflectivity (section 2.2), however the SLM yield is smaller than 100%, and the uncertainty on the lasing wavelength is equal to the grating stopband width. Another more popular scheme, which results in lasing at the Bragg wavelength, is to add a phase shift of π $(= \lambda/4)$ in the grating at the center of the cavity, hence the name quarter wave

shifted (QWS) DFB lasers [5,6].

It is a well known fact [7] that the linewidth gets narrower and the 3dB modulation bandwidth increases with increasing output power. It has also been observed that QWS DFB lasers lose their SLM operation at high output powers for high coupling ($\kappa_n L \equiv \tilde{\kappa}_n$) values [1]. As longer lasers result in narrower linewidths [7], but also in larger $\tilde{\kappa}_n$, and high power operation results in higher modualtion bandwidth, the associated loss of SLM operation at high output powers limits the minimum achievable linewidth in QWS DFB lasers to typically a few MHz, and the modulation bandwidth in DFB lasers to 10–20 GHz. This loss in SLM operation can be explained by LSHB [1]. Due to the nonuniformity of the longitudinal optical intensity distribution the electron density gets depleted more in the center of the laser,where the intensity is maximum, resulting in a "hole" in the longitudinal electron density distribution, hence the name longitudinal spatial holeburning. This nonuniformity in the electron density results in a nonunuformity in the gain distribution, and through the α-parameter [7] in a nonuniform longitudinal effective index distribution. The main effect comes from the nonuniform effective index distribution, which effectively increases the phase shift in the grating [1,8]. As the effective phase shift approaches 2π the DFB laser approaches the behavior of a grating without a phase shift, which has two degenerate lasing modes, resulting in a reduction of the side mode suppression ratio and finally multimode operation. As will be shown later (section 3.2.2), LSHB also results in current (or power) dependent lasing characteristics such as the slope efficiency (nonlinear L-I curves), and lasing wavelength, both undesirable under

analog and digital modulation as they produce chirping and nonlinear modulation distortion.

In the next sections LSHB will be investigated in more detail, organized as follows

1. analysis of LSHB in QWS DFB lasers using the model developed in the previous chapter.

2. discussion of the state of the art in reduction of LSHB

3. analyis and development of new structures with uniform longitudinal intensity distributions, resulting in elimination of LSHB

3.2.2 The quarter wave shifted (QWS) distributed feedback (DFB) laser

A threshold analysis reveals that QWS DFB lasers will lase at the Bragg wavelength for all values of the index coupling coefficient (and $\tilde{\kappa}_\sigma \equiv 0$). The nonuniformity of the longitudinal intensity distribution, and therefore the LSHB, however depends strongly on the value of the normalized index coupling coefficient $\tilde{\kappa}_n$. To characterize the nonununformity of the longitudinal intensity distribution $P_L(\zeta) \equiv P_F(\zeta) + P_B(\zeta)$ a flatness parameter F is defined:

$$F = \frac{1}{< P_L >^2} \int_0^1 [P_L(\zeta) - < P_L >]^2 \, d\zeta \tag{3.1}$$

where $< P_L >$ is the average longitudinal intensity

$$< P_L >= \int_0^1 P_L(\zeta) d\zeta. \tag{3.2}$$

The normalized ($< P_L > \equiv 1$) longitudinal intensity distributions at threshold for $\tilde{\kappa}_n = 1$, 2, and 3 are shown in fig. 3.1 (with F respectively $0.0340, 0.146, 0.537$). From the threshold intensity distributions it is expected that LSHB will have a bigger impact at higher $\tilde{\kappa}_n$ values, and that LSHB should be minimal near $\tilde{\kappa}_n = 1.25$, where the flatness parameter F ($= 0.0116$) is minimal [1].

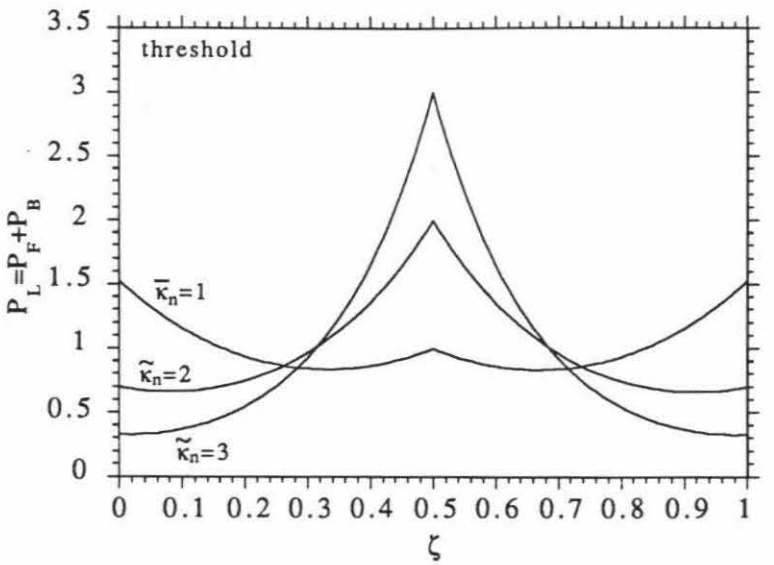

Figure 3.1: Longitudinal power distribution at threshold for $\tilde{\kappa}_n = 1, 2$ and 3

$\tilde{A}$	6.3	$\tilde{C}$	0.0094	$R_1 = R_2$	0
I_{trans}	15.12 mA	$h\nu$	0.8 eV	$\Delta\zeta$	0.01
$\tilde{\alpha}_i$	1.6	$\tilde{\beta}_o$	5323	$n_{eff,o}$	3.283

Table 3.1: Parameter values used for $400\mu m$ long QWS DFB laser

All the calculations above threshold were performed using the parameter values

given in table 3.1 [9] for a $400\mu m$ long laser, and the results are shown in figs. 3.2-3.9.

The output power per facet is shown in fig. 3.2 as a function of the current. For $\tilde{\kappa}_n = 3$, SLM operation is lost just above $2mW$ of output power, while for $\tilde{\kappa}_n = 1$ and 2 SLM operation is maintained up to powers above $20mW$. The L-I curves are superlinear for $\tilde{\kappa}_n = 2$ and 3, and sublinear for $\tilde{\kappa}_n = 1$ due to LSHB. This is evident from the external differential efficiency, shown in fig. 3.3 (solid line) together with the optical efficiency (dashed line) as defined in section 2.7.1. Due to LSHB the optical efficiency η_{opt} and the spontaneous emission current I_{spon} (fig. 3.4) depend on the current I, resulting in an external differential efficiency (2.72) which is different from the optical efficiency near threshold. At high output power the differential efficiency becomes equal to the optical efficiency, but is different from the threshold value.

The normalized detuning factor $\Delta\tilde{\beta}_{th}$ with respect to the Bragg wavelength at threshold, as defined in (2.55), is shown in fig. 3.5. The dependence of the lasing wavelength on the output power , also known as static or adiabatic chirp [10], is due to two effects [11]. The first effect is a shift in average Bragg wavelength due to a shift in average electron density and the corresponding average effective index shift. The second effect is the nonuniformity in the effective index distribution, which pushes the lasing wavelength away from the average Bragg wavelength. The shift in average Bragg wavelength can be deduced from fig. 3.4, as I_{spon} is proportional to the average electron density (2.46). For $\tilde{\kappa}_n = 1$, the average Bragg wavelength increases with power, while it decreases with power for $\tilde{\kappa}_n = 2, 3$. The effect of the nonuniformity in the effective index is illustrated in fig. 3.6 (solid line), with $\Delta\tilde{\beta}_{av}$ the detuning factor

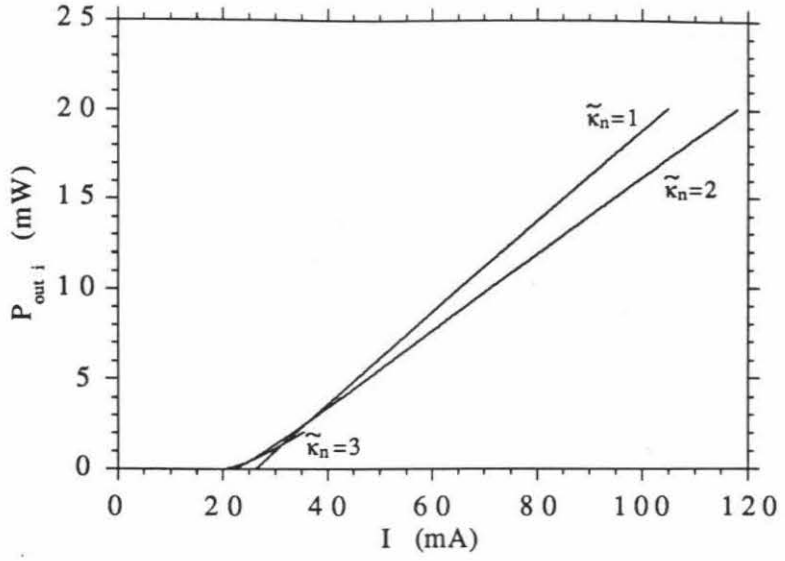

Figure 3.2: Output power per facet as a function of total current for $\tilde{\kappa}_n = 1, 2$ and 3

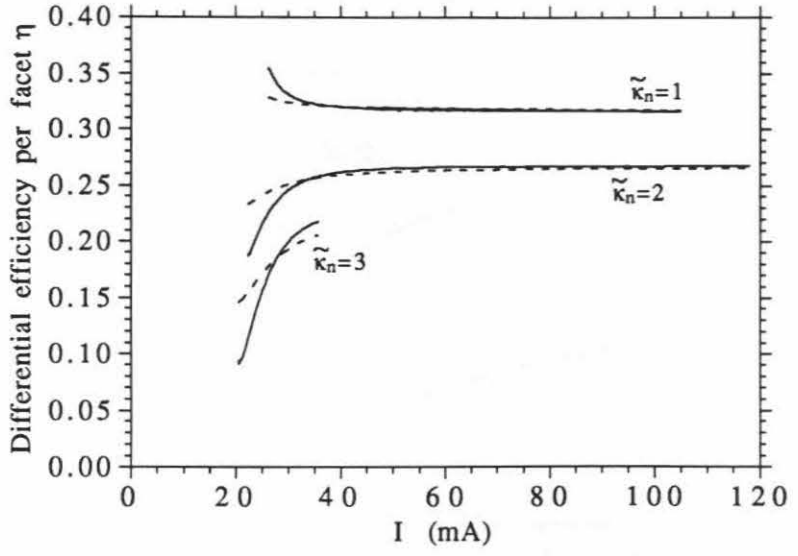

Figure 3.3: External quantum efficiency (solid line) and optical efficiency (dashed line) per facet as a function of total current for $\tilde{\kappa}_n = 1, 2$ and 3

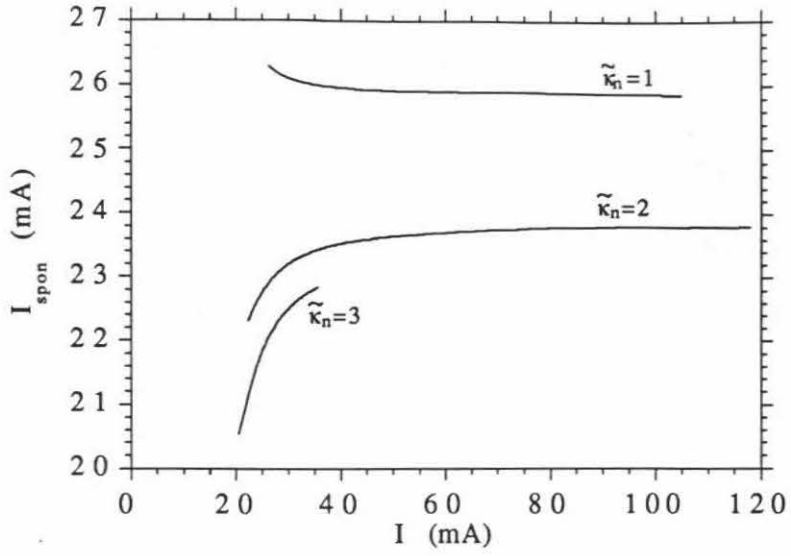

Figure 3.4: Spontaneous emission current as a function of total current for $\tilde{\kappa}_n = 1, 2$ and 3

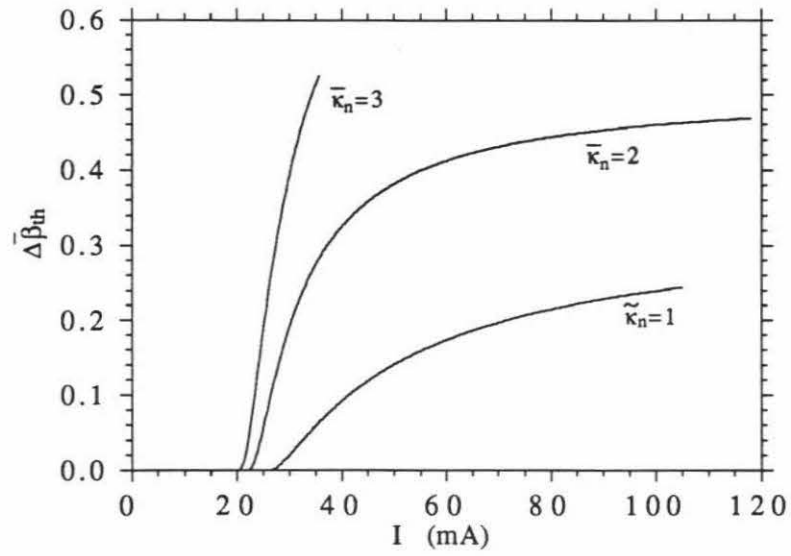

Figure 3.5: Normalized detuning factor relative to threshold Bragg wavelength as a function of total current for $\tilde{\kappa}_n = 1, 2$ and 3

with respect to the average Bragg wavelength, as defined in (2.58).

For $\tilde{\kappa}_n = 1$ the lasing wavelength gets pushed to the short wavelength side of the average Bragg wavelength, while it gets pushed to the long wavelength side for $\tilde{\kappa}_n = 2, 3$. For $\tilde{\kappa}_n = 1$ the effective index in the center of the laser is lower compared to the average effective index (fig. 3.7), and thereby reduces the effective phase shift, resulting in lasing on the short wavelength side of the average Bragg wavelength. For $\tilde{\kappa}_n = 2, 3$ the effective index in the center of the laser is larger compared to the average effective index, resulting in an increase in effective phase shift and lasing on the long wavelength side of the average Bragg wavelength.

The average detuning factor and the round-trip gain of the first side mode are shown in fig. 3.6 (dashed line) and fig. 3.8. For $\tilde{\kappa}_n = 3$ the round-trip gain of the side mode becomes 1 for a total current of about $35mA$, corresponding to about $2mW$ of output power, as the $+1$ side mode moves closer to the average Bragg wavelength, while the lasing mode moves away from the average Bragg wavelength (fig. 3.6), and SLM operation is lost. As discussed in the previous chapter the model cannot be used above this point, as it does not take into account the power present in the side mode. The round-trip gain magnitude (solid line) as a function of the detuning factor $\Delta\tilde{\beta}_{th}$ and the location of the modes (circles) are shown in fig. 3.9 for $\tilde{\kappa}_n = 3$ at different power levels.

For increasing power levels, LSHB decreases the effective index near the facets relative to the average effective index (fig. 3.7). The local Bragg wavelength near the facets decreases resulting in a larger round-trip gain for shorter wavelengths, or posi-

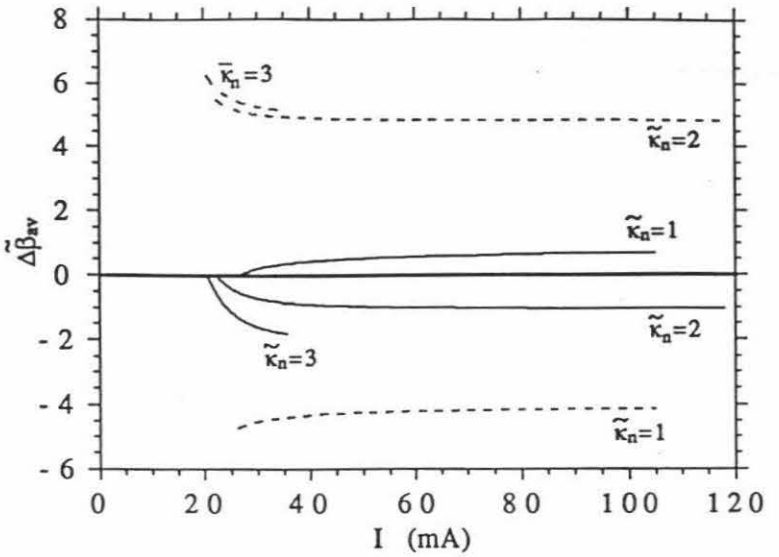

Figure 3.6: Normalized detuning factor relative to average Bragg wavelength as a function of total current for $\tilde{\kappa}_n = 1, 2$ and 3

Solid line: lasing mode; dashed line: first sidemode

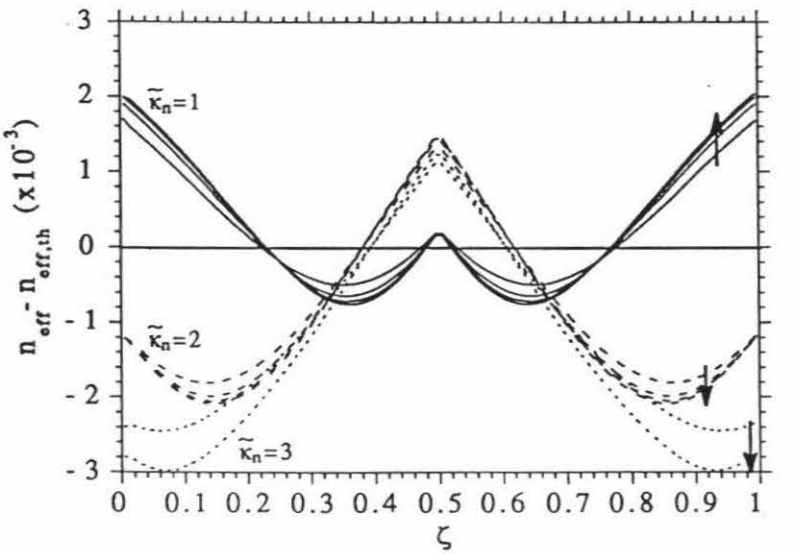

Figure 3.7: Longitudinal effective index distribution for $\tilde{\kappa}_n = 1, 2$ and 3 at different power levels with arrows indicating increasing power

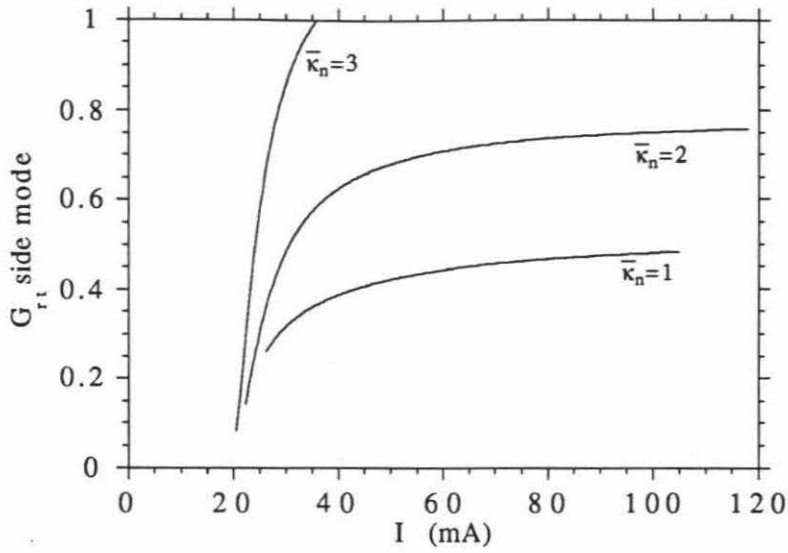

Figure 3.8: Round-trip gain of first side mode in function of total current for $\tilde{\kappa}_n = 1, 2$ and 3

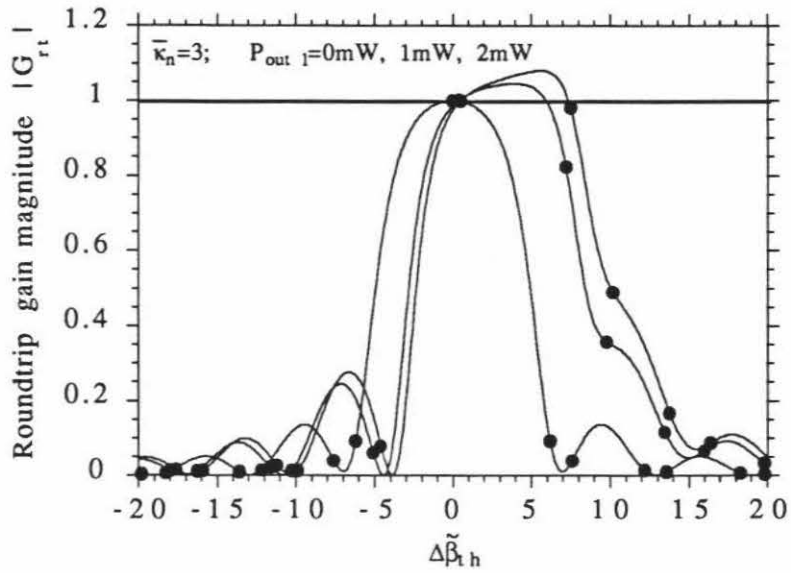

Figure 3.9: Round-trip gain magnitude spectrum (solid line) and mode locations (circles) for $\tilde{\kappa}_n = 3$ at indicated power levels

tive $\Delta\tilde{\beta}_{av}$. The shorter wavelengths are reflected closer to the facets while the longer wavelengths are reflected closer to the center of the laser. The effective cavity length is thus longer for shorter wavelengths, resulting in more gain for these wavelengths. At the same time the average Bragg wavelength shifts to shorter wavelengths (positive $\Delta\tilde{\beta}_{th}$), as discussed above, and the round-trip gain spectrum becomes asymmetric, favoring positive $\Delta\tilde{\beta}_{th}$, while its center moves to larger $\Delta\tilde{\beta}_{th}$, until at some power level the $+1$ mode has a round-trip gain of 1.

For $\tilde{\kappa}_n = 1, 2$ similar changes in the round-trip gain spectrum occur but the round-trip gain of the first side mode never reaches 1. It flattens out at higher power levels (fig. 3.8).

As can be seen from figs. 3.3-3.8, all characteristics of the laser flatten out at higher power levels, and the laser characteristics become quasi power independent. This has been experimentally observed for DFB lasers with $\tilde{\kappa}_n = 2$ [8]. For a laser with uniform pumping ($\tilde{I}_{lo}(\zeta) \equiv const$), the electron density is given by (2.42)

$$\tilde{I}_{lo} - I_{trans}\tilde{N}(\zeta) - \frac{e}{h\nu}\tilde{g}(\zeta)P_L(\zeta) = 0 \tag{3.3}$$

where it is assumed that there is no gain grating ($\Gamma_1 = 0$). At high power levels the spontaneous emission current can be neglected ($I_{trans}\tilde{N}(\zeta) \ll \tilde{I}_{lo}$), resulting in

$$\frac{\tilde{I}_{lo}}{P_{out}} \approx \frac{e}{h\nu}\tilde{g}(\zeta)\frac{P_L(\zeta)}{P_{out}} \tag{3.4}$$

and

$$\tilde{I}_{lo} \sim P_{out}$$

$$P_L(\zeta) \sim P_{out}.$$

The electron density $\tilde{N}(\zeta)$, which is directly related to the gain profile $\tilde{g}(\zeta)$, becomes quasi power independent for QWS DFB lasers with uniform pumping. This can be seen in fig. 3.7 where for $\tilde{\kappa}_n = 1$ and 2 the longitudinal effective index distribution converges to a power independent distribution. In the case of nonuniform pumping however this conclusion cannot be made as the electron density is not inherently clamped or quasi clamped to the threshold value.

For QWS DFB lasers with uniform pumping one can thus conclude that LSHB results in two different cases:

1. For high $\tilde{\kappa}_n$ values the laser loses its SLM operation when the output power is increased above a certain power level.

2. For low enough $\tilde{\kappa}_n$ values LSHB will stabilize before the round-trip gain of the side mode becomes 1, and the lasing characteristics become quasi power independent at high powers. The laser operates SLM at any power level.

The first case is clearly undesirable if high power operation is required, while the second case indicates that a relatively broad range of $\tilde{\kappa}_n$ values exists for which SLM operation is maintained at any power level, and that the optimum value of $\tilde{\kappa}_n = 1.25$, where the power distribution at threshold has the lowest nonuniformity, is not as critical as previously thought [1].

Finally it should be mentioned that effects such as heating, spectral holeburning, and bias dependent leakage current, which have been neglected here, can also result in loss of SLM operation, power dependent characteristics, and limitations in maximum

power. These effects however should not depend strongly on the coupling $\tilde{\kappa}_n$ as is the case for LSHB.

3.3 Laser structures with reduced longitudinal spatial holeburning

If one is mainly concerned with achieving high power SLM operation, then the results of the previous section indicate that QWS DFB lasers with $\tilde{\kappa}_n = 1$ to 2 are the way to go. In many applications however this is not sufficient. To achieve small linewidths for example long lasers are required [7], such that the $\tilde{\kappa}_n = 1$ to 2 requirement can not be easily met. When highly linear laser characteristics are required, such as in analog optical communication systems, the quasi power independent characteristics at high power levels can still not be good enough. It is clear that for such applications LSHB has to be reduced even more. In addition the SLM stability can be degraded by presence of residual facet reflectivities [8]. QWS DFB lasers with $\tilde{\kappa}_n = 2$ require a residual facet reflectivities below 1% to maintain SLM operation up to five times the threshold. In this section we discuss further reduction of LSHB by first looking at the state of the art, and secondly by introducing new optimal structures that have a uniform longitudinal intensity distribution at threshold and are therefore not subjected to LSHB.

3.3.1 State of the art

One of the driving forces for achieving DFB lasers with reduced LSHB is the reduction of the laser linewidth to sub-MHz values by making long lasers that remain SLM at high output powers. Two figures of merit can be used in determining how succesful a structure is in reducing the effect of LSHB. The first one is the minimum linewidth achieved, and the second is the maximum value of $\tilde{\kappa}_n$ for which high power SLM operation is possible. To reduce LSHB four different methods, or a combination of them, have been used.

By using an active material that has a lower α parameter, the nonuniformity in the effective index distribution is reduced even for high $\tilde{\kappa}_n$ values. In [12] it is shown that the important parameter in reducing the effective index nonuniformity is the α-parameter, which determines the ratio of differential index $\tilde{C}$ to differential gain $\tilde{A}$, and not the differential index or optical confinement factor. Multiple quantum well (MQW) material, which has a lower α-parameter than bulk material [13], has resulted in QWS DFB lasers with linewidths as low as $250kHz$ for $1500\mu m$ long lasers with $\tilde{\kappa}_n = 4.5$ and 4mW of output power [14].

Nonuniform pumping can be used to compensate for the hole burned in the electron density, by injecting more electrons where the stimulated emission rate is higher [15,16,17]. Using multi-section bulk QWS DFB lasers with the current through the center section higher than the current through the facet sections linewidths as low as $500kHz$ have been obtained for $1200\mu m$ long lasers with $\tilde{\kappa}_n = 2$–3 and output powers

above $20mW$ [16]. A disadvantage of this scheme is that the currents through the different sections have to be adjusted to minimize LSHB. However this more complicated pumping scheme offers the advantage of wavelength tunability [16] and SLM operation at threshold without the need for a phaseshift in the grating [17].

The third method goes to the heart of the problem, the nonuniformity in the longitudinal intensity distribution. As the cause of all the problems is the phase shift in the center of the cavity, different structures have been proposed and fabricated, resulting in more uniform intensity distributions by achieving this phase shift in a different way. Instead of using one phase shift, multiple phase shifts can be used, where the number of phase shifts, and the amount and location of each phase shift can be optimized [18,19,20]. The phase shift can be achieved by varying the longitudinal effective index in a modulated stripe width (MSW) structure [4]. The grating period can be varied stepwise in a corrugation pitch modulated (CPM) phase shifted structure [21], or continuously as a chirped grating [22]. Using $1200\mu m$ long CPM-MQW-DFB lasers, linewidths as low as $3.6kHz$ have been achieved with $\tilde{\kappa}_n = 4.2$ and an output power of $25mW$ [23,24].

Finally by changing the phase shift to a value lower than $\lambda/4$ SLM operation at high output powers can be maintained, not by reducing LSHB, but by delaying the onset of multimode operation [8]. As the main effect of LSHB for QWS DFB lasers with high $\tilde{\kappa}_n$ is to increase the effective phase shift, reducing the phase shift at threshold pushes the loss of SLM operation to higher output powers, if possible beyond the point where the characteristics become quasi power independent.

3.3.2 Laser structures with uniform longitudinal intensity distributions

To eliminate LSHB the electron density $\tilde{N}(\zeta)$ has to be independent of the optical power level, resulting in a modal gain and effective index distribution that are power independent. The electron density distribution $\tilde{N}(\zeta)$ is given by (2.42):

$$0 = \tilde{I}_{lo}(\zeta) - I_{trans}\tilde{N}(\zeta) - \frac{e}{h\nu}\tilde{g}\left[\tilde{N}(\zeta)\right]\left[P_F(\zeta) + P_B(\zeta) + \frac{\Gamma_1}{\Gamma_o}\mathcal{C}^2 Im\left[e^{i\phi}a(\zeta)b^*(\zeta)\right]\right]. \tag{3.5}$$

The threshold electron density distribution is

$$\tilde{N}_{th}(\zeta) = \frac{\tilde{I}_{th}(\zeta)}{I_{trans}} \tag{3.6}$$

where the ζ dependence of $\tilde{N}_{th}$ allows for nonuniform pumping. To eliminate LSHB the electron density $\tilde{N}$ at all power levels has to equal the threshold electron density: $\tilde{N}(\zeta) \equiv \tilde{N}_{th}(\zeta)$. The current distribution $\tilde{I}_{lo}(\zeta)$ above threshold required to achieve this is

$$\tilde{I}_{lo}(\zeta) = \tilde{I}_{th}(\zeta) + \frac{e}{h\nu}\tilde{g}\left[\tilde{N}_{th}(\zeta)\right]\left[P_F(\zeta) + P_B(\zeta) + \frac{\Gamma_1}{\Gamma_o}\mathcal{C}^2 Im\left[e^{i\phi}a(\zeta)b^*(\zeta)\right]\right]. \tag{3.7}$$

In the case of uniform pumping at threshold, $\tilde{N}$, $\tilde{g}$ and $\tilde{I}_{th}$ are independent of ζ and to keep this ζ independence above threshold, the power distribution factor in (3.7) has to be independent of ζ

$$P_F(\zeta) + P_B(\zeta) + \frac{\Gamma_1}{\Gamma_o}\mathcal{C}^2 Im\left[e^{i\phi}a(\zeta)b^*(\zeta)\right] \equiv const \tag{3.8}$$

In the case of nonuniform pumping at threshold, however, there is no obvious advantage in making the intensity distribution factor in (3.7) ζ independent, as it does not

result in uniform (ζ independent) pumping. In this case (3.7) can be used to determine how the pumping has to be changed in order to eliminate LSHB for any form of longitudinal power distribution. Regions where the stimulated emission is higher will require more additional current. Laser structures with uniform longitudinal intensity distributions are therefore only interesting from a practical point of view, if they can be achieved by uniform pumping ($\tilde{\gamma}(\zeta) \equiv \text{const}$).

Optimal index coupled DFB lasers

For pure index coupling ($\tilde{\kappa}_\sigma \equiv 0$ and $\Gamma_1 \equiv 0$) the uniform intensity distribtion requirement (3.8) becomes

$$|\tilde{a}(\zeta)|^2 + |\tilde{b}(\zeta)|^2 \equiv const \tag{3.9}$$

with $P_F(\zeta) \equiv |\tilde{a}(\zeta)|^2$ and $P_B(\zeta) \equiv |\tilde{b}(\zeta)|^2$, and the complex amplitudes $\tilde{a}$ and $\tilde{b}$ given by the coupled mode equations (2.10,2.11):

$$\frac{d\tilde{a}}{d\zeta} = \left[\tilde{\gamma}(\zeta) - i\Delta\tilde{\beta}'(\zeta)\right]\tilde{a}(\zeta) + \tilde{\kappa}_n(\zeta)e^{-i\phi_s}\tilde{b}(\zeta) \tag{3.10}$$

$$\frac{d\tilde{b}}{d\zeta} = \tilde{\kappa}_n(\zeta)e^{+i\phi_s}\tilde{a}(\zeta) - \left[\tilde{\gamma}(\zeta) - i\Delta\tilde{\beta}'(\zeta)\right]\tilde{b}(\zeta). \tag{3.11}$$

To look for laser structures satisfying (3.9), a treatment similar to [25] is used. The complex amplitudes $\tilde{a}$ and $\tilde{b}$ are written as

$$\tilde{a}(\zeta) = f_a(\zeta)e^{i\phi_a(\zeta)} \tag{3.12}$$

$$\tilde{b}(\zeta) = f_b(\zeta)e^{i\phi_b(\zeta)} \tag{3.13}$$

where f_a, f_b, ϕ_a and ϕ_b are real-valued functions. Substituting this in the coupled

mode equations (3.10,3.11) and using the uniformity condition (3.9) results in

$$2\tilde{\gamma}(\zeta) = \frac{d}{d\zeta}\left[f_a^2(\zeta) - f_b^2(\zeta)\right] \tag{3.14}$$

$$\tilde{\kappa}_n(\zeta)\cos\left[\psi(\zeta)\right] = \frac{d}{d\zeta}\left[f_a(\zeta)f_b(\zeta)\right] \tag{3.15}$$

$$2\Delta\tilde{\beta}'(\zeta) = -\tilde{\kappa}_n(\zeta)\frac{\sin\left[\psi(\zeta)\right]}{f_a(\zeta)f_b(\zeta)} - \frac{d}{d\zeta}\left[\psi(\zeta)\right] \tag{3.16}$$

$$f_a^2(\zeta) + f_b^2(\zeta) \equiv 1 \tag{3.17}$$

where ψ is given by

$$\psi(\zeta) = \phi_a(\zeta) - \phi_b(\zeta) + \phi_s \tag{3.18}$$

and ϕ_s is piecewise uniform, as it includes only the phase shifts in the grating, and not the chirp, which is included in $\Delta\tilde{\beta}'$. The constant in the uniformity condition is arbitrary, and has been taken as 1. The boundary conditions for zero facet reflectivities are:

$$f_a(0) = f_b(1) = 0. \tag{3.19}$$

For uniform pumping, $\tilde{\gamma}(\zeta) \equiv$const, the gain equation (3.14) and uniformity equation (3.17) can be solved using the boundary conditions (3.19), and the only solution with uniform pumping, uniform intensity distribution and zero reflectivities is given by

$$f_a(\zeta) = \sqrt{\zeta} \tag{3.20}$$

$$f_b(\zeta) = \sqrt{1-\zeta} \tag{3.21}$$

with $\tilde{\gamma} \equiv 1$. The index coupling coefficient is then given by, using (3.15):

$$\tilde{\kappa}_n(\zeta)\cos\left[\psi(\zeta)\right] = \frac{1-2\zeta}{2\sqrt{\zeta-\zeta^2}}. \tag{3.22}$$

The only solution with uniform detuning factor and lasing at the Bragg wavelength, $\Delta\tilde{\beta}'(\zeta) \equiv 0$, has to satisfy $\sin[\psi(\zeta)] \equiv 0$ (from (3.16)), resulting in the following structure:

$$\begin{aligned} \tilde{\gamma}(\zeta) &\equiv 1 \\ \tilde{\kappa}_n(\zeta) &= \frac{|1-2\zeta|}{2\sqrt{\zeta-\zeta^2}} \\ \Delta\tilde{\beta}'(\zeta) &\equiv 0 \\ \tilde{a}(\zeta) &= \sqrt{\zeta} \\ \tilde{b}(\zeta) &= e^{i\phi_o}\sqrt{1-\zeta} \end{aligned} \tag{3.23}$$

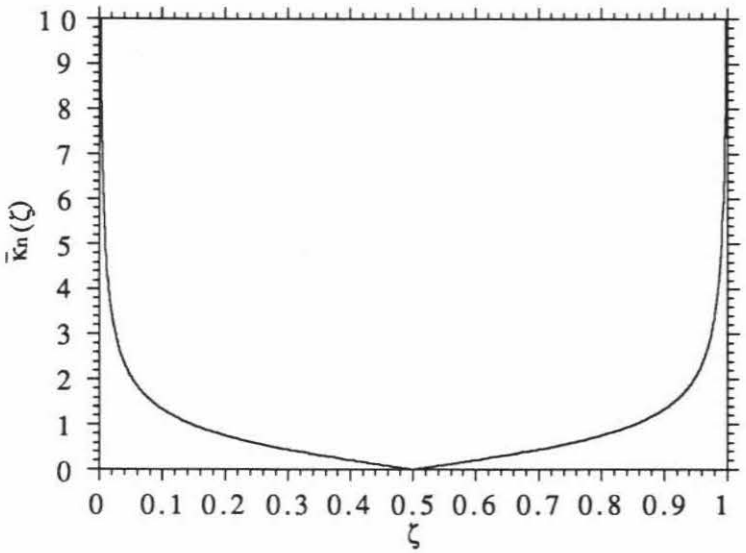

Figure 3.10: Longitudinal index coupling coefficient distribution of optimal structure

where the absolute value in the coupling coefficient expression makes $\tilde{\kappa}_n$ positive as required, and the sign change at $\zeta = \frac{1}{2}$ is achieved by a QWS in the grating. This

uniform intensity solution was analyzed in [25,26] and is shown in fig. 3.10. Other uniform intensity structures with uniform pumping exist, however, they require a nonuniform detuning factor [27], which can be achieved by chirping the grating or by longitudinally varying the effective index.

Two main conclusions can be drawn from this result. First, if LSHB is to be completely eliminated for index coupled DFB lasers with zero facet reflectivities and uniform pumping, the magnitude $\tilde{\kappa}_n(\zeta)$ has to be varied in the longitudinal direction. None of the previous structures tried so far (see section 3.3.1), use a varying coupling coefficient magnitude. They use either a variation in the phase of the coupling coefficient, or nonuniform pumping. Secondly, the optimal structure (3.23) is not physically realizable as it requires an infinite coupling coefficient at the facets. This structure however can be used as an ideal goal by approximating it. It has the advantage that increasing the laser length L improves the uniformity of the intensity distribution (in contrast with the QWS DFB laser), as $\tilde{\kappa}_n \equiv \kappa_n L$ can be made larger at the facets for a fixed maximum grating depth achievable.

The optimal structure (3.23) can be compared with a Fabry-Perot laser with 100% reflectors, which has a uniform intensity distribution, but has zero % of output coupling. In the optimal structure the feedback is concentrated near the facets, and the output coupling is increased by distributing the feedback inwards while maintaining a uniform intensity distribution.

Implementation of DFB structures with varying coupling coefficient

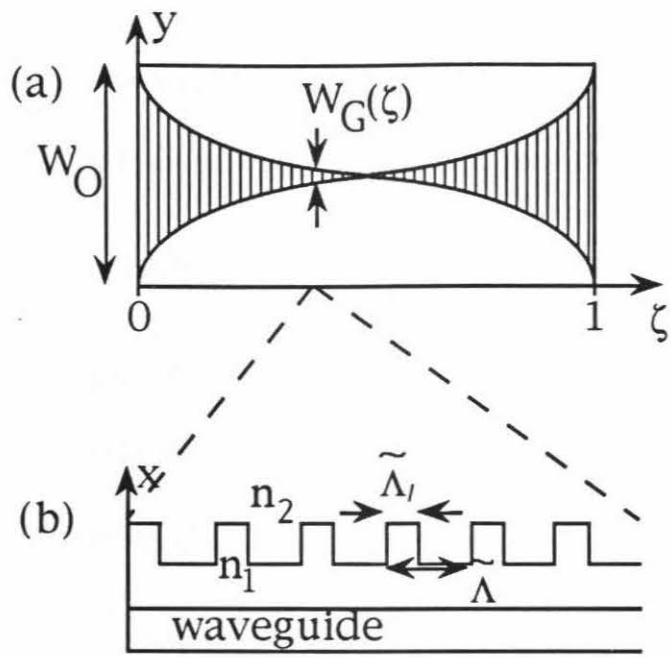

Figure 3.11: Implementation of grating with longitudinally varying coupling coefficient magnitude. (a) top view. (b) magnified side view

An implementation of (3.23) is proposed in [26], by longitudinally varying the grating groove depth, or by varying the grating duty cycle. Both these methods seem rather difficult, however, and the control in achieving a desired coupling coefficient profile is very limited. In this section a new implementation is proposed and discussed. The lateral overlap between the grating and the optical mode can be varied in the longitudinal direction, as is illustrated in fig. 3.11. This can easily be implemented using E-beam lithography or standard optical contact lithography by patterning and

etching a uniform grating, or by patterning the resist before etching the grating.

For TE modes ($\mathbf{E}_{pz} \equiv 0$) the index coupling coefficient is given by (A.69):

$$\tilde{\kappa}_n(\zeta) = \frac{\pi L}{i\lambda_o n_{eff,o}\tilde{\Lambda}(\zeta)} \int_{\zeta-\frac{\tilde{\Lambda}}{2}}^{\zeta+\frac{\tilde{\Lambda}}{2}} \Delta n^2(\zeta') e^{i\frac{2\pi l}{\tilde{\Lambda}}\zeta'} d\zeta' \tag{3.24}$$

with λ_o the vacuum wavelength, $n_{eff,o}$ the effective index of the waveguide without the grating, $\tilde{\Lambda} = \Lambda/L$ the grating period, l the grating order and $\Delta n^2(\zeta)$ given by

$$\Delta n^2(\zeta) = \frac{\iint_{-\infty}^{+\infty} \Delta n^2(x,y,\zeta)|\mathbf{E}_{pt}(x,y)|^2 dxdy}{\iint_{-\infty}^{+\infty} |\mathbf{E}_{pt}(x,y)|^2 dxdy} \tag{3.25}$$

$\Delta n^2(x,y,\zeta)$ is the perturbation from the grating and $\mathbf{E}_{pt}(x,y)$ is the transverse electric field component of the waveguide mode. The grating also changes the average index and a component $\Delta n_{eff,g}(\zeta)$, given by (A.67)

$$\Delta n_{eff,g}(\zeta) = \frac{1}{2n_{eff,o}\tilde{\Lambda}(\zeta)} \int_{\zeta-\frac{\tilde{\Lambda}}{2}}^{\zeta+\frac{\tilde{\Lambda}}{2}} \Delta n^2(\zeta') d\zeta' \tag{3.26}$$

should be added to the effective index.

As an example, the square grating illustrated in fig. 3.11(b) will be discussed. The modulation in the refractive index in this case results in

$$\Delta n^2(\zeta) = (n_2^2 - n_1^2)\frac{W_G(\zeta)}{W_O}\Gamma_{xg}\left[\left(1 - \frac{\tilde{\Lambda}_l}{\tilde{\Lambda}}\right) - \frac{2}{\pi}\sin\left(\pi\frac{\tilde{\Lambda}_l}{\tilde{\Lambda}}\right)\sin\left(\frac{2\pi}{\tilde{\Lambda}}\zeta + \phi_o\right) + \cdots\right] \tag{3.27}$$

where Γ_{xg} is the overlap between the grating and the mode in the transversal (x) direction, $W_G(\zeta)$ is the longitudinally varying grating width in the lateral (y) direction, and W_O is the lateral modal width. The ratio $W_G(\zeta)/W_O$ is < 1 and stands (formally) for the overlap between grating and optical mode in the lateral direction.

The resulting effective index and index coupling coeffcient are:

$$\Delta n_{eff,g}(\zeta) = \frac{n_2^2 - n_1^2}{2n_{eff,o}} \left(1 - \frac{\tilde{\Lambda}_l}{\tilde{\Lambda}}\right) \frac{W_G(\zeta)}{W_O} \Gamma_{xg} \tag{3.28}$$

$$\begin{aligned} \tilde{\kappa}_n(\zeta) &= \frac{2L}{\lambda_o} \frac{\sin\left(\pi \frac{\tilde{\Lambda}_l}{\tilde{\Lambda}}\right)}{1 - \frac{\tilde{\Lambda}_l}{\tilde{\Lambda}}} \Delta n_{eff,g}(\zeta) \\ &= \frac{L}{\lambda_o} \frac{n_2^2 - n_1^2}{n_{eff,o}} \sin\left(\pi \frac{\tilde{\Lambda}_l}{\tilde{\Lambda}}\right) \frac{W_G(\zeta)}{W_O} \Gamma_{xg}. \end{aligned} \tag{3.29}$$

Near the facets the coupling coefficient is limited to a maximum κ_{no}, when the grating extends over the full lateral direction. The corresponding maximum $\tilde{\kappa}_{no}$ scales with the total length of the laser. Longer lasers should therefore result in more uniform intensity distributions. The optimal index coupling coefficient profile can be approximated by setting $\tilde{\kappa}_n \equiv \tilde{\kappa}_{no}$ near the facets, while varying $\tilde{\kappa}_n$ according to (3.23):

$$\tilde{\kappa}_n(\zeta) = \begin{cases} \tilde{\kappa}_{no} & \text{for } 0 < \zeta < \zeta_o \text{ or } 1 - \zeta_o < \zeta < 1 \\ \frac{|1-2\zeta|}{2\sqrt{\zeta - \zeta^2}} & \text{for } \zeta_o < \zeta < 1 - \zeta_o \end{cases} \tag{3.30}$$

with ζ_o determined from $\tilde{\kappa}_n(\zeta_o) = \tilde{\kappa}_{no}$

$$\zeta_o = \frac{1}{2}\left[1 - \frac{\tilde{\kappa}_{no}}{\sqrt{1 + \tilde{\kappa}_{no}^2}}\right]. \tag{3.31}$$

The effective index $n_{eff}(\zeta) = n_{eff,o} + \Delta n_{eff,g}(\zeta)$ varies in the longitudinal direction. To achieve $\Delta\tilde{\beta}'(\zeta) \equiv 0$, the grating has to be chirped or the effective index of the waveguide has to be varied by changing W_O.

$$\begin{aligned} \tilde{\beta}_o(\zeta) &= \tilde{\beta}_o + \frac{2\pi L}{\lambda_o} \Delta n_{eff,g}(\zeta) \\ &= \tilde{\beta}_o + \frac{\pi}{2} \frac{1 - \frac{\tilde{\Lambda}_l}{\tilde{\Lambda}}}{\sin\left(\pi \frac{\tilde{\Lambda}_l}{\tilde{\Lambda}}\right)} \frac{|1 - 2\zeta|}{\sqrt{\zeta - \zeta^2}} \end{aligned} \tag{3.32}$$

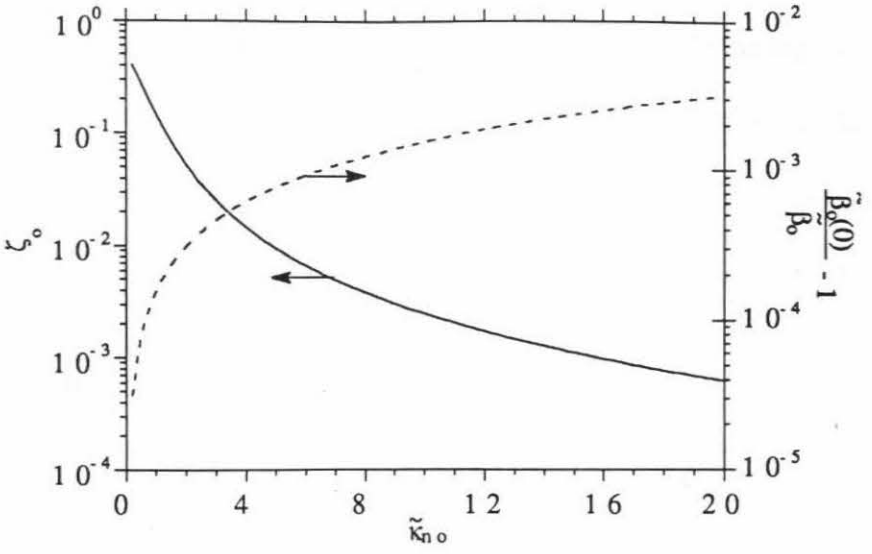

Figure 3.12: ζ_o (solid line) and Bragg wavevector deviation at facets (dashed line) as a function of maximum achievable index coupling coefficient

with

$$\tilde{\beta}_o = \frac{2\pi}{\lambda_o} n_{eff,o} L. \tag{3.33}$$

As $\tilde{\beta}_o$ is typically several thousands (π times the number of grating periods over the total laser length), big changes in the grating period are only required near the facets.

The position ζ_o and the relative change in Bragg wavevector at the facets, which is required to keep $\Delta\tilde{\beta}'(\zeta) \equiv 0$ (assuming $\tilde{\Lambda}_l = \frac{1}{2}\tilde{\Lambda}$ and $\tilde{\beta}_o = 10000$) are shown in fig. 3.12 as a function of the maximum index coupling coefficeint $\tilde{\kappa}_{no}$. The longer the laser the closer ζ_o is to the facets, and the larger the required deviation in Bragg wavevector at the facets. The Bragg deviation at the facets is very small (smaller than 1%) even at high coupling coefficient values, but if the grating is not chirped, the detuning factor $\Delta\tilde{\beta}'(\zeta)$ can be of the order of 10 near the facets. This is a very

large deviation from the optimal value 0, and absence of the detuning compensation should therefore have a noticable effect on the intensity distribution. If $\Delta\tilde{\beta}'(\zeta)$ is too large near the facets, it is technically impossible to completely compensate for the detuning factor, however partial compensation might improve the uniformity of the intensity distribution.

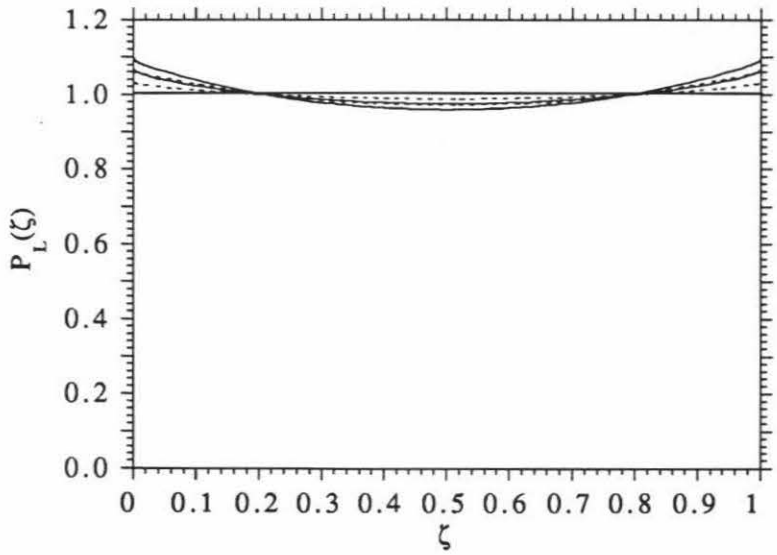

Figure 3.13: Longitudinal intensity distribution for four different structures with $\tilde{\kappa}_{no} = 10$: solid line, and $\tilde{\kappa}_{no} = 20$: dashed line

Using the model described in the previous chapter a simulation was performed for four different structures. All four structures have parameters as in table 3.1 scaled to a laser length of $1500\mu m$. Two of the structure have a maximum index coupling coefficient $\tilde{\kappa}_{no} = 10$ while the two other structures have $\tilde{\kappa}_{no} = 20$. The effective index is varied according to (3.28,3.29) with $\tilde{\Lambda}_l = \frac{1}{2}\tilde{\Lambda}$, and $n_{eff,o}$ uniform. For each value of $\tilde{\kappa}_{no}$ two cases are considered, one where the grating is not chirped and one where

the grating is chirped according to (3.32). The threshold intensity distribution for the four different case are shown in fig. 3.13 with $\tilde{\kappa}_{no} = 10$ as solid line (in all figures) and $\tilde{\kappa}_{no} = 20$ as a dashed line (in all figures). The structures without the chirped grating have a less uniform intensity distribution, though still more uniform than the standard QWS DFB (fig. 3.1).

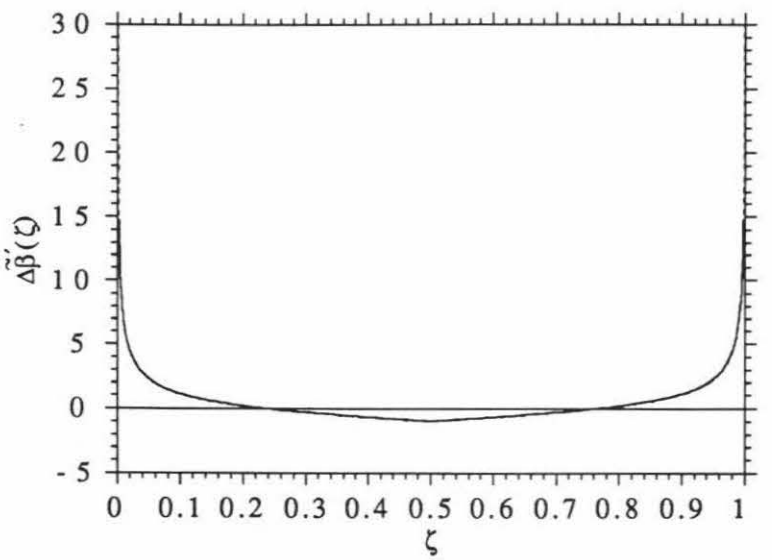

Figure 3.14: Longitudinal detuning factor distribution $\Delta\tilde{\beta}'(\zeta)$ at threshold for four different structures with $\tilde{\kappa}_{no} = 10$: solid line, and $\tilde{\kappa}_{no} = 20$: dashed line

The corresponding longitudinal detuning factor distributions $\Delta\tilde{\beta}'(\zeta)$ at threshold are shown in fig. 3.14. The results of the calculations are shown in figs 3.15-3.17. For the two cases where the grating is not chirped a mode hop occurs at low output power. Due to the uncompensated effective index distribution, and most of the feedback coming from the regions near the facets, where the detuning factor is relatively

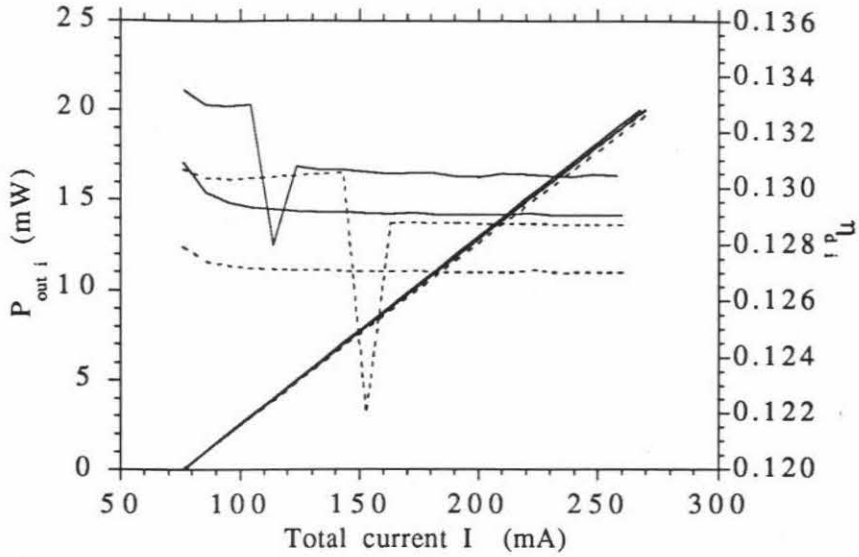

Figure 3.15: Output power and differential efficiency per facet as a function of total current for four different structures with $\tilde{\kappa}_{no} = 10$: solid line, and $\tilde{\kappa}_{no} = 20$: dashed line

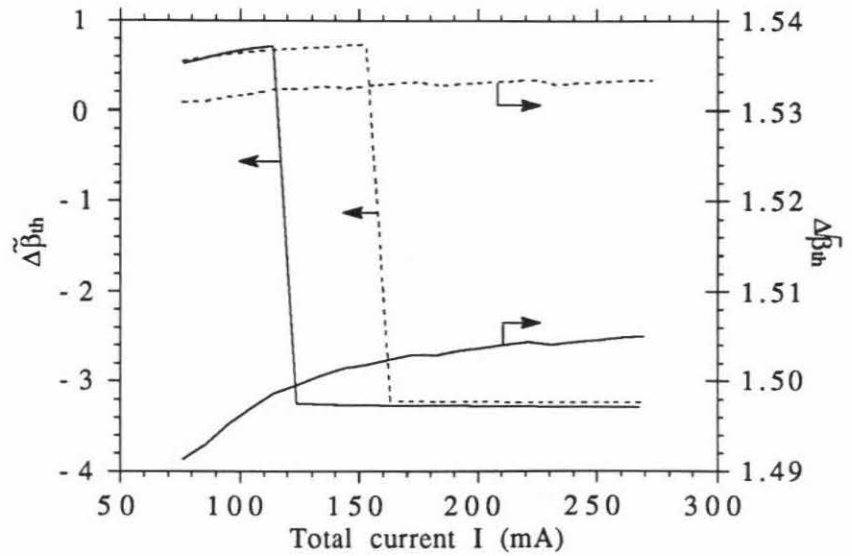

Figure 3.16: $\Delta\tilde{\beta}_{th}$ in function of total current for four different structures with $\tilde{\kappa}_{no} = 10$: solid line, and $\tilde{\kappa}_{no} = 20$: dashed line

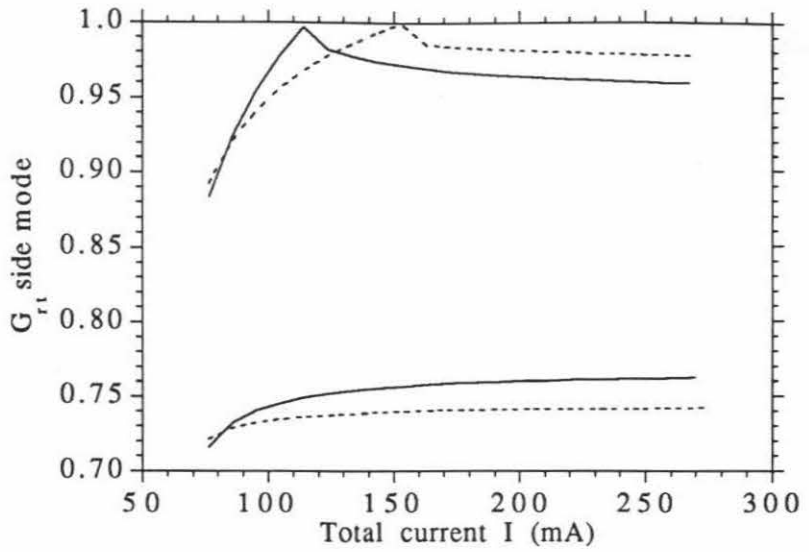

Figure 3.17: Round-trip gain of side mode as a function of total current for four different structures with $\tilde{\kappa}_{no} = 10$: solid line, and $\tilde{\kappa}_{no} = 20$: dashed line

large (fig. 3.14), lasing does not occur at the Bragg wavelength at threshold, as the longitudinal variation of the detuning factor $\Delta\tilde{\beta}'(\zeta)$ adds an effective phase shift to the phase shift in the center of the laser. The round-trip gain of the side mode starts relatively high, and increases due to weak LSHB until a mode hop occurs. In all four cases LSHB only occurs close to threshold, resulting in quasi power independent characteristics for output powers above $5mW$. As expected LSHB is smaller for the structure with larger $\tilde{\kappa}_{no}$. If mode hopping at low powers can be tolerated and if the side mode suppression ratio at high powers is not too low (due to the large round-trip gain of 0.96 for the side mode), the chirp in the grating is not necessary, resulting in a simpler fabrication. If mode hopping cannot be tolerated, then partial compensation

of the detuning factor might do the job, or the π phase shift in the center can be eliminated and replaced by the effective phase shift introduced by $\Delta\tilde{\beta}'(\zeta)$.

Other index coupled structures with uniform intensity profiles

Other index coupled DFB structures with uniform intensity distributions exist, they require nonuniform pumping however and are therefore not necessarily better in eliminating LSHB. The simplest structure is given by

$$\begin{aligned} \tilde{\kappa}_n(\zeta) &= \frac{\pi}{2}\cos(\pi\zeta) \\ \tilde{\gamma}(\zeta) &= \frac{\pi}{2}\sin(\pi\zeta) \\ \Delta\tilde{\beta}'(\zeta) &\equiv 0 \\ \tilde{a}(\zeta) &= \sin\left(\frac{\pi\zeta}{2}\right) \\ \tilde{b}(\zeta) &= e^{i\phi_o}\cos\left(\frac{\pi\zeta}{2}\right) \end{aligned} \tag{3.34}$$

and is discussed in [25,27]. Other similar structures exist and are discussed in [27]. The longitudinal intensity solution for these structures however is not the lowest gain solution, as it is for structure (3.34).

Optimal gain coupled DFB lasers

Since the demonstration of purely gain coupled DFB lasers [28] a lot of attention has been given to this kind of laser. Finding structures with no LSHB, however is more complicated. The uniformity condition is

$$|a(\zeta)|^2 + |b(\zeta)|^2 + \frac{\Gamma_1}{\Gamma_o} Im\left[e^{i\phi}a(\zeta)b^*(\zeta)\right] \equiv const \tag{3.35}$$

where $\Gamma_1 \neq 0$ for gain coupling, while $\Gamma_1 = 0$ for loss coupling, and the coupled mode equations are

$$\frac{d\tilde{a}}{d\zeta} = \left[\tilde{\gamma}(\zeta) - i\Delta\tilde{\beta}'(\zeta)\right]\tilde{a}(\zeta) - i\tilde{\kappa}_\sigma(\zeta)e^{-i\phi_s}\tilde{b}(\zeta) \tag{3.36}$$

$$\frac{d\tilde{b}}{d\zeta} = -i\tilde{\kappa}_\sigma(\zeta)e^{+i\phi_s}\tilde{a}(\zeta) - \left[\tilde{\gamma}(\zeta) - i\Delta\tilde{\beta}'(\zeta)\right]\tilde{b}(\zeta). \tag{3.37}$$

For the case of loss coupling $\Gamma_1 = 0$ it can easily be shown that the following structure satisfies the uniformity condition:

$$\begin{aligned}
\tilde{\kappa}_\sigma &\equiv \frac{\pi}{2} \\
\tilde{\gamma} &\equiv 0 \\
\Delta\tilde{\beta}' &\equiv 0 \\
\tilde{a}(\zeta) &= \sin\left(\frac{\pi}{2}\zeta\right) \\
\tilde{b}(\zeta) &= ie^{i\phi}\cos\left(\frac{\pi}{2}\zeta\right).
\end{aligned} \tag{3.38}$$

Fabrication of a purely loss coupled DFB however is no simple task as some amount of index coupling is always introduced. The effect of index coupling on the intensity distribution of gain coupled DFB lasers is analyzed in [29,30], where it is found that the uniformity of the intensity distribution does not deteriorate too much for $\tilde{\kappa}_n < \tilde{\kappa}_\sigma$.

In the case of gain coupled DFB lasers, where the coupling is obtained by modulating the thickness of the active layer ($\Gamma_1 \neq 0$) the uniformity condition (3.35) is more complex , and it is not clear if a uniform intensity distribution will exist.

3.4 Conclusion

In this chapter the effect of LSHB on SLM DFB lasers was analyzed. It was shown that for uniformely pumped lasers the lasing characteristics become quasi power independent at high output powers for index coupled DFB lasers with coupling coefficients $\tilde{\kappa}_n$ low enough ($\sim$ 1–2) to preserve SLM operation. Structures resulting in reduced LSHB were analyzed, and it was found that to eliminate LSHB, structures with uniform longitudinal intensity distribution are only interesting if they can be achieved by uniform pumping. It was also found that all structures resulting in reduced LSHB that have been fabricated so far, make use of a longitudinal variation of the coupling coefficient phase or nonuniform pumping, and it was shown that in the case of uniform pumping the magnitude of the coupling coefficient has to be varied in the longitudinal direction to completely eliminate LSHB. This new structure however is physically not feasible as it requires an infinite coupling coefficient at the facets. An implementation approximating this new structure was introduced and analyzed, and it was shown that this new structure results in strongly reduced LSHB.

References

[1] H. Soda, Y. Kotaki, H. Sudo, H. Ishikawa, S. Yamakoshi, and H. Imai, *IEEE J. Quantum Electron.*, **23**, 804 (1987)

[2] H. Kogelnik, and C. V. Shank, *J. Appl. Phys*, **43**, 2327 (1972)

[3] W. Streifer, R. D. Burnham, and D. R. Scifres, *IEEE J. Quantum Electron.*, **11**, 154 (1975)

[4] Y. Nakano, and K. Tada, *IEEE J. Quantum Electron.*, **24**, 2017 (1988)

[5] H. A. Haus, and C. V. Shank, *IEEE J. Quantum Electron.*, **12**, 532 (1976)

[6] K. Sekartedjo, N. Eda, K. Furuya, Y. Suematsu, F. Koyama, and T. Tanbun-Ek, *Electron. Lett.*, **20**, 80 (1984)

[7] A. Yariv, **Quantum Electronics**, 3rd ed., ch. 11 and 21 (1989)

[8] M. Okai, S. Tsuji, and N. Chinone, *IEEE J. Quantum Electron.*, **25**, 1314 (1989)

[9] J. E. A. Whiteaway, G. H. B. Thompson, A. J. Collar, and C. J. Armistead, *IEEE J. Quantum Electron.*, **25**, 1261 (1989)

[10] K. Kikuchi, *IEEE J. Quantum Electron.*, **26**, 45 (1990)

[11] T. Yamanaka, S. Seki, and K. Yokoyama, *IEEE Photon. Technol. Lett.*, **3**, 610 (1991)

[12] M. Aoki, K. Uomi, T. Tsuchiya, S. Sasaki, and N. Chinone, *IEEE Photon. Technol. Lett.*, **2**, 617 (1990)

[13] Y. Arakawa, and A. Yariv, *IEEE J. Quantum Electron.*, **21**, 1666 (1985)

[14] M. Kitamura, H. Yamazaki, T. Sasaki, N. Kida, H. Hasumi, and I. Mito, *IEEE Photon. Technol. Lett.*, **2**, 310 (1990)

[15] M. Usami, and S. Akiba, *IEEE J. Quantum Electron.*, **25**, 1245 (1989)

[16] Y. Kotaki, S. Ogita, M. Matsuda, Y. Kuwahara, and H. Ishikawa, *Electron. Lett.*, **25**, 990 (1989)

[17] K. Kikuchi, and H. Tomofuji, *IEEE J. Quantum Electron.*, **26**, 1717 (1990)

[18] T. Kimura, and S. Sugimura, *Electron. Lett.*, **23**, 1014 (1987)

[19] S. Ogita, Y. Kotaki, H. Ishikawa, and H. Imai, *Electron. Lett.*, **24**, 731 (1988)

[20] G. P. Agrawal, and A. H. Bobeck, *IEEE J. Quantum Electron.*, **24**, 2407 (1988)

[21] M. Okai, N. Chinone, H. Taira, and T. Harada, *IEEE Photon. Technol. Lett.*, **1**, 200 (1989)

[22] P. Zhou, and G. S. Lee, *Electron. Lett.*, **26**, 1660 (1990)

[23] M. Okai, T. Tsuchiya, A. Takai, and N. Chinone, *IEEE Photon. Technol. Lett.*, **4**, 526 (1992)

[24] M. Okai, M. Suzuki, T. Taniwatari, and M. Aoki, *CLEO'93, Baltimore*, post-deadline paper CPD4, (1993)

[25] T. Schrans, and A. Yariv, *Appl. Phys. Lett.*, **56**, 1526 (1990)

[26] G. Morthier, K. David, P. Vankwikelberge, and R. Baets, *IEEE Photon. Technol. Lett.*, **2**, 388 (1990)

[27] G. Morthier, and R. Baets, *IEEE J. Lightw. Technol.*, **9**, 1305 (1991)

[28] Y. Luo, Y. Nakano, K. Tada, T. Inoue, H. Hosomatsu, and H. Iwaoka, *Appl. Phys. Lett.*, **56**, 1620 (1990)

[29] E. Kapon, A. Hardy, and A. Katzir *IEEE J. Quantum Electron.*, **18**, 66 (1982)

[30] G. Morthier, P. Vankwikelberge, K. David, and R. Beats, *IEEE Photon. Technol. Lett.*, **2**, 170 (1990)

Chapter 4

Small-signal dynamic theory of single longitudinal mode lasers

4.1 Introduction

In chapter 2 and 3 the effect of longitudinal spatial holeburning (LSHB) on the static characteristics of single longitudinal mode lasers (more specifically QWS DFB lasers) is discussed. For applications such as optical communications the dynamic characteristics (linewidth, and AM and FM modulation response and bandwidth) are as important as the static characteristics.

The modified Schawlow-Townes formula predicts that the linewidth is inversely proportional to the output power of the laser [1]. Measurements however show a linewidth floor at high output powers, and in some cases linewidth rebroadening is observed at high output powers [2]. Several explanations, such as LSHB and spectral

holeburning, have been proposed for this minimum linewidth.

Pure AM modulation or pure FM modulation of semiconductor lasers is practically impossible, due to the α parameter which links the phase of the lasing mode to its intensity. Moreover LSHB causes a static or adiabatic chirp on top of the dynamic chirp and the thermal adiabatic chirp. It is therefore important to have a dynamic model that includes the longitudinal dependence of the lasing mode and the electron density.

The first dynamic models for semiconductor lasers are based on the rate equations [3] for a closed resonator, where the electron density and the longitudinal power distribution are assumed to be uniform. This simple rate equation model can be extended to include FP lasers with multiple sections of uniform electron density and power distribution [4,5], but for lasers with more than three sections the analytic solutions become very complicated. None of these models include the effect of the longitudinal cavity structure on parameters such as the spontaneous emission rate into the lasing mode, the linewidth enhancement factor α and the differential gain. The material values for these parameters are used, and all effects of the nonuniform intensity distribution and the cavity structure are therefore neglected. These models can be applied to DFB lasers by relating the photon lifetime to the reciprocal of the threshold gain, but they cannot correctly take into account the dependence of the photon lifetime on the electron density in gain coupled DFB lasers.

A first improvement on this theory was published by Henry [6], where he used a longitudinal Green's function solution of the wave equation for the spontaneous

emission fluctuations in an open resonator. Although the wave equation becomes nonlinear when LSHB is included, this approach is valid as long as the fluctuations about the operating point are small, and the operating point and Green's function are calculated self-consistently with LSHB. Using this theory, Henry showed that the spontaneous emission rate into the lasing mode is enhanced (and therefore the linewidth) if the facet losses are localized at the physical facets as opposed to distributed over the device as in the closed resonator model. This enhancement factor is close to 1 if the facet reflectivities are close to 100%, but is larger than 2 if the power reflectivities of the facets are smaller than 5%. This theory was then later applied to different laser structures such as DFB and DBR lasers, and composite cavity lasers [7,8]. By including the electron density dependence of the coupling coefficients for DFB lasers with partial gain coupling , it was shown how the modal α parameter can be enhanced or reduced by having a mixture of index and gain coupling [7]. A final improvement was made by Tromborg [9], by adding the longitudinal dependence of the electron density in the rate equations, resulting in an expression for the modal α parameter and the modal spontaneous emission rate.

There is a problem however with the derivation of the rate equations starting from the wave equation. The Green's function derivation is based on the construction of a Wronskian function from the self-consistent static solution. This Wronskian is by definition z-independent. As the solutions of the coupled mode equations are only approximate solutions of the wave equations (slowly varying envelope approximation (SVEA)) the resulting Wronskian is not z-independent, and an approximate constant

value has to be used. It is shown in appendix A that Maxwell's equations should be used instead of the wave equation, as $\nabla.E \neq 0$ for DFB lasers, and as the solutions of the coupled mode equations are "exact" (no SVEA) solutions of Maxwell's equations. A new derivation of the Green's function theory, starting from Maxwell's equation will therefore be given here, resulting in a z-independent Wronskian. Using additional approximations it can be shown that the equations in [9] are equivalent to the "exact" equations derived in this chapter. In addition the theory will be expanded to include the small-signal modulation response, where the longitudinal dependence of the intensity distribution and electron density are taken into account, as well as the dependence of the coupling coefficients on the electron density . As gain compression plays an important role in determining the maximum modulation bandwidth, it will also be included.

4.2 Green's function solution

In chapter 2 the monochromatic electric field $\mathbf{E}(x, y, \zeta; \omega)$ (TE modes) was used, where now the implicit frequency dependence is added to the notation:

$$\mathbf{E}(x, y, \zeta; \omega) = \left[\tilde{a}(\zeta; \omega)e^{-i\tilde{\beta}_o\zeta} + \tilde{b}(\zeta; \omega)e^{+i\tilde{\beta}_o\zeta}\right] \mathbf{E}_{pt}(x, y; \omega) = \tilde{E}(\zeta; \omega)\mathbf{E}_{pt}(x, y; \omega). \tag{4.1}$$

The frequency dependence of the transverse mode $\mathbf{E}_{pt}(x, y)$ will be neglected, as it is much smaller for the time scales considered. The time dependence of the electric

field is then given by

$$\mathbf{e}(x,y,\zeta;t) = e(\zeta;t)\mathbf{E}_{pt}(x,y) \tag{4.2}$$

with $e(\zeta;t)$ given by the Fourier transform relationship

$$e(\zeta;t) = \frac{1}{2\pi}\int_{-\infty}^{+\infty} \tilde{E}(\zeta;\omega)e^{i\omega t}d\omega \tag{4.3}$$

and similar expressions for the Fourier transform pairs of the forward mode ($\tilde{a}(\zeta;\omega)$, $a(\zeta;t)$) and the backward mode ($\tilde{b}(\zeta;\omega)$, $b(\zeta;t)$).

In Appendix A the coupled mode equations for $\tilde{a}$ and $\tilde{b}$ are derived including a polarization term due to the spontaneous emission (for TE modes):

$$\frac{d\tilde{a}}{d\zeta} = \left[\tilde{\gamma}(\zeta) - i\Delta\tilde{\beta}(\zeta)\right]\tilde{a}(\zeta) + \left[\tilde{\kappa}_n(\zeta) - i\tilde{\kappa}_\sigma(\zeta)\right]e^{-i\phi(\zeta)}\tilde{b}(\zeta) + \tilde{P}_{sp,pt}(\zeta)e^{+i\tilde{\beta}_o\zeta} \tag{4.4}$$

$$\frac{d\tilde{b}}{d\zeta} = \left[\tilde{\kappa}_n(\zeta) - i\tilde{\kappa}_\sigma(\zeta)\right]e^{+i\phi(\zeta)}\tilde{a}(\zeta) - \left[\tilde{\gamma}(\zeta) - i\Delta\tilde{\beta}(\zeta)\right]\tilde{b}(\zeta) - \tilde{P}_{sp,pt}(\zeta)e^{-i\tilde{\beta}_o\zeta}. \tag{4.5}$$

The modal polarization term $\tilde{P}_{sp,pt}(\zeta)$ represents the noise source for the spontaneous emission and is given by (A.71)

$$\tilde{P}_{sp,pt}(\zeta) = \frac{\omega L}{4iP_p}\iint_{-\infty}^{+\infty} \mathbf{P}_{sp}(x,y,\zeta;\omega).\mathbf{E}^*_{pt}(x,y)\,dxdy \tag{4.6}$$

where $\mathbf{P}_{sp}(x,y,\zeta;\omega)$ is the polarization giving rise to spontaneous emission, and is related to the spontaneous emission function $\mathbf{F}(x,y,\zeta)$ in [6,9] by

$$\mathbf{P}_{sp}(x,y,\zeta;\omega) = -\frac{\mathbf{F}(x,y,\zeta;\omega)}{\omega^2\mu_o}. \tag{4.7}$$

The Green's function solution for the electric field $\tilde{E}(\zeta;\omega)$, with driving force $\mathbf{F}$, is (appendix B)

$$\tilde{E}(\zeta;\omega) = \frac{1}{W}\int_0^1 G(\zeta,\zeta')\tilde{F}(\zeta';\omega)d\zeta' \tag{4.8}$$

with the Wronskian

$$\begin{aligned} W &= -2i\tilde{\beta}_m\left[E_{RF}(\zeta)E_{LB}(\zeta) - E_{RB}(\zeta)E_{LF}(\zeta)\right] && (4.9)\\ &= -2i\tilde{\beta}_m E_{RF}(\zeta)E_{LB}(\zeta)\left[1 - G_{rt}(\zeta)\right] && (4.10)\\ &\equiv const && (4.11)\end{aligned}$$

the Green's function

$$G(\zeta,\zeta') = h(\zeta'-\zeta)E_L(\zeta)E_R(\zeta') + h(\zeta-\zeta')E_L(\zeta')E_R(\zeta) \tag{4.12}$$

and the driving force

$$\tilde{F}(\zeta;\omega) = \frac{L^2\iint_{-\infty}^{+\infty}\mathbf{F}(x,y,\zeta;\omega).\mathbf{E}^*_{pt}(x,y)dxdy}{\iint_{-\infty}^{+\infty}|\mathbf{E}_{pt}(x,y)|^2dxdy}. \tag{4.13}$$

The subscripts L and R designate fields satisfying the left, respectively right boundary conditions, and F and B designate forward and backward propagating fields. L is the total length of the laser, $\tilde{\beta}_m$ the propagation constant of the mode, and $h(\zeta)$ the Heavyside function.

The Wronskian is a functional of $\Delta\tilde{\beta}(\zeta)$, $\tilde{\gamma}(\zeta)$, $\tilde{\kappa}_n(\zeta)$, and $\tilde{\kappa}_\sigma(\zeta)$ (and thus implicitely a functional of ω and $\tilde{N}(\zeta)$) which will be formally written as $W[\tilde{\beta}(\zeta),\tilde{\kappa}(\zeta)]$ (with $\tilde{\beta} = \Delta\tilde{\beta} + i\gamma$ and $\tilde{\kappa} = \tilde{\kappa}_n - i\tilde{\kappa}_\sigma$). The lasing condition follows from (4.8) by requiring a solution $\tilde{E}(\zeta;\omega) \neq 0$ when $\tilde{F}(\zeta;\omega) = 0$:

$$W\left[\tilde{\beta}(\zeta),\tilde{\kappa}(\zeta)\right] \equiv 0 \tag{4.14}$$

giving, using (4.10), the more familiar condition $G_{rt}(\zeta) = 1$. When $W = 0$ the boundary conditions on both sides are satisfied simultaneously, and therefore

$$E_R(\zeta) \equiv E_L(\zeta) \equiv E_o(\zeta). \tag{4.15}$$

The Green's function G is then

$$G(\zeta, \zeta') = E_o(\zeta)E_o(\zeta'). \tag{4.16}$$

When the driving force $\tilde{F} \neq 0$, the Wronskian is not quite zero, and "$\tilde{\beta}$" does not equal to the lasing condition values. A Taylor expansion around these values will therefore be performed for the Wronskian. If the deviation from the lasing condition is not too large, (4.15) and (4.16) can still be used in (4.8)

$$\tilde{E}(\zeta;\omega) = \tilde{A}(\omega)E_o(\zeta) \tag{4.17}$$

with

$$\tilde{A}(\omega) = \frac{1}{W\left[\tilde{\beta}(\zeta), \tilde{\kappa}(\zeta)\right]} \int_0^1 E_o(\zeta')\tilde{F}(\zeta';\omega)d\zeta'. \tag{4.18}$$

Expansion of the Wronskian around the lasing condition gives (appendix B)

$$W\left[\tilde{\beta}(\zeta), \tilde{\kappa}(\zeta)\right] = \int_0^1 \left[\frac{\delta W}{\delta\tilde{\beta}(\zeta)}\delta\tilde{\beta}(\zeta) + \frac{\delta W}{\delta\tilde{\kappa}(\zeta)}\delta\tilde{\kappa}(\zeta)\right] d\zeta \tag{4.19}$$

where $\delta W/\delta\tilde{\beta}$ and $\delta W/\delta\tilde{\kappa}$ are the functional derivatives of the Wronskian (appendix B)

$$\frac{\delta W}{\delta\tilde{\beta}(\zeta)} = 4\tilde{\beta}_m^* E_{oF}(\zeta)E_{oB}(\zeta) \tag{4.20}$$

$$\frac{\delta W}{\delta\tilde{\kappa}(\zeta)} = -2i\tilde{\beta}_m^* \left[E_{oF}^2(\zeta)e^{i\left(2\tilde{\beta}_o\zeta+\phi\right)} - E_{oB}^2(\zeta)e^{-i\left(2\tilde{\beta}_o\zeta+\phi\right)}\right] \tag{4.21}$$

and

$$\delta\tilde{\beta}(\zeta) = \frac{\partial\tilde{\beta}}{\partial\omega}(\omega-\omega_o) + \frac{\partial\tilde{\beta}}{\partial\tilde{N}}\left[\tilde{N}(\zeta)-\tilde{N}_o(\zeta)\right] + \frac{\partial\tilde{\beta}}{\partial S}(S-S_o) \tag{4.22}$$

$$\delta\tilde{\kappa}(\zeta) = \frac{\partial\tilde{\kappa}}{\partial\omega}(\omega-\omega_o) + \frac{\partial\tilde{\kappa}}{\partial\tilde{N}}\left[\tilde{N}(\zeta)-\tilde{N}_o(\zeta)\right] + \frac{\partial\tilde{\kappa}}{\partial S}(S-S_o) \tag{4.23}$$

with ω_o and $\tilde{N}_o(\zeta)$ the solutions to the lasing condition for an average power S_o. The third term represents the effects of gain compression, with S the average power in the cavity, normalized to the transparency current $I_{trans} = eV_aN_o/\tau_S$

$$S = \frac{e}{h\nu}\frac{1}{I_{trans}}\int_0^1 \left[P_F(\zeta)+P_B(\zeta)\right]d\zeta. \tag{4.24}$$

The gain compression is assumed to be only dependent on the average power as it is introduced here only to include the limited modulation bandwidth. When gain compression is present, the equation for the modal gain (2.30) has to be modified to the nonlinear gain form

$$\tilde{g}(\zeta) = \frac{\tilde{A}\left[\tilde{N}(\zeta)-1\right]}{1+\epsilon S} = \frac{\tilde{g}_L(\zeta)}{1+\epsilon S} \tag{4.25}$$

with ϵ the gain compression factor and $\tilde{g}_L$ the linear gain. The refractive index is assumed to be unaffected by gain compression and is given by (2.33). Solution of the lasing condition (4.14), results in a modal gain $\tilde{g} = \tilde{g}_w = 2\tilde{\gamma}_w + \tilde{\alpha}_i$. The index and gain coupling coefficients are then given by:

$$\tilde{\kappa}_\sigma = \tilde{\kappa}_{\sigma 2} - \frac{1}{4}\frac{\Gamma_1}{\Gamma_o}\tilde{g}_w \tag{4.26}$$

$$\tilde{\kappa}_n = \tilde{\kappa}_{n2} \mp \frac{\alpha}{4}\frac{\Gamma_1}{\Gamma_o}\tilde{g}_L \tag{4.27}$$

where the discussion at the end of section 2.5 has been extended to include the electron density dependence of the index coupling coefficient. The coupling coefficents $\tilde{\kappa}_{\sigma 2}$ and

$\tilde{\kappa}_{n2}$ are the electron density independent parts, while the $\mp$ sign in (4.27) depends on whether the grating is between the active layer and a cladding layer with refractive index $n_{cladding} < n_{active}$ where the upper sign is used, or $n_{cladding} > n_{active}$ where the lower sign is used. The sign convention for the coupling coefficients result from the grating definition (2.5) and (2.37) (with $\Gamma_1 > 0$). With the gain coupling coefficient defined as (2.50), a gain grating corresponds to $\tilde{\kappa}_\sigma < 0$, while a loss grating has $\tilde{\kappa}_{\sigma 2} > 0$. As other gratings, not involving the active layer, can be present in the structure, $\tilde{\kappa}_{n2}$ can be either positive or negative, depending on the relative position and refractive indices of the layers involved [10]. When $\tilde{\kappa}_n > 0$ the gain and index coupling are in phase, while they are out of phase when $\tilde{\kappa}_n < 0$. For most partially gain coupled lasers $n_{cladding} < n_{active}$, and an increase in electron density will therefore result in a decrease (increase) in index coupling magnitude for in phase (out of phase) coupling, while it will always result in an increase in gain coupling magnitude (as long as $\tilde{\kappa}_{\sigma 2}$ is small enough).

The derivatives of $\tilde{\beta}$ and $\tilde{\kappa}$ at the operating point S_o are

$$\frac{\partial \tilde{\beta}}{\partial \omega} = \frac{L}{v_g}\left(1 + i\frac{1}{2}G_\omega\right) \tag{4.28}$$

$$\frac{\partial \tilde{\beta}}{\partial \tilde{N}} = \frac{i}{2}\left(\frac{1}{1+\epsilon S_o} + i\alpha\right)\tilde{A} \tag{4.29}$$

$$\frac{\partial \tilde{\beta}}{\partial S} = -\frac{i}{2}\frac{\epsilon \tilde{g}_w}{1+\epsilon S_o} \tag{4.30}$$

$$\frac{\partial \tilde{\kappa}}{\partial \omega} = \frac{\tilde{\kappa}_o}{\omega_o} \tag{4.31}$$

$$\frac{\partial \tilde{\kappa}}{\partial \tilde{N}} = \frac{i}{4}\frac{\Gamma_1}{\Gamma_o}\tilde{A}\left(\frac{1}{1+\epsilon S_o} \pm i\alpha\right) \tag{4.32}$$

$$\frac{\partial \tilde{\kappa}}{\partial S} = -\frac{i}{4}\frac{\Gamma_1}{\Gamma_o}\frac{\epsilon \tilde{g}_w}{1+\epsilon S_o} \tag{4.33}$$

with v_g the group velocity, $G_\omega = v_g \partial g/\partial\omega$ the detuning from the gain peak, $\tilde{A}$ the normalized differential gain, α the aforementioned material α parameter, and the coupling coefficient is assumed to vary linearly with frequency (A.69,A.70).

Inverse Fourier transforming the complex amplitude $\tilde{A}(\omega)$ with

$$A(t) = \frac{e^{-i\omega_o t}}{2\pi} \int_0^{+\infty} \tilde{A}(\omega) e^{i\omega t} d\omega \tag{4.34}$$

and applying this on (4.18) expanded about the lasing condition,

$$\begin{aligned} \frac{\partial W}{\partial \omega} (\omega - \omega_o)\, \tilde{A}(\omega) &= -\tilde{A}(\omega) \int_0^1 \left[\frac{\delta W}{\delta \tilde{\beta}(\zeta)} \frac{\partial \tilde{\beta}(\zeta)}{\partial \tilde{N}} + \frac{\delta W}{\delta \tilde{\kappa}(\zeta)} \frac{\partial \tilde{\kappa}(\zeta)}{\partial \tilde{N}} \right] \Delta \tilde{N}(\zeta) d\zeta \\ &- \tilde{A}(\omega) \frac{\partial W}{\partial S} \Delta S + \int_0^1 E_o(\zeta) \tilde{F}(\zeta;\omega) d\zeta \end{aligned} \tag{4.35}$$

with

$$\frac{\partial W}{\partial \omega} = \int_0^1 \left[\frac{\delta W}{\delta \tilde{\beta}(\zeta)} \frac{\partial \tilde{\beta}(\zeta)}{\partial \omega} + \frac{\delta W}{\delta \tilde{\kappa}(\zeta)} \frac{\partial \tilde{\kappa}(\zeta)}{\partial \omega} \right] d\zeta \tag{4.36}$$

$$\frac{\partial W}{\partial S} = \int_0^1 \left[\frac{\delta W}{\delta \tilde{\beta}(\zeta)} \frac{\partial \tilde{\beta}(\zeta)}{\partial S} + \frac{\delta W}{\delta \tilde{\kappa}(\zeta)} \frac{\partial \tilde{\kappa}(\zeta)}{\partial S} \right] d\zeta \tag{4.37}$$

results in a differential equation for the time dependent complex amplitude $A(t)$:

$$\frac{dA}{dt} = A(t) \int_0^1 C_N(\zeta) \Delta \tilde{N}(\zeta;t) d\zeta + A(t) C_S \Delta S(t) + F_A(t) \tag{4.38}$$

with

$$C_N(\zeta) = -i \frac{\frac{\delta W}{\delta \tilde{\beta}(\zeta)} \frac{\partial \tilde{\beta}(\zeta)}{\partial \tilde{N}} + \frac{\delta W}{\delta \tilde{\kappa}(\zeta)} \frac{\partial \tilde{\kappa}(\zeta)}{\partial \tilde{N}}}{\frac{\partial W}{\partial \omega}} = -i \frac{\frac{\delta W}{\delta \tilde{N}(\zeta)}}{\frac{\partial W}{\partial \omega}} \tag{4.39}$$

and

$$C_S = -i \frac{\frac{\partial W}{\partial S}}{\frac{\partial W}{\partial \omega}}. \tag{4.40}$$

The noise source $F_A(t)$ is related to the polarization function $\tilde{F}$:

$$F_A(t) = \frac{i}{2\pi \frac{\partial W}{\partial \omega}} \int_0^1 E_o(\zeta) \left[\int_0^{+\infty} \tilde{F}(\zeta;\omega) e^{i(\omega-\omega_o)t} d\omega \right] d\zeta. \tag{4.41}$$

If a closed form expression for the Wronskian is known (appendix B), the partial derivatives with respect to ω and S as defined in (4.36) and (4.37) can be calculated by directly differentiating this closed form expression.

In this derivation it has been assumed that the electron density does not change in time when applying the Fourier transforms. The time dependence of the electron density can be included if the electron density changes slower than the inverse gain bandwidth, so that the steady state response for the gain can be used. This is known as the rate equation approximation.

A more workable set of rate equations can be derived if the intensity $S(t)$ and the phase $\varphi(t)$ of the electric field are used:

$$A(t) = \sqrt{S(t)}e^{i\varphi(t)} \tag{4.42}$$

resulting in

$$\frac{dS}{dt} = S(t)\int_0^1 G_N(\zeta)\Delta\tilde{N}(\zeta;t)d\zeta + G_S\Delta S(t)S(t) + 2Re\left[A^*(t)F_A(t)\right] \tag{4.43}$$

$$\frac{d\varphi}{dt} = \frac{1}{2}\int_0^1 \alpha_N(\zeta)G_N(\zeta)\Delta\tilde{N}(\zeta;t)d\zeta + \frac{1}{2}\alpha_S G_S\Delta S(t) + \frac{1}{S(t)}Im\left[A^*(t)F_A(t)\right] \tag{4.44}$$

with

$$G_N(\zeta) = 2Re\left[C_N(\zeta)\right] \tag{4.45}$$

$$G_S = 2Re\left[C_S\right] \tag{4.46}$$

$$\alpha_N(\zeta) = \frac{Im\left[C_N(\zeta)\right]}{Re\left[C_N(\zeta)\right]} \tag{4.47}$$

$$\alpha_S = \frac{Im\left[C_S\right]}{Re\left[C_S\right]}. \tag{4.48}$$

G_X $(X = N, S)$ is the modal differential gain, and modal α_X the corresponding α-parameter. As will be seen later, even if the gain compression has no effect on the refractive index (the material value of $\alpha_S = 0$), the modal value of α_S, given by (4.48), can be nonzero.

The statistical properties of the complex noise function $F_A(t)$ are derived from **F** (appendix A: (A.7), (A.8) and (A.9)) as in [6,9]:

$$< F_A(t) > \;=\; 0 \tag{4.49}$$

$$< F_A(t)F_A^*(t') > \;=\; R\delta(t-t'). \tag{4.50}$$

The δ-function in (4.50) is only valid for time scales longer than the inverse gain bandwidth, and

$$R = \frac{2\hbar\omega^3 L^2}{c^3\varepsilon_o}\frac{1}{\left|\frac{\partial W}{\partial\omega}\right|^2}\int_0^1 |E_o(\zeta)|^2\,\tilde{g}_w(\zeta)n_{eff}(\zeta)n_{sp}(\zeta)d\zeta \tag{4.51}$$

with $\tilde{g}_w$ the modal gain, n_{eff} the effective index, and n_{sp} the spontaneous emission factor. If a grating on the active layer is present, the mixing of the standing wave with the modulation of the local spontaneous emission rate will result in an additional slowly varying term (see section 2.5) such that $|E_o(\zeta)|^2\,\tilde{g}(\zeta)$ in (4.51) should be replaced by [11]:

$$|E_o(\zeta)|^2\,\tilde{g}(\zeta) \rightarrow \left[|E_{oF}(\zeta)|^2 + |E_{oB}(\zeta)|^2 + \frac{\Gamma_1}{\Gamma_o}Im\left[E_{oF}(\zeta)E_{oB}^*(\zeta)e^{i(2\tilde{\beta}_o\zeta+\phi}\right]\right]\tilde{g}(\zeta). \tag{4.52}$$

The real-valued noise functions $F_S(t)$ for the intensity and $F_\varphi(t)$ for the phase are defined as

$$2A^*(t)F_A(t) = R + F_S(t) + 2iS_oF_\varphi(t) \tag{4.53}$$

with following moments [6,9]:

$$< F_S(t) > = 0 \tag{4.54}$$

$$< F_\varphi(t) > = 0 \tag{4.55}$$

$$< F_S(t)F_S(t') > = 2RS_o\delta(t-t') \tag{4.56}$$

$$< F_\varphi(t)F_\varphi(t') > = \frac{R}{2S_o}\delta(t-t') \tag{4.57}$$

$$< F_S(t)F_\varphi(t') > = < F_S(t')F_\varphi(t) >= 0 \tag{4.58}$$

where S_o is the steady state value of the intensity.

The rate equations for the intensity and phase are then

$$\frac{dS}{dt} = S(t)\int_0^1 G_N(\zeta)\Delta\tilde{N}(\zeta;t)d\zeta + G_S\Delta S(t)S(t) + R + F_S(t) \tag{4.59}$$

$$\frac{d\varphi}{dt} = \frac{1}{2}\int_0^1 \alpha_N(\zeta)G_N(\zeta)\Delta\tilde{N}(\zeta;t)d\zeta + \frac{1}{2}\alpha_S G_S\Delta S(t) + F_\varphi(t) \tag{4.60}$$

the first term in (4.59) is the stimulated emission rate net of loss, the second term is damping due to gain compression, and the third term R is the total spontaneous emission rate into the lasing mode. It is evident from (4.51) that R depends on the longitudinal overlap between the mode and the active material (the longitudinal confinement), as well as on the dynamics of the mode (expressed in $\partial W/\partial\omega$). During the derivation of (4.51), (4.59) and (4.60), no assumptions have been made on the cavity solutions $E_o(\zeta)$. This equation can thus be used for any complex optical cavity, ranging from simple FP lasers, to more complex DFB structures, and any compound external cavity. Once the compound cavity modal electric field $E_o(\zeta)$, and its Wronskian are known, the dynamic equations can be constructed as described

previously. The only limitation is due to the first order Taylor expansion of the Wronskian. If the frequency deviation from ω_o (very high speed modulation), or the modulation amplitude becomes too large, a higher order Taylor expansion is needed. One application not discussed in this thesis is the linewidth reduction observed by coupling a laser to a dispersive external feedback [8].

Equations (4.9), (4.20), (4.21), (4.36), (4.37),(4.39), (4.40), and (4.51) are derived directly from Maxwell's equations. The corresponding expressions in [9], which are derived from the "incorrect" wave equation, can be shown to be equivalent under the additional assumption $\tilde{\beta}_o \gg \tilde{g}, \Delta\tilde{\beta}, \tilde{\kappa}_n, \tilde{\kappa}_\sigma$. The dependence of the Wronskian on the coupling coefficient is not explicitely treated in [9]. One would think, in light of the wave equation, that the coupling coefficient can be treated as a periodic variation of the propagation constant, and that the expression (4.20) can be used. This seems to be incorrect, as (4.21) should be used. The treatment in [9] can thus not easily be expanded to DFB lasers with partial gain coupling, where the gain and index coupling coefficient depend on the electron density.

4.3 Small-signal analysis of the rate equations

4.3.1 The electron density rate equation

In order to perform a small-signal analysis, a rate equation for the electron density $\tilde{N}(\zeta;t)$ is necessary. The treatment in section 2.5 can be expanded to include gain

compression, resulting in a modified version of (2.42):

$$eV_aN_o\frac{\partial\tilde{N}}{\partial t} = \tilde{I}_{lo}(\zeta;t) - I_{trans}\tilde{N}(\zeta;t) - I_{trans}\frac{\tilde{g}_L(\zeta;t)}{1+\epsilon S(t)}S(t)P_o(\zeta) + eV_aF_N(\zeta;t) \quad (4.61)$$

with $F_N(\zeta;t)$ the noise source associated with the electrons, and $S(t)P_o(\zeta)$ the modal power distribution

$$P_o(\zeta) \sim |a(\zeta)|^2 + |b(\zeta)|^2 + \frac{\Gamma_1}{\Gamma_o}Im\left[e^{i\phi}a(\zeta)b^*(\zeta)\right]. \quad (4.62)$$

The time dependence of P_o (dynamic LSHB) has been ignored here as it requires solution of a complicated integral equation [9]. The effect of static LSHB however is included through the nonuniformity of P_o and $\tilde{N}$ and their self-consistency.

The average power $S(t)$ in the cavity is related to the output power P_{out1} through the Poynting vector

$$p_B(\zeta;t) = -\iint_{-\infty}^{+\infty}\left[\mathbf{e}_B(x,y,\zeta;t)\times\mathbf{h}_B(x,y,\zeta;t)\right].\mathbf{e}_z dxdy \quad (4.63)$$

with p_B the local, instantaneous backward propagating power. Using (4.2) for the backward mode, (A.74) for TE modes, (4.3), (4.17), (4.34), (4.42), and $\iint|\mathbf{E}_{pt}|^2dxdy = 1$ gives

$$p_B(\zeta;t) = \frac{n_{eff}}{R_c}\left[E_{oB}(\zeta)\sqrt{S(t)}e^{i(\omega_o t+\varphi(t))} + c.c.\right]^2 \quad (4.64)$$

with R_c the characteristic impedance of vacuum.

The time-average backward power, where the averaging is over many optical periods, but over a time much shorter than all other time dependences, is

$$P_B(\zeta;t) = < p_B(\zeta;t) > = \frac{2n_{eff}}{R_c}S(t)\left|E_{oB}(\zeta)\right|^2 \quad (4.65)$$

and a similar expression for $P_F(\zeta;t)$. Using (2.53), the following relation with the output power exists

$$P_{out1}(t) = \frac{2\,(1-R_1)\,n_{eff}S(t)\,|E_{oB}(0)|^2}{R_c}. \tag{4.66}$$

If $S(t)$ is to represent the average power in the cavity, normalized to the transparency current I_{trans} (4.24), the electric fields E_{oF} and E_{oB} have to be normalized as

$$\int_0^1 \left[|E_{oF}(\zeta)|^2 + |E_{oB}(\zeta)|^2\right] d\zeta \equiv \frac{h\nu}{e}\frac{R_c I_{trans}}{2n_{eff}}. \tag{4.67}$$

The statistical characteristics of $F_N(\zeta;t)$ include the pumping noise and are given by

$$< F_N(\zeta;t) > \;=\; 0 \tag{4.68}$$

$$< F_N(\zeta;t)F_N(\zeta;t') > \;=\; 2D_{NN}\delta(\zeta-\zeta')\delta(t-t'). \tag{4.69}$$

The diffusion coefficient D_{NN} depends on the pumping, and lies beyond the scope of this chapter. It should be noted however that (4.69) assumes a white noise. To include 1/f noise from the pumping, (4.69) has to be modified. Due to the randomness associated with the stimulated emission term in (4.61), a correlation exists between the noise functions F_S and F_N

$$< F_N(\zeta;t)F_S(t') >= 2D_{NS}\delta(t-t'). \tag{4.70}$$

Different controversial expressions have been proposed for D_{NS}. Resolution of this controversy lies beyond the scope of this chapter.

4.3.2 The small-signal rate equations

The dynamic variables $\tilde{I}_{lo}$, $\tilde{N}$, S, and $\Delta\omega = d\varphi/dt$ are expanded into three components. The first one is the solution to the lasing condition (4.14) (assumes $R = 0$) with subscript w, second the deviation in steady state due to $R \neq 0$ with subscript s, and third the time dependent small signal δ

$$\tilde{I}_{lo}(\zeta;t) = \tilde{I}_{lo,w}(\zeta) + \Delta\tilde{I}_{lo,s}(\zeta) + \delta\tilde{I}_{lo}(\zeta;t) \tag{4.71}$$

$$\tilde{N}(\zeta;t) = \tilde{N}_w(\zeta) + \Delta\tilde{N}_s(\zeta) + \delta\tilde{N}(\zeta;t) \tag{4.72}$$

$$S(t) = \underbrace{S_o}_{W=0} + S_o\delta S(t) = S_o\left[1 + \delta S(t)\right] \tag{4.73}$$

$$\Delta\omega(t) = \frac{d\varphi}{dt} = \Delta\omega_s + \delta\omega(t). \tag{4.74}$$

The lasing condition (4.14) is solved as in chapter 2 under the assumption that a power level S_o is present. Addition of gain compression does not complicate the calculation. Setting $R \neq 0$ does not change the power level, but the electron density $\Delta\tilde{N}_s$ and the current $\Delta\tilde{I}_{lo,s}$, as well as the lasing frequency $\Delta\omega_s$. Solving for the steady-state electron density gives

$$-\frac{R}{S_o} = \int_0^1 G_N(\zeta)\Delta\tilde{N}_s(\zeta)d\zeta \tag{4.75}$$

$$\Delta\tilde{N}_s(\zeta) = \frac{1}{1 + \frac{\tilde{A}S_oP_o(\zeta)}{1+\epsilon S_o}}\frac{\Delta\tilde{I}_{lo,s}(\zeta)}{I_{trans}}. \tag{4.76}$$

The profile of $\Delta\tilde{I}_{lo,s}(\zeta)$ is usually known, up to a multiplicative constant, from the pumping scheme (e.g., for uniform pumping, $\Delta\tilde{I}_{lo,s}(\zeta) \equiv const$). Substitution of (4.76) into (4.75) can then be used to solve for this multiplicative constant. The

steady-state frequency shift is then given by

$$\Delta\omega_s = \frac{1}{2}\int_0^1 \alpha_N(\zeta)G_N(\zeta)\Delta\tilde{N}_s(\zeta)d\zeta. \tag{4.77}$$

The spectrum of the laser and the side mode suppression ratio can be calculated by using $\tilde{N(\zeta)} = \tilde{N}_w(\zeta) + \Delta\tilde{N}_s(\zeta)$ in calculating the amplified spontaneous emission spectrum as described in section 2.8.

The small-signal rate equations derived from (4.59), (4.60), and (4.61) are

$$\frac{\partial\delta\tilde{N}}{\partial t} = \frac{1}{\tau_S}\frac{\delta\tilde{I}_{lo}(\zeta;t)}{I_{trans}} - \Gamma_N(\zeta)\delta\tilde{N}(\zeta;t) - \frac{\tilde{g}_s(\zeta)}{1+\epsilon S_o}\frac{S_oP_o(\zeta)}{\tau_S}\delta S + \frac{F_N(\zeta;t)}{N_o} \tag{4.78}$$

$$\frac{d\delta S}{dt} = -\Gamma_S\delta S + \int_0^1 G_N(\zeta)\delta\tilde{N}(\zeta;t)d\zeta + \frac{F_S(t)}{\tilde{S}_o} \tag{4.79}$$

$$\delta\omega(t) = \frac{1}{2}\int_0^1 \alpha_N(\zeta)G_N(\zeta)\delta\tilde{N}(\zeta;t)d\zeta + \frac{1}{2}\alpha_S G_S S_o\delta S + F_\varphi(t) \tag{4.80}$$

with $\tilde{g}_s(\zeta)$ the the steady-state modal gain

$$\tilde{g}_s(\zeta) = \tilde{g}_w(\zeta) + \Delta\tilde{g}_s(\zeta) = \tilde{g}_w(\zeta) + \frac{\tilde{A}\Delta\tilde{N}_s(\zeta)}{1+\epsilon S_o} \tag{4.81}$$

and Γ_S and $\Gamma_N(\zeta)$ the damping rates:

$$\Gamma_S = \frac{R}{S_o} - G_S S_o \tag{4.82}$$

$$\Gamma_N(\zeta) = \frac{1}{\tau_S}\left[1 + \frac{\tilde{A}}{1+\epsilon S_o}S_oP_o(\zeta)\right]. \tag{4.83}$$

The damping of the intensity (4.82) is due to two components, the spontaneous emission rate and the gain compression. The damping due to the spontaneous emission rate is caused by the fact that the steady-state operating point differs from the threshold equation solution when $R \neq 0$. The optical gain is not clamped to the threshold

gain ($\tilde{g}_s \neq \tilde{g}_w$), resuling in damping for the intensity. The difference between the threshold gain and the steady-state gain (and therefore the corresponding the damping) is invertionally proportional to the power. At high powers, the intensity damping Γ_S is therefore mainly due to gain compression, and $\tilde{g}_s \approx \tilde{g}_w$.

In order to calculate the modulation characteristics and the noise properties, a harmonic analysis ($e^{i\Omega t}$) is performed on the small-signal rate equations. The modulation is the reponse to the excitation $\delta\tilde{I}_{lo}$, while the noise is determined by F_S, F_φ and F_N.

4.3.3 The relaxation oscillation and the characteristic function

The characteristic frequencies of the rate equations (4.78) and (4.79) are found by setting the driving terms $\delta\tilde{I}_{lo} = 0$, $F_N = 0$ and $F_S = 0$, and requiring nonzero solutions for $\delta\tilde{N}$ and δS. The characteristic equation is

$$D(\Omega) = \int_0^1 \frac{[\Omega_R(\zeta) + \Omega - i\Gamma_R(\zeta)]\,[\Omega_R(\zeta) - \Omega + i\Gamma_R(\zeta)]}{i\Omega + \Gamma_N(\zeta)} d\zeta = 0 \tag{4.84}$$

with $\Omega_R(\zeta)$ the local relaxation frequency, and $\Gamma_R(\zeta)$ the local damping rate, given by

$$\Omega_R^2(\zeta) = \frac{G_N(\zeta)\tilde{g}_s(\zeta)S_oP_o(\zeta)}{(1+\epsilon S_o)\tau_S} - \frac{1}{4}[\Gamma_S - \Gamma_N(\zeta)]^2 \tag{4.85}$$

$$\Gamma_R(\zeta) = \frac{1}{2}[\Gamma_S + \Gamma_N(\zeta)]\,. \tag{4.86}$$

Solution of (4.84) gives the complex characteristic frequencies (or poles) of the system.

4.3.4 Modulation characteristics

The modulation characteristics are found by setting $F_N = 0$, $F_S = 0$ and $F_\varphi = 0$ in (4.78)-(4.80), and solving in function of $\delta\tilde{I}_{lo}(\zeta;\Omega)$. The relative intensity modulation response is

$$\delta S(\Omega) = \frac{1}{\tau_S D(\Omega)} \int_0^1 \frac{G_N(\zeta)}{i\Omega + \Gamma_N(\zeta)} \frac{\delta\tilde{I}_{lo}(\zeta;\Omega)}{I_{trans}} d\zeta. \tag{4.87}$$

The frequency modulation response ($\delta\omega = 2\pi\delta f$)is related to this intensity modulation response by

$$\begin{aligned} \frac{\delta\omega(\Omega)}{\delta S(\Omega)} &= \frac{\tilde{\alpha}_{N1}(\Omega)}{2} \int_0^1 \frac{2i\Omega\Gamma_R(\zeta) - \Omega^2}{i\Omega + \Gamma_N(\zeta)} d\zeta \\ &+ \frac{\tilde{\alpha}_{N1}(\Omega) - \tilde{\alpha}_{N2}(\Omega)}{2} \int_0^1 \frac{\Omega_R^2(\zeta) + \Gamma_R^2(\zeta)}{i\Omega + \Gamma_N(\zeta)} d\zeta \\ &+ \frac{1}{2} \int_0^1 \frac{\alpha_N(\zeta)\Gamma_S\Gamma_N(\zeta)}{i\Omega + \Gamma_N(\zeta)} d\zeta + \frac{1}{2}\alpha_S G_S S_o \end{aligned} \tag{4.88}$$

with

$$\tilde{\alpha}_{N1}(\Omega) = \frac{\int_0^1 \frac{\alpha_N(\zeta)G_N(\zeta)}{i\Omega+\Gamma_N(\zeta)} \frac{\delta\tilde{I}_{lo}(\zeta;\Omega)}{I_{trans}} d\zeta}{\int_0^1 \frac{G_N(\zeta)}{i\Omega+\Gamma_N(\zeta)} \frac{\delta\tilde{I}_{lo}(\zeta;\Omega)}{I_{trans}} d\zeta} \tag{4.89}$$

$$\tilde{\alpha}_{N2}(\Omega) = \frac{\int_0^1 \alpha_N(\zeta) \frac{\Omega_R^2(\zeta)+\Gamma_R^2(\zeta)}{i\Omega+\Gamma_N(\zeta)} d\zeta}{\int_0^1 \frac{\Omega_R^2(\zeta)+\Gamma_R^2(\zeta)}{i\Omega+\Gamma_N(\zeta)} d\zeta}. \tag{4.90}$$

In order to identify the different terms in (4.88), the behavior of the FM modulation $\delta\omega(\Omega)$ for $\Omega \rightarrow 0$ is investigated:

$$\frac{\delta\omega(\Omega)}{\delta S(\Omega)} \rightarrow i\frac{\tilde{\alpha}_{N1}(0)}{2}\left[\Omega\int_0^1 \frac{2\Gamma_R(\zeta)}{\Gamma_N(\zeta)}d\zeta - iD(0)\frac{\tilde{\alpha}_{N1}(0)-\tilde{\alpha}_{N2}(0)}{\tilde{\alpha}_{N1}(0)}\right]$$

$$+\frac{1}{2}\Gamma_S\int_0^1 \alpha_N(\zeta)d\zeta + \frac{1}{2}\alpha_S G_S S_o. \tag{4.91}$$

The first term in (4.91) is zero at $\Omega = 0$ and corresponds to the dynamic chirp, the other three terms are nonzero at $\Omega = 0$ and correspond to the adiabatic chirp. This adiabatic chirp consists of three components. A first component is due to the ζ dependence of the electron density and power distribution $\tilde{\alpha}_{N2}$, and to the pumping scheme $\tilde{\alpha}_{N1}$. A second component is due to the damping of the intensity, which results in adiabatic chirp through its effect on the electron density. The third component is a direct effect of gain compression on the frequency for $\alpha_S \neq 0$. For completeness a temperature dependent adiabatic chirp should be added at low frequencies, with a cutoff frequency on the order of 10MHz.

When $\tilde{\alpha}_{N1}(\Omega) = \tilde{\alpha}_{N2}(\Omega)$, the first adiabatic chirp component is zero. In order to achieve this the current modulation distribution has to satisfy

$$\frac{\delta\tilde{I}_{lo}(\zeta;\Omega)}{I_{trans}} \sim \frac{\Omega_R^2(\zeta)+\Gamma_R^2(\zeta)}{G_N(\zeta)}. \tag{4.92}$$

If the current modulation is uniform, there is an adiabatic chirp due to the nonuniformity of the electron density and power distribution, as $\tilde{\alpha}_{N1}(\Omega) \neq \tilde{\alpha}_{N2}(\Omega)$, if $\alpha_N \neq$ const.

4.3.5 The noise spectra and the spontaneous emission linewidth

Solution of (4.78)-(4.80) with $\delta\tilde{I}_{lo} = 0$ gives for the single mode relative intensity noise (RIN) spectrum

$$\delta S(\Omega) = \frac{1}{D(\Omega)}\left[\frac{F_S(\Omega)}{S_o} + \int_0^1 \frac{G_N(\zeta)}{i\Omega + \Gamma_N(\zeta)}\frac{F_N(\zeta;\Omega)}{N_o}d\zeta\right] \tag{4.93}$$

and for the frequency noise spectrum

$$\delta\omega(\Omega) = F_\varphi(\Omega) - \tilde{\alpha}_{LW}(\Omega)\frac{F_S(\Omega)}{2S_o} + \frac{1}{2}\int_0^1 [\alpha_N(\zeta) - \tilde{\alpha}_{LW}(\Omega)]\frac{G_N(\zeta)}{i\Omega + \Gamma_N(\zeta)}\frac{F_N(\zeta;\Omega)}{N_o}d\zeta \tag{4.94}$$

with

$$\tilde{\alpha}_{LW}(\Omega) = \frac{\tilde{\alpha}_{N2}(\Omega)}{D(\Omega)}\int_0^1 \frac{\Omega_R^2(\zeta) + \Gamma_R^2(\zeta)}{i\Omega + \Gamma_N(\zeta)}d\zeta - \frac{1}{D(\Omega)}\int_0^1 \left[\frac{\alpha_N(\zeta)\Gamma_S\Gamma_N(\zeta)}{i\Omega + \Gamma_N(\zeta)} + \alpha_S G_S S_o\right]d\zeta. \tag{4.95}$$

The noise spectra F_S, F_φ and F_N are assumed white ((4.56), (4.57) and (4.69)) with magnitudes

$$|F_S(\Omega)| = \sqrt{2RS_o} \tag{4.96}$$

$$|F_\varphi(\Omega)| = \sqrt{\frac{R}{2S_o}} \tag{4.97}$$

$$|F_N(\zeta;\Omega)| = \sqrt{2D_{NN}(\zeta)}. \tag{4.98}$$

The intensity noise is much lower than the frequency noise, and can be neglected in the linewidth calculation. If the frequency noise spectrum is much broader (typically $\sim$ GHz) than the linewidth, the white noise approximation for the linewidth can be

used [12]

$$\Delta\nu = \frac{1}{2\pi}\int_{-\infty}^{+\infty} < \delta\omega(t)\delta\omega(t+\tau) > d\tau = \frac{1}{2\pi} < |\delta\omega(\Omega=0)|^2 > . \tag{4.99}$$

The frequency noise spectrum at $\Omega = 0$ is given by

$$\delta\omega(\Omega=0) = F_\varphi(0) - \alpha_{LW}\frac{F_S(0)}{2S_o} + \int_0^1 K(\zeta)F_N(\zeta;0)d\zeta \tag{4.100}$$

with α_{LW} the linewidth enhancement factor

$$\alpha_{LW} = \tilde{\alpha}_{LW}(0) = \tilde{\alpha}_{N2}(0) + \frac{1}{D(0)}\int_0^1 \left[\alpha_N(\zeta)\left(G_S S_o - \frac{R}{S_o}\right) - \alpha_S G_S S_o\right] d\zeta \tag{4.101}$$

$$\tilde{\alpha}_{N2}(0) = \frac{1}{D(0)}\int_0^1 \alpha_N(\zeta)\frac{\Omega_R^2(\zeta)+\Gamma_R^2(\zeta)}{\Gamma_N(\zeta)}d\zeta \tag{4.102}$$

$$D(0) = \int_0^1 \frac{\Omega_R^2(\zeta)+\Gamma_R^2(\zeta)}{\Gamma_N(\zeta)}d\zeta \tag{4.103}$$

$$K(\zeta) = [\alpha_N(\zeta) - \alpha_{LW}]\frac{G_N(\zeta)}{N_o\Gamma_N(\zeta)}. \tag{4.104}$$

The linewidth consits of three components $\Delta\nu = \Delta\nu_{sp} + \Delta\nu_{NN} + \Delta\nu_{NS}$, the spontaneous emission linewidth $\Delta\nu_{sp}$, the electron density noise component $\Delta\nu_{NN}$, and the stimulated emission component $\Delta\nu_{NS}$ given by

$$\Delta\nu_{sp} = \frac{R}{4\pi S_o}\left(1+\alpha_{LW}^2\right) \tag{4.105}$$

$$\Delta\nu_{NN} = \frac{1}{\pi}\int_0^1 K^2(\zeta)D_{NN}(\zeta)d\zeta \tag{4.106}$$

$$\Delta\nu_{NS} = -\frac{\alpha_{LW}}{\pi S_o}\int_0^1 K(\zeta)D_{NS}(\zeta)d\zeta. \tag{4.107}$$

4.4 Dynamic characteristics of the quarter wave shifted (QWS) distributed feedback (DFB) laser

The noise and modulation characteristics for QWS DFB lasers, analyzed in section 3.2.2, are calculated and the results are shown in figs. 4.1-4.5. The dynamic parameters used are shown in table 4.1.

α	4	n_g	4
L	400μm	τ_s	4 ns
G_ω	0	ϵ	0

Table 4.1: Dynamic parameters used for QWS DFB laser

4.4.1 The spontaneous emission linewidth

The spontaneous emission factor is taken as

$$n_{sp}(\zeta) = \frac{\tilde{N}(\zeta)}{\tilde{N}(\zeta) - 1} \tag{4.108}$$

resulting in a local spontaneous emission rate into the lasing mode, that is proportional to the local electron density.

$$n_{sp}(\zeta)\tilde{g}(\zeta) = \tilde{A}\tilde{N}(\zeta). \tag{4.109}$$

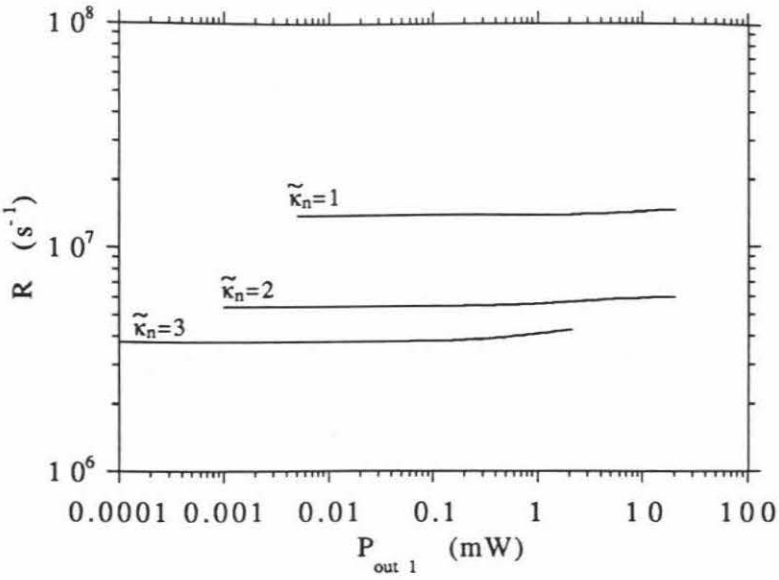

Figure 4.1: Spontaneous emission rate R into lasing mode as a function of output power for different values of $\tilde{\kappa}_n$

The spontaneous emission rate R into the lasing mode is shown in fig. 4.1 as a function of the output power for different values of the coupling coefficient. The difference in electron density ($\tilde{N}_{th} = 1.74$ for $\tilde{\kappa}_n = 1$, and $\tilde{N}_{th} = 1.36$ for $\tilde{\kappa}_n = 3$) can not explain the large difference in R. The larger spontaneous emission rate at smaller coupling coefficients is due to the open resonator enhancement [6]; modes that are strongly coupled to the outside (low $\tilde{\kappa}_n$) have an enhanced spontaneous emission rate.

The linewidth enhancemeent factor α_{LW} is shown in fig. 4.2 (solid line) as a function of the output power, while the dashed line is α_{LW} calculated using the electron density and power distribution at threshold. At low output powers α_{LW} is smaller than the material value, due to the high damping from the spontaneous emission rate (R/S_o) in (4.82) and (4.48). At high output powers $\alpha_{LW} = \alpha$ (dashed

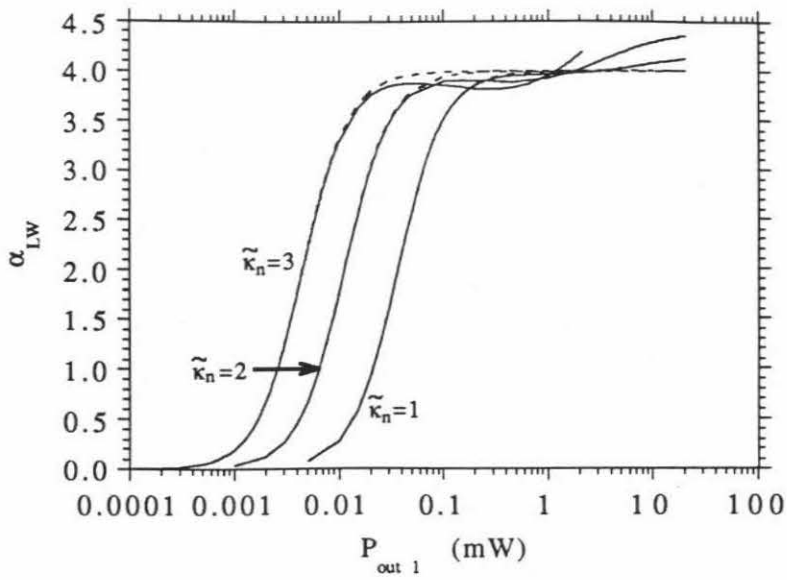

Figure 4.2: Linewidth enhancement factor α_{LW} as a function of output power for different values of $\tilde{\kappa}_n$

line) if the uniform threshold electron density is used. The effect of LSHB is clearly visible, as R and α_{LW} depend on the output power and is different from the material value α, however, the spontaneous emission rate R and linewidth enhancement factor α_{LW} become quasi power independent at high enough output power.

The local $\alpha_N(\zeta)$ and differential gain $G_N(\zeta)$ are shown in figs. 4.3 and 4.4 for $\tilde{\kappa}_n = 1$ (solid line) and $\tilde{\kappa}_n = 2$ (dashed line) for an output power of 0, 10 and 20mW (with increasing output power indicated by the arrows). At threshold the effective index is uniform and $\Delta\tilde{\beta}(\zeta) \equiv 0$, resulting in an $\alpha_N(\zeta)$ that is uniform and equal to the material value, while above threshold $\Delta\tilde{\beta}(\zeta)$ is not constant due to LSHB and $\alpha_N(\zeta)$ is not uniform, resulting in a linewidth enhancement factor α_{LW} that is different from the material value.

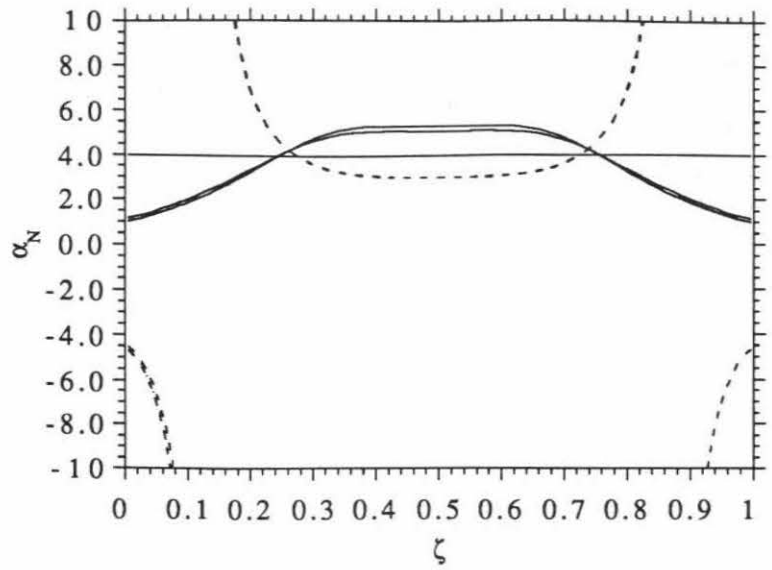

Figure 4.3: Local α parameter distribution for $\tilde{\kappa}_n = 1$ (solid line) and $\tilde{\kappa}_n = 2$ (dashed line), and for 0, 10 and 20mW of output power

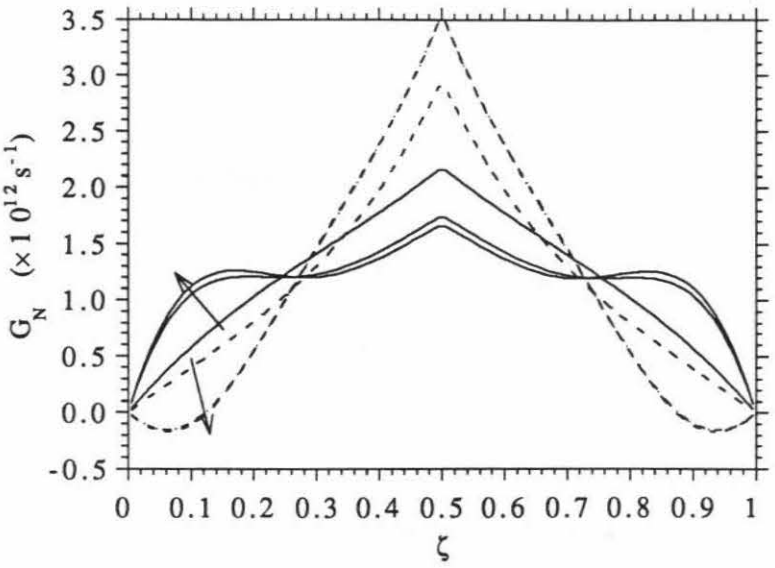

Figure 4.4: Local differential gain distribution for $\tilde{\kappa}_n = 1$ (solid line) and $\tilde{\kappa}_n = 2$ (dashed line), and for 0, 10 and 20mW of output power (with increasing output power indicated by the arrows)

The differential gain $G_N(\zeta)$ is not uniform as can be seen in fig. 4.4. A fixed change in the electron density will have a different effect on the optical intensity depending on where along the longitudinal direction this change occurs. For the case of $\tilde{\kappa}_n = 2$ an increase in electron density near the facets can result in a decrease in intensity at high enough output power as the differential gain $G_N(\zeta)$ is negative near the facets. This negative G_N also explains the sign change in α_N for $\tilde{\kappa}_n = 2$.

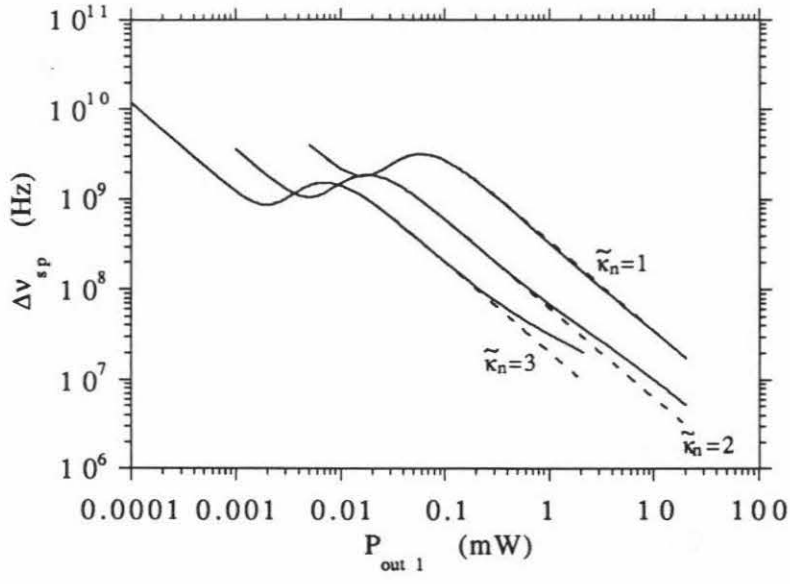

Figure 4.5: Spontaneous emission linewidth as a function of output power for different values of $\tilde{\kappa}_n$

The spontaneous emission linewidth $\Delta\nu_{sp}$ is shown in fig. 4.5 (solid line) as a function of the output power. The dashed line corresponds to $\Delta\nu_{sp}$ using the uniform threshold electron density distribution. Due to the quasi power independence of R and α_{LW} at high output powers, $\Delta\nu_{sp}$ becomes proportional to $1/P_o$. LSHB can thus not account for the rebroadening or minimum linewidth observed in DFB lasers.

Possible explanations for the rebroadening or minimum linewidth are other noise sources, such as pumping noise and stimulated emission noise ($\Delta\nu_{NN}$ and $\Delta\nu_{NS}$), which become dominant once the spontaneous emission noise ($\Delta\nu_{sp}$) becomes small enough at high output powers. These additional noise sources can have a $1/f$ component, which dominates at low frequencies, as has been observed and analyzed in [13]-[16]. Nonlinear gain, as for example due to spectral holeburning, has been a candidate for explanation of the minimum linewidth. It has been found however that nonlinear gain alone has a negligable effect on the spontaneous emission linewidth [17]. The presence of side modes combined with nonlinear gain however can result in a linewidth component that increases with the side mode power [18] and a minimum in the linewidth. This increase in side mode power can be caused by LSHB or spectral holeburning. All the mechanisms described above can give rise to a minimum linewidth; the dominating mechanism however can vary from laser to laser. It is clear however that LSHB alone cannot cause a minimum linewidth for a single mode laser.

4.4.2 The modulation response and the adiabatic chirp

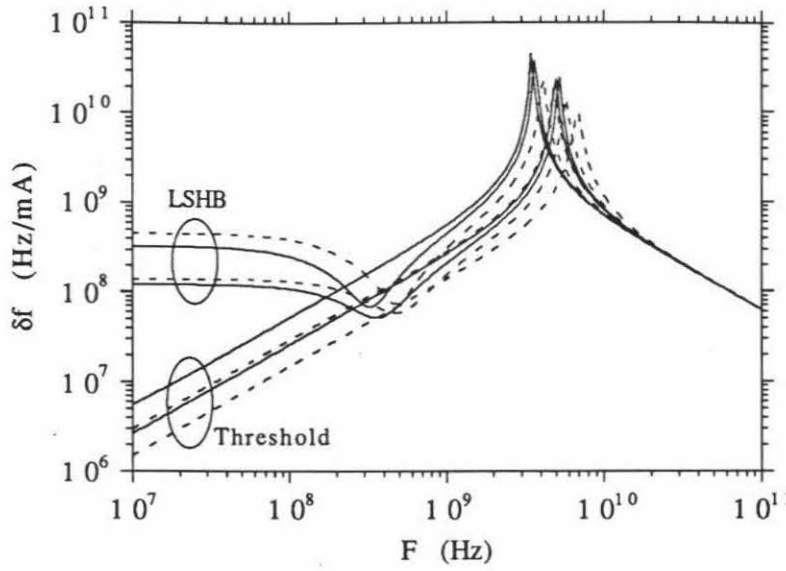

Figure 4.6: FM modulation magnitude for $\tilde{\kappa}_n = 1$ (solid line) and $\tilde{\kappa}_n = 2$ (dashed line) and P_{out1} =10mW, 20mW

Fig. 4.6 shows the magnitude of the FM modulation response under conditions as indicated in the caption. As a comparison the FM response is shown using the threshold distributions and the distributions self-consistent with LSHB. If the threshold distributions are used, $\alpha_N(\zeta) \equiv$ constant (fig. 4.3) and as a result the first adiabatic chirp component in (4.88) is zero and the adiabatic chirp due to the spontaneous emission damping is negligible ($\sim 10^6$Hz). If the self-consistent distributions for the electron density and the power are used however, $\alpha_N(\zeta)$ is not constant any more, and $\tilde{\alpha}_{N1}(\Omega) \neq \tilde{\alpha}_{N2}(\Omega)$ and the first adiabatic chirp component in (4.88) is not zero, but on the order of 100MHz/mA.

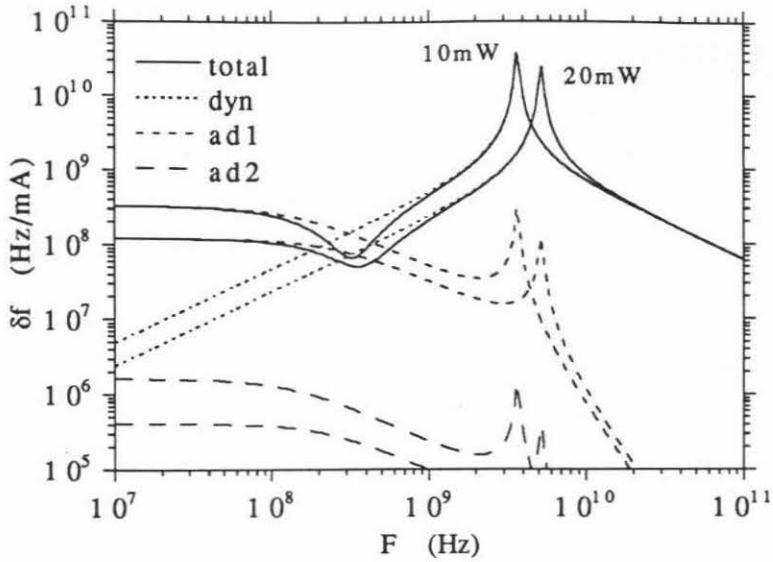

Figure 4.7: Chirp components magnitude for $\tilde{\kappa}_n = 1$ and P_{out1} =10mW, 20mW

The different chirp components for $\tilde{\kappa}_n = 1$ are shown in fig. 4.7 for an output power of 10mW and 20mW. At low modulation frequencies (< 50MHz) the adiabatic chirp due to LSHB dominates, while at high modulation frequencies (> 1GHz) the dynamic chirp dominates. The adiabatic chirp due to spontaneous emission damping (ad2 in fig. 4.7) is at least two orders of magnitude smaller than the adiabatic chirp from LSHB, while the third adiabatic chirp component in (4.88) is zero as gain compression has been neglected here ($\epsilon = 0 \Rightarrow \alpha_S \equiv 0$).

4.5 Dynamic characteristics of partially gain coupled DFB lasers

Since the initial theoretical work on DFB lasers in the early 70's [19] it has been known that gain coupled (GC) DFB lasers offer a distinct advantage over index coupled (IC) DFB lasers as SLM operation is obtained without the need for asymmetric facet reflections or phase shifts in the grating. Due to the more complicated fabrication of GC DFB lasers, it is not until recently [20,21] that GC DFB lasers have been demonstrated, and most of the DFB work has concentrated on IC structures. It has been predicted, and demonstrated in some cases, that GC DFB lasers have additional advantages over IC DFB lasers, such as more uniform intensity distributions and therefore reduced LSHB [22,23] (section 3.3.2), smaller sensitivity to facet reflections or external feedback [24,25], and high side mode suppression ratio [20].

More recently some enhanced dynamic properties have been predicted for partially GC DFB, such as reduction in the linewidth enhancement factor for out-of-phase coupling [7,26,27,28,29], increased 3dB modulation bandwidth for out-of-phase coupling [30,31] and increased FM magnitude for in-phase coupling [30]. The highest 3dB modulation bandwidth measured so far for partially GC DFB lasers is 22GHz [32]. The models used for these predictions however show some inconsistencies. Gain compression is included in the expression for the gain, but not for the coupling coefficient as in (4.32,4.33); the standing wave term in the expression for $P_o(\zeta)$ is not included (in some cases this standing wave term can significantly affect the uniformity of P_o).

The models in [30,31] are large-signal models and require intensive numerical iterations to calculate the dynamics around one operating point, while the model used in [28] is based on the Wronskian model developed in [9], but never actually gives expressions for the functional derivatives (4.20,4.21).

In this section the theory developed in this chapter will be applied to partially GC DFB lasers to explain the predictions mentioned above.

4.5.1 Uniform electron density modulation

When the modulation of the electron density is assumed to be uniform, the ζ dependence in (4.38) can be integrated out, and a ζ independent formulation can be used (this is different from using the uniform threshold distribution as (4.78) results in a nonuniform $\delta\tilde{N}$ under uniform current modulation). For a uniform grating with index coupling $\tilde{\kappa}_n$, gain coupling $\tilde{\kappa}_\sigma$ and zero facet reflectivities, the Wronskian is given by

$$W = \frac{2i\tilde{\beta}_m \mathcal{N}}{\tilde{\kappa}} \left(\tilde{S} \coth \tilde{S} + i\tilde{\beta} \right) \tag{4.110}$$

with $\tilde{\beta} = \Delta\tilde{\beta} + i\tilde{\gamma}$, $\tilde{\kappa} = \tilde{\kappa}_n - i\tilde{\kappa}_\sigma$, $\mathcal{N}$ a normalization constant to satisfy (4.67)

$$\mathcal{N} \frac{|\tilde{\kappa}|^2}{\left|\tilde{S}\right|^2} \left(\frac{\sinh 2\tilde{S}_r}{2\tilde{S}_r} - \frac{\sin 2\tilde{S}_i}{2\tilde{S}_i} \right) = \frac{h\nu}{e} \frac{R_c I_{trans}}{2n_{eff}} \tag{4.111}$$

and $\tilde{S} = \tilde{S}_r + i\tilde{S}_i = \sqrt{\tilde{\kappa}^2 - \tilde{\beta}^2}$.

The lasing condition ($W = 0$) is

$$\tilde{S} \coth \tilde{S} = -i\tilde{\beta} \tag{4.112}$$

and the derivatives of the Wronskian with respect to $\tilde{\beta}$ and $\tilde{\kappa}$ at the lasing condition are

$$\frac{\partial W}{\partial \tilde{\beta}} = \int_0^1 \frac{\delta W}{\delta \tilde{\beta}} d\zeta = \frac{2i\tilde{\beta}_m \tilde{\kappa} \mathcal{N}}{\tilde{S}^2} \left(i - \tilde{\beta}\right) \tag{4.113}$$

$$\frac{\partial W}{\partial \tilde{\kappa}} = \int_0^1 \frac{\delta W}{\delta \tilde{\kappa}} d\zeta = \frac{2i\tilde{\beta}_m \mathcal{N}}{\tilde{S}^2} \left(\tilde{\kappa}^2 - i\tilde{\beta}\right). \tag{4.114}$$

The differential gain G_N and α_N are then ζ independent and given by

$$G_N = 2Re\left[C_N\right] \tag{4.115}$$

$$\alpha_N = \frac{Im\left[C_N\right]}{Re\left[C_N\right]} \tag{4.116}$$

with

$$C_N = -i \frac{\frac{\partial W}{\partial \tilde{\beta}} \frac{\partial \tilde{\beta}}{\partial \tilde{N}} + \frac{\partial W}{\partial \tilde{\kappa}} \frac{\partial \tilde{\kappa}}{\partial \tilde{N}}}{\frac{\partial W}{\partial \omega}}. \tag{4.117}$$

The ζ independent damping factors Γ_N, Γ_S and Γ_R, and relaxation frequency Ω_R can be defined as in (4.83), (4.82), (4.86), and (4.85) with $S_o P_o(\zeta)$ replaced by the average power S_o. The 3dB frequency F_{3dB} is then given by

$$F_{3dB} = \frac{1}{2\pi} \sqrt{\Omega_R^2 - \Gamma_R^2 + 2\sqrt{\Omega_R^4 + \Omega_R^2 \Gamma_R^2 + \Gamma_R^4}}. \tag{4.118}$$

Calculations were performed for various modulation depths Γ_1/Γ_0 of the optical confinement factor, and various values of the index coupling coefficient $\tilde{\kappa}_n$ (with negative values corresponding to out-of-phase and positive values to in-phase coupling). The parameters used are the same as in section 4.4, except for the gain compression factor which was taken as $\epsilon = 0.02$. The results at an high average power level in the cavity $S_o = 10$ are shown in figs. 4.8 and 4.9. The relaxation oscillation frequency

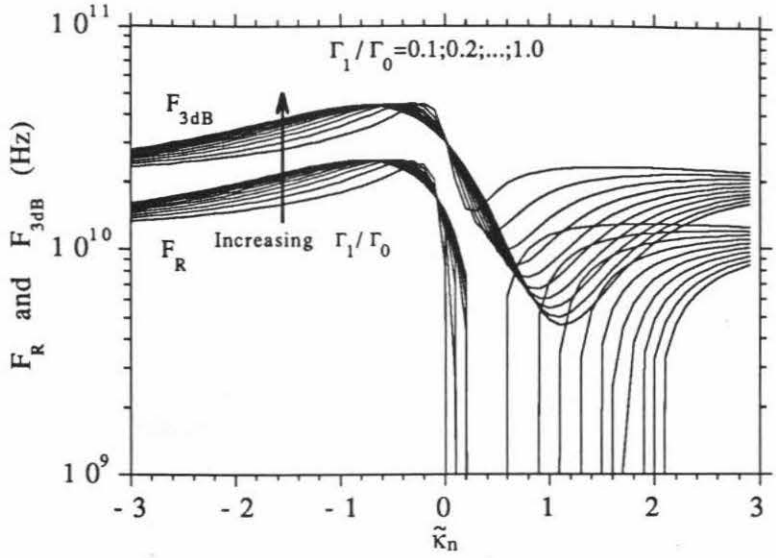

Figure 4.8: Relaxation frequency and 3dB frequency for partially gain coupled DFB lasers

F_R and the 3dB modulation frequency F_{3dB} are shown in fig. 4.8 as a function of the amount of index coupling for various modulation depths of the active layer optical confinement factor. For a same magnitude of index coupling, the 3dB modulation frequency can be up to 10 times larger for out-of-phase coupling compared to in-phase coupling. Increasing the modulation depth of the optical confinement factor (Γ_1/Γ_0), results in an increase (decrease) in the modulation bandwidth for out-of-phase (in-phase) coupling. For out-of-phase (in-phase) coupling an increase in the electron density increases (decreases) the feedback, and therefore enhances (reduces) the differential gain G_N. For in-phase coupling the differential gain G_N can be reduced enough to result in over damping and no relaxation oscillations occurs (fig. 4.8).

The linewidth enhancement factor α_{LW} is shown in fig. 4.9 as a function of the

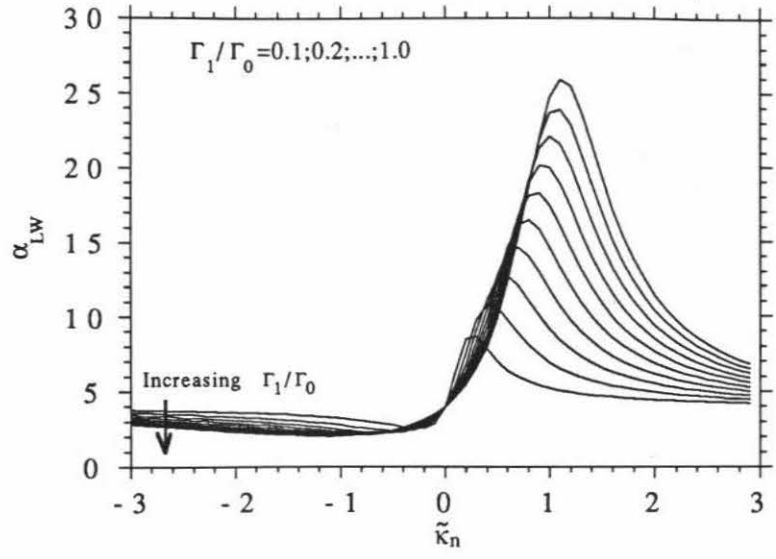

Figure 4.9: Linewidth enhancement factor for partially gain coupled DFB lasers

amount of index coupling at various modulation depths of the active layer optical confinement factor. Due to the enhanced (reduced) differential gain G_N the linewidth enhancement factor α_{LW} is reduced (enhanced) for out-of-phase (in-phase) coupling.

4.5.2 Uniform current modulation

When the current modulation instead of the electron density modulation is assumed to be uniform the ζ-dependent formulas have to be used. The modulation characteristics for a partially GC DFB laser with moderate index coupling $|\tilde{\kappa}_n| = 1$ and an optical confinement factor modulation $\Gamma_1/\Gamma_0 = 0.5$ were calculated using the threshold distributions for an average power in the cavity $S_o = 1$, which corresponds to just under 18mW of output power per facet. The distributions $G_N(\zeta)$, $\alpha_N(\zeta)$ and $F_R(\zeta)$ are shown in figs. 4.10, 4.11, and 4.12 respectively for out-of-phase coupling

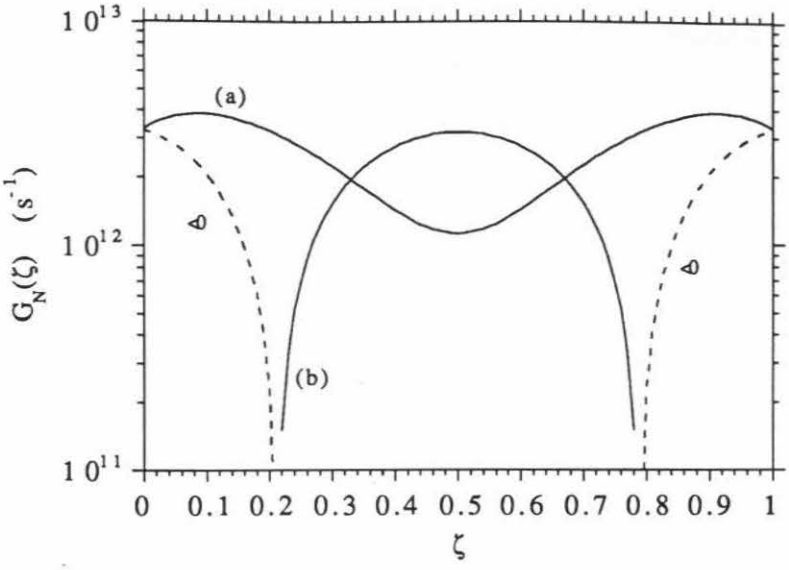

Figure 4.10: Local differential gain distribution for out-of-phase (a) and in-phase (b) coupling in partially gain coupled DFB lasers

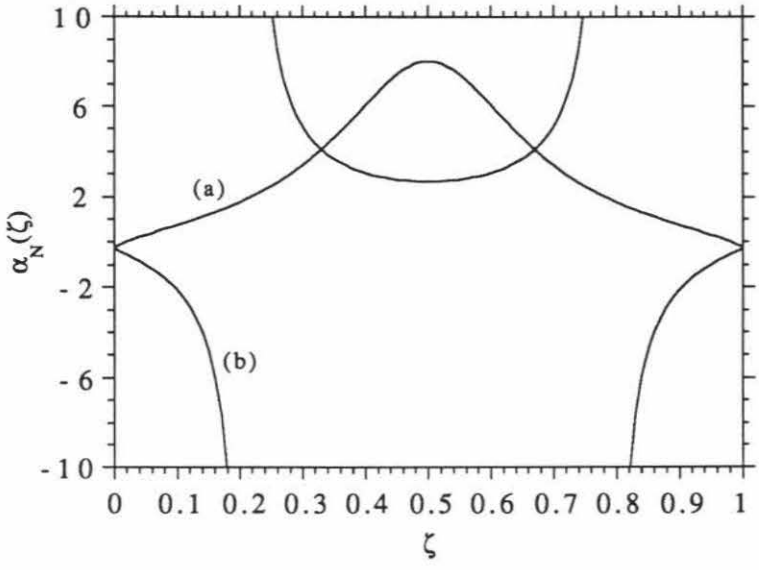

Figure 4.11: Local α_N distribution for out-of-phase (a) and in-phase (b) coupling in partially gain coupled DFB lasers

(a) and in-phase coupling (b). For the case of in-phase coupling the differential gain G_N is negative near the facets. An increase in the electron density near the facets will therefore result in a decrease in power. Due to the dependence of the coupling coefficient on the electron density the chirp factor $\alpha_N(\zeta)$ is nonuniform even if the uniform electron density distribution is used (for the QWS DFB α_N is constant when the threshold distribution is used). This will result in an adiabatic chirp ($\tilde{\alpha}_{N1} \neq \tilde{\alpha}_{N2}$) in (4.88). The change in sign in α_N for in-phase coupling, merely reflects the change in sign of G_N, such that $\alpha_N G_N$ in (4.80) remains positive for all ζ.

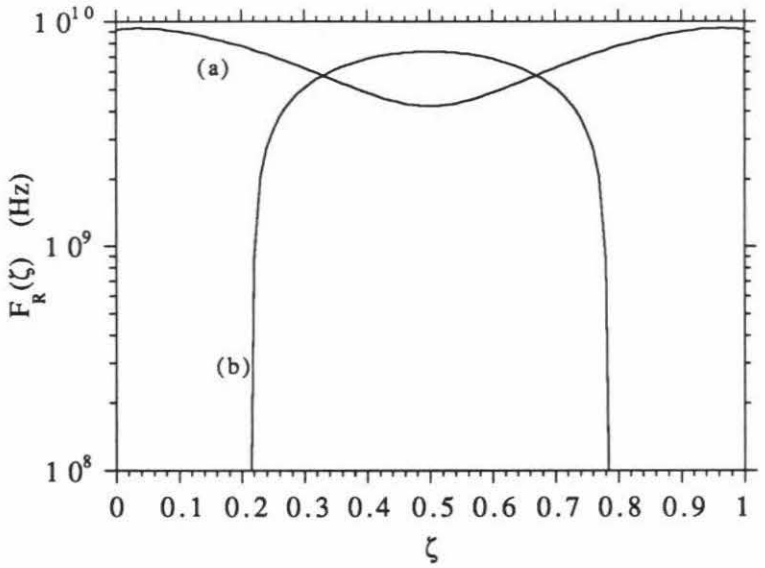

Figure 4.12: Local relaxation frequency distribution for out-of-phase coupling (a) and in-phase coupling (b) in partially gain coupled DFB lasers

From fig. 4.12 it can be seen that, due to the reduced or negative G_N near the facets for in-phase coupling, the relaxation frequency becomes imaginary (over damped) near the facets.

Fig. 4.13 shows the relative AM modulation response for out-of-phase (a) and in-phase (b) coupling. The relaxation frequency is about 7 times larger in the case of out-of-phase coupling. The damping Γ_R is the same in both cases, but as the relaxation

oscillation frequency is much smaller for in-phase coupling, this results in a much weaker peak. At higher powers, the in-phase coupling case becomes over damped and no oscillation peak occurs.

The FM response is shown in fig. 4.14, and it can be seen that the adiabatic chirp is about 5 times as large in the case of in-phase coupling. The decomposition of the chirp in the dynamic and the three adiabatic components is shown in fig. 4.15 for out-of-phase coupling and fig. 4.16 for in-phase coupling.

The adiabatic chirp is dominated by the component ad1 due to the nonuniformity of α_N. The component due to damping (ad2) is about the same at low frequencies for both cases, and the third component (ad3) due to α_S is about two orders of magnitude smaller than the total adiabatic chirp. The difference in the adiabatic chirp component ad1 in the two cases is due to the difference in $\tilde{\alpha}_{N1}$ and $\tilde{\alpha}_{N2}$ which are shown in fig. 4.17. The difference between $\tilde{\alpha}_{N1}$ and $\tilde{\alpha}_{N2}$, which determines the adiabatic chirp, is much larger in the case of in-phase coupling. The magnitude of $\tilde{\alpha}_{N1}$, which determines the dynamic chirp is much larger for in-phase coupling, and increases with frequency. This explains why the chirp at high frequencies in fig. 4.14 is nearly the same in both cases, even though the roll off starts at lower frequencies for in-phase coupling.

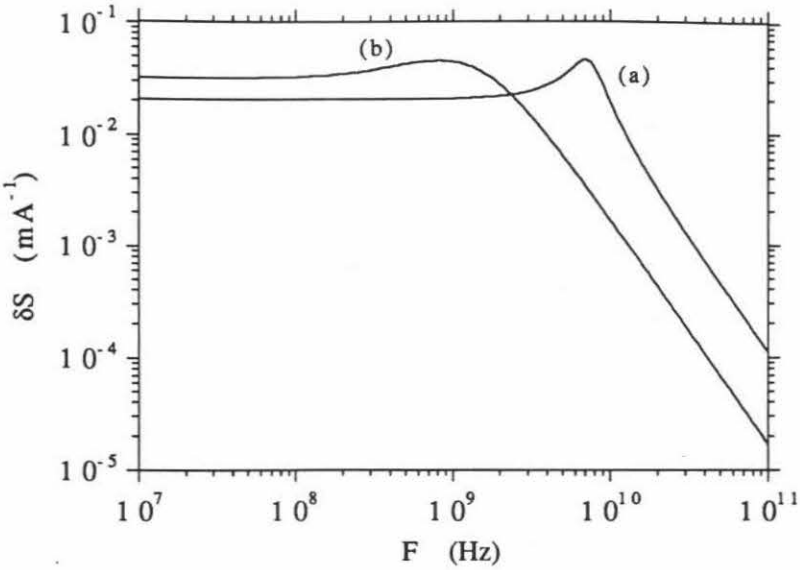

Figure 4.13: AM modulation response for out-of-phase (a) and in-phase (b) coupling in partially gain coupled DFB lasers

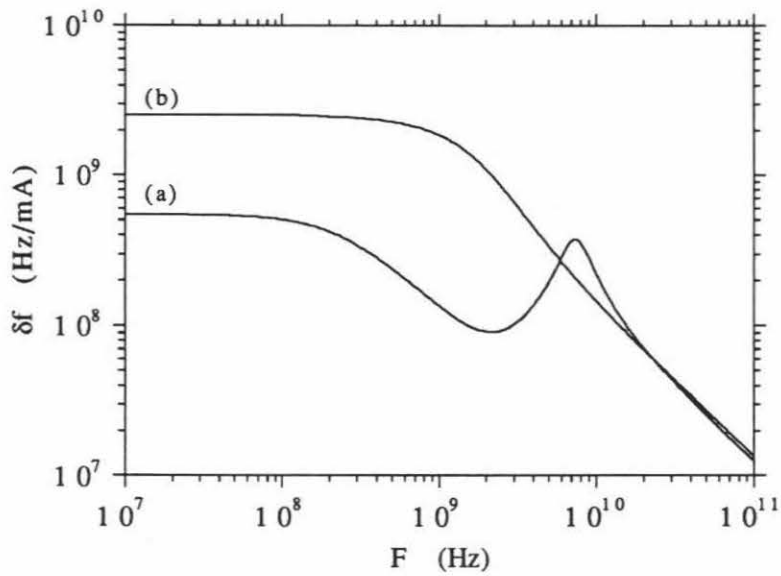

Figure 4.14: FM modulation response for out-of-phase (a) and in-phase (b) coupling in partially gain coupled DFB lasers

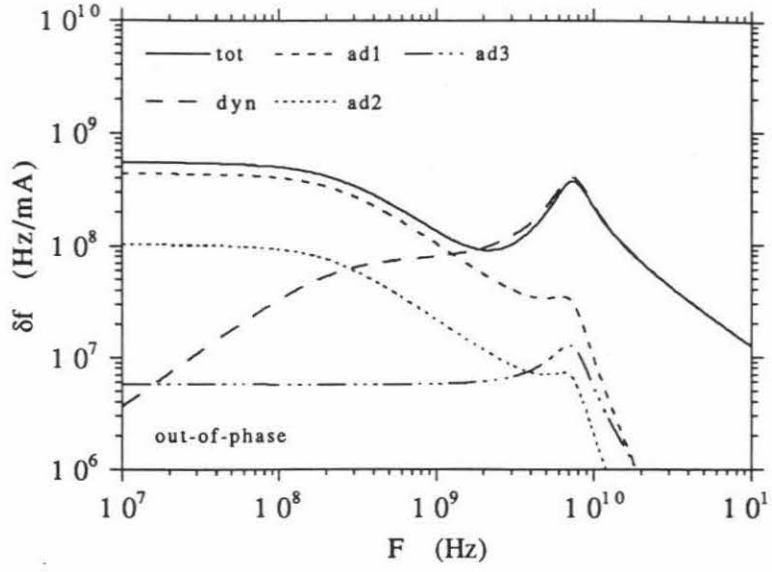

Figure 4.15: Chirp components for out-of-phase coupling in partially gain coupled DFB lasers

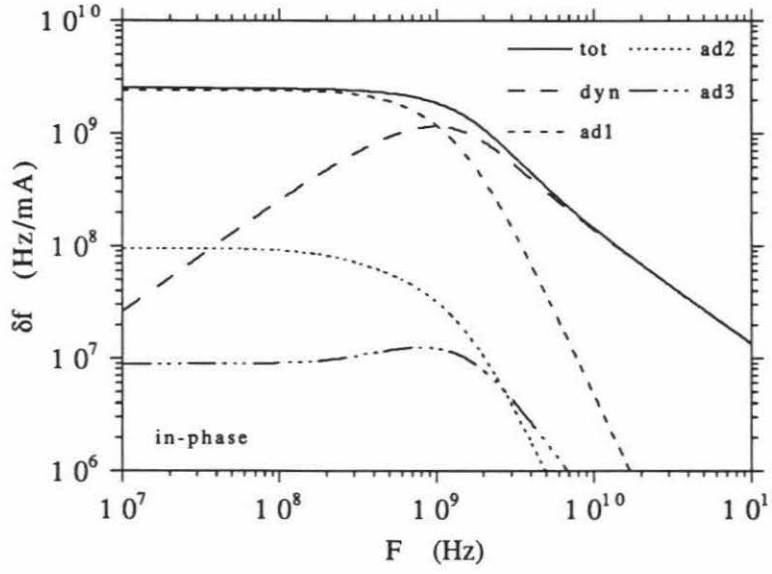

Figure 4.16: Chirp components for in-phase coupling in partially gain coupled DFB lasers

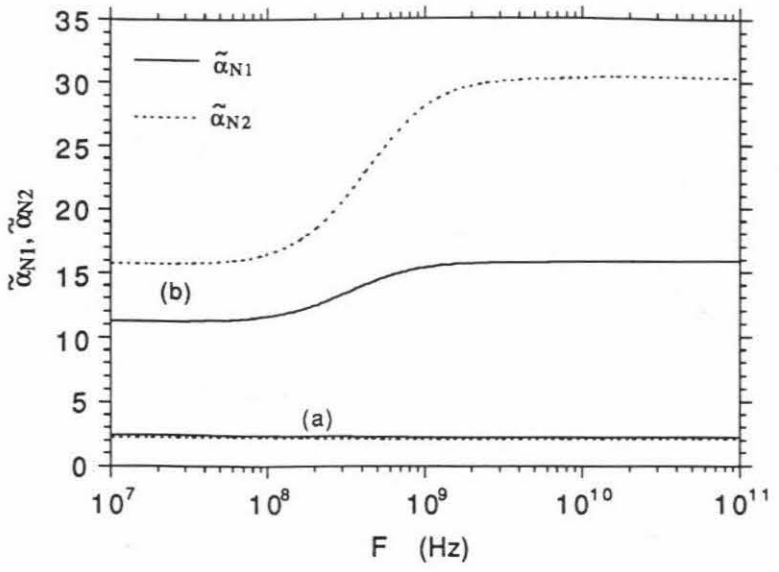

Figure 4.17: Chirp factors $\tilde{\alpha}_{N1}$ and $\tilde{\alpha}_{N2}$ for out-of-phase (a) and in-phase (b) coupling in partially gain coupled DFB lasers

4.6 Conclusion

In this chapter a small-signal dynamic model for SLM lasers including gain coupling was derived, starting from a Green's function solution of Maxwell's equations. The model takes into account the cavity structure through the longitudinal dependence of the optical field and the electron density, the dependence of the gain and index coupling coefficient on the electron density, and the effect of gain compression on the gain and the coupling coefficient. The model can be used above threshold in a self-consistent way if the modal distributions are calculated by including LSHB. The only limitation to the model is that it is a small-signal model, and can thus only be used for small deviations in electron density and lasing frequency around the operating

point.

An expression was derived for the spontaneous emission rate into the lasing mode, showing that the spontaneous emission rate depends on the modal distribution and the modal dynamics. An expression for the linewidth enhancement factor that enters the linewidth formula was derived, showing how structural effects can result in a value different from the material value. By applying the model to a QWS DFB laser, it was shown that LSHB is not responsible for the linewidth floor or rebroadening observed in measurements. Small signal AM and FM modulation response expressions were derived, and different components in the FM response were identified as a dynamic chirp and three different adiabatic chirp components. It was shown how the nonuniformity in the electron density, due to LSHB, causes a dominating adiabatic chirp in the FM response of QWS DFB lasers.

Finally the model was applied to partially gain coupled DFB lasers, where, due to the dependence of the coupling coefficient on the electron density, the differential gain can be enhanced (reduced) for out-of-phase (in-phase) coupling by increasing the modulation of the optical confinement factor. This results in an increased 3dB modulation bandwidth and decreased linewidth enhancement factor for out-of-phase coupling, and an increased FM modulation at low frequencies for in-phase coupling.

References

[1] C. H. Henry, *IEEE J. Quantum Electron.*, **18**, 259 (1982)

[2] T. L. Koch, and U. Koren, *J. Lightw. Technol.*, **8**, 274 (1990)

[3] A. Yariv, **Quantum Electronics**, 3rd ed., ch. 11 (1989)

[4] R. J. Lang, and A. Yariv, *IEEE J. Quantum Electron.*, **21**, 1683 (1985)

[5] R. J. Lang, and A. Yariv, *IEEE J. Quantum Electron.*, **22**, 436 (1986)

[6] C. H. Henry, *J. Lightwave Technol.*, **4**, 288 (1986)

[7] L. Olofsson, and T.G. Brown, *IEEE J. Quantum Electron.*, **28**, 1450 (1992)

[8] G.-H. Duan, P. Gallion, and G. Debarge, *IEEE J. Quantum Electron.*, **26**, 32 (1990)

[9] B. Tromborg, H. Olesen, and X. Pan, *IEEE J. Quantum Electron.*, **27**, 178 (1991)

[10] Y. Luo, Y. Nakano, and K. Tada, *Appl. Phys. Lett.*, **56**, 1620 (1990)

[11] T. W. Johannes, and W. Harth, *Electron. Lett.*, **28**, 1347 (1992)

[12] A. Yariv, **Quantum Electronics**, 3rd ed., ch. 21 (1989)

[13] K. Kikuchi, *Electron. Lett.*, **24**, 1001 (1988)

[14] K. Kikuchi, *IEEE J. Quantum Electron.*, **25**, 684 (1989)

[15] M. Okai, T. Tsuchiya, K. Uomi, N. Chinone, and T. Harada, *IEEE Photon. Technol. Lett.*, **3**, 427 (1991)

[16] M. Okai, T. Tsuchiya, A. Takai, and N. Chinone, *IEEE Photon. Technol. Lett.*, **4**, 526 (1992)

[17] X. Pan, H. Olesen, and B. Tromborg, *Electron. Lett.*, **26**, 1074 (1990)

[18] U. Krüger, and K. Petermann, *IEEE J. Quantum Electron.*, **24**, 2355 (1988)

[19] H. Kogelnik, and C. V. Shank, *J. Appl. Phys.*, **43**, 2327 (1972)

[20] Y. Luo, Y. Nakano, K. Tada, T. Inoue, H. Hosomatsu, and H. Iwaoka, *IEEE J. Quantum Electron.*, **27**, 1724 (1991)

[21] G. P. Li, T. Makino, R. Moore, N. Puetz, K.-W. Leong, and H. Lu, *IEEE J. Quantum Electron.*, **29**, 1736 (1993)

[22] E. Kapon, A. Hardy, and A. Katzir, *IEEE J. Quantum Electron.*, **18**, 66 (1982)

[23] G. Morthier, P. Vankwikelberge, K. David, and R. Baets, *IEEE Photon. Technol. Lett.*, **2**, 170 (1990)

[24] Y. Nakano, Y. Luo, and K. Tada, *Appl. Phys. Lett.*, **55**, 1606 (1989)

[25] Y. Nakano, Y. Deguchi, K. Ikeda, Y. Luo, and K. Tada, *IEEE J. Quantum Electron.*, **27**, 1732 (1991)

[26] Y. Luo, R. Takahashi, Y. Nakano, K. Tada, T. Kamiya, H. Hosomatsu, and H. Iwaoka, *Appl. Phys. Lett.*, **59**, 37 (1991)

[27] A. J. Lowery, *Electron. Lett.*, **28**, 2295 (1992)

[28] K. Kudo, S. Arai, and J. I. Shim, *IEEE J. Quantum. Electron.*, **29**, 1769 (1993)

[29] H. Lu, G. P. Li, and T. Makino, *Appl. Phys. Lett.*, **63**, 589 (1993)

[30] L. M. Zhang, and J. E. Carroll, *IEEE Photon. Technol. Lett.*, **5**, 506 (1993)

[31] A. J. Lowery, and D. Novak, *Electron. Lett.*, **29**, 461 (1993)

[32] H. Lu, S. McGarry, G. P. Li, and T. Makino, *Electron. Lett.*, **29**, 1369 (1993)

Part II

Spectral characteristics of passively mode-locked quantum well lasers

Chapter 5

Introduction

5.1 Passive mode-locking

One of the most active research areas in lasers is the generation of short optical pulses with pulse widths ranging from several picoseconds down to the femtosecond range. Applications for these pulses can be found in dynamic measurements of systems on subpicosecond time scales, such as in solid-state physics, biochemistry, molecular dynamics, and ultrafast electronics and optoelectronics [1]. Some applications can be found in optical communications, such as an optical pulse source for time division multiplexing (TDM) and generation of soliton pulses for long haul optical fiber transmission. To generate pulses much shorter than the typical inversion lifetimes, nonlinear techniques have to be used such as mode-locking, gain switching and Q-switching. Of all these techniques mode-locking has resulted in the shortest pulses.

Mode-locking of a laser is achieved by a modulation of the net cavity gain (or refractive index) at the cavity round-trip frequency, such that energy is transferred between the longitudinal cavity modes, resulting in a phase-locked multimode spectrum. The coherence of the multiple modes results in an optical pulse train with pulse widths proportional to the reciprocal of the phase-locked spectral bandwidth [2].

The modulation at the cavity round-trip frequency can be generated by an external RF signal as in active mode-locking, or it can be generated internally by the optical pulse train itself as in passive mode-locking. Passive mode-locking can best be understood in the time domain, by considering the effects of different elements (gain, loss, dispersion) on a pulse circulating in the cavity. Several theoretical descriptions of passive mode-locking in the time domain have been published, with most of the effort concentrating on the existence of a stable pulse solution [3]–[8]. The main results on the existence of a stable pulse solution are summarized below. The different elements in the cavity are a gain element, a saturable absorber and a dipersive element as illustrated in fig. 5.1.

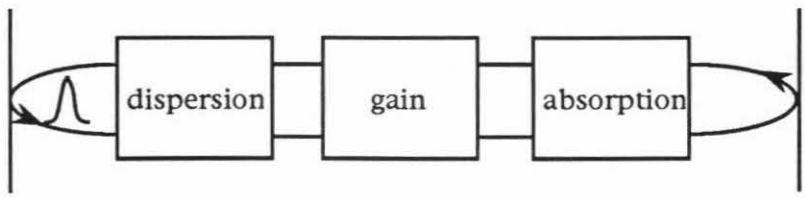

Figure 5.1: Passive mode-locked laser cavity

The saturable absorber provides the pulse shortening (spectral broadening) mech-

anism, while the dispersive element introduces pulse broadening (spectral narrowing) and is usually dominated by a bandwidth limiting effect such as the optical gain bandwidth. The time dependence of the optical intensity, the loss and the gain are shown in fig. 5.2, illustrating the requirements for stable passive mode-locking. The existence of a stable circulating pulse requires net gain for the center of the pulse and net loss for the tails of the pulse, resulting in pulse compression (spectral broadening) for each pass of the pulse. Once the pulse is short enough, the pulse broadening (spectral narrowing) per pass due to the dispersive element will equal the pulse narrowing, and a stable pulse can exist. The excess energy generated in the center of the pulse is transferred to the tails, resulting in total net round-trip gain of zero at each point in time.

As illustrated in fig. 5.2 three requirements have to be satisfied:

1. For the center of the pulse to experience net gain, the absorber has to saturate faster than the gain.

2. For the trailing edge of the pulse to experience net loss when the absorber recovery is slow compared to the pulse width, the gain has to saturate below the total loss.

3. For the leading edge of the pulse to experience net loss, the absorber has to recover faster than the gain.

When the pumping of the gain element is too large, the gain becomes larger than the loss before the arrival of the next pulse and the leading edge experiences net

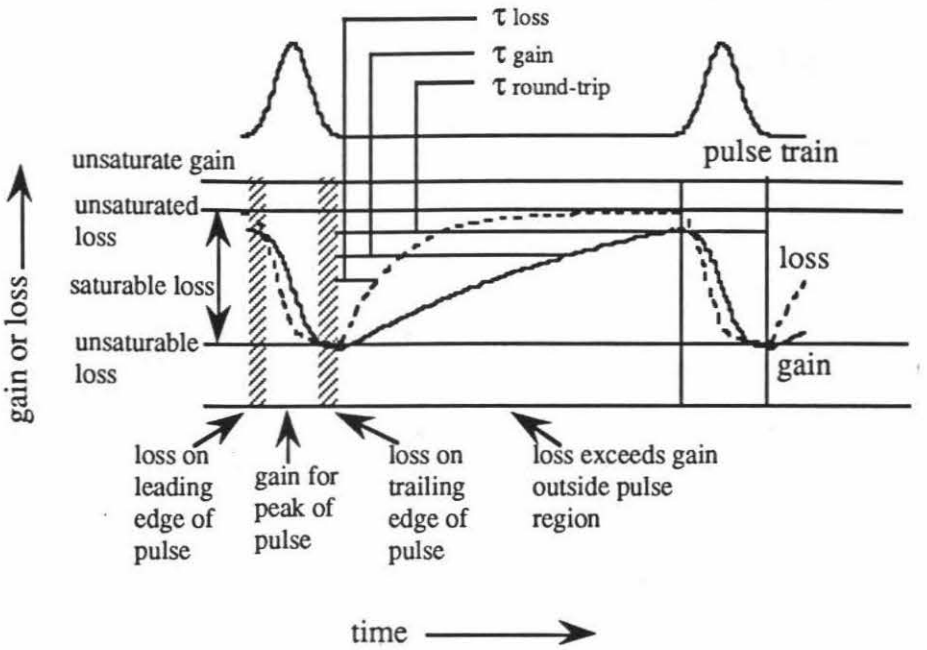

Figure 5.2: Gain and loss dynamics of passively mode-locked laser

gain. The pulse becomes unstable, and mode-locking is lost or the laser switches to mode-locking in a higher harmonic of the round-trip frequency, thereby reducing the gain recovery between consecutive pulses [9,10]. When the pumping of the gain element is too low, the generated pulse energy is too low to saturate the gain below the saturated loss and the trailing edge of the pulse experiences net gain. The pulse becomes unstable and mode-locking is lost or the laser switches to mode-locking in a lower harmonic of the round-trip frequency. In the lower harmonic the gain before the arrival of the pulse is larger such that larger pulse energies can be generated [9,10].

Generation of ultrashort pulses requires a broad gain spectrum as well as a broad-band absorber. Pulses as short as 30 fs with external compression to 6 fs have

been generated by passively mode-locked dye lasers [11]. Since the demonstration of self-mode-locking in Ti:sapphire in 1991 [12], the Ti:sapphire laser has become the technology leader for sub-50fs pulse generation, with pulses as short as 11fs [13]. Discovery of self-mode-locking in Ti:sapphire lasers has also opened a whole new field in passive mode-locking, where the saturable absorber is replaced by an intensity dependent loss or gain mechanism, such as self focussing.

5.2 Mode-locking of semiconductor lasers

Besides the usual advantages of semiconductor lasers, such as low cost, small size and efficient electrical pumping, the electronic band structure of semiconductors and its associated broad gain spectrum [14] are very suitable for mode-locking and generation of ultra short pulses. By coupling a semiconductor laser to an external cavity active mode-locking was demonstrated in 1978 [17] and passive mode-locking in 1980 [18]. The saturable absorber in these lasers was provided by aging induced degraded regions along the laser. Controlled introduction of saturable absorption by proton bombarding one of the mirror facets was reported in [19,20], resulting in passive mode-locking with subpicosecond multiple pulses. A good and thorough review on the early work in mode-locking of semiconductor lasers can be found in [21] and [22].

Clean subpicosecond pulses were obtained for the first time using an external multiple quantum well (MQW) absorber [23]. The low saturation energy of the exciton feature in the MQW provides a fast absorber saturation, and the absorber recovery

time was reduced by proton bombarding the the MQW absorber. Improvements on this setup has resulted in 207fs pulse widths and 160W of peak power after external amplification and external pulse compression [24].

Passive mode-locking of a multi-section buried heterostructure laser coupled to an external cavity was first demonstrated in 1983 [15] with 35ps pulse widths. The pulse shape showed a pronounced fine structure however, indicating mode-locking in spectral clusters. Improvement on passive mode-locking of multi-section lasers is possible by making use of the following very attractive properties of MQW lasers:

- Due to the flat two-dimensional density of states the gain at a fixed wavelength saturates at high current injection[16]. This sublinear behavior of the gain in function of the bias results in a saturation energy for a forward biased gain section that can be several times larger than the saturation energy in an reverse (or "sub-transparency") biased absorber section.

- Due to the electric field across a reverse biased pn-junction the electrons generated in the absorber section can be extracted faster than under forward bias. The absorber recovery time is shorter than the gain recovery time.

Passive mode-locking of a two-section MQW laser coupled to an external cavity has resulted in clean pulses with typical pulse widths of 8ps and pulse repetition rates up to 7GHz [9] at harmonics of the cavity round-trip frequency. The noise characteristics and the long term stability of these lasers were measured, showing very low timing jitter (5.5 ps for a pulse repetition rate of 546 MHz) and very low pulse

energy fluctuations (<0.52%) [25]. The pulse energy is determined by the saturation energy of the gain section and is typically a few pJ [10].

Mode-locking of MQW lasers coupled to an external cavity results in stable pulse trains as the pulse round-trip time is of the same order of magnitude as the gain recovery time. This allows strong gain saturation with almost complete gain recovery before the arrival of the next pulse. Strong gain saturation however is not a requirement, and passive mode-locking of monolithic structures has been demonstrated with pulse repetition rates larger than 100 GHz [26]-[28] and as high as 350 GHz [29]. As the pulse round-trip time for monolithic devices is much shorter than the gain recovery time, the net gain modulation necessary for mode-locking is much weaker and stability of the pulse train becomes an issue.

5.3 Outline of part II

The implications of the broad gain spectrum of MQW lasers on passive mode-locking of two-section lasers coupled to an external cavity is investigated experimentally in chapter 6. Broad-band tuning of the center wavelength of the optical spectrum is demonstrated, with a tuning range as high as 26 nm at an average wavelength of 840 nm (~3%), pulse widths of a few ps and bandwidths of a few nm. The time-bandwidth products are typically 10 times larger than the transform limit. It is then shown, by compressing the pulses to sub-ps pulse widths, that this excess bandwidth is due to a strong linear upchirp of the pulse. Near transform limited pulse widths as

low as 320 fs are measured, with a compression factor of 15 and 1.9 W of peak power.

A pulse propagation model through saturable media with self-phase-modulation (SPM) is developed in chapter 7 and applied to a two-section structure to demonstrate the chirping mechanisms present in passively mode-locked MQW lasers. The α-parameter, and the associated change in refractive index under saturation in the gain section is shown to give rise to SPM, which combined with the pulse shaping mechanism of the saturable absorber imprints a linear upchirp on the pulses. Properties such as the pulse shape asymmetry, pulse tails, and the transform limit are discussed.

References

[1] W. Kaiser (ed.), **Ultrafast Laser Pulses and Applications**, Springer-Verlag (1988)

[2] A. Yariv, **Quantum Electronics**, 3rd ed., ch. 20 (1987)

[3] G. H. C. New, *Opt. Comm.*, **6**, 188 (1972)

[4] G. H. C. New, *IEEE J. Quantum Electron.*, **10**, 115 (1974)

[5] H. A. Haus, *J. Appl. Phys.*, **46**, 3049 (1974)

[6] H. A. Haus, *IEEE J. Quantum Electron.*, **11**, 736 (1975)

[7] P. W. Smith, Y. Silberberg, and D. A. B. Miller, *J. Opt. Soc. Am. B*, **2**, 1228 (1985)

[8] H. A. Haus, and Y. Silberberg, *J. Opt. Soc. Am. B*, **2**, 1237 (1985)

[9] S. Sanders, A. Yariv, J. Paslaski, J. E. Ungar, and H. A. Zarem, *Appl. Phys. Lett.*, **58**, 681 (1991)

[10] S. Sanders, **Passive Mode-Locking and Millimeter-Wave Modulation of Quantum Well Lasers**, *Ph. D. Thesis*, California Institute of Technology (1992)

[11] R. L. Fork, C. H. Brito Cruz, P. C. Becker, and C. V. Shank, *Opt. Lett.*, **12**, 483 (1987)

[12] D. E. Spence, P. N. Kean, and W. Sibbett, *Opt. Lett.*, **16**, 42 (1991)

[13] M. T. Asaki, C.-P. Huang, D. Garvey, J. Zhou, H. Kapteyn, and M. Murnane, *Opt. Lett.*, **18**, 977 (1993).

[14] A. Yariv, **Quantum Electronics**, 3rd ed., ch. 11 (1987)

[15] C. Harder, J. S. Smith, K. Y. Lau, and A. Yariv, *Appl. Phys. Lett.*, **42**, 772 (1983)

[16] A. Yariv, **Quantum Electronics**, 3rd ed., ch. 12 (1987)

[17] P. T. Ho, L. A. Glasser, E. P. Ippen, and H. A. Haus, *Appl. Phys. Lett.*, **33**, 241 (1978)

[18] E. P. Ippen, D. J. Eilenberger, and R. W. Dixon, *Appl. Phys. Lett.*, **37**, 267 (1980)

[19] J. P. van der Ziel, W. T. Tsang, R. A. Logan, R. M. Mikulyak, and W. M. Augustyniak, *Appl. Phys. Lett.*, **39**, 525 (1981)

[20] H. Yokoyama, H. Ito, and H. Inaba, *Appl. Phys. Lett.*, **40**, 105 (1982).

[21] H. A. Haus, *Jap. J. Appl. Phys.*, **20**, 1007 (1981)

[22] J. P. van der Ziel, **Semiconductors and Semimetals, 22B**, ch. 1 (1985)

[23] Y. Silberberg, and P. W. Smith, *IEEE J. Quantum Electron.*, **22**, 759 (1986).

[24] P. J. Delfyett, L. Florez, N. Stoffel, T. Gmitter, N. Andreadakis, G. Alphonse, and W. Ceislik, *Opt. Lett.*, **17**, 670 (1992)

[25] S. Sanders, T. Schrans, A. Yariv, J. Paslaski, J. E. Ungar, and H. A. Zarem, *Appl. Phys. Lett.*, **59**, 1275 (1991)

[26] P. P. Vasil'ev, and A. B. Sergeev, *Electron. Lett.*, **25**, 1049 (1989)

[27] S. Sanders, L. Eng, J. Paslaski, and A. Yariv, *Appl. Phys. Lett.*, **56**, 310 (1990)

[28] S. Sanders, L. Eng, and A. Yariv, *Electron. Lett.*, **26**, 1087 (1990)

[29] Y. K. Chen, M. C. Wu, T. Tanbun-Ek, R. A. Logan, and M. A. Chin, *Appl. Phys. Lett.*, **58**, 1253 (1991)

Chapter 6

Broad-band wavelength tuning and subpicosecond pulse compression from passively mode-locked lasers

6.1 Introduction

In this chapter experimental results on the spectral characteristics of passively mode-locked two-section multiple quantum well (MQW) lasers coupled to an external cavity are presented. The flat two-dimensional density of states of a quantum well laser has resulted in a single mode tuning range of more than 100 nm in GaAs [1,2]. The theoretical limit for the pulse width of a 100 nm wide spectrum is about 10 fs. The

spectral width measured for passively mode-locked two-section lasers is typically a few nm [3] and the pulse width is typically a few ps [4,5], with time-bandwidth products of several times the transform limit. These experimental results indicate that two issues have to be addressed. First, if MQW lasers can provide gain and absorption over tens of nm, but the mode-locked spectrum is only a few nm wide, can this spectrum be tuned over a broad wavelength range? Second, is the excess bandwidth generated due to a deterministic chirp during the pulse or to random noise? If the excess bandwidth is due to chirping, all wavelengths are phase-locked and pulse compression is possible when the chirp has a dominant linear component. If the excess bandwidth is due to random noise, spectral filtering will result in time-bandwidth products closer to the transform limit.

Wavelength tuning of an actively mode-locked laser only requires a medium with a broad gain spectrum, and tuning ranges of 33 nm [6], 60 nm [7,8] and 40 nm [9] were measured at wavelengths of 0.82 μm, 1.3 μm and 1.55 μm respectively. Wavelength tuning of passively mode-locked lasers requires a broad gain spectrum and a broad absorber spectrum. Only limited temperature tuning of monolithic passively mode-locked lasers has been demonstrated with a tuning range of 8.8 nm at a wavelength of 1.55 μm. Pulse widths for actively mode-locked lasers were typically 10–20 ps [6]–[9], reduced to 3.7 ps after external pulse compression [7]. The pulse shaping mechanism of the saturable absorber in passive mode-locking usually results in shorter pulses, and sub-ps pulses as low as 207 fs have been demonstrated [10] using an external MQW absorber. The relatively narrow exciton peak of the MQW was used as a

saturable absorber and wavelength tuning was not possible.

Recently active mode-locking of optically pumped external cavity surface emitting MQW lasers has been reported [11,12] with full width half maximum (FWHM) of the intensity autocorrelation of 153 fs at 1.5 μm [11] and 324 fs at 0.89 μm [12] after external pulse compression with a grating pair. Using soliton effects in an optical fiber these pulses were further compressed down to FWHM of 21 fs at 1.5 μm [13]. All the compressed pulses (grating pair or soliton effects) however had large and long pedestals, containing more than 50% of the pulse energy. In these cases the FWHM cannot be considered a true measurement of the pulse width, and a more appropriate measurement taking into account the pulse energy distribution should be used.

In the next sections measurements on the spectral characteristics of two-section MQW lasers passively mode-locked in an external cavity will be discussed. First broad-band wavelength tuning will be demonstrated, after which pulse compression to sub-ps near transform limited pulses will be discussed.

6.2 The external cavity laser setup

6.2.1 The device structure

The two-section lasers described in this chapter were provided by Ortel Corporation, Alhambra, and are similar to the devices used in previous mode-locking experiments [4,5]. A cross section of the laser structure is shown in fig. 6.1. The MOCVD grown quadruple quantum well structure has on each side a 0.2μm linearly graded separate

(a)

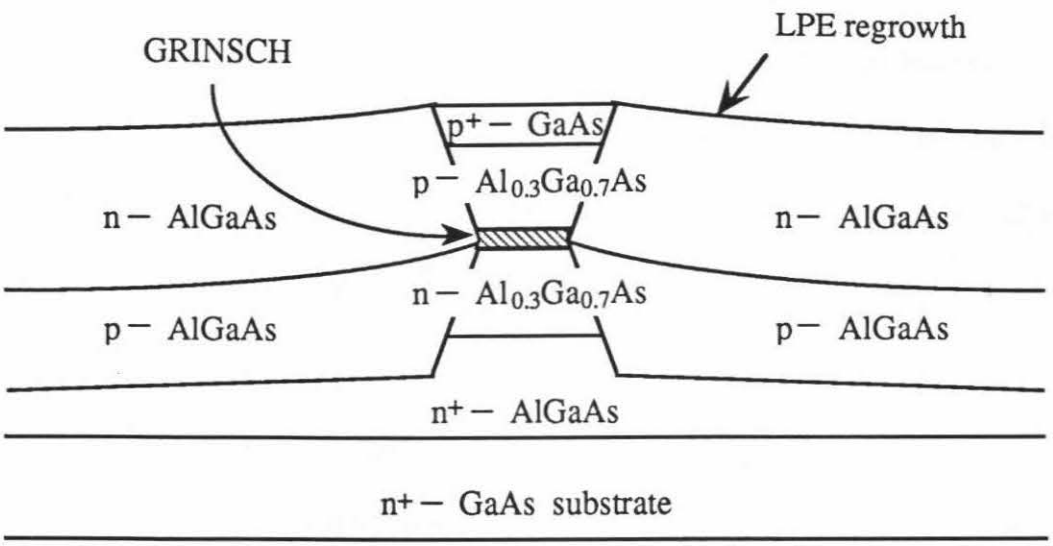

(b) GRINSCH

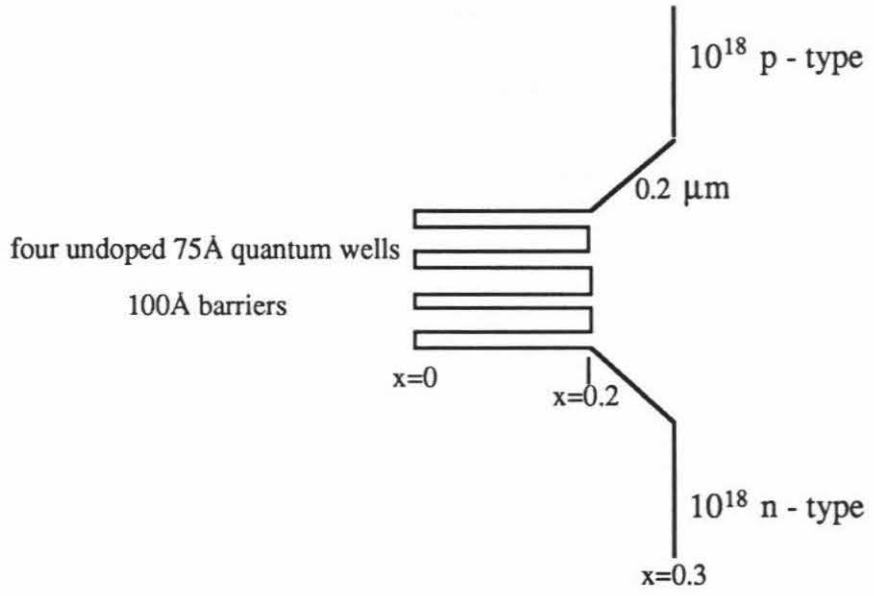

Figure 6.1: Laser structure

optical confinement structure from the Al concentration in the barrier (x=0.2) to the Al concentration in the cladding layer (x=0.3). After the first epitaxial growth a 2μm stripe was etched through the active layer, and an LPE regrowth was performed to obtain a burried structure for lateral optical and carrier confinement. Multiple contacts were defined by selective Zn diffusion to provide a p^+ cap layer, after which top and bottom Au contacts were deposited. The isolation between the contacts was provided by a 50μm gap without Zn diffusion, resulting in an isolation resistance $>10k\Omega$. The wafer was then cleaved to obtain two-section devices with a 60μm absorber section and a 450μm gain section. The lasers were mounted junction side up and both sections were wirebonded. The facet on the absorber side was HR coated to 90% reflectivity to enhance absorber saturation, and the facet on the gain side was AR coated to $\sim$ 5% to allow coupling to an external cavity. The laser mount was then mounted on an aluminum block whose temperature could be monitored with a thermistor and controlled with a TE cooler.

Both sections were biased through a bias tee with the high frequency terminal terminated by 50Ω. The gain section was biased by a DC current source, while the absorber section was grounded under mode-locked operation to provide fast recovery for the absorber [5]. The threshold current of the lasers without external feedback and with floating absorber is typically 40mA.

6.2.2 The external cavity for wavelength tuning

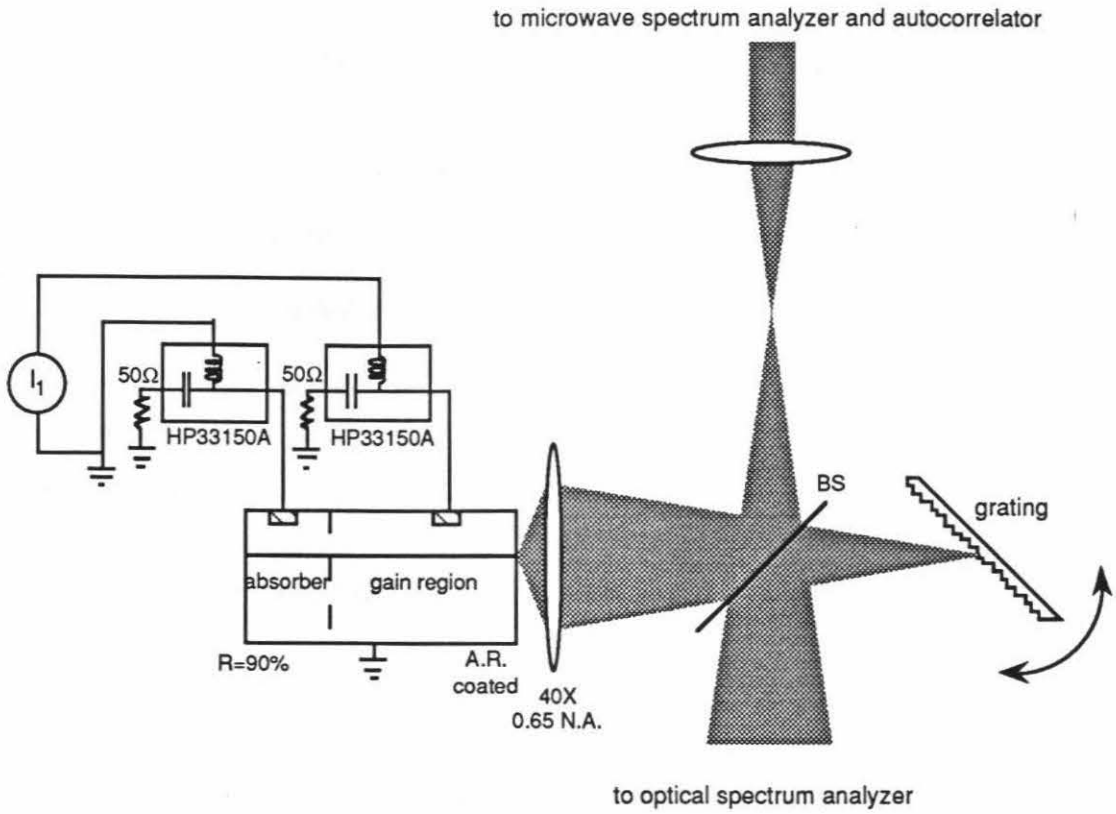

Figure 6.2: External cavity with grating setup 1

The laser beam from the AR coated gain facet was focussed on a 600 lines/mm grating mounted in Littrow configuration to provide feedback into the laser (fig. 6.2). The grating equation for the defracted beam of order -1 is

$$\sin\alpha = \frac{\lambda}{nd} - \sin\gamma \tag{6.1}$$

with γ the incidence angle , α the exit angle (both with respect to the grating normal), λ the vacuum wavelength, n the refractive index, and d the grating period (=1/600 mm). For Littrow configuration $\alpha = \gamma$, and the wavelength coupled back into the laser is given by (n=1)

$$\lambda = 2d \sin \gamma. \tag{6.2}$$

In order to feed back λ=840nm, an angle of 14.6° with the grating normal is required. The spectral bandwidth that is coupled back into the laser depends on the angular spread of the incident beam, and is found by differentiating (6.2)

$$\Delta\lambda = 2d \cos \gamma \Delta\gamma. \tag{6.3}$$

The angular spread of the beam is determined by diffraction

$$\Delta\gamma = \frac{\lambda}{D} \tag{6.4}$$

with D the beam diameter at the beam waist. As the beam is not normally incident on the grating, the illuminated part of the grating is $D/\cos\gamma$, resulting in

$$\frac{\Delta\lambda}{\lambda} = \frac{2}{N} \tag{6.5}$$

with $N = D/d\cos\gamma$ the number of grating lines illuminated by the beam, also known as the grating resolution.

For a beam collimated on the grating the diameter D is typically larger than 5mm (N=3100), giving a spectral bandwidth $\Delta\lambda$=0.54nm (or $\Delta\nu$=230GHz), which can only result in mode-locking with pulse widths larger than 1 ps. A beam focussed on the grating however results in a much smaller N, thereby allowing a broader spectral

range to be coupled back into the laser, and mode-locking with subpicosecond pulse widths should be possible. Previous noise measurements on the mode-locked laser also indicated that a focussed beam with a mirror in place of the grating results in more stable mode-locking [5]. Wavelength tuning is obtained by rotating the grating (6.3) with a tuning sensitivity of $\Delta\lambda/\Delta\gamma$=56nm/°.

6.3 Broad-band wavelength tuning

6.3.1 Experimental setup 1

In a first experiment [21] a 9% pellicle beam splitter (BS) placed at a 45° angle was used to couple the light out to an optical grating spectrometer on one side and a second harmonic (SH) collinear intensity autocorrelator and microwave spectrum analyzer on the other side (fig. 6.2). The external cavity length was about 30cm, resulting in a round-trip frequency of 561MHz. Due to the relatively low feedback, and hysteresis in the L-I curve [4] the laser was turned on with the absorber floating to avoid exposure to high gain section currents. After setting the gain current to an appropriate value the absorber was grounded and the laser switched to mode-locked operation. By adjusting the gain current, mode-locking in the first harmonic of the round-trip frequency is obtained. During all measurements the temperature of the laser mount stayed at 22.5°C.

The minimum gain current needed for mode-locking in the 1st harmonic is shown in fig. 6.3 as a function of the center wavelength of the spectrum (full circles). The

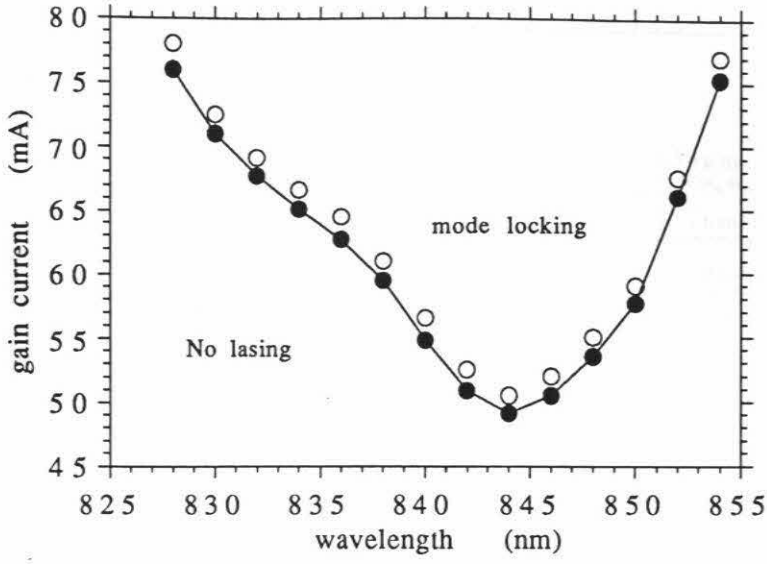

Figure 6.3: Mode-locking range (solid circles) in funtion of gain current and wavelength

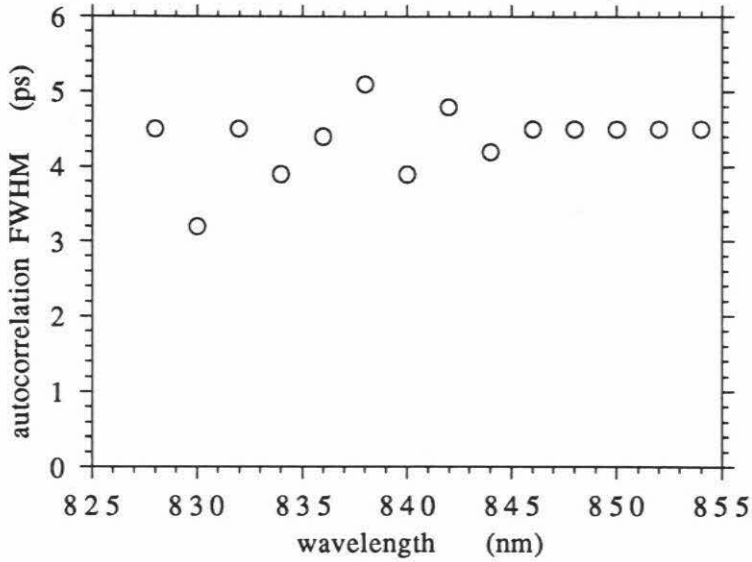

Figure 6.4: Autocorrelation full width half maximum (FWHM) as a function of wavelength

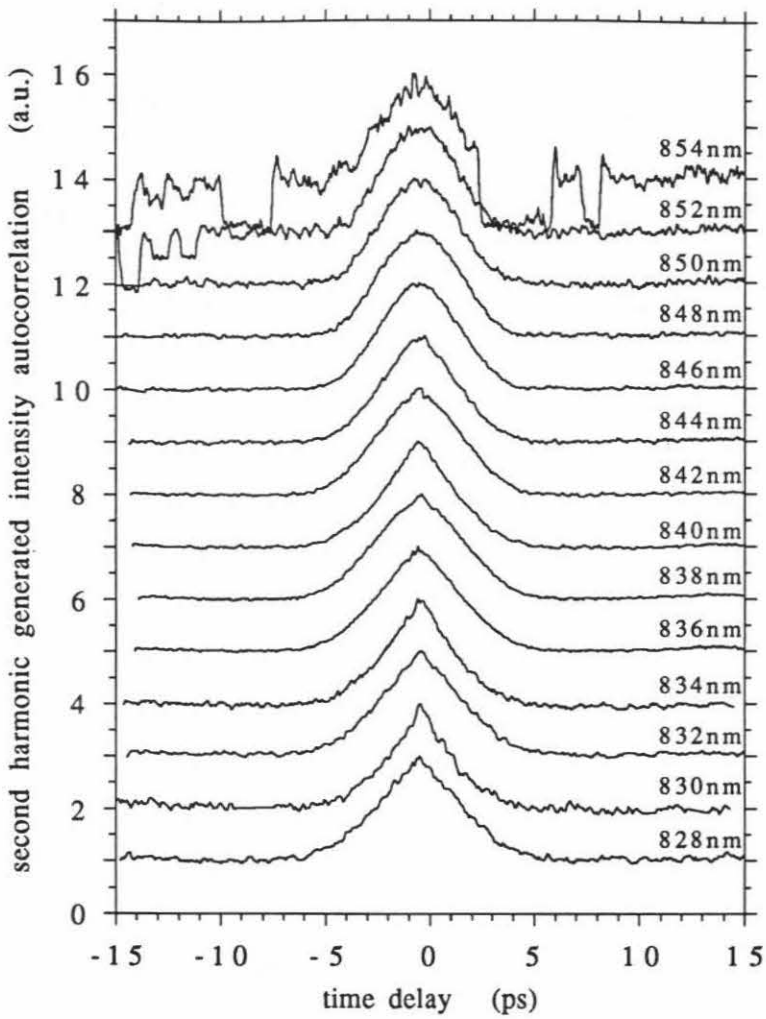

Figure 6.5: Intensity autocorrelations at different wavelengths

tuning range is 26nm and is the broadest tuning range measured for passively mode-locked semiconductor lasers. Intensity autocorrelations were measured at different wavelengths as indicated by the open circles in fig. 6.3, and the autocorrelation FWHM are shown in fig. 6.4 as a function of the wavelength. The typical deconvolved pulse width (assuming a hyperbolic secant pulse shape) is 3 ps. The spectral width is typically 2.5 nm, resulting in a time-bandwidth product of 3.2 which is about

10 times the transform limit of 0.31 . The intensity autocorrelations are shown in fig. 6.5 for different wavelengths.

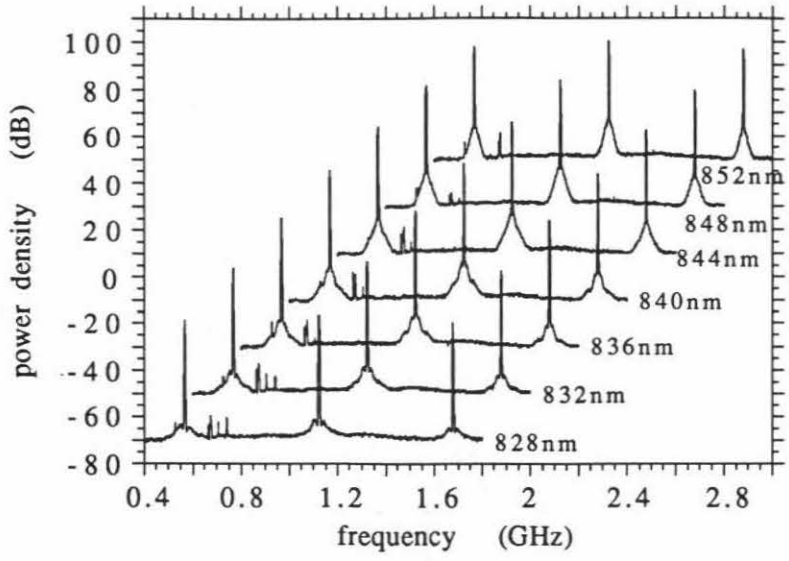

Figure 6.6: Intensity power spectra at different wavelengths (consecutive traces are displaced by 0.2GHz and 20dB)

The power spectrum of the intensity was measured from the photocurrent of a ~12 GHz bandwidth followed by a 0.5–4.5 GHz bandwidth 35dB low noise amplifier and an HP8565a microwave spectrum analyzer. Intensity power spectra are shown in fig. 6.6 for different wavelengths, indicating stable mode-locking with the noise 3 MHz from the signal at least 30dB below the signal level. The signals observed near 530 MHz and 700 MHz are part of the background. At the longer wavelength edge of the tuning range, the laser was less stable, resulting in higher noise bands and turn off of the laser under external perturbation (fig. 6.5, 854nm trace).

6.3.2 Experimental setup 2

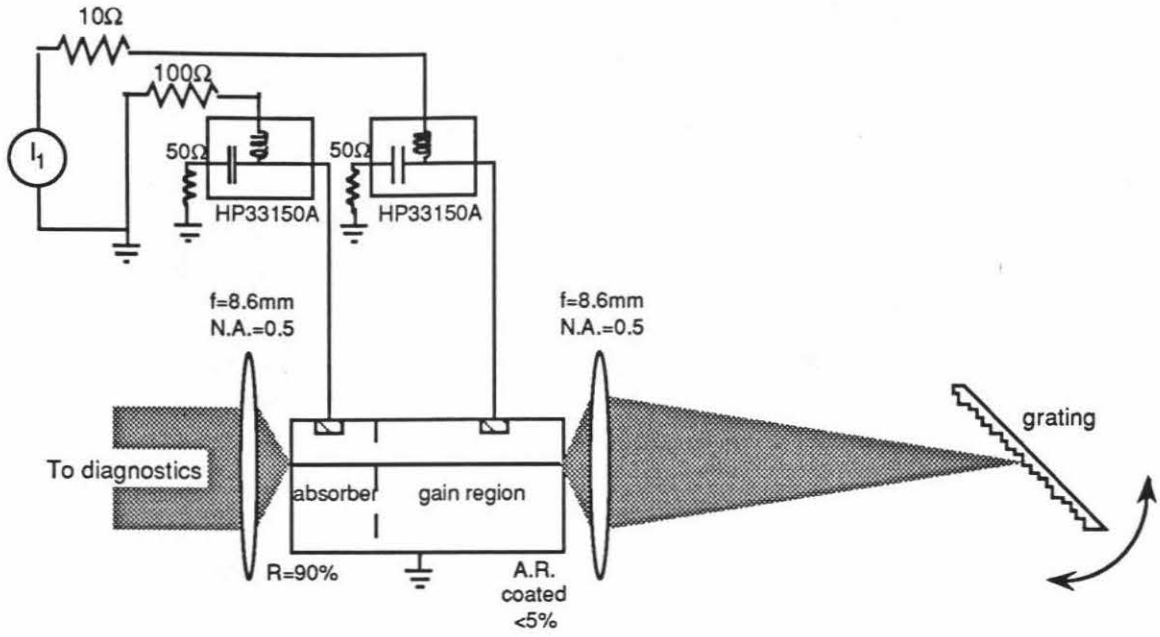

Figure 6.7: External cavity with grating setup 2

To allow operation at lower currents the laser mount was modified, such that the light coming out of the HR coated absorber facet could be used as the output, and the beam splitter could be removed, thereby increasing the external feedback level (fig. 6.7). By increasing the gain current, the laser could be mode-locked at higher harmonics of the round-trip frequency (586 MHz). The wavelength and current ranges for which mode-locking was obtained is shown in fig. 6.8 for the different harmonics. During the measurements the laser mount was maintained at a temperature of 22°C.

A tuning range of 12 nm was measured for the first harmonic. The upper current

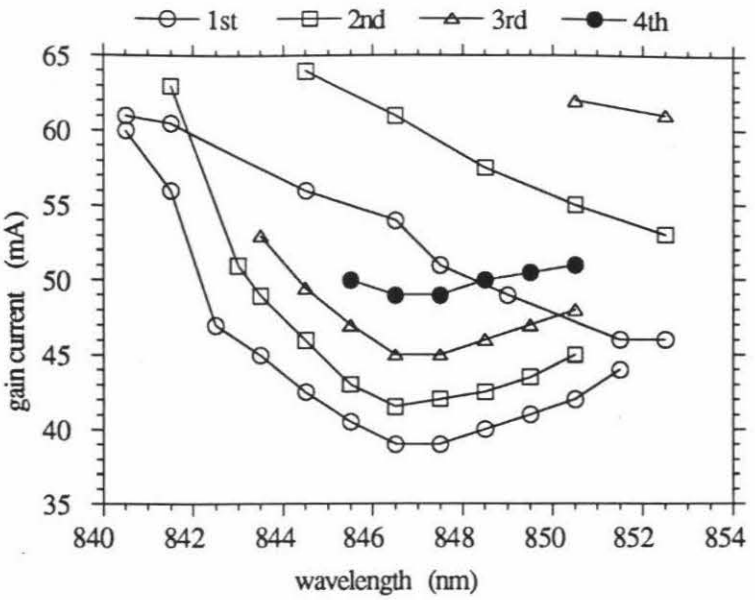

Figure 6.8: Mode-locking ranges for different harmonics as a function of gain current and wavelength

limit for the higher harmonics was not measured for all wavelengths to avoid exposing the laser to high gain currents. Measurements of the pulse energy, autocorrelation FWHM and spectral FWHM were performed at the operating points in the first harmonic, as indicated by the solid circles in fig. 6.9, with the open circles indicating the range for which stable mode-locking in the first harmonic is obtained. The pulse energy is shown in fig. 6.10 for the different operating points, and is small as the output is taken out of the HR coated facet after passing through the saturable absorber.

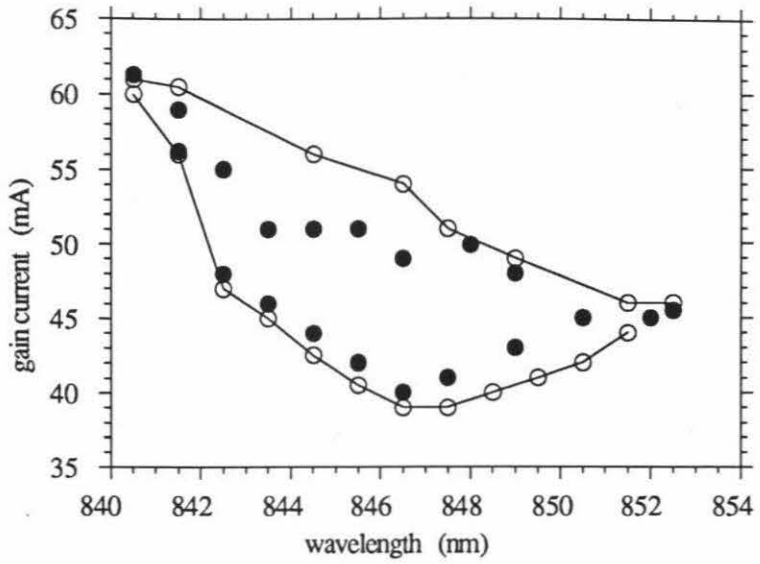

Figure 6.9: Mode-locking range for 1st harmonic as a function of gain current and wavelength (open circles)

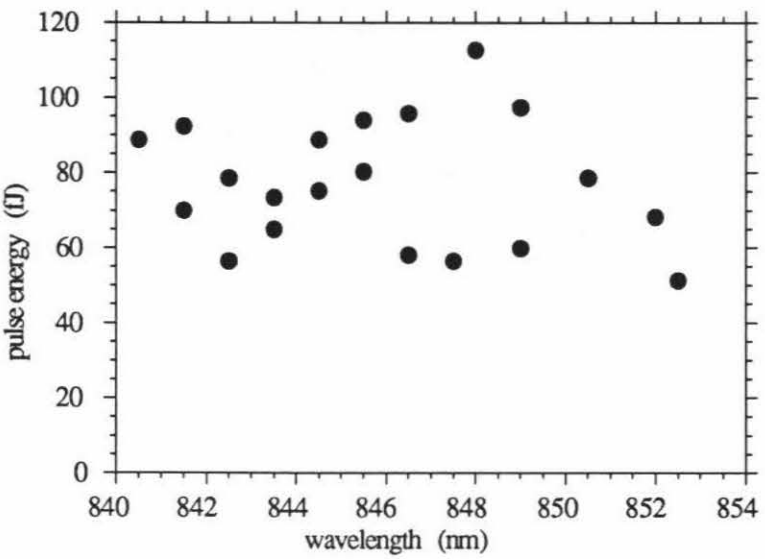

Figure 6.10: Pulse energy as a function of wavelength

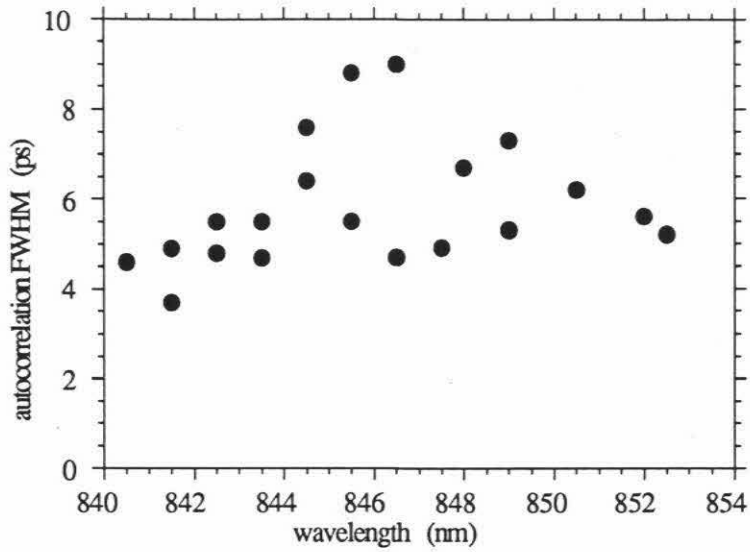

Figure 6.11: Autocorrelation full width half maximum (FWHM) as a function of wavelength

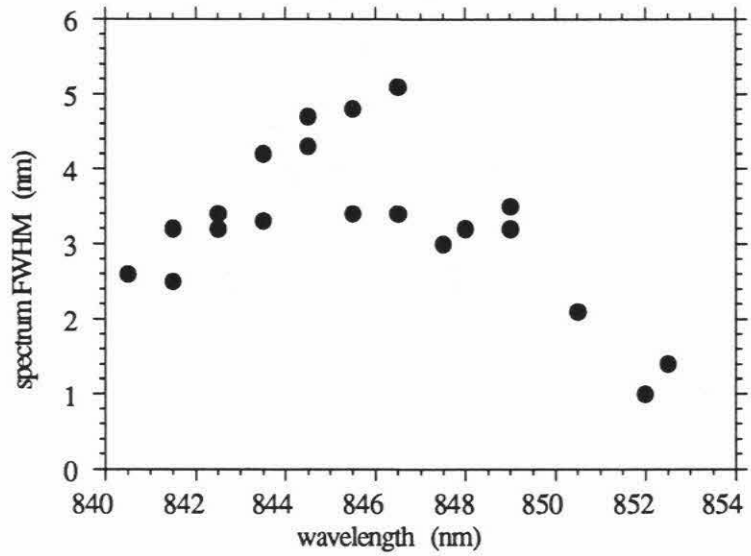

Figure 6.12: Spectrum full width half maximum (FWHM) as a function of wavelength

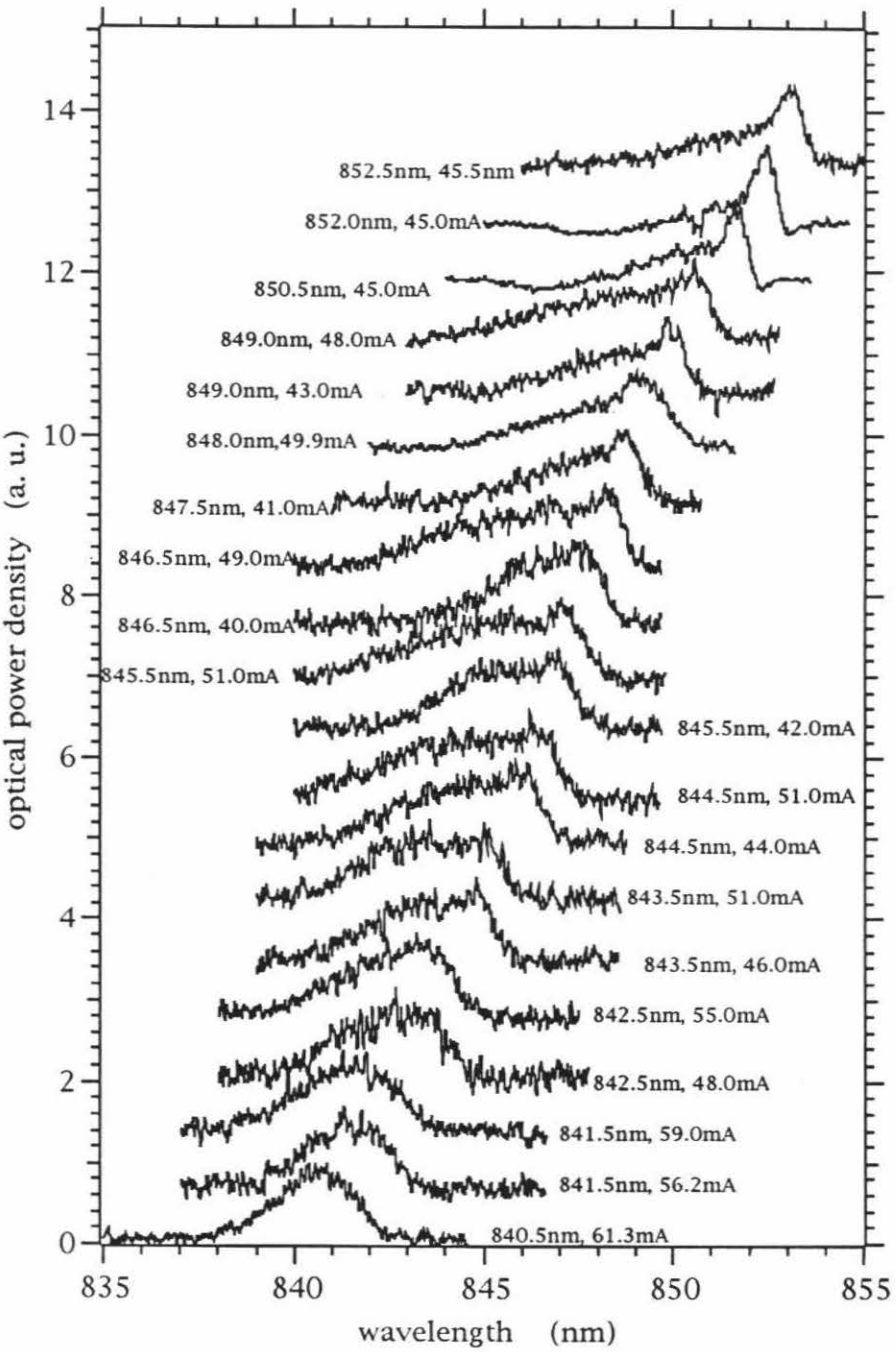

Figure 6.13: Optical spectra for different wavelengths and gain currents

The FWHM of the autocorrelations is shown in fig. 6.11, where higher currents result in longer pulses. The FWHM of the corresponding optical spectrum is measured using a monochromator and is shown in fig. 6.12, with higher currents resulting in a broader spectrum. The "narrower" spectrum at the long wavelength side of the tuning range is due to a stronger asymmetry in the spectrum at these wavelengths fig. 6.13. The time-bandwidth product of the pulse ranges from 1.5 on the long wavelength side to 12.2 at higher gain currents.

At some wavelengths weak satellite pulses can be observed in the autocorrelations(fig. 6.14) centered at a time delay of about 13ps, corresponding to the round-trip time between the two semiconductor facets (L$\approx$560μm). These satellite pulses are attributed to a residual reflection from the AR coated gain facet, but may be partially suppressed by the presence of the monolithically integrated saturable absorber [15]. If the intensity pulse train, including the satellite pulse is given by

$$I(t) = f(t) + cf(t - T_1) \tag{6.6}$$

where the satellite pulse is a delayed and attenuated version of the main pulse, it can be shown that the ratio r in the intensity autocorrelation peaks is given by

$$r = \frac{c}{1 + c^2} \tag{6.7}$$

from which the energy ratio c can be derived

$$c = \frac{1 - \sqrt{1 - 4r^2}}{2r}. \tag{6.8}$$

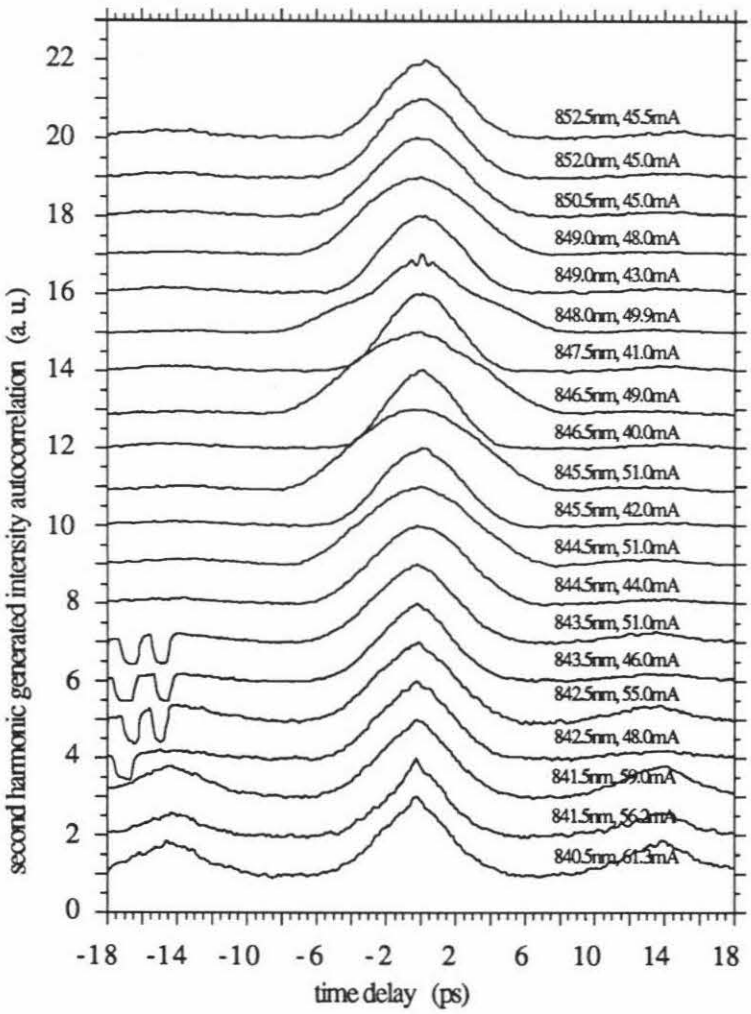

Figure 6.14: Intensity autocorrelations at different wavelengths and gain currents

The pulse energies in fig. 6.10 were not corrected for the energy in the satellite pulse, which was lower than 10% except at the short wavelength side of the tuning range where the satellite pulse could contain as much as 50% of the energy (fig. 6.14). This seems to indicate that the AR coating was higher than 5% for wavelengths shorter than 840 nm for this particular laser device and may explain why the tuning range was limited on the short wavelength side to 12 nm compared to the 26 nm

observed with a different laser device in the previous experiment.

6.4 Compression to subpicosecond pulsewidths

The high time-bandwidth products measured in the previous section indicate that excess optical bandwidth is present (depending on the exact pulse shape the time-bandwidth product can be as low as 0.31 for hyperbolic secant pulses, 0.44 for Gaussian pulses). This excess bandwidth can be due to noise during and between the pulses, or to a deterministic time dependence of the optical phase. In the first case the coherence time of the pulse is shorter than the pulse width, and not much can be done to the pulse except narrowing the spectrum, thereby increasing the coherence time until it is equal to the pulse width. In the second case the pulse is said to be chirped, and the pulse can be compressed in time using a linear time-invariant system if the deterministic time dependence of the optical phase is known.

6.4.1 Chirped pulses

The electric field of a pulse train with a complex pulse shape $f(t)$ is given by

$$e(t) = e^{i\omega_o t} \sum_n f(t - nT) \tag{6.9}$$

with ω_o the optical frequency and T the period of the pulse train. The optical spectrum $\tilde{E}(\Omega)$ ($\Omega = \omega - \omega_o$) of this pulse train consists of a set of δ-functions with

their magnitude determined by the spectrum $\tilde{F}(\Omega)$ of the pulse shape $f(t)$:

$$\tilde{E}(\Omega) = \frac{2\pi}{T}\sum_n \tilde{F}(\frac{2\pi n}{T})\delta(\Omega - \frac{2\pi n}{T}). \tag{6.10}$$

The pulse train can thus be expanded in a superposition of complex harmonics:

$$e(t) = e^{i\omega_o t}\frac{1}{T}\sum_n \tilde{F}(\frac{2\pi n}{T})e^{i\frac{2\pi n}{T}t}. \tag{6.11}$$

The intensity of the pulse train is given by

$$I(t) = |e(t)|^2 = \left|\sum_n f(t-nT)\right|^2 = \sum_n |f(t-nT)|^2 \tag{6.12}$$

where the last equal sign only holds if the pulse width is much shorter than the pulse period T. To analyze the pulse train it suffices to analyze a single pulse $f(t)$.

A Gaussian pulse with a linear chirp A in the instantaneous frequency is given by

$$f(t) = e^{-(1-iA)\left(\frac{t}{\tau_p}\right)^2} = \sqrt{I_1(t)}e^{i\phi(t)}. \tag{6.13}$$

The instantaneous frequency, defined as $\omega(t) = \omega_o + d\phi/dt$ is

$$\omega(t) = \omega_o + 2A\frac{t}{\tau_p^2} \tag{6.14}$$

and increases linearly with time. The spectrum of the pulse is given by

$$\tilde{F}(\Omega) = \sqrt{\frac{\pi\tau_p^2}{1-iA}}e^{-\frac{1+iA}{4(1+A^2)}(\Omega\tau_p)^2}. \tag{6.15}$$

The full width half maximum (FWHM) $\Delta\tau$ of the pulse is

$$\Delta\tau = \sqrt{2\ln 2}\tau_p, \tag{6.16}$$

the FWHM $\Delta\nu$ of the spectrum is

$$\Delta\nu = \frac{\sqrt{2\ln 2}}{\pi\tau_p}\sqrt{1+A^2} \tag{6.17}$$

with a time-bandwidth product

$$\Delta\tau\Delta\nu = \frac{2\ln 2}{\pi}\sqrt{1+A^2} \tag{6.18}$$

and the transform limit ($A = 0$) given by $2\ln 2/\pi = 0.44$. Adding frequency chirp in the time domain broadens the spectrum for a fixed pulse width, and adds a frequency dependent phase in the spectrum. This frequency dependent phase can be removed by a linear time-invariant phase filter, keeping the magnitude of the spectrum intact

$$\tilde{F}_c(\Omega) = \sqrt{\frac{\pi\tau_p^2}{1-iA}}e^{-\frac{1}{4(1+A^2)}(\Omega\tau_p)^2} \tag{6.19}$$

resulting in a compressed pulse in time domain

$$f_c(t) = \sqrt{1+iA}\,e^{-(1+A^2)\left(\frac{t}{\tau_p}\right)^2} \tag{6.20}$$

with a compressed pulse width of

$$\Delta\tau_c = \frac{\Delta\tau}{\sqrt{1+A^2}} \tag{6.21}$$

resulting in a time-bandwidth product equal to the transform limit.

Similarly it can be shown that for a fixed spectral width $\Delta\nu$, the shortest Gaussian pulse is obtained when the phase has no quadratic phase component. A chirped Gaussian pulse with spectrum

$$\tilde{F}(\Omega) = e^{-(1+iB)(\frac{\Omega}{\Omega_p})^2} \tag{6.22}$$

and spectral FWHM

$$\Delta\nu = \sqrt{2\ln 2}\frac{\Omega_p}{2\pi} \tag{6.23}$$

has a pulse shape

$$f(t) = \sqrt{\frac{\Omega_p^2}{4\pi(1+iB)}}\, e^{-\frac{1-iB}{4(1+B^2)}(\Omega_p t)^2} \tag{6.24}$$

with pulse width

$$\Delta\tau = \frac{\sqrt{8\ln 2}}{\Omega_p}\sqrt{1+B^2}. \tag{6.25}$$

This pulse width is minimal when no chirping is present (B=0).

For simplicity the analysis has been performed on Gaussian pulses where a quadratic phase component in time results in a quadratic phase component in frequency. For other pulse shapes this one to one relationship between quadratic components does not hold. If a linear instantaneous frequency chirp is added to a chirpless pulse $f_o(t)$

$$f(t) = f_o(t)\, e^{iA\left(\frac{t}{\tau_p}\right)^2} \tag{6.26}$$

the spectrum becomes a convolution ($*$) of the chirpless spectrum with a quadratic phase

$$\tilde{F}(\Omega) = \sqrt{\frac{i\pi\tau_p^2}{A}}\tilde{F}_o(\Omega) * e^{-i\frac{(\Omega\tau_p)^2}{4A}} \tag{6.27}$$

which can be written as

$$\tilde{F}(\Omega) = 2\pi e^{-i\frac{(\Omega\tau_p)^2}{4A}}\left[f_o(t) * e^{iA\left(\frac{t}{\tau_p}\right)^2}\right]_{t=\frac{\Omega\tau_p^2}{2A}}. \tag{6.28}$$

The convolution in (6.28) has in general a frequency dependent phase, resulting in cubic and higher order terms in the phase of the spectrum.

In general one can say however that, in time domain, a constant phase shift is irrelevant, a phase linear with time corresponds to a constant frequency shift, a quadratic phase dependence results in a linear frequency chirp, and a cubic or higher order phase dependence results in a nonlinear chirp. Similarly in frequency domain, a constant phase is irrelevant, a phase linear with frequency corresponds to a constant group delay, a quadratic phase corresponds to a linear group delay dispersion, and a cubic or higher order phase dependence results in nonlinear group delay dispersion. A linear frequency chirp will in general result in a linear and nonlinear group delay dispersion, while a linear group delay dispersion will result in a linear and nonlinear frequency chirp.

6.4.2 Pulse compression filters

Different linear phase filters have been proposed and used for pulse compression, such as dispersion in optical fibers [16], diffraction in a grating pair [17], and refraction in a prism pair [18]. All of these systems however allow only one sign of chirp. To be able to access both signs of chirp, a telescope can be used in between the two gratings or prisms [18]. As the sign of the chirp in the passively mode-locked two-section quantum well lasers is a priori unknown, a dual grating telescope compressor is used and shown in fig. 6.15. This system was analyzed in [19] using diffraction integrals for Gaussian beams. A simpler analysis using plane waves is given here.

It is well known that a point source $\delta(x-x_o, y-y_o)$ in the front focal plane of the first lens is imaged by the telescope into a point $\delta(x+x_o, y+y_o)$ in the back focal plane

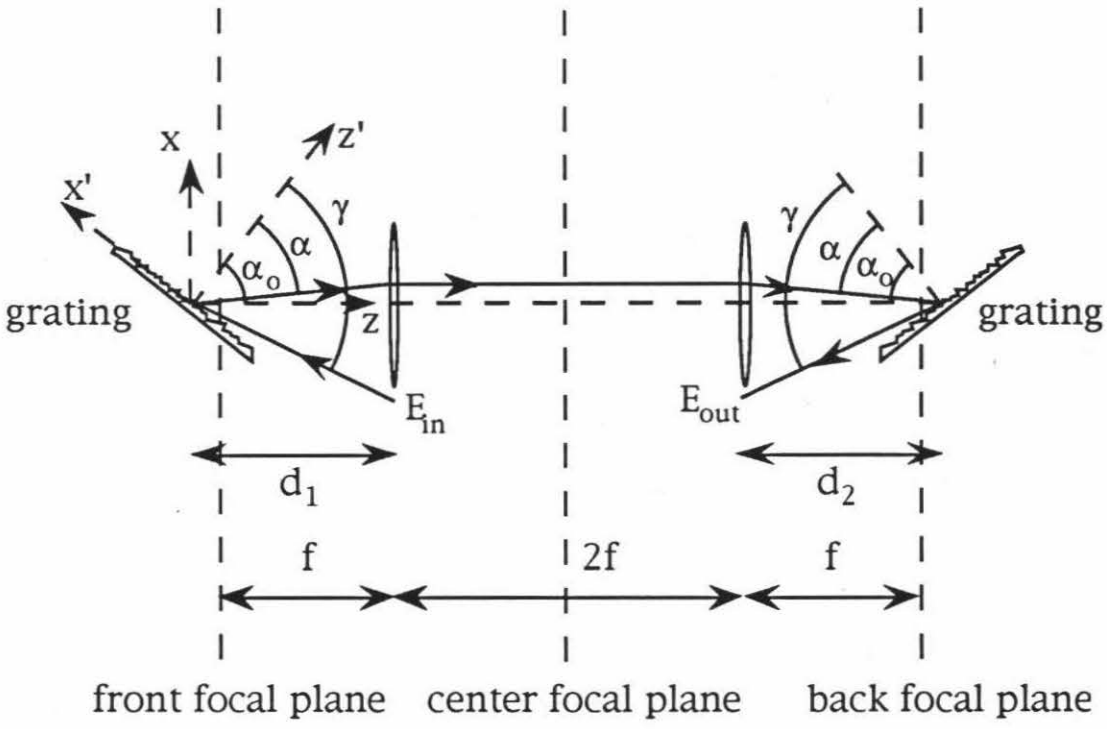

Figure 6.15: Grating telescope compressor

of the second lens [20]. As this is the impulse response of a system (the telescope) linear in the spatial coordinates, the Fourier transform of this impulse response gives the response to a plane wave incident on the telescope. An incident plane wave

$$E_{in} = Ae^{-ik_x x} \tag{6.29}$$

with A the complex amplitude (magnitude and phase) of the plane wave in the front focal plane, will give a plane wave in the back focal plane

$$E_{out} = Ae^{+ik_x x}. \tag{6.30}$$

The y dependence is neglected here for simplicity of notation, as all the dispersion

from the gratings is in the x direction. The phase delay seen by a plane wave between the two outer focal planes is independent of the angle of incidence (k_x), and the only effect of the telescope is a 180° rotation.

The response of the grating to a plane wave is shown in fig. 6.15 The incident plane wave electric field is

$$E_{in}(x', z') = E_o e^{-ik(x' \sin\gamma - z' \cos\gamma)} \tag{6.31}$$

with $k = 2\pi/\lambda = \omega/c$, and λ the wavelength. The electric field on the grating is $E_{in}(x', z' = 0)$ and the diffracted beam of order -1 on the grating is given by

$$E_{-1}(x', z' = 0) = r_{-1} E_o e^{-ikx' \sin\gamma} e^{i\frac{2\pi x'}{d}} = r_{-1} E_o e^{+ikx' \sin\alpha} \tag{6.32}$$

with r_{-1} the reflection coefficient for the -1 order (x' independent), and d the grating groove period. The plane wave exiting the grating in the -1 order is then given by

$$E_{-1}(x', z') = r_{-1} E_o e^{+ik(x' \sin\alpha - z' \cos\alpha)}. \tag{6.33}$$

The grating equation which relates the incident angle to the exit angle is derived from (6.32)

$$\sin\alpha = \frac{\lambda}{d} - \sin\gamma. \tag{6.34}$$

If the angle between the grating normal and the telescope axis is α_o then the electric field at plane $z = 0$ is given by

$$E_1(x, z = 0) = r_{-1} E_o e^{-ikx \sin(\alpha_o - \alpha)} \tag{6.35}$$

and the electric field in the front focal plane is

$$E_1(x, z = d_1 - f) = r_{-1} E_o e^{-ik(d_1 - f)\cos(\alpha_o - \alpha)} e^{-ikx \sin(\alpha_o - \alpha)} \tag{6.36}$$

with d_1 the distance between the first grating and the first lens along the telescope axis, and f the focal length of the lens. The electric field in the back focal plane of the telescope is then (using (6.29,6.30))

$$E_2(x, z = f - d_2) = r_{-1} E_o e^{-ik(d_1 - f)\cos(\alpha_o - \alpha)} e^{+ikx\sin(\alpha_o - \alpha)} \tag{6.37}$$

and the electric field near the plane "$z = 0$" of the second grating is

$$E_2(x, z) = r_{-1} E_o e^{-ik(d_1 - f)\cos(\alpha_o - \alpha)} e^{+ik(f - d_2)\cos(\alpha_o - \alpha)} e^{+ikx\sin(\alpha_o - \alpha)} e^{-ikz\cos(\alpha_o - \alpha)}. \tag{6.38}$$

In the x', z' system of the second grating this is

$$E_2(x', z') = r_{-1} E_o e^{-ik(d_1 + d_2 - 2f)\cos(\alpha_o - \alpha)} e^{+ik(x'\sin\alpha + z'\cos\alpha)}. \tag{6.39}$$

The diffracted beam of of order -1 on the second grating is then given by

$$E_{out}(x', z' = 0) = r_{-1}^2 E_o e^{-ik(d_1 + d_2 - 2f)\cos(\alpha_o - \alpha)} e^{+ikx'\sin\alpha} e^{-i\frac{2\pi x'}{d}} \tag{6.40}$$

and using the grating equation (6.34) this becomes

$$E_{out}(x', z' = 0) = r_{-1}^2 E_o e^{-ik(d_1 + d_2 - 2f)\cos(\alpha_o - \alpha)} e^{-ikx'\sin\gamma}. \tag{6.41}$$

The phase delay picked up by the plane wave is thus

$$\phi_c = k\,(d_1 + d_2 - 2f)\cos\,(\alpha_o - \alpha)\,. \tag{6.42}$$

All other phase delays picked up during propagation are linear with k and thus with frequency, resulting in a constant group delay and are irrelevant for pulse compression. The phase (6.42) however will result in group delay dispersion as α is a

function of ω. The group delay $\tau_g(\omega)$ is given by

$$\tau_g(\omega) = \frac{\partial \phi_c}{\partial \omega} = \frac{d_1 + d_2 - 2f}{c \cos \alpha} \left[\cos \alpha_o + \sin \gamma \sin (\alpha - \alpha_o)\right] \tag{6.43}$$

and the group delay dispersion by

$$\frac{\partial \tau_g}{\partial \omega} = \frac{\partial^2 \phi_c}{\partial \omega^2} = - \frac{4\pi^2 c (d_1 + d_2 - 2f)}{\omega^3 d^2} \frac{\cos \alpha_o}{\cos^3 \alpha}. \tag{6.44}$$

The grating telescope compressor acts as a linear filter on the pulse train with as frequency transfer function $H(\omega) = e^{-i\phi_c(\omega)}$ with

$$\phi_c(\omega) = \phi_c(\omega_o) + (\omega - \omega_o)\, \tau_g + \frac{1}{2} \frac{\partial \tau_g}{\partial \omega} (\omega - \omega_o)^2 + O\left[(\omega - \omega_o)^3\right]. \tag{6.45}$$

The term in $(\omega - \omega_o)^2$ will result in pulse compression or pulse broadening, depending on the chirp in the input pulse and the position of the gratings (d_1 and d_2) with respect to the front and back focal planes. If the gratings are placed outside the two outer focal planes ($d_1 + d_2 - 2f > 0$) the group velocity dispersion ($\partial v_g / \partial \lambda$) is negative, as for a grating pair without the telescope, and if the gratings are placed inside the two outer focal planes ($d_1 + d_2 - 2f < 0$), the group delay dispersion is positive as in a single mode fiber for a wavelength around 840nm. For Gaussian pulses with a time-bandwidth product of 5, and an autocorrelation FWHM of 6ps, the quadratic phase component in the spectrum is $\pm 0.28\ (\text{ps})^2 (\omega - \omega_o)^2$. A grating pair with 2000 lines/mm, and an angle α_o ($\approx \alpha$) with the telescope axis of 60° ($\gamma \approx 55°$), requires a grating "spacing" $|d_1 + d_2 - 2f| = 3.3$cm to compress the pulses at a wavelength of 845nm to their transform limit of 0.37 ps.

For finite beam sizes different frequencies will come out of the compressor with a frequency dependent displacement perpendicular to the output beam [17,19]. The

main consequence of this displacement is a filtering of the magnitude of the spectrum, resulting in a narrower spectrum and a broader minimum pulse width achievable [19]. To avoid this broadening, the compressed pulse can be sent back through the compressor with a retroreflector, or a wide enough beam can be used.

6.5 Subpicosecond pulsewidth experiments

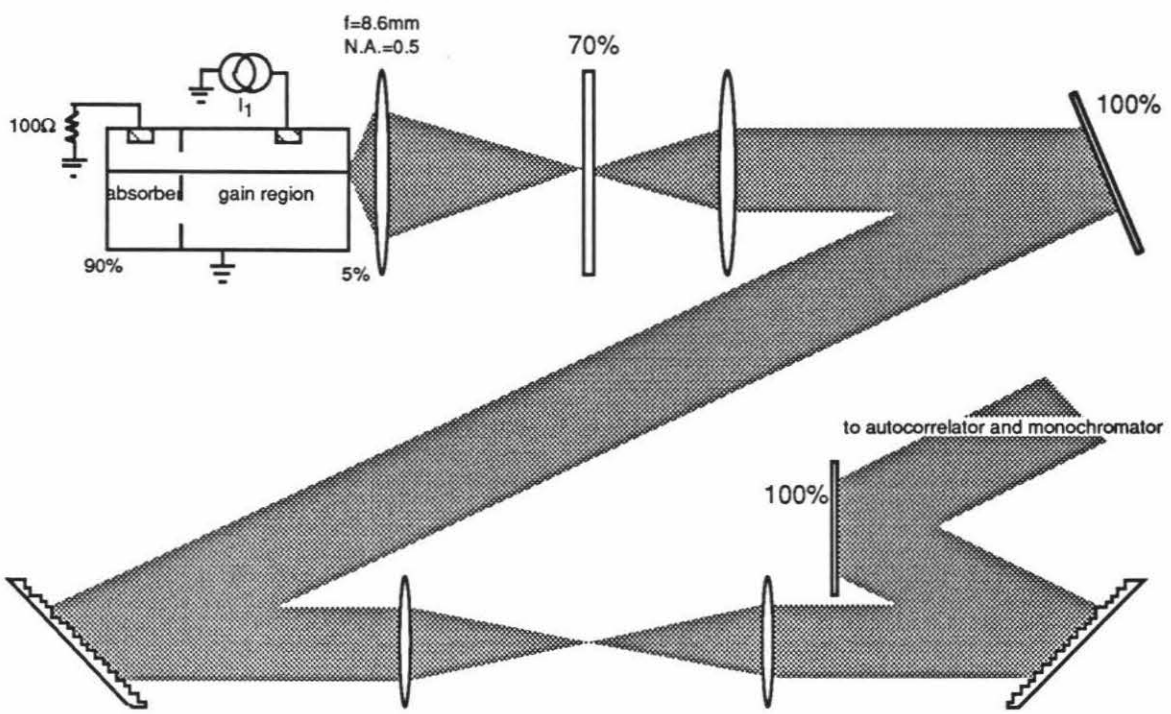

Figure 6.16: External cavity laser with pulse compressor setup

In order to have a larger energy per pulse, the setup shown in fig. 6.16 was used. The grating was replaced by a 70% mirror and the beam transmitted through this

mirror was sent through the grating telescope compressor. The beam size coming out of the laser was several mm, such that the compressor could be used in a single pass mode without causing noticable broadening due to the frequency dependent beam displacement. After exiting the telescope compressor, the beam is directed to the collinear autocorrelator for pulse width measurements or the monochromator for spectral measurements. All measurements were performed in the 1st harmonic of the round-trip frequency (558MHz), which was obtained for gain currents between 39 and 48mA.

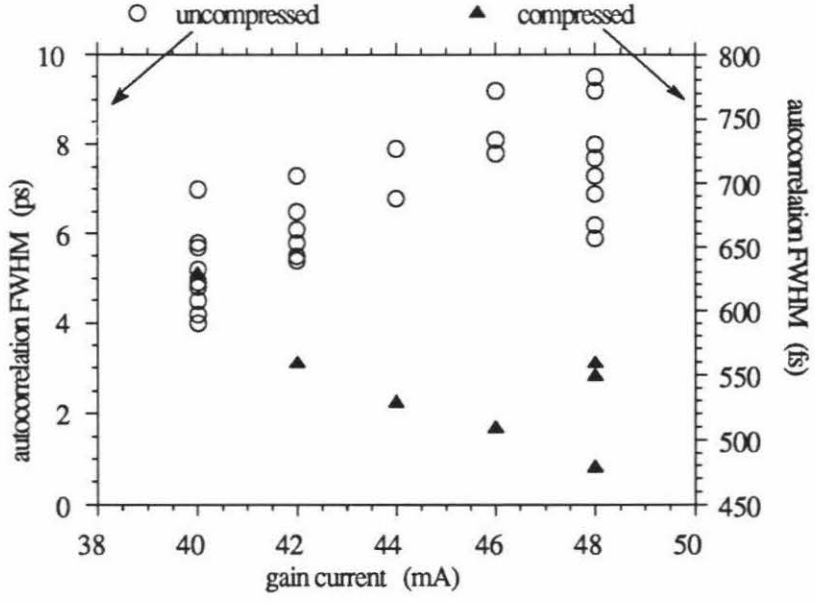

Figure 6.17: Uncompressed (circles) and compressed (triangles) pulse widths as a function of gain current

The uncompressed pulse widths coming out of the laser were very sensitive to the cavity alignment, with different pulse widths coinciding with small spectral changes.

The FWHM of the autocorrelation is shown in fig. 6.17 as a function of the gain current for different cavity alignments. For a fixed cavity alignment the pulse width and the spectral width tend to increase with increasing gain current. The compressed pulse width as shown in fig. 6.17 decreases with gain current, agreeing with the larger bandwidths for higher gain currents. The shortest compressed pulse width is typically 360fs after deconvolving with a factor of 1.543 for hyperbolic secant pulse shapes, with an optical bandwidth of typically 1.1THz, giving a time-bandwidth product of 0.39. All compressed pulse were obtained with the compressor in the region of negative group velocity dispersion, corresponding to an upchirp (blue shift) during the pulse.

Deconvolved pulse widths as low as 320fs [21] were measured for a gain current of 48mA. An autocorrelation trace of a 330fs pulse is shown in fig. 6.18a, together with the uncompressed pulse (fig. 6.18b). The uncompressed pulse has a deconvolved pulse width of 5.2ps and time-bandwidth product of 6.8. The large compression factor (>15) indicates that the pulse has a strong linear chirp component. Satellite pulses are observed at a time delay of 14.2ps, corresponding to the round-trip time between the two facets of the 510μm long laser. The satellite pulses contain less than 10% of the pulse energy, and are attributed to the residual reflection at the AR coated facet. Compression of the satellite pulse indicates that it is a replica of the main pulse through reflection of the facets.

The corresponding optical spectrum of the compressed pulse is shown in fig. 6.19 and has a FWHM of $\sim$ 3nm (1.2THz), giving a time-bandwidth product of 0.4, close to the transform limit. A fringe resolved autocorrelation [22] was measured, and is

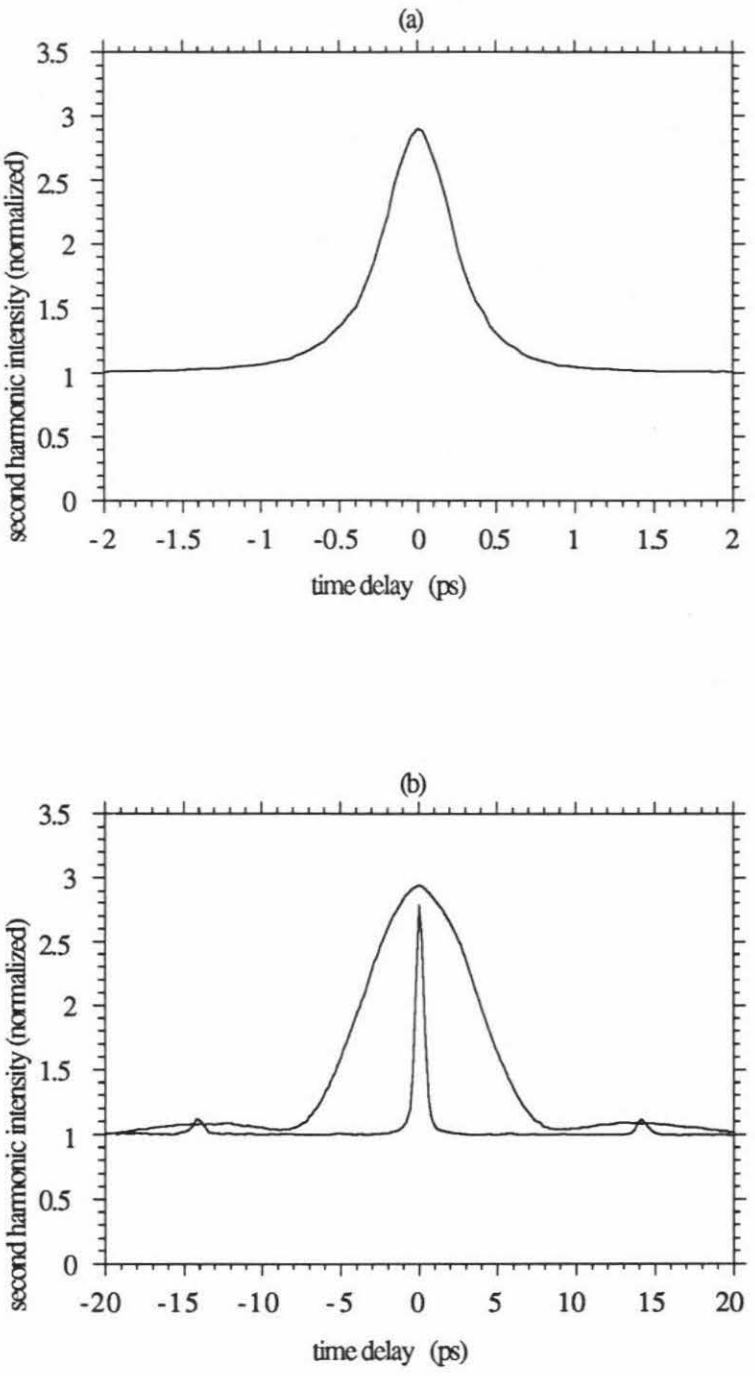

Figure 6.18: (a) Intensity autocorrelation of compressed pulse. (b) Intensity autocorrelation of uncompressed and compressed pulse

shown in fig. 6.20. The fringes are visible over the full pulse width, indicating that the pulse is very close to the transform limit, and that very little nonlinear chirp is present. Presence of nonlinear chirp after compression usually shows up as long tails in the autocorrelation traces [23]. The optical spectrum (fig. 6.19) shows a modulation at 71GHz, the round-trip frequency between the two semiconductor facets. Compression to near transform limited pulses shows that the residual reflectivity at the AR coated facet does not prevent mode-locking over a bandwidth larger than 71GHz semiconductor mode spacing, but merely results in weak satellite pulses.

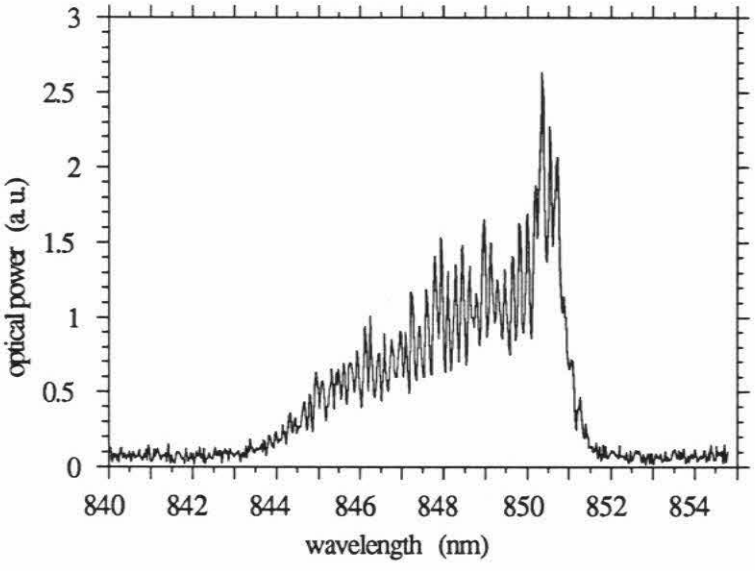

Figure 6.19: Optical spectrum of compressed pulse

Typical pulse energies coming out of the laser were 1.3pJ, and 0.6pJ after losses in the compressor, corresponding to a peak power of 2W for a 330fs long pulse.

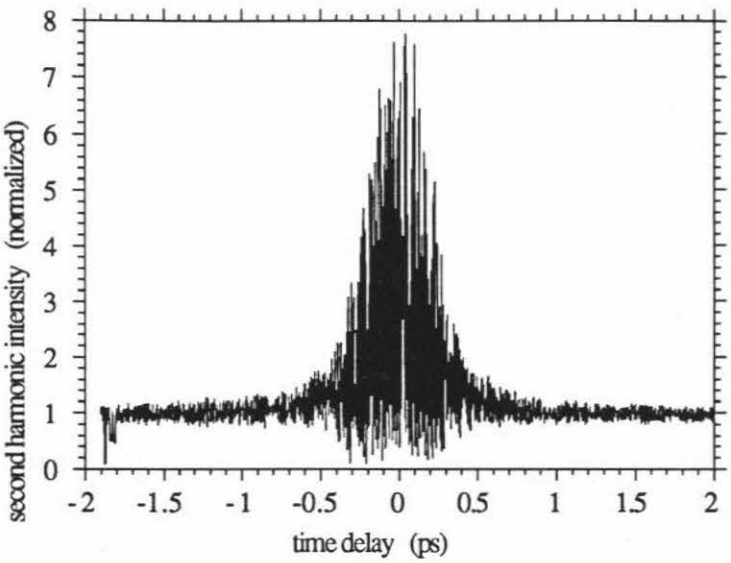

Figure 6.20: Fringe resolved autocorrelation of compressed pulse

6.6 Conclusion

In this chapter broad-band wavelength tuning of passively mode-locked two-section multiple quantum well lasers coupled to an external cavity was demonstrated. Typical tuning ranges on the order of 15 nm at 840 nm can obtained, and a maximum of 26 nm was demonstrated. This is the broadest tuning range reported for passively mode-locked semiconductor lasers. The pulses emitted by the laser are several picoseconds long with time-bandwidth products of several times the transform limit. By using external pulse compression with a grating telescope compressor, it was then shown that the large time-bandwidth products are due to a linear upchirp during the pulse. The pulses were compressed by a factor as large as 15, down to near transform limited pulse widths as low as 320 fs. At the time of the measurements these were the shortest

pulses reported for two-section passively mode-locked MQW lasers. This pulse width has been lowered since then in a continuation of the work presented in this chapter, by combining the wavelength tuning with the external pulse compression. A tuning range of 16 nm was measured with compressed pulse widths below 600 fs, and as low as 260 fs [23], with the shorter pulses nearly transform limited and the longer pulses about 2 times the transform limit. The near transform limited pulses after compression indicate that the upchirp of the pulses is extremely linear, while the 2 times transform limit is due to a nonlinear chirp component, which cannot be compensated for with the compressor used in the setup.

Combining the experimental results presented in this chapter with previous experiments on the low noise performance of these lasers [5], indicates that passively mode-locked two-section MQW lasers coupled to an external cavity, are getting close to commercial applications for low cost, low power, wavelength tunable, subpicosecond pulses.

References

[1] D. Mehuys, M. Mittelstein, A. Yariv, R. Sarfaty, and J. E. Ungar, *Electron. Lett.*, **25**, 143 (1989)

[2] M. Mittelstein, D. Mehuys, A. Yariv, J. E. Ungar, and R. Sarfaty, *Appl. Phys. Lett.*, **54**, 1092 (1989)

[3] S. Sanders, **Passive Mode-Locking and Millimeter-Wave Modulation of Quantum Well Lasers**, *Ph. D. Thesis*, California Institute of Technology (1992)

[4] S. Sanders, A. Yariv, J. Paslaski, J. E. Ungar, and H. A. Zarem, *Appl. Phys. Lett.*, **58**, 681 (1991)

[5] S. Sanders, T. Schrans, A. Yariv, J. Paslaski, J. E. Ungar, and H. A. Zarem, *Appl. Phys. Lett.*, **59**, 1275 (1991)

[6] M. Serenyi, J. Kuhl, and E. O. Göbel, *Appl. Phys. Lett.*, **50**, 1213 (1987)

[7] J. M. Wiesenfeld, M. Kuznetsov, and A. S. Hou, *IEEE Photon. Technol. Lett.*, **2**, 319 (1990)

[8] A. S. Hou, R. S. Tucker, and G. Eisenstein, *IEEE Photon. Technol. Lett.*, **2**, 322 (1990)

[9] D. M. Bird, R. M. Fatah, M. K. Cox, P. D. Constantine, J. C. Regnault, and K. H. Cameron, *Electron. Lett.*, **26**, 2086 (1990)

[10] P. J. Delfyett, L. Florez, N. Stoffel, T. Gmitter, N. Andreadakis, G. Alphonse, and W. Ceislik, *Opt. Lett.*, **17**, 670 (1992)

[11] W.-H. Xiang, S. R. Friberg, K. Watanabe, S. Machida, W. Jiang, H. Iwamura, and Y. Yamamoto, *Opt. Lett.*, **16**, 1394 (1991)

[12] W. B. Jiang, R. Mirin, and J. E. Bowers, *Appl. Phys. Lett.*, **60**, 677 (1992)

[13] W.-H. Xiang, S. R. Friberg, K. Watanabe, S. Machida, Y. Sakai, H. Iwamura, and Y. Yamamoto, *Appl. Phys. Lett.*, **59**, 2076 (1991)

[14] T. Schrans, S. Sanders, and A. Yariv, *IEEE Photon. Technol. Lett.*, **4**, 323 (1992)

[15] D. J. Derickson, R. J. Helkey, A. Mar, J. R. Karin, J. E. Bowers, and R. L. Thornton, *IEEE Photon. Technol. Lett.*, **4**, 333 (1992)

[16] D. Marcuse, *Appl. Optics*, **20**, 3573 (1981)

[17] E. B. Treacy, *IEEE J. Quantum Electron.*, **5**, 454 (1969)

[18] O. E. Martinez, J. P. Gordon, and R. L. Fork, *J. Opt. Soc. Am. A*, **1**, 1003 (1984)

[19] O. E. Martinez, *IEEE J. Quantum Electron.*, **23**, 59 (1987)

[20] J. W. Goodman, **Introduction to Fourier Optics**, ch. 5, 6 and 7, (1968)

[21] T. Schrans, R. A. Salvatore, S. Sanders, and A. Yariv, *Electron. Lett.*, **28**, 1480 (1992)

[22] J.-C. M. Diels, J. J. Fontaine, I. C. McMichael, and F. Simoni, *Appl. Opt.*, **24**, 1270 (1985)

[23] R. A. Salvatore, T. Schrans, and A. Yariv, *IEEE Photon. Technol. Lett.*, **5**, 756 (1993)

Chapter 7

Pulse propagation and self-phase-modulation in saturable media

7.1 Introduction

In the previous chapter experimental results on passive mode-locking of two-section quantum well lasers in an external cavity indicated that the large time-bandwidth products measured are due to strong chirping of the pulse [1,2], allowing for external pulse compression to subpicosecond pulse widths. The large compression factors ($\sim$ 15) and the near transform limited pulse widths measured, indicate that the chirp is very linear and that the nonlinear chirp remaining after compression is very small. From the compressor setup it was found that the pulses emitted by the laser have an

upchirp (blue shift). Other groups have reported pulse compression to near transform limited pulse widths using similar structures [3] (upchirp), a hybridly mode-locked laser with an external quantum well absorber [4] (upchirp), and optically pumped active mode-locking of VCSEL in an external cavity with a downchirp [5] or an upchirp [6]. It should be noted that while actively mode-locking can result in either an upchirp or downchirp, structures using a saturable absorber have only shown an upchirp.

A qualitative explanation for the chirping is based on self-phase-modulation due to the gain and absorber saturation. The mode-locking mechanism is an interaction between pulse compression (spectral broadening) and pulse broadening (spectral narrowing). The pulse compression is obtained by a modulation of the net gain of the device such that the center of the pulse sees net gain, while the tails of the pulse see a net loss. The pulse broadening mechanism are usually group velocity dispersion (GVD) and the finite spectral bandwidth of the gain medium (gain dispersion). Under stable mode-locked operation the pulse compression per round-trip is equal to the pulse broadening per round-trip and the pulse reproduces itself. For semiconductor lasers however there is an additional mechanism that contributes to the spectral broadening, namely the self-phase-modulation (SPM) due to the change in electron density induced by the pulse and the dependence of the refractive index on the electron density. Stable mode-locking is then obtained when the spectral broadening per round-trip due to pulse compression and SPM is equal to the spectral narrowing per round-trip due to the finite gain bandwidth. The amount of chirp increases with

each round-trip until equilibrium is reached, resulting in chirped pulses with large time-bandwidth products.

While this qualitative treatment explains how SPM can result in chirped pulses, a more rigorous analysis is necessary to explain the strong linearity and the sign of the chirp induced by SPM. Different models have been developed for passively mode-locked lasers using a time domain analysis [7,8,9,10,11], resulting in analytic expressions for the pulse shape, the pulse energy and the pulse width by making several approximations. These models however do not include SPM as they were developed for dye lasers where the refractive index does not depend on the inversion level. Other drawbacks of these models are that they assume symmetric pulse shapes and pulse energies much smaller than the saturation energy of the absorber and gain, while both assumptions are not valid for semiconductor lasers. The leading edge of the pulse is determined by saturation of the absorber, while the trailing edge is determined by the saturation of the gain, and as the saturation energies for absorber and gain are different, asymmetric pulse shapes should be expected. For semiconductor lasers where the gain and the absorber are strongly saturated, the pulse energy is of the same order of magnitude as the saturation energy of the active media [12].

More recently a model based on the traveling wave rate equations was developed for active mode-locking [13], where the effects of SPM are neglected, and for passive mode-locking of two-section lasers [3] where SPM is briefly discussed. Several models of pulse propagation through laser amplifiers have been developed, including SPM [14], gain dispersion (finite gain bandwidth) [15] and other fast gain dynamics [16,17].

Recently fast gain dynamics were discovered in semiconductor laser amplifiers using pump-probe measurements techniques [18,19,20,21]. These dynamics were attributed to carrier heating induced by free carrier absorption and two photon absorption [17, 21], and have time constants associated to intraband scattering that are on the order of 100fs. It was found that the fast gain dynamics have little effect on picosecond pulses, and are only important for subpicosecond pulses [16,17]. For the passively mode-locked two-section lasers studied here, the pulses propagating in the cavity are on the order of picoseconds, such that these fast gain dynamics can be neglected. The only time constants are then the carrier recovery time which is on the order of 1 ns for the gain section, and 100 ps for a reverse biased absorber. As these recovery times are much larger than the pulse widths, gain and absorption recovery can be neglected during passage of the pulse and will only be taken into account once the pulse has passed.

To include the effects of SPM and gain dispersion the frequency dependence of the gain and refractive index has to be included. As pointed out in [16] this frequency dependence was erroneously introduced in [15] as the frequency dependence of the α-parameter was ignored. In the next section a simple model will be used to calculate the frequency dependence of the real and imaginary part of the complex susceptibility χ. Once the correct frequency dependence of χ is determined, the traveling wave rate equation for the complex magnitude of the optical field will be derived together with a rate equation for the gain and the absorption. Solution of these coupled nonlinear rate equations will be discussed and applied two-section laser structures as used in

the experiments of the previous chapter.

7.2 The frequency dependence of the complex susceptibility

The complex susceptibility $\chi(E = \hbar\omega)$ in a semiconductor is given by [22]

$$\chi(E) = \chi'(E) - i\chi''(E) = \frac{\mu^2}{\epsilon_0 \hbar} \int_0^{+\infty} \frac{\rho(E_0)\left[f_v\left(E_v(E_0)\right) - f_c\left(E_c(E_0)\right)\right]}{E - E_0 + iE_2} dE_0 \qquad (7.1)$$

with μ the matrix element, $\rho(E_0)$ the reduced density of states, f_v (f_c) the fermi factor for the valence (conduction) band, and E_2 the lineshape broadening. The fermi factors and the reduced density of states have to be determined for the laser structure used in the experiments.

The quantum well structure of the lasers is shown in fig. 7.1 where the barrier height for the conduction band is ΔE_c=0.17eV and ΔE_v=0.084eV for x=0.2. Coupling between the quantum wells will be ignored and the location of the subbands for finite well depths can be calculated in a straigthforward way [23]. Following subbands are found for the conduction band ($m_c = 0.067m_e, m_v = 0.46m_e$):

$$E_{1c} = 0.044eV$$

$$E_{2c} = 0.15eV$$

and for the valence band:

$$E_{1v} = -E_G - 0.009eV$$

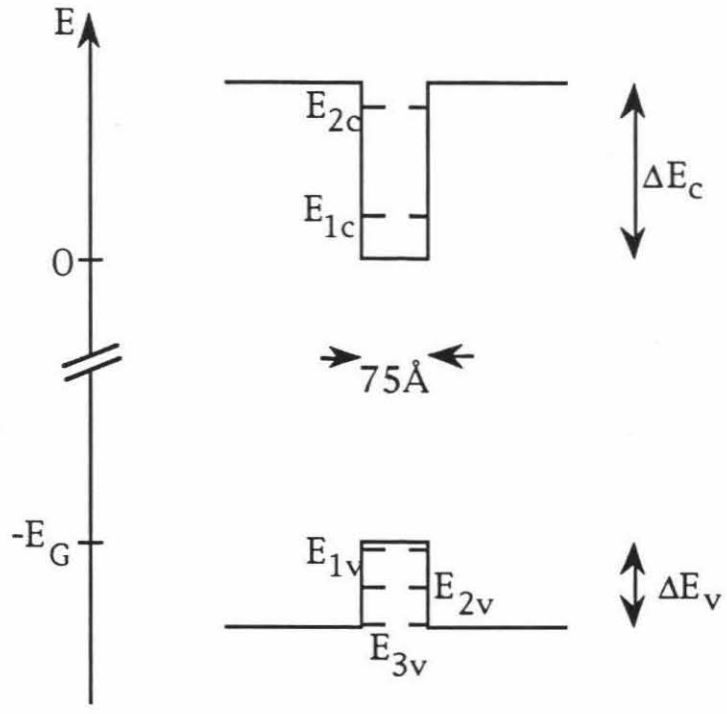

Figure 7.1: Quantum well structure

$$E_{2v} = -E_G - 0.035eV$$

$$E_{3v} = -E_G - 0.073eV$$

with E_G the bandgap, and zero energy corresponding to the bottom of the conduction band in bulk material. Using the k-selection rule the energy states E_c in the conduction band and E_v in the valence band interacting with a photon of energy E_0 are (transitions between the n=1 conduction subband and n=3 valence subband are neglected for the photon energies of interest)

$$E_c(E_0) = \begin{cases} E_{1c} + \frac{m_r}{m_c}(E_0 - E_{1c} + E_{1v}) & \text{n=1 \& } E_0 > E_{1c} - E_{1v} \\ E_{2c} + \frac{m_r}{m_c}(E_0 - E_{2c} + E_{2v}) & \text{n=2 \& } E_0 > E_{2c} - E_{2v} \\ \Delta E_c + \frac{m_r}{m_c}(E_0 - E_G - \Delta E_G) & \text{continuum \& } E_0 > E_G + \Delta E_G \end{cases} \tag{7.2}$$

$$E_v(E_0) = \begin{cases} E_{1v} - \frac{m_r}{m_v}(E_0 - E_{1c} + E_{1v}) & \text{n=1 \& } E_0 > E_{1c} - E_{1v} \\ E_{2v} - \frac{m_r}{m_v}(E_0 - E_{2c} + E_{2v}) & \text{n=2 \& } E_0 > E_{2c} - E_{2v} \\ -E_G - \Delta E_v + \frac{m_r}{m_v}(E_0 - E_G - \Delta E_G) & \text{continuum \& } E_0 > E_G + \Delta E_G \end{cases} \tag{7.3}$$

with $\Delta E_G = \Delta E_c + \Delta E_v$, E_G the bulk band gap of GaAs (1.4eV), $m_c = 0.067m_e$ ($m_v = 0.46m_e$) the conduction (valence) band effective mass, and m_r the reduced effective mass ($1/m_r = 1/m_c + 1/m_v$).

The reduced density of states $\rho(E_0)$ is given by

$$\begin{aligned} \rho(E_0) = & \frac{m_r}{\pi\hbar^2 L_z} H(E_0 - E_{1c} + E_{1v}) + \frac{m_r}{\pi\hbar^2 L_z} H(E_0 - E_{2c} + E_{2v}) \\ + & \frac{1}{2\pi^2}\left(\frac{2m_r}{\hbar^2}\right)^{3/2} (E_0 - E_G - \Delta E_G)^{1/2} H(E_0 - E_G - \Delta E_G) \end{aligned}$$

with $L_z = 75\mathring{A}$ the quantum well thickness, and H the heavyside function.

The electron density N and the hole density P are given by

$$\begin{aligned} N = & \frac{m_c kT}{\pi\hbar^2 L_z} \ln\left\{\left[1 + e^{-(E_{1c} - E_{Fc})/kT}\right]\left[1 + e^{-(E_{2c} - E_{Fc})/kT}\right]\right\} \\ + & \frac{1}{4}\left(\frac{2m_c kT}{\pi\hbar^2}\right)^{3/2} e^{-(\Delta E_c - E_{Fc})/kT} \end{aligned} \tag{7.4}$$

$$P = \frac{m_v kT}{\pi\hbar^2 L_z} \ln\left\{\left[1+e^{+(E_{1v}-E_{Fv})/kT}\right]\left[1+e^{+(E_{2v}-E_{Fv})/kT}\right]\left[1+e^{+(E_{3v}-E_{Fv})/kT}\right]\right\}$$
$$+ \frac{1}{4}\left(\frac{2m_v kT}{\pi\hbar^2}\right)^{3/2} e^{+(\Delta E_v - E_{Fv})/kT}. \qquad (7.5)$$

The quasi-fermi level for the conduction band E_{Fc} and valence band E_{Fv} are related through the neutrality condition, which for undoped material is $N = P$.

The susceptibility was calculated for different pumping levels by choosing E_{Fc} and solving $N = P$ for E_{Fv} after which the integral in (7.1) can be calculated. The results are shown in fig. 7.2 for the real part $E\chi'(E)$ and fig. 7.3 for the imaginary part $E\chi''(E)$ ($\sim$ gain) at different pumping levels. In the region of gain (1.45 eV–1.6 eV) the slope of $E\chi'(E)$ versus E is seen to be quasi-independent of the pumping level (fig. 7.2), the corresponding group velocity component is thus independent of the gain. The curvature of $E\chi'(E)$ is small, and quasi-independent of the pumping level, hence the associated group velocity dispersion is small and quasi-independent of the gain. The slope and curvature of the gain however are dependent on the gain as illustrated in fig. 7.3.

The α-parameter, defined as

$$\alpha(E) = \frac{\Delta\chi'(E)}{\Delta\chi''(E)} \qquad (7.6)$$

with Δ referring to different pumping levels and fixed photon energy, is shown in fig. 7.4 as a function of photon energy at different pumping levels. In the region of absorption (low pumping level) the α-parameter is small compared to its value at

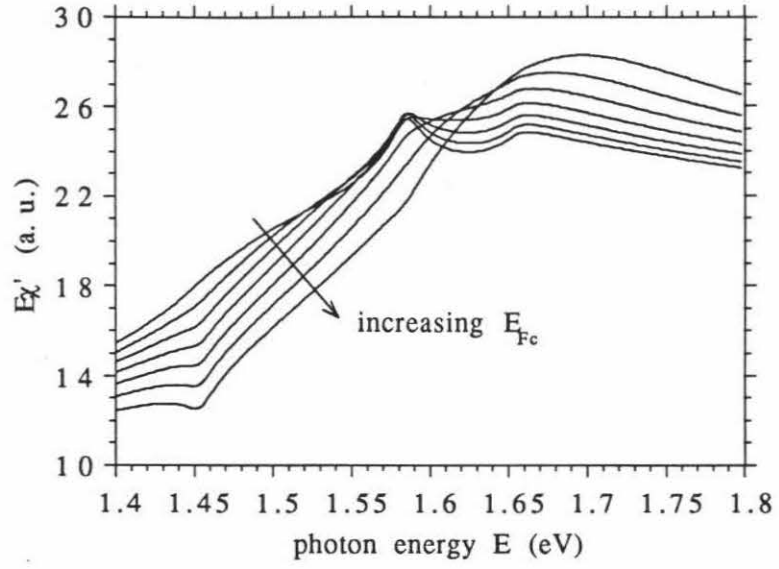

Figure 7.2: Real part of susceptibility as a function of photon energy at different pumping levels

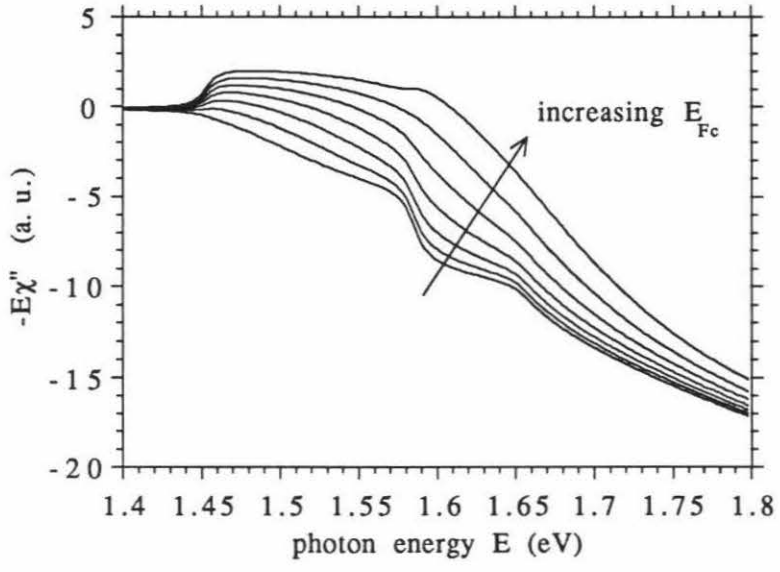

Figure 7.3: Imaginary part of susceptibility as a function of photon energy at different pumping levels

higher pumping, as is also evidenced by the quasi independence of $E\chi'(E)$ on the pumping level at low pumping levels (fig. 7.2). The α-parameter in the absorber is thus very small, and the associated SPM due to the saturation of the absorption will be small, as most of the change in the refractive index will occur while the absorption is getting bleached, and most of the light is absorbed.

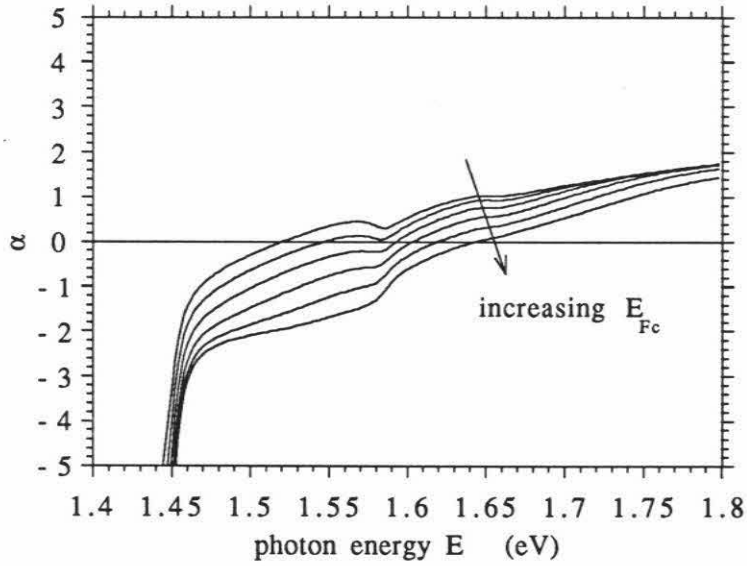

Figure 7.4: α-parameter as a function of photon energy at different pumping levels

From this simple model the following conclusions (similar to the results in [16]) are drawn for use in the pulse propagation model

- The dependence of the real part of χ on the photon energy is quasi independent on the pumping level.
- The dependence of the imaginary part of χ on the photon energy depends on the pumping level.

- The α-parameter under absorption is much smaller than under gain.

7.3 The traveling wave rate equation

The traveling wave rate equation for the optical field can be derived from the wave equation using the slowly varying envelope approximation (SVEA) [14,24]. A different derivation is given here starting from Maxwell's equations, based on the formalism derived in appendix A without making use of the SVEA. Maxwell's equation in this case are given by

$$\nabla \times \mathbf{e}(x,y,z,t) = -\mu_o \frac{\partial \mathbf{h}}{\partial t} \tag{7.7}$$

$$\nabla \times \mathbf{h}(x,y,z,t) = \epsilon_o n_b^2 \frac{\partial \mathbf{e}}{\partial t} + \frac{\partial \mathbf{p_N}}{\partial t} \tag{7.8}$$

with $n_b(x,y)$ the cold waveguide refractive index, and $\mathbf{p_N}(x,y,z,t)$ the polarization generated by the electron density.

In the case of pulse propagation through a saturable medium only one transverse mode has to be taken into account and the complex amplitude $a(z,t)$ is defined as

$$\mathbf{e}(x,y,z,t) = a(z,t)e^{+i(\omega_0 t - \beta_0 z)}\mathbf{E_m}(x,y) \tag{7.9}$$

with ω_0 and β_0 appropriately chosen reference frequency and wavevector, and $\mathbf{E_m}$ the transverse modal distribution.

The equations in appendix A are derived for the frequency domain where

$$\tilde{E}(z,\omega) = \tilde{a}(z,\omega)e^{-i\beta_0 z} = \int_0^{+\infty} a(z,t)e^{+i(\omega_0 t - \beta_0 z)}e^{-i\omega t}dt. \tag{7.10}$$

The equation for $\tilde{a}(z,\omega)$ follows then from (A.62) with $\kappa_n = \kappa_\sigma = 0$:

$$\frac{\partial \tilde{a}}{\partial z} = -\left(\frac{\alpha_i}{2} + i\Delta\beta\right)\tilde{a}(z,\omega) + P_N(z,\omega)e^{+i\beta_0 z}. \tag{7.11}$$

In the derivation of (A.62), the polarization was assumed to be due to spontaneous emission. This is not necessary, however, and the polarization $\mathbf{P}(x,y,z,\omega)$ can also be due to the electron density. In this case $\gamma = \alpha_i/2$ as the material gain is now included in $\mathbf{P}$. For TE modes the polarization function $P_N(z,\omega)$ is related to P_N by

$$P_N(z,\omega) = -\frac{i\omega\mu_o c}{2n_{eff}} \iint_{-\infty}^{+\infty} \mathbf{P_N}(x,y,z,\omega).\mathbf{E_m}^*(x,y)dxdy \tag{7.12}$$

with $\mathbf{E_m}$ normalized to $\iint_{-\infty}^{+\infty} |\mathbf{E_m}(x,y)|^2\, dxdy = 1$, and $\mathbf{P_N}(x,y,z,\omega)$ the Fourier transform of $\mathbf{p_N}(x,y,z,t)$.

Using the susceptibilty $\chi(x,y,z,\omega)$ for the electron density, P_N becomes

$$P_N(z,\omega) = -\frac{i\omega}{2cn_{eff}}\Gamma\chi(z,\omega)\tilde{E}(z,\omega) \tag{7.13}$$

substituting this in (7.11) gives:

$$\frac{\partial \tilde{E}}{\partial z} = -\left(\frac{\alpha_i}{2} + i\beta\right)\tilde{E}(z,\omega) - \frac{i\omega\Gamma}{2cn_{eff}}\chi(z,\omega)\tilde{E}(z,\omega). \tag{7.14}$$

To go back to the time domain equation the frequency dependence of β and χ has to be included:

$$\begin{aligned}\beta &= \beta_0 + \frac{d\beta}{d\omega}(\omega-\omega_0) + \frac{1}{2}\frac{d^2\beta}{d\omega^2}(\omega-\omega_0)^2 \\ &= \beta_0 + \frac{\omega-\omega_0}{v_g} + \frac{1}{2}\beta_2(\omega-\omega_0)^2\end{aligned}$$

with $\beta_0 = \omega_0 n_{eff}/c$, $v_g = d\omega/d\beta$ the group velocity, $\beta_2 = d^2\beta/d\omega^2$ the dispersion of the cold waveguide, and only terms up to second order in $(\omega-\omega_0)$ are considered.

Similarly χ is given by

$$\begin{aligned}\frac{\omega\chi}{n_{eff}} &= \frac{\omega_0\left[\chi'(\omega_0)-i\chi''(\omega_0)\right]}{n_{eff}} \\ &+ \left[\frac{\partial}{\partial\omega}\left(\frac{\omega\chi'(\omega)}{n_{eff}}\right)-i\frac{\partial}{\partial\omega}\left(\frac{\omega\chi''(\omega)}{n_{eff}}\right)\right]_{\omega=\omega_0}(\omega-\omega_0) \\ &+ \frac{1}{2}\left[\frac{\partial^2}{\partial\omega^2}\left(\frac{\omega\chi'(\omega)}{n_{eff}}\right)-i\frac{\partial^2}{\partial\omega^2}\left(\frac{\omega\chi''(\omega)}{n_{eff}}\right)\right]_{\omega=\omega_0}(\omega-\omega_0)^2.\end{aligned}$$

The modal gain g is related to χ by

$$g(\omega) = -\frac{\omega\Gamma\chi''(\omega)}{cn_{eff}} \tag{7.15}$$

and

$$-\frac{i\omega_0\Gamma\chi(\omega_0)}{2cn_{eff}} = \frac{g(\omega_0)}{2}(1+i\alpha). \tag{7.16}$$

Substituting this in (7.14) and inverse Fourier transforming using $(\omega-\omega_0)\rightarrow -i\partial/\partial t$ gives a traveling wave rate equation (with $g_0 = g(\omega_0)$)

$$\begin{aligned}\frac{\partial a}{\partial z}+\frac{1}{v_g}\frac{\partial a}{\partial t}-\frac{i\beta_2}{2}\frac{\partial^2 a}{\partial t^2} &= \left[\frac{g_0(z,t)}{2}(1+i\alpha)-\frac{\alpha_i}{2}\right]a(z,t) \\ &+ \frac{i\Gamma}{2c}\left[\frac{\partial}{\partial\omega}\left(\frac{\omega\chi''(\omega)}{n_eff}\right)+i\frac{\partial}{\partial\omega}\left(\frac{\omega\chi'(\omega)}{n_eff}\right)\right]_{\omega=\omega_0}\frac{\partial a}{\partial t} \\ &+ \frac{\Gamma}{4c}\left[\frac{\partial^2}{\partial\omega^2}\left(\frac{\omega\chi''(\omega)}{n_eff}\right)+i\frac{\partial^2}{\partial\omega^2}\left(\frac{\omega\chi'(\omega)}{n_eff}\right)\right]_{\omega=\omega_0}\frac{\partial^2 a}{\partial t^2}.\end{aligned}$$

As was pointed out in the previous section the derivatives of $\omega\chi'(\omega)$ are quasi-independent of the electron density. The change in these derivatives due to saturation under pulse propagation will therefore be ignored such that $(\partial/\partial\omega)(\omega\chi'/n_{eff})$ can be absorbed in the group velocity v_g and $(\partial^2/\partial\omega^2)(\omega\chi'/n_{eff})$ in the dispersion β_2. The dependence of χ'' on the frequency however cannot be neglected. As χ'' is related to

the gain, a parabolic gain profile will be assumed:

$$g(\omega) = g_p \left[1 - T_2^2(\omega - \omega_c)^2\right] \tag{7.17}$$

with g_p the peak gain at frequency ω_c and $1/\pi T_2$ the gain bandwidth. This gives

$$\begin{aligned} g(\omega_0) &= g_p \left[1 - T_2^2(\omega_0 - \omega_c)^2\right] && (7.18)\\ \frac{\Gamma}{2c}\frac{\partial}{\partial\omega}\left(\frac{\omega\chi''(\omega)}{n_{eff}}\right)\Bigg|_{\omega=\omega_0} &= g_p T_2^2(\omega_0 - \omega_c) && (7.19)\\ \frac{\Gamma}{4c}\frac{\partial^2}{\partial\omega^2}\left(\frac{\omega\chi''(\omega)}{n_{eff}}\right)\Bigg|_{\omega=\omega_0} &= \frac{g_p T_2^2}{2}. && (7.20) \end{aligned}$$

Substitution in the traveling wave rate equation results in

$$\begin{aligned} \frac{\partial a}{\partial z} + \frac{1}{v_g}\frac{\partial a}{\partial t} - i\frac{\beta_2}{2}\frac{\partial^2 a}{\partial t^2} &= \frac{g_p(z,t)}{2}(1+i\alpha)\left[1 - T_2^2(\omega_0-\omega_c)^2\right]a(z,t) - \frac{\alpha_i}{2}a(z,t)\\ &+ ig_p(z,t)T_2^2(\omega_0-\omega_c)\frac{\partial a}{\partial t} + \frac{g_p(z,t)T_2^2}{2}\frac{\partial^2 a}{\partial t^2} \end{aligned} \tag{7.21}$$

where the time dependence of $g_p(z,t)$ has been included now, while it was ignored in the inverse Fourier transform. This is justified as the change in the peak gain under saturation of picosecond pulses is much slower than the response time of the polarization to the electric field, such that it can be adiabatically eliminated (also known as the rate equation approximation). The dependence of the spectral width T_2 and location of the gain maximum ω_c on the peak gain will be ignored.

The traveling rate wave equation (7.21) can be simplified by applying a coordinate transformation to an observer moving with the pulse at the group velocity v_g.

$$\tau = \frac{t - \frac{z}{v_g}}{T_0} \qquad\qquad \zeta = \frac{z}{L}$$

where the local time τ has been normalized to T_0 and the position ζ is normalized to the length L. The traveling wave rate equation becomes

$$\begin{aligned}\frac{\partial a}{\partial \zeta} - i\frac{\tilde{\beta}_2}{2}\frac{\partial^2 a}{\partial \tau^2} &= \frac{\tilde{g}_p(\zeta,\tau)}{2}(1+i\alpha)\left[1 - d^2(\tilde{\omega}_0 - \tilde{\omega}_c)^2\right] a(\zeta,\tau) - \frac{\tilde{\alpha}_i}{2}a(\zeta,\tau) \\ &+ i\tilde{g}_p(\zeta,\tau)d^2(\tilde{\omega}_0 - \tilde{\omega}_c)\frac{\partial a}{\partial \tau} + \tilde{g}_p(\zeta,\tau)\frac{d^2}{2}\frac{\partial^2 a}{\partial \tau^2} \end{aligned} \tag{7.22}$$

with $\tilde{\beta}_2 = \beta_2 L/T_0^2$, $\tilde{g}_p = g_p L$, $d = T_2/T_0$, $\tilde{\omega}_{c,0} = \omega_{c,0}T_0$ and $\tilde{\alpha}_i = \alpha_i L$.

The rate equation for the peak gain is given by

$$\frac{\partial \tilde{g}_p}{\partial \tau} = -\frac{\tilde{g}_p(\zeta,\tau) - \tilde{g}_0}{\tilde{\tau}_g} - \tilde{g}_p(\zeta,\tau)\left[1 - d^2(\tilde{\omega}_0 - \tilde{\omega}_c)^2\right]\frac{|a(\zeta,\tau)|^2}{\tilde{E}_{sat}} \tag{7.23}$$

with $\tilde{g}_0 = g_0 L$ the normalized unsaturated (or small signal) peak gain, $\tilde{\tau}_g = \tau_g/T_0$ the normalized carrier lifetime, and $\tilde{E}_{sat} = E_{sat}/T_0$ the normalized saturation energy. The following assumptions have been made in deriving (7.23):

- The peak gain is linear with the carrier density: $g_p = \Gamma A(N - N_0)$
- The carrier recovery rate is linear with the carrier density: $R = N/\tau_g$
- The average frequency of $a(\zeta,\tau)$ is zero ($\tilde{\omega}_0$ is then the average optical frequency)
- The spectral width of $a(\zeta,\tau)$ has been ignored

7.4 Solution of the traveling wave rate equations

Analytic solutions of the set of coupled nonlinear partial differential equations (7.22) and (7.23) only exist for specific situations, such that numerical solutions of these equations will be necessary. There are two interesting cases where analytic solutions can be found. The first one is the case of frequency independent gain (no gain dispersion), and the second one is the case of low pulse energy (no gain saturation).

7.4.1 Frequency independent gain

When the carrier lifetime $\tilde{\tau}_g$ is much longer than the pulse width of $a(\zeta,\tau)$, the carrier recovery term in (7.23) can be ignored during the passage of the pulse, and (7.23) can be integrated:

$$\tilde{g}_p(\zeta,\tau) = \tilde{g}_{ini}(\zeta)e^{-\left[1-d^2(\tilde{\omega}_0-\tilde{\omega}_c)^2\right]U(\zeta,\tau)} \tag{7.24}$$

with

$$U(\zeta,\tau) = \frac{1}{\tilde{E}_{sat}}\int_{-\infty}^{\tau} |a(\zeta,\tau')|^2\, d\tau' \tag{7.25}$$

the normalized pulse energy up to time τ, and $\tilde{g}_{ini}(\zeta) = \tilde{g}_p(\zeta,-\infty)$ the peak gain before the arrival of the pulse. This approximation is valid for picosecond pulses propagating through semiconductor materials as the carrier recovery time are typically on the order of 1ns for the gain section and 100ps for the absorber section.

When the finite gain bandwidth is neglected ($d = 0$) and the internal losses and dispersion are zero ($\alpha_i = 0$, $\beta_2 = 0$), the traveling wave equation has an analytic

solution [3,14,24]. If the complex amplitude $a(\zeta,\tau)$ is known at some plane ζ for all τ:

$$a(\zeta,\tau) = \sqrt{P(\zeta,\tau)}e^{-i\phi(\zeta,\tau)} \tag{7.26}$$

the intensity P and phase ϕ at plane $\zeta + \Delta\zeta$ are given by

$$P(\zeta+\Delta\zeta,\tau) = \frac{P(\zeta,\tau)}{1-(1-G_{ini}^{-1})e^{-[1-d^2(\tilde{\omega}_0-\tilde{\omega}_c)^2]U(\zeta,\tau)}} \tag{7.27}$$

and

$$\phi(\zeta+\Delta\zeta,\tau) = \phi(\zeta,\tau) + \frac{\alpha}{2}\ln\left[1-(1-G_{ini}^{-1})\,e^{-\left[1-d^2(\tilde{\omega}_0-\tilde{\omega}_c)^2\right]U(\zeta,\tau)}\right] \tag{7.28}$$

with G_{ini} the initial pulse gain between ζ and $\zeta+\Delta\zeta$

$$G_{ini} = G(\tau=-\infty) = e^{\left[1-d^2(\tilde{\omega}_0-\tilde{\omega}_c)^2\right]\int_{\zeta}^{\zeta+\Delta\zeta}\tilde{g}_{ini}(\zeta)d\zeta}. \tag{7.29}$$

The instantaneous frequency $\tilde{\omega}(\zeta+\Delta\zeta,\tau) = \partial\phi/\partial\tau$ is

$$\tilde{\omega}(\zeta+\Delta\zeta,\tau) = \tilde{\omega}(\zeta,\tau) - \frac{\alpha}{2}(1-G_{ini}^{-1})\left[1-d^2(\tilde{\omega}_0-\tilde{\omega}_c)^2\right]\frac{P(\zeta+\Delta\zeta,\tau)}{\tilde{E}_{sat}}e^{-\left[1-d^2(\tilde{\omega}_0-\tilde{\omega}_c)^2\right]U(\zeta,\tau)} \tag{7.30}$$

where the second term is the SPM due to the refractive index change associated with gain saturation.

The peak gain at position ζ and time τ is

$$\tilde{g}_p(\zeta,\tau) = -\frac{1}{\left[1-d^2(\tilde{\omega}_0-\tilde{\omega}_c)^2\right]\Delta\zeta}\ln\left[1-(1-G_{ini}^{-1})e^{-\left[1-d^2(\tilde{\omega}_0-\tilde{\omega}_c)^2\right]U(\zeta,\tau)}\right]. \tag{7.31}$$

7.4.2 Low pulse energy

When the pulse energy is much smaller than the saturation energy, the peak gain is time independent $\tilde{g}_p(\zeta,\tau) \equiv \tilde{g}_{ini} \equiv \tilde{g}_0$. The traveling wave rate equation (7.22 becomes linear, and can be solved in the frequency domain

$$\frac{\partial \tilde{A}}{\partial \zeta} = \left\{ \frac{\tilde{g}_0}{2}(1+i\alpha)\left[1-d^2(\tilde{\omega}_0-\tilde{\omega}_c)^2\right] - \frac{\tilde{\alpha}_i}{2} - \tilde{g}_0 d^2(\tilde{\omega}_0-\tilde{\omega}_c)\Omega - \frac{\tilde{g}_0}{2}d^2\Omega^2 - i\frac{\tilde{\beta}_2}{2}\Omega^2 \right\} \tilde{A}(\zeta,\Omega) \tag{7.32}$$

with solution

$$\tilde{A}(\zeta+\Delta\zeta,\Omega) = e^{\left\{\frac{\tilde{g}_0}{2}(1+i\alpha)\left[1-d^2(\tilde{\omega}_0-\tilde{\omega}_c)^2\right]-\frac{\tilde{\alpha}_i}{2}-\tilde{g}_0 d^2(\tilde{\omega}_0-\tilde{\omega}_c)\Omega-(\frac{\tilde{g}_0}{2}d^2+i\frac{\tilde{\beta}_2}{2})\Omega^2\right\}\Delta\zeta} \tilde{A}(\zeta,\Omega). \tag{7.33}$$

7.4.3 Numerical solution algorithm

When both saturation and gain dispersion are present the formal solution (7.24,7.25) of (7.23) can still be used, but (7.22) has to be solved numerically and self-consistent with (7.24) by propagating $a(\zeta,\tau)$ over a distance $\Delta\zeta$. The (i+1)th iteration on the complex amplitude at $\zeta+\Delta\zeta$ at any time τ is given by

$$a^{(i+1)}(\zeta+\Delta\zeta,\tau) = a(\zeta,\tau)e^{h^{(i)}(\zeta+\frac{\Delta\zeta}{2},\tau)\Delta\zeta} \tag{7.34}$$

with

$$h^{(i)}(\zeta+\frac{\Delta\zeta}{2},\tau) = \frac{\tilde{g}_p^{(i)}}{2}(1+i\alpha)\left[1-d^2(\tilde{\omega}_0-\tilde{\omega}_c)^2\right]-\frac{\tilde{\alpha}_i}{2}+i\tilde{g}_p^{(i)}d^2(\tilde{\omega}_0-\tilde{\omega}_c)\left(\frac{1}{a^{(i)}}\frac{\partial a^{(i)}}{\partial\tau}\right)$$
$$+ \frac{\tilde{g}_p^{(i)}d^2+i\tilde{\beta}_2}{2}\left(\frac{1}{a^{(i)}}\frac{\partial^2 a^{(i)}}{\partial\tau^2}\right). \qquad (7.35)$$

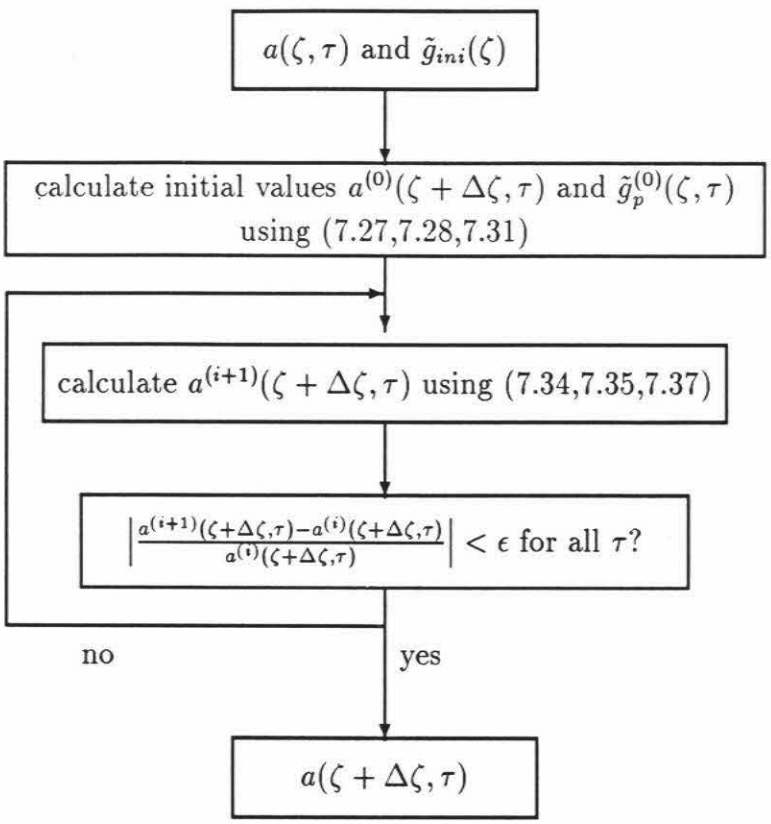

Figure 7.5: Propagation algorithm

Due to the quasi-exponential increase of the complex amplitude a, its value at $\zeta+\Delta\zeta/2$ is taken as the geometrical mean

$$a^{(i)}(\zeta+\frac{\Delta\zeta}{2},\tau)=\sqrt{a^{(i)}(\zeta,\tau)a^{(i)}(\zeta+\Delta\zeta,\tau)} \qquad (7.36)$$

and

$$\tilde{g}_p^{(i)}(\zeta + \frac{\Delta\zeta}{2}, \tau) = \tilde{g}_{ini}(\zeta + \frac{\Delta\zeta}{2}) e^{-\left[1-d^2(\tilde{\omega}_0-\tilde{\omega}_c)^2\right]U^{(i)}(\zeta+\frac{\Delta\zeta}{2},\tau)}. \tag{7.37}$$

The initial guesses $a^{(0)}$ and $\tilde{g}_p^{(0)}$ are calculated using the frequency independent gain solutions (7.27,7.28,7.29,7.31). The solution algorithm is summarized in fig. 7.5 If the center of the spectrum of a moves too far from $\tilde{\omega} - \tilde{\omega}_0 = 0$ due to SPM or detuning from the gain peak ($\tilde{\omega}_c \neq \tilde{\omega}_0$) during the iteration, the reference frequency $\tilde{\omega}_0$ is changed to the center of the spectrum of a.

7.5 Two-section passively mode-locked lasers

Two-section lasers similar as the lasers used in the experiments described in chapter 6 were simulated. Starting with an initial pulse shape and width, the pulse is propagated through a gain section, an absorber section, the partially saturated absorber section, and the partially saturated gain section. The gain and absorber recovery is neglected during propagation through these four sections as the round-trip time is typically 10–20 ps. After the pulse has propagated through the four sections, the absorber section is assumed to recover completely to its unsaturated value

$$\tilde{a}_{ini} \equiv \tilde{a}_0 \tag{7.38}$$

while the gain section only recovers partly as required for stable mode-locked operation. The initial peak gain $\tilde{g}_{ini}(\zeta)$ before the next passage of the pulse is found by solving (7.23) with $a \equiv 0$, giving

$$\tilde{g}_{ini}(\zeta) = \tilde{g}_0 + [\tilde{g}_p(\zeta, -\infty) - \tilde{g}_0]\, e^{-\frac{\tilde{\tau}_r}{\tilde{\tau}_g}} \tag{7.39}$$

with $\tilde{g}_0$ the unsaturated gain (corresponding to the gain current), $\tilde{g}_p(\zeta, -\infty)$ the peak gain at plane ζ after passage of the pulse, and $\tilde{\tau}_r$ the round-trip time in the external cavity. After propagating through the external cavity a fraction R_{ext} of the power is coupled back into the partly recovered gain section. This iteration is continued until the pulse energy, pulse width and the spectral width converge. All pulse energies are normalized to the saturation energy of the gain section ($E_{sat,g}$), and the saturation energy of the absorber ($E_{sat,a}$) is determined by the s-parameter:

$$s = \frac{E_{sat,g}}{E_{sat,a}}. \tag{7.40}$$

7.5.1 No self-phase-modulation

When no SPM is present ($\alpha = 0$) the pulses are expected to be transform limited. The pulse shape however is still unknown. Simulations have been performed for different gain bias levels $\tilde{g}_0$ and parameters as indicated in table 7.1.

The reference time is taken as $T_0 = 1$ ps and the gain bandwidth is then 1.6 THz for d =0.1. For a gain recovery time of 2 ns, the round-trip frequency $1/\tau_r$ is 500 MHz. Simulations were performed starting with a Gaussian and with a hyperbolic secant pulse shape, but the self-consistent pulse shapes are independent of the initial pulse shape. The results are shown in figs. 7.6–7.10.

	gain section	absorber section
$e^{\tilde{g}_0}$	variable	-13dB
d	0.1	0
$\tilde{\omega}_c$	$\tilde{\omega}_0$	—
α	0	0
$\tilde{\alpha}_i$	0	0
$\tilde{\beta}_2$	0	0
$R_{ext} = 0.1$	$\tilde{\tau}_r = \tilde{\tau}_g$	$s = 3$

Table 7.1: Parameter values used for two-section laser simulation

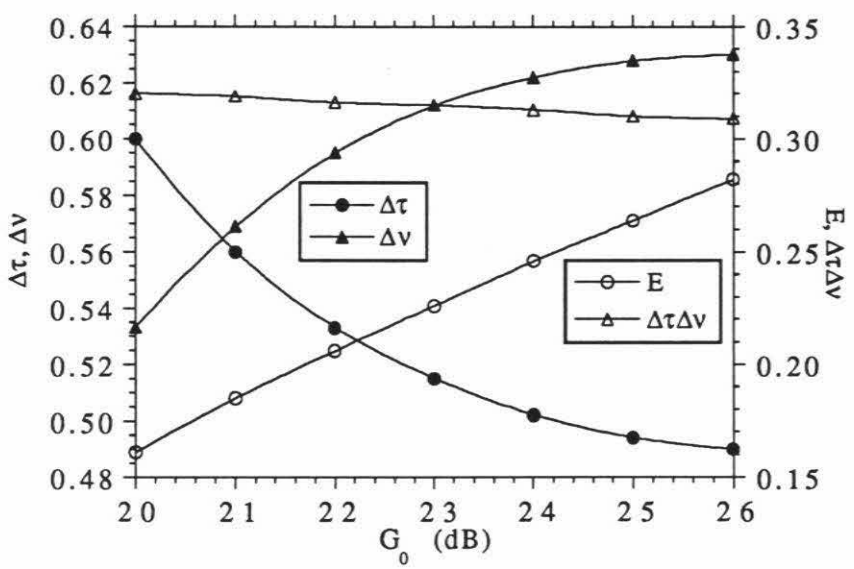

Figure 7.6: Pulse energy, pulse width, spectral width and time-bandwidth product as a function of unsaturated gain

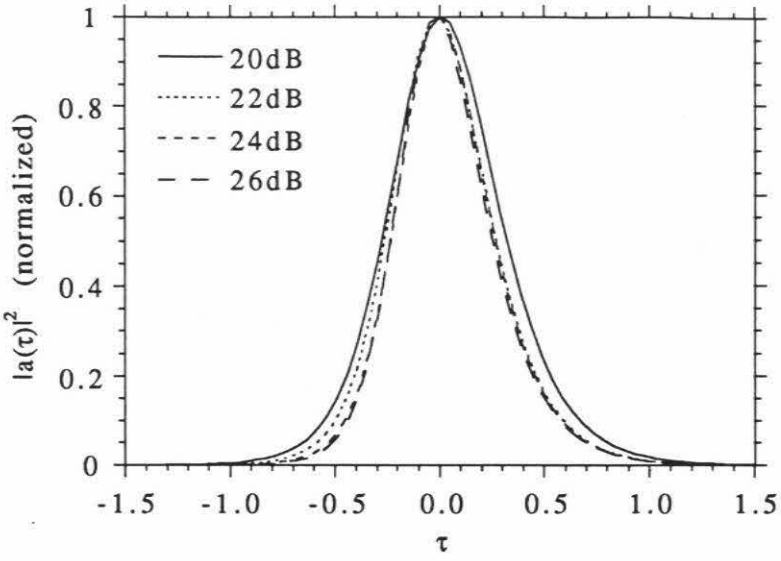

Figure 7.7: Pulse shapes for different values of unsaturated gain

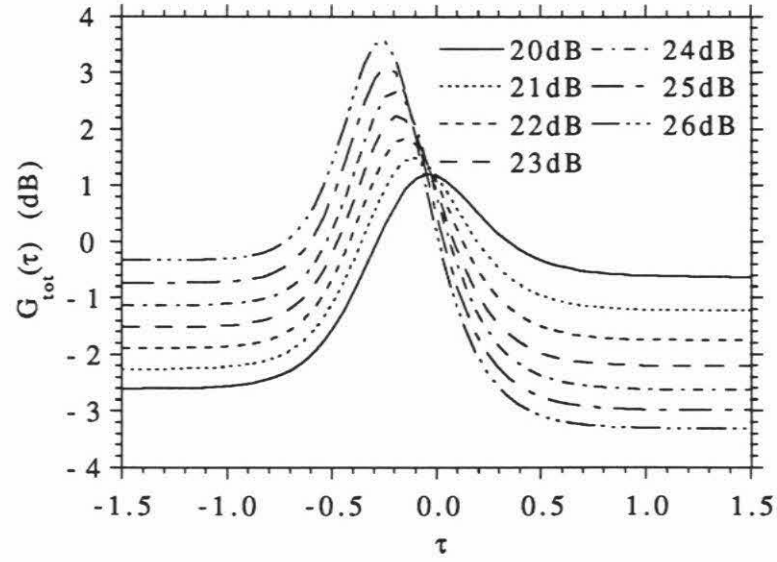

Figure 7.8: Total pulse gain for different values of unsaturated gain

The pulse energy, pulse width, spectral width and time-bandwidth product are shown in fig. 7.6 as a function of the pumping $G_0 = \exp(\tilde{g}_0)$. The pulse width decreases, the spectral width increases and the pulse energy increases with pumping, in agreement with the analytical sech^2 solutions of [10]. The spectral width is about 1/3 of the gain bandwidth, and the time-bandwidth product is quasi-constant at 0.31 (close to the sech^2 transform limit) and the pulse shapes are shown in fig. 7.7 for four values of G_0. The leading edge of the pulse is determined by the saturation of the absorber and is steeper than the trailing edge which is determined by the larger saturation energy $E_{sat,g}$ of the gain region. At higher pulse energies the saturation of the absorber is faster, resulting in a steeper rise time for higher pumping G_0.

The total gain $G_{tot}(\tau)$ defined as

$$G_{tot}(\tau) = e^{\int_{gain,1} \tilde{g}_p(\zeta,\tau)d\zeta + \int_{abs,1} \tilde{g}_p(\zeta,\tau)d\zeta + \int_{abs,2} \tilde{g}_p(\zeta,\tau)d\zeta + \int_{gain,2} \tilde{g}_p(\zeta,\tau)d\zeta} \tag{7.41}$$

is shown in fig. 7.8 for the different pumping levels. At low pumping levels ($G_0 = 20$ dB) the pulse energy is just large enough to saturate the gain and provide net loss for the trailing edge of the pulse. At high pumping levels ($G_0 = 26$ dB) the gain recovery is still low enough to provide net loss for the leading edge of the pulse. The input pulse shape, output pulse shape and total gain G_{tot} are shown in fig. 7.9 for $G_0 = 23$ dB. The pulse shaping mechanism due to the time dependent gain advances the pulse in time compared to the group delay through the two-section structure as the gain peaks befor the peak of the pulse. The pulse shape is compared to a sech^2 and a Gaussian pulse with same FWHM on a logaritmic scale in fig. 7.10 for G_0

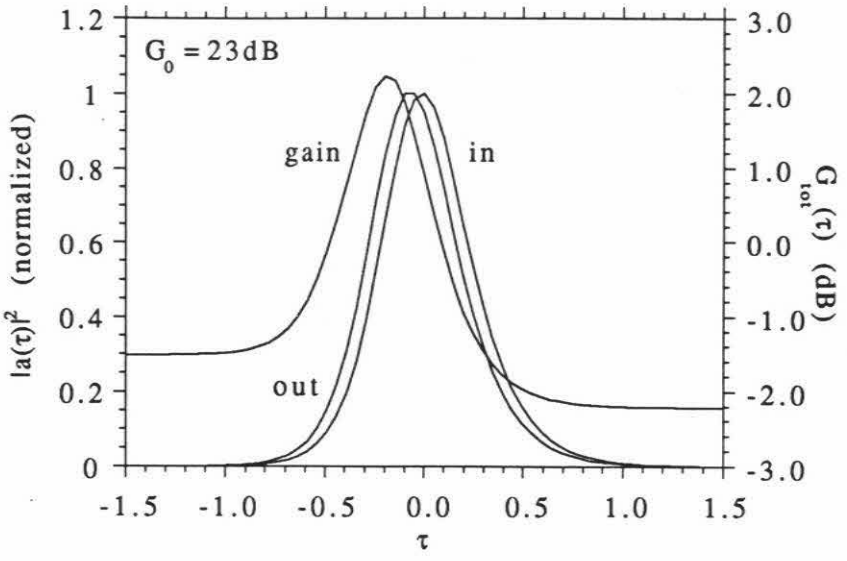

Figure 7.9: Total gain, input pulse and output pulse for $G_0 = 23$ dB

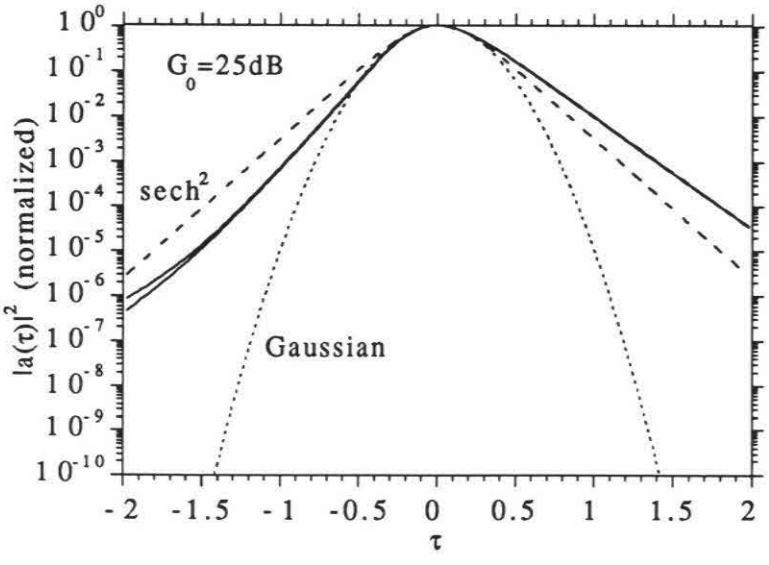

Figure 7.10: Pulse shape comparison with Gaussian and sech^2 pulse shapes

= 25 dB. Both tails of the asymmetric pulse shape have a behaviour closer to the exponential tails of the sech^2 than to the Gaussian tails. The two pulse shapes shown were obtained with a sech^2 pulse and a Gaussian pulse as initial pulse shape, and the difference in the self-consistent pulse shape is only visible in the tails.

7.5.2 Self-phase-modulation

When the α-parameter of the gain region is different from zero, the additional mechanism of self-phase-modulation makes the equilibrium between the pulse narrowing or spectral broadening on one side, and the pulse broadening or spectral narrowing on the other side, more complicated. Convergence in pulse width, spectral width and pulse energy cannot be obtained, as it is too hard to guess a good initial pulse shape with the right amount of chirp, and centered around the right frequency. The SPM induced by the gain region will add to the chirp and shift the frequency spectrum for each round-trip, resulting in creation of spectral side lobes (as is typically observed for SPM induced nonlinear chirp), and other spectral and temporal instabilities.

Without achieving self-consistency in pulse shape and chirp, it is still possible however to understand the chirping mechanisms present by investigating the effects of each section on a pulse. When there is no gain dispersion, the instantaneous frequency is given by (7.30) and for low pulse energies the chirp imprinted on the pulse is proportional to the intensity pulse shape. For increasing pulse energies, this proportionality with the pulse shape is damped in time by the energy content of the pulse. As the typical pulse energies in the passively mode-locked lasers are moderate

(on the order of the saturation energy), the chirp imprinted on the pulse has a down and up shape similar to the pulse shape and is thus highly nonlinear. The linear chirp measured for the passively mode-locked lasers can thus not simply come from saturation of the gain region and the associated SPM, but has to come from a more subtle interaction between the different sections.

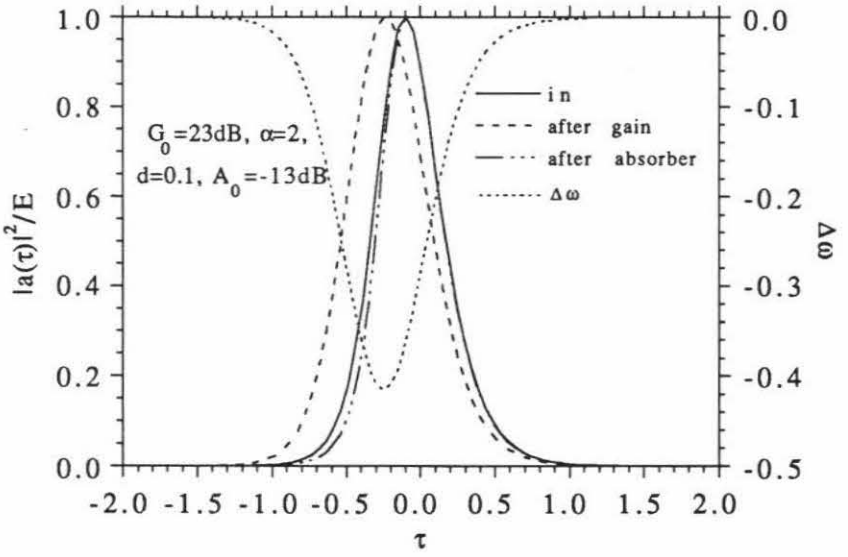

Figure 7.11: Pulse shape and chirp after propagation through a gain region and an absorber region

In order to investigate this, the pulse shapes obtained in the previous section (α=0) were propagated through the same two-section device with the only difference being an α=2 in the gain region (α=0 in the absorber). The results for G_0=23dB are shown in fig. 7.11 for propagation through the gain region followed by propagation through the absorber region. The input pulse (solid line) has no chirp, and after propagation through the gain region two pulse shaping mechanisms can be observed.

First, due to saturation of the gain, the leading edge of the pulse experiences more gain, such that the pulse is advanced in time relative to the group delay (dashed line). Second, a nonlinear down and up chirp has been imprinted on the pulse as discussed above (dotted line), and the chirp is clearly nonlinear. This pulse was then propagated through the absorber region with the following pulse shaping effects. As the leading edge of the pulse is used to saturate the absorber, it is attenuated and the pulse is delayed in time relative to the group delay. As α was taken as zero, no additional SPM is imprinted on the pulse. Even for the small α's that should be used for the absorber, the corresponding up and down chirp will be small compared to the chirp imposed by the gain region. The main effect of this cutting off of the leading edge of the pulse by the absorber, is that the downchirp that is present in the leading edge becomes less important as the power present during the downchirp is much smaller than during the upchirp, and the chirp on the pulse becomes predominantly upward with a strong linear component. Repeated propagation through a combination of saturable gain region with SPM and saturable absorber region, should therefore result in pulses with a strong linear upchirp.

7.6 Conclusion

In this chapter a simple pulse propagation model for saturable media with SPM was developed. First a study of the material parameters was performed to determine the frequency and electron density dependence of the susceptibility of MQW material.

It was found then that only the frequency dependence of the imaginary part of the susceptibility (the gain) depends strongly on the electron density. It was also found that the α-parameter for an absorber section should be very small. Simulation of a two-section device with α=0 was performed, and it was found that the pulse shapes are asymetric with exponential tails, and time-bandwidth products around 0.31.

Simulation of pulse propagation through a saturable gain region with SPM (α=2), followed by a saturable absorber, showed that a combination of SPM in the gain region and absorption in the absorber can lead to a predominantly linear upchirp as the downchirp in the leading edge of the pulse is attenuated in order to saturate the absorber.

Providing there are no other bandwidth limiting elements in the cavity, a broader pulse spectrum should be possible by using optimized devices which demonstrate a broader gain spectrum. It is wellknown that QW material has a broad and flat gain spectrum when operated near the onset of the second quantized state. By optimizing the number of quantum wells and the laser length, it should therefore be possible to generate broader mode-locked spectra, and if the chirp on the pulses still has a strong linear component 100 fs pulses and maybe shorter should be possible.

References

[1] T. Schrans, R. A. Salvatore, S. Sanders, and A. Yariv, *Electron. Lett.*, **28**,1480 (1992)

[2] R. A. Salvatore, T. Schrans, and A. Yariv, *IEEE Photon. Technol. Lett.*, **5**, 756 (1993)

[3] D. J. Derickson, R. J. Helkey, A. Mar, J. R. Karin, J. G. Wasserbauer, and J. E. Bowers, *IEEE J. Quantum Electron.*, **28**, 2186 (1992)

[4] P. J. Delfyett, L. Florez, N. Stoffel, T. Gmitter, N. Andreadakis, G. Alphonse, and W. Ceislik, *Opt. Lett.*, **17**, 670 (1992)

[5] W. B. Jiang, R. Mirin, and J. E. Bowers, *Appl. Phys. Lett.*, **60**, 677 (1992)

[6] W.-H. Xiang, S. R. Friberg, K. Watanabe, S. Machida, W. Jiang, H. Iwamura, and Y. Yamamoto, *Opt. Lett.*, **16**, 1394 (1991)

[7] G. H. C. New, *Opt. Comm.*, **6**, 188 (1975)

[8] G. H. C. New, *IEEE J. Quantum Electron.*, **10**, 115 (1974)

[9] H. A. Haus, *J. Appl. Phys.*, **46**, 3049 (1975)

[10] H. A. Haus, *IEEE J. Quantum Electron.*, **11**, 736 (1975)

[11] H. A. Haus, and Y. Silberberg, *J. Opt. Soc. Am. B*, **2**, 1237 (1985)

[12] S. Sanders, A. Yariv, J. Paslaski, J. E. Ungar, and H. A. Zarem, *Appl. Phys. Lett.*, **58**, 681 (1991)

[13] J. E. Bowers, P. A. Morton, A. Mar, and S. W. Corzine, *IEEE J. Quantum Electron.*, **25**, 1426 (1989)

[14] G. P. Agrawal, and N. A. Olsson, *IEEE J. Quantum Electron.*, **25**, 2297 (1989)

[15] G. P. Agrawal, *IEEE J. Quantum Electron.*, **27**, 1843 (1991)

[16] A. Dienes, J. P. Heritage, M. Y. Hong, and Y. H. Chang, *Opt. Lett.*, **17**, 1602 (1992)

[17] M. Y. Hong, Y. H. Chang, A. Dienes, J. P. Heritage, and P. J. Delfyett, *IEEE J. Quantum Electron.*, to be published

[18] M. S. Stix, M. P. Kesler, and E. P. Ippen, *Appl. Phys. Lett.*, **48**, 1722 (1986)

[19] K. L. Hall, E. P. Ippen, and G. Eisenstein, *Appl. Phys. Lett.*, **56**, 1740 (1990)

[20] C. T. Hultgren, and E. P. Ippen, *Appl. Phys. Lett.*, **59**, 635 (1991)

[21] P. J. Delfyett, Y. Silberberg, and G. A. Alphonse, *Appl. Phys. Lett.*, **59**, 10 (1991)

[22] K. Vahala, L. C. Chiu, S. Margalit, and A. Yariv, *Appl. Phys. Lett.*, **42**, 631 (1983)

[23] A. Yariv, **Quamtum Electronics**, 3rd ed., ch. 12 (1989)

[24] A. E. Siegman, **Lasers**, ch. 10 (1986)

Appendix A

The coupled mode equations

The first derivation of the coupled mode equation started from the wave equation and can be found in [1]. Even though the resulting equations and coupling coefficient expressions for TE modes are correct, they are reached by making unnecessary approximations. A first approximation made is

$$0 = \nabla.(\varepsilon \mathbf{E}) \approx \varepsilon \nabla.\mathbf{E} \Rightarrow \nabla.\mathbf{E} = 0. \tag{A.1}$$

For this approximation to be valid, the dielectric constant ε should not vary much over one wavelength, which is not the case for DFB lasers as the grating in ε has a periodicity of half a wavelength.

The second approximation made is the slowly varying envelope approximation (SVEA), where the second-order derivatives with respect to z (the longitudinal direction) are neglected.

The coupled mode equations can be derived directly from Maxwell's equations

without using these two approximations [2]–[4]. A discussion of why the two approximations yield the correct coupled mode equations can be found in [5]. In this appendix the derivation of the coupled mode equations directly from Maxwell's equations is summarized, with inclusion of the spontaneous emission polarization necessary for noise calculations.

Maxwell's equations in frequency domain ($e^{i\omega t}$) for the DFB laser are given by

$$\nabla \times \mathbf{E} = -i\omega\mu_o \mathbf{H} \tag{A.2}$$

$$\nabla \times \mathbf{H} = i\omega\varepsilon_o \left[n^2(x,y,z) - i\frac{\sigma(x,y,z)}{\omega\varepsilon_o} \right] \mathbf{E} + i\omega \mathbf{P}_{sp} \tag{A.3}$$

$$\nabla . \left[\left(n^2(x,y,z) - i\frac{\sigma(x,y,z)}{\omega\varepsilon_o} \right) \mathbf{E} \right] = 0 \tag{A.4}$$

$$\nabla . \mathbf{H} = 0 \tag{A.5}$$

where $n^2(x,y,z)$ includes the grating and waveguide, $\sigma(x,y,z)$ includes the gain and losses as well as a gain or loss grating, and $\mathbf{P}_{sp}$ is a Langevin noise source describing the spontaneous emission. It is related to $\mathbf{F}(x,y,z;\omega)$ in [6,7] by

$$\mathbf{P}_{sp}(x,y,z;\omega) = -\frac{\mathbf{F}(x,y,z;\omega)}{\omega^2\mu_o} \tag{A.6}$$

with following statistical properties (where $< \cdots >$ denotes ensemble average):

$$\langle \mathbf{F}(x,y,z;\omega) \rangle = 0 \tag{A.7}$$

$$\langle \mathbf{F}(x,y,z;\omega) . \mathbf{F}^*(x',y',z';\omega') \rangle = 2D_{FF^*}\delta(x-x',y-y',z-z')\delta(\omega-\omega'). \tag{A.8}$$

The spontaneous emission noise is thus completely uncorrelated in space and frequency, and using the dissipation fluctuation theorem one finds [6,7]

$$2D_{FF^*} = \frac{4\pi\hbar\omega^3 g(x,y,z) n(x,y,z) n_{sp}(x,y,z)}{c^3\varepsilon_o} \tag{A.9}$$

where g is the material gain, n the material real index, and n_{sp} the spontaneous emission factor which relates the spontaneous emission rate to the stimulated emission rate.

The electric field and magnetic field are developed in terms of the modes of an ideal waveguide $n_o(x,y)$ (i.e., no grating, no gain):

$$\mathbf{E}(x,y,z) = \sum_{q>0} \tilde{a}_q(z)\mathbf{E}_{qt}(x,y) + \sum_{q>0} \tilde{c}_q(z)\mathbf{E}_{qz}(x,y) \tag{A.10}$$

$$\mathbf{H}(x,y,z) = \sum_{q>0} \tilde{b}_q(z)\mathbf{H}_{qt}(x,y) + \sum_{q>0} \tilde{d}_q(z)\mathbf{H}_{qz}(x,y). \tag{A.11}$$

The summation stands for a summation over all modes (guided and radiation modes), $q > 0$ as the coefficients include forward and backward propagating modes (hence the different coefficients for $\mathbf{E}$ and $\mathbf{H}$), and the subscript t stands for the transversal (x,y) component and z for the longitudinal component. The modal fields $(\mathbf{E}_q(x,y)e^{-i\beta_q z}$ and $\mathbf{H}_q(x,y)e^{-i\beta_q z}$ satisfy Maxwell's equations for $n_o(x,y)$:

$$\nabla \times \mathbf{E}_q e^{-i\beta_q z} = -i\omega\mu_o \mathbf{H}_q e^{-i\beta_q z} \tag{A.12}$$

$$\nabla \times \mathbf{H}_q e^{-i\beta_q z} = i\omega\varepsilon_o n_o^2(x,y)\mathbf{E}_q e^{-i\beta_q z} \tag{A.13}$$

$$\nabla . \left(n_o^2(x,y)\mathbf{E}_q e^{-i\beta_q z}\right) = 0 \tag{A.14}$$

$$\nabla . \mathbf{H}_q e^{-i\beta_q z} = 0. \tag{A.15}$$

Splitting (A.12,A.13) in transversal and longitudinal components (using $\nabla = \nabla_t + \mathbf{e}_z \frac{\partial}{\partial z}$) gives:

$$\nabla_t \times \mathbf{E}_{qz} - i\beta_q \mathbf{e}_z \times \mathbf{E}_{qt} = -i\omega\mu_o \mathbf{H}_{qt} \tag{A.16}$$

$$\nabla_t \times \mathbf{H}_{qz} - i\beta_q \mathbf{e}_z \times \mathbf{H}_{qt} = i\omega\varepsilon_o n_o^2 \mathbf{E}_{qt} \tag{A.17}$$

$$\mathbf{H}_{qz} = \frac{i}{\omega\mu_o} \nabla_t \times \mathbf{E}_{qt} \tag{A.18}$$

$$\mathbf{E}_{qz} = -\frac{i}{\omega\varepsilon_o n_o^2} \nabla_t \times \mathbf{H}_{qt}. \tag{A.19}$$

Replacing q by $-q$ yields following relationships between the forward and the backward propagating modes:

$$\beta_{-q} = -\beta_q \;\; ; \;\; \mathbf{E}_{-qt} = \mathbf{E}_{qt} \;\; ; \;\; \mathbf{H}_{-qt} = -\mathbf{H}_{qt} \;\; ; \;\; \mathbf{E}_{-qz} = -\mathbf{E}_{qz} \;\; ; \;\; \mathbf{H}_{-qz} = \mathbf{H}_{qz} \tag{A.20}$$

The longitudinal components of (A.2,A.3) can be used to solve for $\mathbf{H}_z$ and $\mathbf{E}_z$ using (A.18,A.19):

$$\mathbf{E}(x,y,z) = \sum_{q>0} \tilde{a}_q(z)\mathbf{E}_{qt}(x,y) + \frac{n_o^2(x,y)}{n^2(x,y,z) - i\frac{\sigma(x,y,z)}{\omega\varepsilon_o}} \sum_{q>0} \tilde{b}_q(z)\mathbf{E}_{qz}(x,y) - \frac{\mathbf{P}_{spz}}{\varepsilon_o n^2 - i\frac{\sigma}{\omega}} \tag{A.21}$$

$$\mathbf{H}(x,y,z) = \sum_{q>0} \tilde{b}_q(z)\mathbf{H}_{qt}(x,y) + \sum_{q>0} \tilde{a}_q(z)\mathbf{H}_{qz}(x,y). \tag{A.22}$$

The coupled mode equations are then derived using the Lorentz reciprocity relation, which states that given $(\mathbf{E}_1, \mathbf{H}_1)$ and $(\mathbf{E}_2, \mathbf{H}_2)$ that satisfy following equations:

$$\begin{cases} \nabla \times \mathbf{E}_1 = -i\omega\mu_o \mathbf{H}_1 \\ \nabla \times \mathbf{H}_1 = i\omega\varepsilon_o n_1^2 \mathbf{E}_1 + i\omega \mathbf{P}_{sp} \end{cases} \qquad \begin{cases} \nabla \times \mathbf{E}_2 = -i\omega\mu_o \mathbf{H}_2 \\ \nabla \times \mathbf{H}_2 = i\omega\varepsilon_o n_2^2 \mathbf{E}_2 \end{cases} \tag{A.23}$$

the following relationship exists:

$$\iint_{-\infty}^{+\infty} \frac{\partial}{\partial z}\left(\mathbf{E}_{1t}\times\mathbf{H}_{2t}^{*}+\mathbf{E}_{2t}^{*}\times\mathbf{H}_{1t}\right).\mathbf{e}_z dxdy = -i\omega\varepsilon_o \iint_{-\infty}^{+\infty}\left[n_1^2-\left(n_2^2\right)^{*}\right]\mathbf{E}_1.\mathbf{E}_2^{*}dxdy$$
$$-i\omega\iint_{-\infty}^{+\infty}\mathbf{P}_{sp}.\mathbf{E}_2^{*}dxdy. \qquad (A.24)$$

This is the Lorentz reciprocity relation expanded to include the spontaneous emission polarization. Using this theorem orthogonality of the modes can be derived:

$$\frac{1}{2}\iint_{-\infty}^{+\infty}\left(\mathbf{E}_{qt}\times\mathbf{H}_{pt}^{*}\right).\mathbf{e}_z dxdy = P_p\delta_{pq}. \qquad (A.25)$$

To apply this to the DFB laser, n_1 and n_2 are taken as

$$n_1^2 = n^2(x,y,z) - i\frac{\sigma(x,y,z)}{\omega\varepsilon_o} \qquad (A.26)$$

$$n_2^2 = n_o^2(x,y) \qquad (A.27)$$

($\mathbf{E}_1$,$\mathbf{H}_1$) is given by(A.21,A.22), and ($\mathbf{E}_2$,$\mathbf{H}_2$) is a forward mode p

$$\mathbf{E}_2 = \mathbf{E}_p e^{-i\beta_p z} \qquad (A.28)$$

$$\mathbf{H}_2 = \mathbf{H}_p e^{-i\beta_p z}. \qquad (A.29)$$

Substitution of this in the Lorentz reciprocity relation (A.24) gives, using the orthogonality of the modes (A.25):

$$\frac{d}{dz}\left[\tilde{a}_p(z)+\tilde{b}_p(z)\right]+i\beta_p\left[\tilde{a}_p(z)+\tilde{b}_p(z)\right] =$$
$$2\sum_{q>0}\overline{K}_{pq}(z)\tilde{a}_q(z)+2\sum_{q>0}\overline{k}_{pq}(z)\tilde{b}_q(z)+2p_{sp,p}(z)+2P_{sp,pt}(z)+2P_{sp,pz}(z)$$
$$(A.30)$$

with

$$\overline{K}_{pq}(z) = \frac{\omega\varepsilon_o}{4iP_p}\iint_{-\infty}^{+\infty}\left[n^2(x,y,z) - i\frac{\sigma(x,y,z)}{\omega\varepsilon_o} - n_o^2(x,y)\right]\mathbf{E}_{qt}(x,y).\mathbf{E}_{pt}^*(x,y)dxdy \tag{A.31}$$

$$\overline{k}_{pq}(z) = \frac{\omega\varepsilon_o}{4iP_p}\iint_{-\infty}^{+\infty}\frac{\left[n^2(x,y,z) - i\frac{\sigma(x,y,z)}{\omega\varepsilon_o} - n_o^2(x,y)\right]n_o^2(x,y)}{n^2(x,y,z) - i\frac{\sigma(x,y,z)}{\omega\varepsilon_o}}\mathbf{E}_{qz}(x,y).\mathbf{E}_{pz}^*(x,y)dxdy \tag{A.32}$$

$$p_{sp,p}(z) = \frac{i\omega}{4P_p}\iint_{-\infty}^{+\infty}\frac{n^2(x,y,z) - i\frac{\sigma(x,y,z)}{\omega\varepsilon_o} - n_o^2(x,y)}{n^2(x,y,z) - i\frac{\sigma(x,y,z)}{\omega\varepsilon_o}}\mathbf{P}_{sp}(x,y,z).\mathbf{E}_{pz}^*(x,y)dxdy \tag{A.33}$$

$$P_{sp,pt}(z) = \frac{\omega}{4iP_p}\iint_{-\infty}^{+\infty}\mathbf{P}_{sp}(x,y,z).\mathbf{E}_{pt}^*(x,y)dxdy \tag{A.34}$$

$$P_{sp,pt}(z) = \frac{\omega}{4iP_p}\iint_{-\infty}^{+\infty}\mathbf{P}_{sp}(x,y,z).\mathbf{E}_{pz}^*(x,y)dxdy. \tag{A.35}$$

Using a backward mode $-p$ for $(\mathbf{E}_2,\mathbf{H}_2)$ and using (A.20), (A.24) gives

$$\frac{d}{dz}\left[\tilde{a}_p(z) - \tilde{b}_p(z)\right] - i\beta_p\left[\tilde{a}_p(z) - \tilde{b}_p(z)\right] =$$

$$-2\sum_{q>0}\overline{K}_{pq}(z)\tilde{a}_q(z) + 2\sum_{q>0}\overline{k}_{pq}(z)\tilde{b}_q(z) + 2p_{sp,p}(z) - 2P_{sp,pt}(z) + 2P_{sp,pz}(z) \tag{A.36}$$

The coefficients $\tilde{a}_p(z)$ and $\tilde{a}_p(z)$ can be expanded as

$$\tilde{a}_p(z) = a_p(z) + b_p(z)$$

$$\tilde{b}_p(z) = a_p(z) - b_p(z)$$

such that a_p and b_p satisfy the following equations

$$\frac{da_p}{dz} + i\beta_p a_p(z) = \sum_{q>0} K_{pq}^{aa}(z)a_q(z) + \sum_{q>0} K_{pq}^{ab}(z)b_q(z) + p_{sp,p}(z) + P_{sp,pt}(z) + P_{sp,pz}(z) \tag{A.37}$$

$$\frac{db_p}{dz} - i\beta_p b_p(z) = \sum_{q>0} K_{pq}^{ba}(z)a_q(z) + \sum_{q>0} K_{pq}^{bb}(z)b_q(z) + p_{sp,p}(z) - P_{sp,pt}(z) + P_{sp,pz}(z) \tag{A.38}$$

with

$$\begin{aligned} K_{pq}^{aa}(z) &= \overline{K}_{pq}(z) + \overline{k}_{pq}(z) = -K_{pq}^{bb}(z) \\ K_{pq}^{ab}(z) &= \overline{K}_{pq}(z) - \overline{k}_{pq}(z) = -K_{pq}^{ba}(z). \end{aligned} \tag{A.39}$$

The coefficients in the expansions (A.21,A.22) can thus be written as a superposition of a forward propagating mode $a_p(z)$ and a backward propagating mode $b_p(z)$. Equations (A.37,A.38) are the most general form of the coupled mode equations, with the coupling given by (A.39). These equations are valid for any n_1, e.g., a DFB laser, a codirectional coupler or any other structure. The only approximation made so far is that the electric and magnetic field can be expanded into modes of the ideal waveguide. These ideal modes are found by solving (A.12–A.15), while (A.37,A.38) have been obtained by only considering (A.2,A.3). In particular the modes satisfy (A.14),

while the actual electric field has to satisfy (A.4),which includes boundary conditions for layered waveguides, as they are a consequence of (A.4).

The DFB structure can now be introduced in the equations by assuming that $n^2(x,y,z) = n_o^2(x,y)+\Delta n^2(x,y,z)$ and $\sigma(x,y,z)$ are (quasi) periodic in z with (quasi) period Λ. Splitting all K_{pq}'s in an index part and a gain part

$$K_{pq}^{uv}(z) = K_{pq,n}^{uv}(z) + K_{pq,\sigma}^{uv}(z) \qquad u = a,b \;\; \& \;\; v = a,b \tag{A.40}$$

$$\overline{K}_{pq}(z) = \overline{K}_{pq,n}(z) + \overline{K}_{pq,\sigma}(z) \tag{A.41}$$

$$\overline{k}_{pq}(z) = \overline{k}_{pq,n}(z) + \overline{k}_{pq,\sigma}(z) \tag{A.42}$$

the (quasi) periodic functions $K_{pq,n}^{uv}(z)$ and $K_{pq,\sigma}^{uv}(z)$ can be expanded in a localized Fourier series:

$$K_{pq,n}^{uv}(z) = \sum_{\ell=-\infty}^{+\infty} K_{pq,n,\ell}^{uv}(z) e^{i\frac{2\pi\ell}{\Lambda}z} \qquad u = a,b \;\; \& \;\; v = a,b \tag{A.43}$$

with the local fourier coefficients given by

$$K_{pq,n,\ell}^{uv}(z) = \frac{1}{\Lambda}\int_{z-\frac{\Lambda}{2}}^{z+\frac{\Lambda}{2}} K_{pq,n}^{uv}(z') e^{-i\frac{2\pi\ell}{\Lambda}z'} dz' \tag{A.44}$$

and a similar expression for the σ coefficients. This local Fourier series is only valid if the Fourier coefficients do not vary too much over one grating period.

The slowly varying modal amplitudes $A_q(z)$ and $B_q(z)$ are defined as

$$A_q(z) = a_q(z) e^{+i\beta_q z} \tag{A.45}$$

$$B_q(z) = b_q(z) e^{-i\beta_q z}. \tag{A.46}$$

Substituting this in (A.37,A.38) and using the local Fourier series (A.43) gives

$$\begin{aligned}\frac{dA_p}{dz} &= \sum_{q>0}\sum_{\ell=-\infty}^{+\infty} A_q(z)\left[K^{aa}_{pq,n,\ell}(z)+K^{aa}_{pq,\sigma,\ell}(z)\right]e^{-i\left(\beta_q-\beta_p-\frac{2\pi\ell}{\Lambda}\right)z}\\ &+\sum_{q>0}\sum_{\ell=-\infty}^{+\infty} B_q(z)\left[K^{ab}_{pq,n,\ell}(z)+K^{ab}_{pq,\sigma,\ell}(z)\right]e^{+i\left(\beta_q+\beta_p+\frac{2\pi\ell}{\Lambda}\right)z}\\ &+p_{sp,p}(z)e^{+i\beta_p z}+P_{sp,pt}(z)e^{+i\beta_p z}+P_{sp,pz}(z)e^{+i\beta_p z} \qquad \text{(A.47)}\end{aligned}$$

$$\begin{aligned}\frac{dB_p}{dz} &= \sum_{q>0}\sum_{\ell=-\infty}^{+\infty} A_q(z)\left[K^{ba}_{pq,n,\ell}(z)+K^{ba}_{pq,\sigma,\ell}(z)\right]e^{-i\left(\beta_q+\beta_p-\frac{2\pi\ell}{\Lambda}\right)z}\\ &+\sum_{q>0}\sum_{\ell=-\infty}^{+\infty} B_q(z)\left[K^{bb}_{pq,n,\ell}(z)+K^{bb}_{pq,\sigma,\ell}(z)\right]e^{+i\left(\beta_q-\beta_p+\frac{2\pi\ell}{\Lambda}\right)z}\\ &+p_{sp,p}(z)e^{-i\beta_p z}-P_{sp,pt}(z)e^{-i\beta_p z}+P_{sp,pz}(z)e^{-i\beta_p z}. \qquad \text{(A.48)}\end{aligned}$$

For a DFB laser there is some ℓ_o (the order of the grating) and some p for which $\beta_p \approx \frac{\pi\ell_o}{\Lambda} \equiv \beta_o$. In all sumations over q and ℓ only these terms that vary slowly in the phase will play an important role:

$$\begin{aligned}\frac{dA_p}{dz} &= A_p(z)\left[K^{aa}_{pp,n,0}(z)+K^{aa}_{pp,\sigma,0}(z)\right]+B_q(z)\left[K^{ab}_{pp,n,-\ell_o}(z)+K^{ab}_{pp,\sigma,-\ell_o}(z)\right]e^{+2i\Delta\beta z}\\ &+p_{sp,p}(z)e^{+i\beta_p z}+P_{sp,pt}(z)e^{+i\beta_p z}+P_{sp,pz}(z)e^{+i\beta_p z} \qquad \text{(A.49)}\end{aligned}$$

$$\begin{aligned}\frac{dB_p}{dz} &= A_p(z)\left[K^{ba}_{pp,n,\ell_o}(z)+K^{ba}_{pp,\sigma,\ell_o}(z)\right]e^{-2i\Delta\beta z}+B_q(z)\left[K^{bb}_{pp,n,0}(z)+K^{bb}_{pp,\sigma,0}(z)\right]\\ &+p_{sp,p}(z)e^{-i\beta_p z}-P_{sp,pt}(z)e^{-i\beta_p z}+P_{sp,pz}(z)e^{-i\beta_p z} \qquad \text{(A.50)}\end{aligned}$$

with

$$\Delta\beta = \beta_p - \frac{\pi\ell_o}{\Lambda} = \beta_p - \beta_o. \qquad \text{(A.51)}$$

From these equations the gain $\gamma(z)$, effective index component from the grating $\Delta n_{eff,g}(z)$, index coupling coeffcients $\kappa_n(z)$ and gain (loss) coupling coefficients $\kappa_\sigma(z)$ can be defined:

$$-i\frac{\omega}{c}\Delta n_{eff,g}(z) = K^{aa}_{pp,n,0}(z) = -K^{bb}_{pp,n,0}(z) \tag{A.52}$$

$$\gamma(z) = K^{aa}_{pp,\sigma,0}(z) = -K^{bb}_{pp,\sigma,0}(z) \tag{A.53}$$

$$\kappa_n(z) = K^{ab}_{pp,n,-\ell_o}(z) = \left[K^{ba}_{pp,n,\ell_o}(z)\right]^* \tag{A.54}$$

$$i\kappa_\sigma(z) = -K^{ab}_{pp,\sigma,-\ell_o}(z) = \left[K^{ba}_{pp,\sigma,\ell_o}(z)\right]^*. \tag{A.55}$$

This gives:

$$\Delta n_{eff,g}(z) = \frac{\varepsilon_o c}{4P_p\Lambda}\int_{z-\frac{\Lambda}{2}}^{z+\frac{\Lambda}{2}} dz' \iint_{-\infty}^{+\infty} dxdy \left[\Delta n^2 \left|\mathbf{E}_{pt}\right|^2 + \frac{n_o^2}{n^4+\frac{\sigma^2}{\omega^2\varepsilon_o^2}}\left(n^2\Delta n^2 + \frac{\sigma^2}{\omega^2\varepsilon_o^2}\right)\left|\mathbf{E}_{pz}\right|^2\right] \tag{A.56}$$

$$\gamma(z) = -\frac{1}{4P_p\Lambda}\int_{z-\frac{\Lambda}{2}}^{z+\frac{\Lambda}{2}} dz' \iint_{-\infty}^{+\infty} dxdy\ \sigma \left[\left|\mathbf{E}_{pt}\right|^2 + \frac{n_o^4}{n^4+\frac{\sigma^2}{\omega^2\varepsilon_o^2}}\left|\mathbf{E}_{pz}\right|^2\right] \tag{A.57}$$

$$\kappa_n(z) = \frac{\omega\varepsilon_o}{4iP_p\Lambda}\int_{z-\frac{\Lambda}{2}}^{z+\frac{\Lambda}{2}} dz' \iint_{-\infty}^{+\infty} dxdy \left[\Delta n^2 \left|\mathbf{E}_{pt}\right|^2 - \frac{n_o^2}{n^4+\frac{\sigma^2}{\omega^2\varepsilon_o^2}}\left(n^2\Delta n^2 + \frac{\sigma^2}{\omega^2\varepsilon_o^2}\right)\left|\mathbf{E}_{pz}\right|^2\right] e^{i\frac{2\pi\ell_o}{\Lambda}z'} \tag{A.58}$$

$$\kappa_\sigma(z) = -\frac{i}{4P_p\Lambda}\int_{z-\frac{\Lambda}{2}}^{z+\frac{\Lambda}{2}} dz' \iint_{-\infty}^{+\infty} dxdy\ \sigma \left[\left|\mathbf{E}_{pt}\right|^2 - \frac{n_o^4}{n^4+\frac{\sigma^2}{\omega^2\varepsilon_o^2}}\left|\mathbf{E}_{pz}\right|^2\right] e^{i\frac{2\pi\ell_o}{\Lambda}z'}. \tag{A.59}$$

Redefining the slowly varying modal amplitudes $a(\zeta)$ and $b(\zeta)$ as

$$a_p(z) = A_p(z)e^{-i\beta_p z} = a(\zeta)e^{-i\tilde{\beta}_o\zeta} \tag{A.60}$$

$$b_p(z) = B_p(z)e^{+i\beta_p z} = b(\zeta)e^{+i\tilde{\beta}_o\zeta} \tag{A.61}$$

with $\zeta = \frac{z}{L}$, $\tilde{\beta}_o = \beta_o L$ the Bragg wavevector (all "~" refer to normalization to the total length L of the laser), and substituting this in (A.49,A.50) gives the final form of the coupled mode equations

$$\begin{aligned}\frac{da}{d\zeta} &= \left[\tilde{\gamma}(\zeta) - i\Delta\tilde{\beta}(\zeta)\right] a(\zeta) + \left[\tilde{\kappa}_n(\zeta) - i\tilde{\kappa}_\sigma(\zeta)\right] e^{-i\phi(\zeta)} b(\zeta) \\ &\quad + \tilde{p}_{sp,p}(\zeta) e^{+i\tilde{\beta}_o\zeta} + \tilde{P}_{sp,pt}(\zeta) e^{+i\tilde{\beta}_o\zeta} + \tilde{P}_{sp,pz}(\zeta) e^{+i\tilde{\beta}_o\zeta} \qquad \text{(A.62)}\end{aligned}$$

$$\begin{aligned}\frac{db}{d\zeta} &= \left[\tilde{\kappa}_n(\zeta) - i\tilde{\kappa}_\sigma(\zeta)\right] e^{+i\phi(\zeta)} a(\zeta) - \left[\tilde{\gamma}(\zeta) - i\Delta\tilde{\beta}(\zeta)\right] b(\zeta) \\ &\quad + \tilde{p}_{sp,p}(\zeta) e^{-i\tilde{\beta}_o\zeta} - \tilde{P}_{sp,pt}(\zeta) e^{-i\tilde{\beta}_o\zeta} + \tilde{P}_{sp,pz}(\zeta) e^{-i\tilde{\beta}_o\zeta} \qquad \text{(A.63)}\end{aligned}$$

where $\tilde{\kappa}_n(\zeta)$ and $\tilde{\kappa}_\sigma(\zeta)$ now stand for the magnitudes of the coupling coefficients, while the phase of the coupling coefficients is incorporated in $\phi(\zeta)$

$$\tilde{\kappa}_n(\zeta) e^{-i\phi(\zeta)} = \kappa_n(\zeta) L \qquad \text{(A.64)}$$

$$\tilde{\kappa}_\sigma(\zeta) e^{-i\phi(\zeta)} = \kappa_\sigma(\zeta) L \qquad \text{(A.65)}$$

and the detuning factor $\Delta\tilde{\beta}(\zeta)$ is given by

$$\Delta\tilde{\beta}(\zeta) = \left[\beta_p + \frac{\omega}{c}\Delta n_{eff,g}(\zeta) - \beta_o\right] L = \frac{\omega}{c} n_{eff}(\zeta) L - \tilde{\beta}_o. \qquad \text{(A.66)}$$

For TE modes ($\mathbf{E}_z \equiv 0$) all expressions are simpler and given by

$$\Delta n_{eff,g}(\zeta) = \frac{\varepsilon_o c \tilde{\beta}_o}{4\pi P_p \ell_o} \int_{\zeta-\frac{\tilde{\Lambda}}{2}}^{\zeta+\frac{\tilde{\Lambda}}{2}} d\zeta' \iint_{-\infty}^{+\infty} dxdy \; \Delta n^2(x,y,\zeta') \, |\mathbf{E}_{pt}(x,y)|^2 \tag{A.67}$$

$$\tilde{\gamma}(\zeta) = -\frac{\tilde{\beta}_o L}{4\pi P_p \ell_o} \int_{\zeta-\frac{\tilde{\Lambda}}{2}}^{\zeta+\frac{\tilde{\Lambda}}{2}} d\zeta' \iint_{-\infty}^{+\infty} dxdy \; \sigma(x,y,\zeta') \, |\mathbf{E}_{pt}(x,y)|^2 \tag{A.68}$$

$$\tilde{\kappa}_n(\zeta) e^{-i\phi(\zeta)} = \frac{\omega \varepsilon_o \tilde{\beta}_o L}{4\pi i P_p \ell_o} \int_{\zeta-\frac{\tilde{\Lambda}}{2}}^{\zeta+\frac{\tilde{\Lambda}}{2}} d\zeta' \iint_{-\infty}^{+\infty} dxdy \; \Delta n^2(x,y,\zeta') \, |\mathbf{E}_{pt}(x,y)|^2 \, e^{i2\tilde{\beta}_o \zeta'} \tag{A.69}$$

$$\tilde{\kappa}_\sigma(\zeta) e^{-i\phi(\zeta)} = \frac{\tilde{\beta}_o L}{4\pi i P_p \ell_o} \int_{\zeta-\frac{\tilde{\Lambda}}{2}}^{\zeta+\frac{\tilde{\Lambda}}{2}} d\zeta' \iint_{-\infty}^{+\infty} dxdy \; \sigma(x,y,\zeta') \, |\mathbf{E}_{pt}(x,y)|^2 \, e^{i2\tilde{\beta}_o \zeta'} \tag{A.70}$$

$$\tilde{P}_{sp,pt}(\zeta) = \frac{\omega L}{4 i P_p} \iint_{-\infty}^{+\infty} \mathbf{P}_{sp}(x,y,\zeta) . \mathbf{E}^*_{pt}(x,y) \; dxdy \tag{A.71}$$

$$\tilde{P}_{sp,pz}(\zeta) \equiv 0 \tag{A.72}$$

$$\tilde{p}_{sp,p}(\zeta) \equiv 0 \tag{A.73}$$

$$P_p = \frac{1}{2} \iint_{-\infty}^{+\infty} \left[\mathbf{E}_{pt}(x,y) \times \mathbf{H}^*_{pt}(x,y) \right] . \mathbf{e}_z \; dxdy = \frac{\beta^*_p}{2\omega\mu_o} \iint_{-\infty}^{+\infty} |\mathbf{E}_{pt}(x,y)|^2 \; dxdy \tag{A.74}$$

where β_p is real for index guided (loss- or gainless) waveguides.

References

[1] A. Yariv, **Quantum Electronics**, 3rd ed., ch. 22 (1989)

[2] D. Marcuse, **Theory of Dielectric Optical Waveguides**, 2nd ed., ch. 3 (1991)

[3] W. Streifer, M. Osiński, and A. Hardy, *J. Lightwave Technol.*, **5**, 1 (1987)

[4] S.-L. Chuang, *J. Lightwave Technol.*, **5**, 5 (1987)

[5] B. Crosignani, P. Di Porto, and A. Yariv, *Optics Comm.*, **78**, 237 (1990)

[6] C. H. Henry, *J. Lightwave Technol.*, **4**, 288 (1986)

[7] B. J. Tromborg, H. Olesen, and X. Pan, *IEEE J. Quantum Electron.*, **27**, 178 (1991)

Appendix B

The single mode Green's function, the Wronskian, and its functional derivatives

B.1 The Green's function and the Wronskian

The coupled mode equations are derived in appendix A, including the driving force due to a polarization term, (A.62), (A.63) and can be written in vectorial form as

$$\frac{d\mathbf{Z}}{d\zeta} = \mathbf{M}(\zeta)\mathbf{Z}(\zeta) + \mathbf{P}(\zeta) \tag{B.1}$$

with

$$\mathbf{Z}(\zeta) = \begin{bmatrix} a(\zeta) \\ b(\zeta) \end{bmatrix} \tag{B.2}$$

$$\mathbf{M}(\zeta) = \begin{bmatrix} \tilde{\gamma}(\zeta) - i\Delta\tilde{\beta}(\zeta) & [\tilde{\kappa}_n(\zeta) - i\tilde{\kappa}_\sigma(\zeta)]\, e^{-i\phi} \\ [\tilde{\kappa}_n(\zeta) - i\tilde{\kappa}_\sigma(\zeta)]\, e^{+i\phi} & -\tilde{\gamma}(\zeta) + i\Delta\tilde{\beta}(\zeta) \end{bmatrix} \tag{B.3}$$

$$\mathbf{P}(\zeta) = \begin{bmatrix} \tilde{P}_{sp,pt}(\zeta) e^{+i\tilde{\beta}_o\zeta} \\ -\tilde{P}_{sp,pt}(\zeta) e^{-i\tilde{\beta}_o\zeta} \end{bmatrix} \tag{B.4}$$

and where the expression for $\mathbf{P}$ is only valid for TE modes.

Two independent solutions of the homogeneous ($\mathbf{P} = 0$) coupled mode equations can be found by satisfying the boundary conditions on the left ($\mathbf{Z}_L(\zeta)$) or on the right ($\mathbf{Z}_R(\zeta)$). In order to find the Green's function, $\mathbf{G}_1(\zeta, \zeta')$ is defined as the solution to

$$\frac{d\mathbf{G}_1}{d\zeta} = \mathbf{M}(\zeta)\mathbf{G}_1(\zeta, \zeta') + \begin{bmatrix} \delta(\zeta - \zeta') \\ 0 \end{bmatrix} \tag{B.5}$$

satisfying all boundary conditions. Solving this equation gives

$$\mathbf{G}_1(\zeta, \zeta') = \begin{cases} \mathcal{C}_1(\zeta')\mathbf{Z}_L(\zeta) & \zeta < \zeta' \\ \mathcal{C}_2(\zeta')\mathbf{Z}_R(\zeta) & \zeta > \zeta' \end{cases} \tag{B.6}$$

with continuity at $\zeta = \zeta'$ requiring

$$\mathcal{C}_1(\zeta') = \frac{b_R(\zeta')}{b_L(\zeta')a_R(\zeta') - a_L(\zeta')b_R(\zeta')} \tag{B.7}$$

$$\mathcal{C}_2(\zeta') = \frac{b_L(\zeta')}{b_L(\zeta')a_R(\zeta') - a_L(\zeta')b_R(\zeta')}. \tag{B.8}$$

Similarly a function $\mathbf{G}_2(\zeta, \zeta')$ is defined from

$$\frac{d\mathbf{G}_2}{d\zeta} = \mathbf{M}(\zeta)\mathbf{G}_2(\zeta, \zeta') + \begin{bmatrix} 0 \\ -\delta(\zeta - \zeta') \end{bmatrix} \tag{B.9}$$

satisfying all boundary conditions and resulting in

$$\mathbf{G}_2(\zeta, \zeta') = \begin{cases} \mathcal{C}_3(\zeta')\mathbf{Z}_L(\zeta) & \zeta < \zeta' \\ \mathcal{C}_4(\zeta')\mathbf{Z}_R(\zeta) & \zeta > \zeta' \end{cases} \tag{B.10}$$

with

$$\mathcal{C}_3(\zeta') = \frac{a_R(\zeta')}{b_L(\zeta')a_R(\zeta') - a_L(\zeta')b_R(\zeta')} \tag{B.11}$$

$$\mathcal{C}_2(\zeta') = \frac{b_L(\zeta')}{b_L(\zeta')a_R(\zeta') - a_L(\zeta')b_R(\zeta')}. \tag{B.12}$$

The Green's function solution to (B.1) with $\mathbf{P}$ given by (B.4) is then

$$\mathbf{Z}(\zeta) = \frac{-2i\tilde{\beta}_m}{W}\int_0^1 \mathbf{G}(\zeta,\zeta')\mathbf{P}(\zeta')d\zeta' \tag{B.13}$$

with the Wronskian W given by

$$\begin{aligned} W &= -2i\tilde{\beta}_m\left[a_R(\zeta')b_L(\zeta') - b_R(\zeta')a_L(\zeta')\right] \\ &= -2i\tilde{\beta}_m \det\left[\mathbf{Z}_R(\zeta') \quad \mathbf{Z}_L(\zeta')\right] \end{aligned} \tag{B.14}$$

and

$$\mathbf{G}(\zeta,\zeta') = \begin{cases} \mathbf{Z}_L(\zeta)\mathbf{Z}_R^T(\zeta') & \zeta < \zeta' \\ \mathbf{Z}_R(\zeta)\mathbf{Z}_L^T(\zeta') & \zeta > \zeta' \end{cases}. \tag{B.15}$$

The Wronskian W is taken out of the integral in (B.13) as it can be shown that W is ζ independent:

$$\frac{dW}{d\zeta} = (M_{11} + M_{22})\,W \equiv 0 \tag{B.16}$$

as $M_{11} + M_{22} \equiv 0$ (B.3).

The electric field is related to the forward (a) and backward (b) mode by

$$\tilde{E}(\zeta) = a(\zeta)e^{-i\tilde{\beta}_o\zeta} + b(\zeta)e^{bi\tilde{\beta}_o\zeta} \tag{B.17}$$

and has as Green's function solution

$$\tilde{E}(\zeta) = \frac{1}{W}\int_0^1 G(\zeta,\zeta')\tilde{F}(\zeta')d\zeta' \tag{B.18}$$

with

$$G(\zeta,\zeta') = \begin{cases} E_L(\zeta)E_R(\zeta') & \zeta < \zeta' \\ E_R(\zeta)E_L(\zeta') & \zeta > \zeta' \end{cases} \tag{B.19}$$

$$W = -2i\tilde{\beta}_m \left[E_{RF}(\zeta)E_{LB}(\zeta) - E_{RB}(\zeta)E_{LF}(\zeta)\right] \tag{B.20}$$

$$\tilde{F}(\zeta) = \frac{L^2 \iint_{-\infty}^{+\infty} \mathbf{F}(x,y,\zeta).\mathbf{E}^*_{pt}(x,y)dxdy}{\iint_{-\infty}^{+\infty} |\mathbf{E}_{pt}(x,y)|^2 dxdy}. \tag{B.21}$$

Equations (A.6) (A.71) and (A.74) have been used in the derivation of $\tilde{F}$.

B.2 The functional derivatives of the Wronskian

If a change in the Wronskian can be written as

$$\delta W\left[\tilde{\beta}(\zeta),\tilde{\kappa}(\zeta)\right] = \int_0^1 \left[U_1(\zeta')\delta\tilde{\beta}(\zeta') + U_2(\zeta')\delta\tilde{\kappa}(\zeta')\right] d\zeta' \tag{B.22}$$

then U_1 and U_2 are by definition the functional derivatives

$$U_1(\zeta) = \frac{\delta W}{\delta\tilde{\beta}(\zeta)} \tag{B.23}$$

$$U_2(\zeta) = \frac{\delta W}{\delta\tilde{\kappa}(\zeta)}. \tag{B.24}$$

From the definition (B.14) of the Wronskian, a change in W is given by

$$\delta W = -2i\tilde{\beta}_m \left\{[b_L \quad -a_L]\,\delta\mathbf{Z}_R - [b_R \quad -a_R]\,\delta\mathbf{Z}_L\right\} \tag{B.25}$$

with $\tilde{\beta}$ representing $\Delta\tilde{\beta} + i\tilde{\gamma}$ and $\tilde{\kappa}$ representing $\tilde{\kappa}_n - i\tilde{\kappa}_\sigma$. The effect of a change $\delta\tilde{\beta}$ and $\delta\tilde{\kappa}$ on the solutions $\mathbf{Z}_{L,R}$ of the coupled mode equations (B.1) is a solution of

$$\frac{d\delta\mathbf{Z}_{L,R}}{d\zeta} = \mathbf{M}(\zeta)\delta\mathbf{Z}_{L,R}(\zeta) + \delta\mathbf{M}(\zeta)\mathbf{Z}_{L,R}(\zeta) \tag{B.26}$$

with

$$\delta\mathbf{M}(\zeta) = \begin{bmatrix} -i\delta\tilde{\beta}(\zeta) & \delta\tilde{\kappa}(\zeta)e^{-i\phi} \\ \delta\tilde{\kappa}(\zeta)e^{+i\phi} & +i\delta\tilde{\beta}(\zeta) \end{bmatrix}. \tag{B.27}$$

Equation (B.26) is identical to (B.1) with $\mathbf{P}$ replaced by $\delta\mathbf{M}\ \mathbf{Z}_{L,R}$ and can thus be solved using the Green's function (B.13) with addition of an arbitrary solution of the homogeous equation:

$$\delta\mathbf{Z}_{L,R}(\zeta) = -\frac{2\tilde{\beta}_m}{W}\int_0^1 \mathbf{G}(\zeta,\zeta')\begin{bmatrix} b_{L,R}(\zeta') \\ a_{L,R}(\zeta') \end{bmatrix}\delta\tilde{\beta}(\zeta')d\zeta'$$

$$+ \frac{2i\tilde{\beta}_m}{W}\int_0^1 \mathbf{G}(\zeta,\zeta')\begin{bmatrix} a_{L,R}(\zeta')e^{i\phi} \\ -b_{L,R}(\zeta')e^{-i\phi} \end{bmatrix}\delta\tilde{\kappa}(\zeta')d\zeta' + \mathcal{C}_{1L,R}\mathbf{Z}_L(\zeta) + \mathcal{C}_{2L,R}\mathbf{Z}_R(\zeta). \tag{B.28}$$

As the boundary conditions for any solution of (B.1) are fixed by the laser structure, the boundary conditions for $\delta\mathbf{Z}_{L,R}$ are

$$\delta\mathbf{Z}_L(0) = 0 \tag{B.29}$$

$$\delta\mathbf{Z}_R(1) = 0. \tag{B.30}$$

Solving (B.29) for $\mathcal{C}_{1L}$ and $\mathcal{C}_{2L}$ using (B.28) and $\mathbf{G}(0,\zeta') = \mathbf{Z}_L(0)\mathbf{Z}_R^T(\zeta')$ gives

$$\mathcal{C}_{1L} = \frac{2\tilde{\beta}_m}{W}\int_0^1 \mathbf{Z}_R^T(\zeta')\begin{bmatrix} b_L(\zeta') \\ a_L(\zeta') \end{bmatrix}\delta\tilde{\beta}(\zeta')d\zeta'$$

$$- \frac{2i\tilde{\beta}_m}{W}\int_0^1 \mathbf{Z}_R^T(\zeta')\begin{bmatrix} a_L(\zeta')e^{i\phi} \\ -b_L(\zeta')e^{-i\phi} \end{bmatrix}\delta\tilde{\kappa}(\zeta')d\zeta' \tag{B.31}$$

$$\mathcal{C}_{2L} = 0. \tag{B.32}$$

Solving (B.30) for $\mathcal{C}_{1R}$ and $\mathcal{C}_{2R}$ using (B.28) and $\mathbf{G}(1,\zeta') = \mathbf{Z}_R(1)\mathbf{Z}_L^T(\zeta')$ gives

$$\mathcal{C}_{1R} = 0 \tag{B.33}$$

$$\mathcal{C}_{2R} = \frac{2\tilde{\beta}_m}{W}\int_0^1 \mathbf{Z}_L^T(\zeta')\begin{bmatrix} b_R(\zeta') \\ a_R(\zeta') \end{bmatrix}\delta\tilde{\beta}(\zeta')d\zeta' - \frac{2i\tilde{\beta}_m}{W}\int_0^1 \mathbf{Z}_L^T(\zeta')\begin{bmatrix} a_R(\zeta')e^{i\phi} \\ -b_R(\zeta')e^{-i\phi} \end{bmatrix}\delta\tilde{\kappa}(\zeta')d\zeta'. \tag{B.34}$$

Substituting (B.28), (B.31)-(B.34) into the expression (B.25) for δW gives

$$\delta W = 2\tilde{\beta}_m\int_0^1 \left[a_L(\zeta')b_R(\zeta') + a_R(\zeta')b_L(\zeta')\right]\delta\tilde{\beta}(\zeta')d\zeta' - 2i\tilde{\beta}_m\int_0^1 \left[a_L(\zeta')a_R(\zeta')e^{i\phi} - b_L(\zeta')b_R(\zeta')e^{-i\phi}\right]\delta\tilde{\kappa}(\zeta')d\zeta'. \tag{B.35}$$

The functional derivatives are thus, using (B.17) and (B.22)-(B.24):

$$\frac{\delta W}{\delta\tilde{\beta}(\zeta)} = 2\tilde{\beta}_m\left[E_{LF}(\zeta)E_{RB}(\zeta) + E_{RF}(\zeta)E_{LB}(\zeta)\right] \tag{B.36}$$

$$\frac{\delta W}{\delta\tilde{\kappa}(\zeta)} = -2i\tilde{\beta}_m\left[E_{LF}(\zeta)E_{RF}(\zeta)e^{i(2\tilde{\beta}_o\zeta+\phi)} - E_{LB}(\zeta)E_{RB}(\zeta)e^{-i(2\tilde{\beta}_o\zeta+\phi)}\right]. \tag{B.37}$$

When the lasing condition $W = 0$ is satisfied, the fields E_L and E_R satisfy $E_L = E_R = E_o$, and the functional derivatives become

$$\frac{\delta W}{\delta\tilde{\beta}(\zeta)} = 4\tilde{\beta}_m E_{oF}(\zeta)E_{oB}(\zeta) \tag{B.38}$$

$$\frac{\delta W}{\delta\tilde{\kappa}(\zeta)} = -2i\tilde{\beta}_m\left[E_{oF}^2(\zeta)e^{i(2\tilde{\beta}_o\zeta+\phi)} - E_{oB}^2(\zeta)e^{-i(2\tilde{\beta}_o\zeta+\phi)}\right]. \tag{B.39}$$